

Understanding and applying extracellular recordings
in awake, behaving animals

Thesis by

Matthew Nelson

In Partial Fulfillment of the Requirements for the
Degree of Doctor of Philosophy

California Institute of Technology

Pasadena, California

2012

Defended July 6, 2011

Submitted online June 8, 2012

Acknowledgement

I must extend my deepest thanks and appreciation to my advisor Pierre Pouget for his continued support, scientific contributions, belief in me and helpful advice.

I wish to thank the CNS option for giving me the chance to complete my thesis in the unorthodox manner in which I have done it. In particular, I must also give my deepest appreciation and gratitude to Shin Shimojo for supporting and guiding me through the process of changing labs and institutions, and for finding the time to follow through with me during my years in graduate school to see that I completed it. I do sincerely appreciate the chance that I have been given with this, and I intend to capitalize on it by having a productive and innovative career that positively affects the field.

For their support and contribution to the work that I did in their labs, I sincerely thank Richard Andersen, Jeff Schall and Laurent Venance. Individually, I sincerely thank Richard Andersen for being supportive of me when changing labs and thereafter; Jeff Schall for taking me into his lab and guiding me while I was there; and Laurent Venance for being a terrific collaborator and making possible the important projects we have done with him. I also sincerely thank Bijan Pesaran for teaching me the technique of electrophysiological recordings and, through this experience, the mindset of a good experimentalist; and Clementine Boesch for all her work on the patch-clamp experiments, for being an overall nice person and for being patient enough to tolerate my crappy French and still consistently speak to me in that language, which has helped my use of it.

Finally, I wish to thank my parents for being good supportive parents and letting me lead my own life while wanting me to lead it the best that I can.

Abstract

Section I of this thesis presents specific projects applying extracellular recordings in macaques. The results demonstrate a novel relative position code employed by individual neurons in the dorsal premotor cortex during reaches and saccades, which may be important for hand-eye coordination. Another project suggests low-frequency coherence between dorsal premotor and posterior parietal cortices participates in making internally guided decisions of where to reach. Section II investigates analysis of data collected with this technique. One project compares methodologies for computing trial-by-trial coherence among neuron ensembles, and another documents how the innate nonstationarity of animal behavior can affect conclusions of certain analyses. Section III investigates the acquisition of extracellular electrophysiological data to understand how these recorded voltages relate to underlying neural activity. One project verifies a physical model of the microelectrode recording circuit using electrodes suspended in saline. Some lower-input impedance head stages used in the field are shown to result in electrode impedance and frequency-dependent amplitude attenuations and phase shifts of recorded signals. Other projects present a theoretical argument that local field potentials (LFPs) recorded from in-depth microelectrodes should be independent of electrode impedance within the range of impedances typically used. A simple physical model shows that if and only if gradients of LFP coherence exist at a scale finer than an electrode's recording site size, lower-impedance electrodes report higher coherence. However this is not expected to occur between different microelectrodes, but could explain differences between microelectrode and EEG recordings. The final project uses simultaneous extracellular and intracellular recordings in corticostriatal rat brain slices to show that frequency-dependent phase shifts and amplitude attenuations occur in neural tissue itself and characterize the transfer function between the intracellular and extracellular voltages. Inhomogenous microscale obstructions inherent in neural tissue are shown to differentially distort

current flow depending on the severity of the obstructions. This challenges existing beliefs about the nature of current flow in the brain, and should be considered when interpreting electrophysiological data.

Table of contents

Introduction	1
Section I. Results from awake, behaving extracellular recording projects— Neural activity underlying hand-eye coordination and reach decisions in dorsal premotor cortex and parietal reach region	4
Chapter 1: Dorsal premotor neurons encode the relative position of the hand, eye and goal during reach planning	5
Chapter 2: A relative position code for saccades in dorsal premotor cortex	36
Chapter 3: Free choice activates a decision circuit between frontal and parietal cortex	77
Section II: Investigations of analytical methodology for awake, behaving extracellular recording data	97
Chapter 4: Analysis of per-trial correlations of ensemble spike-spike coherence	98
Chapter 5: Nonindependent and nonstationary response times in stopping stepping saccade tasks	126
Section III: Investigations of the acquisition of extracellular recordings in awake behaving animals: Understanding how the recorded voltage relates to neural activity	179
Chapter 6: Review of signal distortion through metal microelectrode recording circuits and filters	180
Chapter 7: Do electrode properties create a problem in interpreting local field potential recordings?	239
Chapter 8: Physical model of coherent potentials measured with different electrode recording site sizes	251
Chapter 9: Electrical signal distortion in neural tissue on a microscale	287
Chapter contributions and status of publications	319

Introduction

How do we know what we know about the brain? Different methodologies have revealed many things. The advent of in vivo extracellular recording has been an important methodological advance in neuroscience and much knowledge of the workings of the brain has been gained from its application.

I have used this technique for my doctoral thesis in several projects investigating how the brain coordinates hand and eye movements, and makes choices of which targets to reach to. The results of these projects are discussed in Section 1 of this thesis. In Chapter 1 we discover and describe a novel frame of spatial reference for the neural activity in dorsal premotor cortex (PMd) when an animal prepares a reach movement. In Chapter 2 we show that this same spatial frame of reference applies to neuronal activity in the same area, PMd, when the animal is preparing a saccade, indicating that this area and this reference frame may be important for hand-eye coordination. In Chapter 3 we describe how there is increased long-range neuronal coherence between PMd and the parietal reach region when the animal makes an internally guided choice about where to reach rather than following instructions.

Following this work, to improve our understanding of the use of electrophysiology in awake behaving animals, I have investigated some practical issues involving analyses of this data (Section II). In Chapter 4 we compare various methods for per-trial correlations of neuronal coherence across an ensemble of simultaneously recorded spike trains with other metrics of neural and behavioral activity. This is a challenge because typically multiple trials are needed to obtain coherence estimates, which are themselves analogous to correlations across estimates. We find that a leave-one-trial-out method which has appeared previously in the literature performed the best. In addition to neural activity, behavioral data are of importance in this technique, and reaction time in particular has proven to be a very useful measure to provide insight on neural processes. However, our behavior, and indeed our neural processes, are never static over time. In Chapter 5 we

document the nonstationarity of response times in a stopping and a stepping task in humans and monkeys, and show how this can affect some analyses in surprising ways if not anticipated and accounted for.

Finally, I have investigated some issues involving physical acquisition of electrophysiological data, in particular how recorded voltages relate to neural activity (Section III). In Chapter 6 we show the properties of the recording circuit, in particular the relation between the electrode impedance and the first amplifier input impedance, as well as any analog filters used during acquisition can induce distortions between the voltages recorded and the neural activity known to be at the electrode tip in an artificial saline recording. In Chapter 7, we describe an important theoretical argument that describes why the impedance of metal microelectrodes should not be expected to appreciably affect recorded local field potential activity. This argument follows from the nature of the system that we demonstrated in Chapter 6 and other quantitative data gleaned from various sources. We investigate this question further in Chapter 8 where we use a simple physical model to show that any differences in the recording of coherence relating to electrode size, shape or impedance requires a spatial gradient of distantly coherent activity in the tissue itself. When such an activity profile does exist however, the model shows that very low-impedance electrodes are expected to report higher coherence between areas on average. Altogether this suggests a possible subtle difference in the types of activity signals reported between large scalp or cortical surface electrodes and microelectrodes, but likely not between microelectrodes of different impedances within the range of those typically used in extracellular recordings. And last, in Chapter 9, we document signal distortion that can occur within the brain itself by investigating the relationship between intracellular voltages and simultaneously recorded extracellular voltages using a novel application of existing extracellular and intracellular recording techniques in rat brain slice preparations. We furthermore show that the presence or absence or

inhomogenous microscale obstructions of current flow that are inherently present in local neural tissue surrounding sources of electrical activity differentially affects this signal distortion.

Section I: Results from awake, behaving extracellular recording projects— Neural activity underlying hand-eye coordination and reach decisions in dorsal premotor cortex and parietal reach region

Chapter 1

Dorsal premotor neurons encode the relative position of the hand, eye and goal during reach planning

BACKGROUND

Reaching to pick up a cup often involves not only generating a pattern of muscle activity in the arm that will move the limb and grasp the cup, but also coordinating a movement of the eyes to the same place. These visually guided movements require sensory-motor transformations to convert incoming visual information about target location into outgoing patterns of muscle activity (Andersen and Buneo, 2002; Kalaska et al., 1997; Shadmehr and Wise, 2005). Work investigating reference frames has been useful for understanding the transformations needed to guide individual movements of the hand and eye. In contrast, the reference frames involved in coordinating these movements are likely to play a major role in understanding interactions between the saccadic and reach systems but have received relatively little attention.

One reason for this dearth of investigation is that reference frames are almost always defined as centered on individual body parts such as the eye or hand rather than multiple body parts. Eye-centered reference frames have been found in eye movement areas (Barash et al., 1991b; Goldberg and Bruce, 1990; Mays and Sparks, 1980) and in the parietal reach region (PRR) of posterior parietal cortex (PPC) which is at an early stage of the reaching pathway (Batista et al., 1999). Reference frames centered on other body parts, such as the hand, are stable across eye movements and are well-suited for the motor output stage of reaches (Graziano and Gross, 1998). Such body-part centered reference frames are thought to be present in the dorsal premotor (Caminiti et al., 1990; Caminiti et al., 1991; Crammond and Kalaska, 1994; Fu et al., 1993; Johnson et al., 1996; Shen and Alexander, 1997) (PMd) and ventral premotor (Fogassi et al., 1992; Graziano et al., 1994; Kakei et al., 2001) (PMv) areas of frontal cortex.

Here, we investigate reference frames that can be centered on multiple body parts as well as just one body part. For example, we can define a reference frame centered on the hand, the eye, and the hand with respect to the eye. In such an encoding, the same activity is present when the three variables, hand, eye and target, have a particular configuration, even though they may

occupy different absolute positions in space. Relative position is also useful for performing the sensory-motor transformations between spatial systems that are necessary for coordination because this reference frame can be used to go directly from an eye-centered reference frame into a hand-centered reference frame and back again (Buneo and Andersen, 2006).

To see whether eye position signals in premotor cortex are combined with hand and target position in a relative position code, we recorded a population of neurons in the PMd cortex of two monkeys during a delayed reach task in which we independently varied the position of the eye, hand and target across a range of locations. Another population of neurons in MIP was recorded under identical conditions for comparison.

RESULTS

Behavioral task and reference frame analysis

Movement commands can be represented in two complementary spaces — an extrinsic space given by the endpoints of movements and an intrinsic space given by the joint angles and muscle activations needed to achieve the movement endpoint. While eye and arm movements have distinct intrinsic spaces they can be considered to share a common extrinsic space where both movements can be coordinated. **Figure 1.1a** shows the geometry of the extrinsic space. The motor command for the saccade needs the position of the target with respect to the eye, T_E , while the motor command for the reach needs the position of the target with respect to the hand, T_H . These movement vectors are related to each other through another vector, the relative position of the hand and eye, which can equally be viewed as hand position with respect to the eye or eye position with respect to the hand (H_E and E_H). We will refer to this vector as H_E , equivalent to the hand in eye coordinates (Buneo and Andersen 2006). To coordinate hand and eye movements, the brain needs to integrate these pieces of information so neural responses can depend on eye position, hand position and target position.

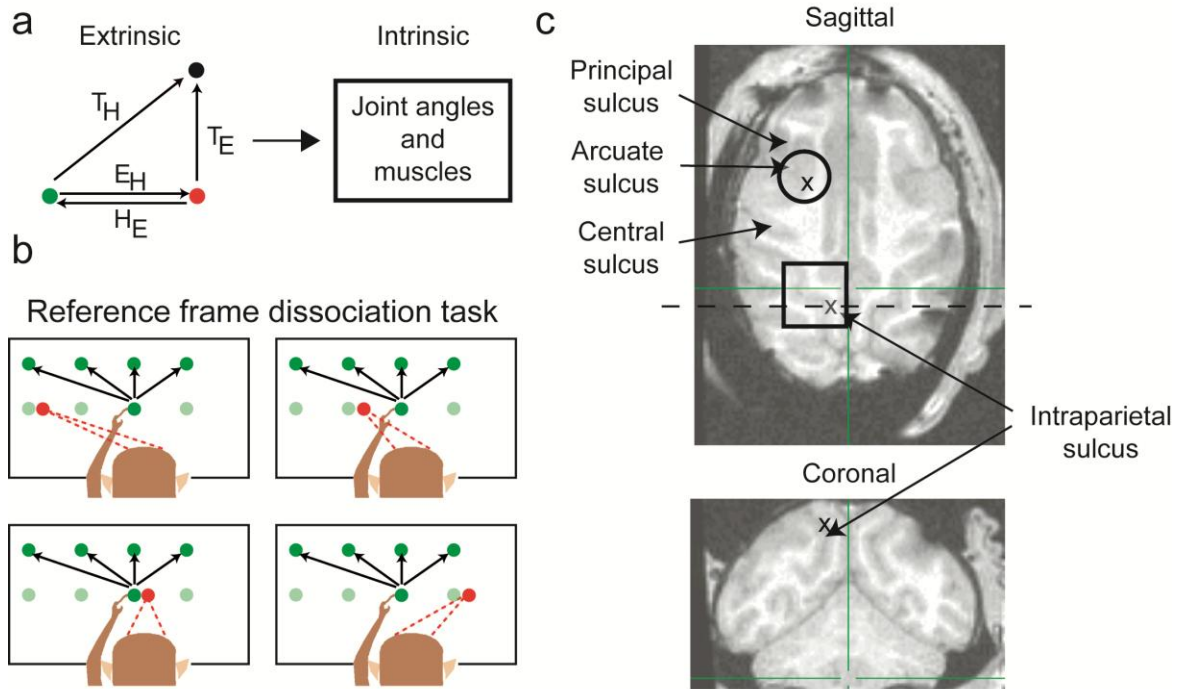


Figure 1.1

Since all three vectors may be simultaneously represented in single-cell activity, we developed a reference frame dissociation task (**Fig 1.1b**), to independently control eye, hand and target position and then analyzed neuronal responses to all three variables. In this task, we instructed eye and hand position to one of four locations and then instructed a delayed reach without a saccade to a target at one of four positions above or below the starting point (see **Methods**). Independently controlling each variable across a range of values was necessary to allow us to determine the spatial reference frame by distinguishing between a representation of the target in eye coordinates, the target in hand coordinates and the relative position of the hand and eye.

The panels of **Figure 1.2** illustrate three idealized neuronal responses to the reference frame dissociation task each illustrating a different reference frame. The firing rate is modeled as a Gaussian response field and, in **Figs. 1.2a and 1.2b**, multiplied by a monotonic “gain field” (Andersen et al., 1985). Responses are represented as three two-dimensional matrices at the

response field peak consisting of the firing rate at each of four target and eye positions (target-eye, TE), hand and eye positions (hand-eye, HE) and target and hand positions (target-hand, TH). The eye-centered cell has a reference frame centered on the eye with a gain field of hand position and encodes the vector T_E (**Fig 2a**). The hand-centered cell has a reference frame centered on the hand with a gain field of eye position and encodes the vector T_H (**Fig 2b**). The relative position cell has a reference frame centered on the hand and eye so that the activity encodes the relative position of the hand and eye and encodes three vectors, T_E , T_H and H_E (**Fig 2c**).

Idealized neuronal responses

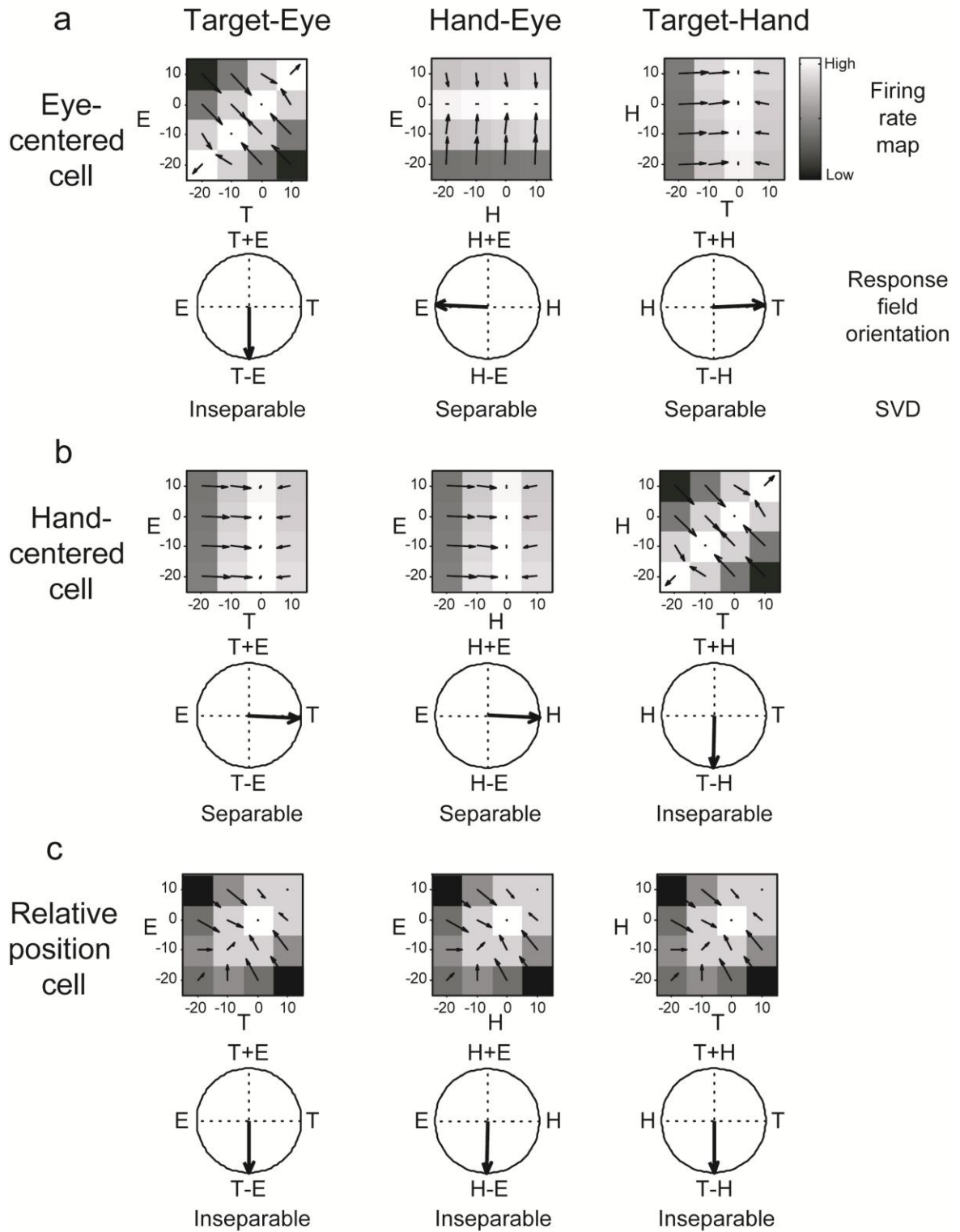


Figure 1.2

We used separability, determined from a singular value decomposition, and response field

orientation, determined from a gradient analysis (see **Methods**), of each of the three response matrices to differentiate between the reference frames. Separability decides whether the variables are combined in a gain field. If the response is inseparable then the response field orientation is useful for quantifying how much the response shifts as the variables are changed. For the idealized responses, the eye-centered cell has an inseparable TE response whose orientation is -90° , a separable HE response whose orientation is 177° and a separable TH response whose orientation is 3° (**Fig 1.2a**). The hand-centered cell has a separable TE response whose orientation is -3° , a separable HE response whose orientation is -3° and an inseparable TH response whose orientation is -90° (**Fig 1.2b**). The relative position cell has inseparable TE, HE and TH responses all of whose orientations are -90° (**Fig 1.2c**). Note that while gain fields can modulate the responses (see, for example, the HE plot of the eye-centered cell), they cannot make them inseparable. In contrast, inseparable encoding of a pair of variables with a response field orientation of -90° indicates the encoding is a vector and not a gain field.

Separable and inseparable eye-hand-target tuning

We recorded the activity of 111 PMd neurons (73 Monkey Z, 38 Monkey E) and 48 MIP neurons (42 Monkey Z, 6 Monkey E) during the reference frame dissociation task to determine the reference frame of cells in each area (**Fig 1.1b; Methods**). **Figure 1.3** shows the response of an example PMd cell during this task. Changing hand or eye position for a given target position results in a robust change in firing, visible by comparing rasters of the same color across neighboring panels either within rows or columns. Similar changes in firing are also present when changing target position for a given hand and eye position, visible by comparing rasters of different colors in the same panel.

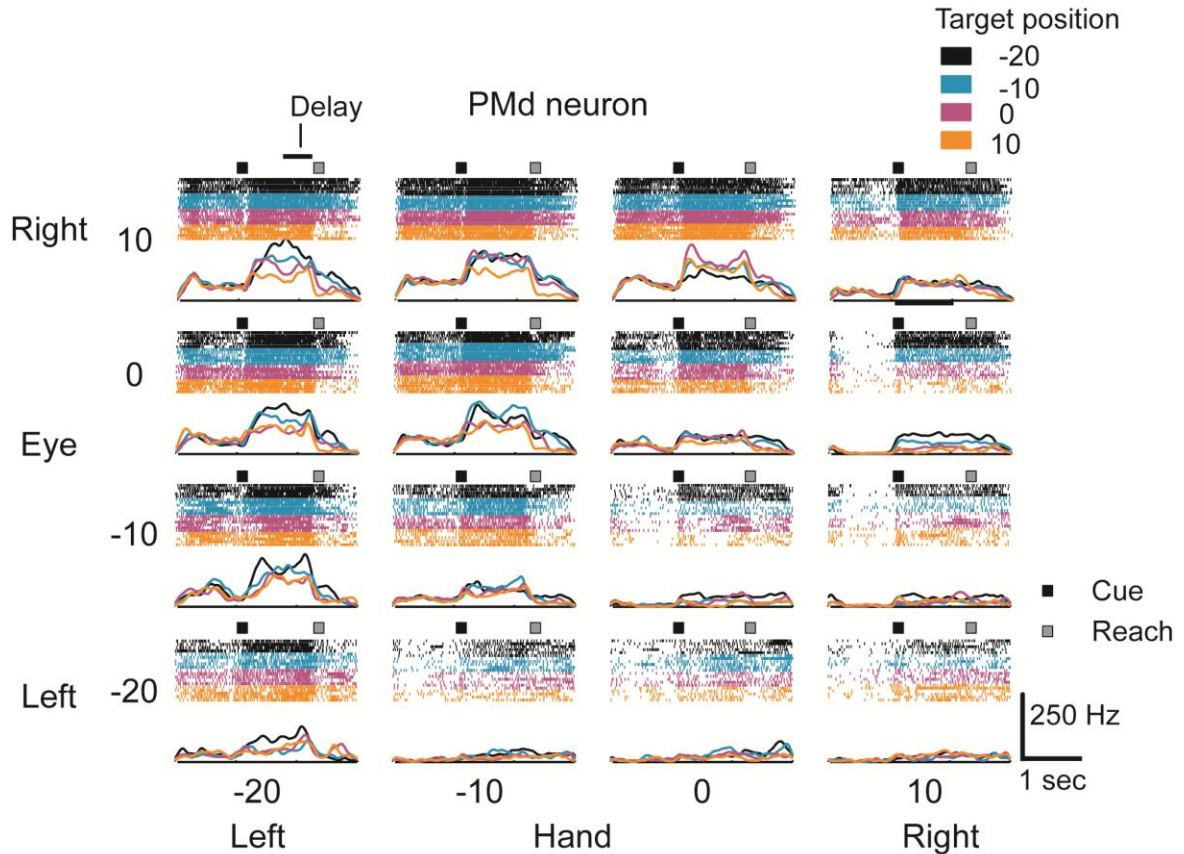


Figure 1.3

Figure 1.4 shows the TE, HE and TH response matrices for the example PMd cell in **Figure 1.3** at the peak of the response field during the delay period. Plotting the data in this way shows how the TE response is suppressed for the target to the right of the eye and increases as the target is moved further to the left of the eye. Similar effects are present for the HE and TH responses. By analyzing the TE, HE and TH response matrices we found the TE, HE and TH responses were inseparable for this cell ($p < 0.05$) and the orientations were all diagonal, with a dominance of eye and hand position over target position (TE response field orientation: -130° , **Fig 1.4d**; HE response field orientation -77° , **Fig 1.4e**; TH response field orientation: -146° , **Fig 1.4f**). Since all the variable pair responses are inseparable for this cell the influence of one variable on another is not due to a gain field modulating a response centered on one variable. Therefore, this cell is a relative position cell.

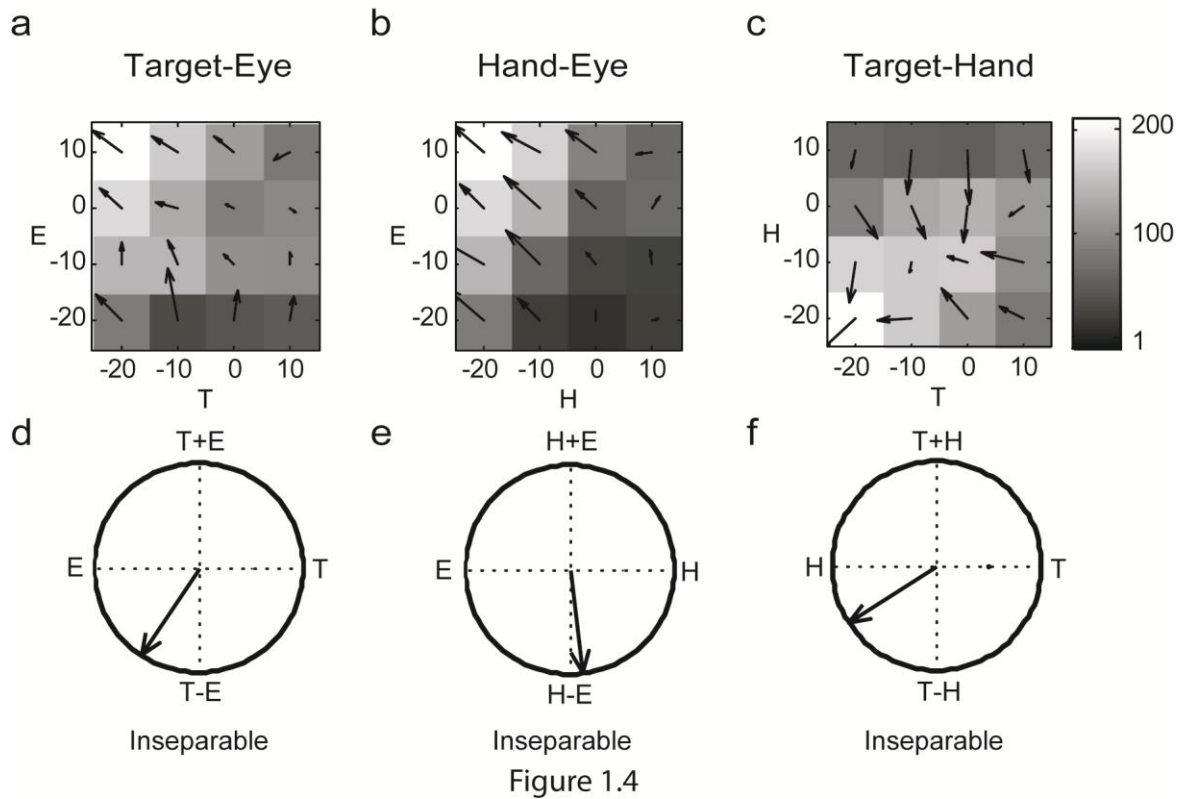
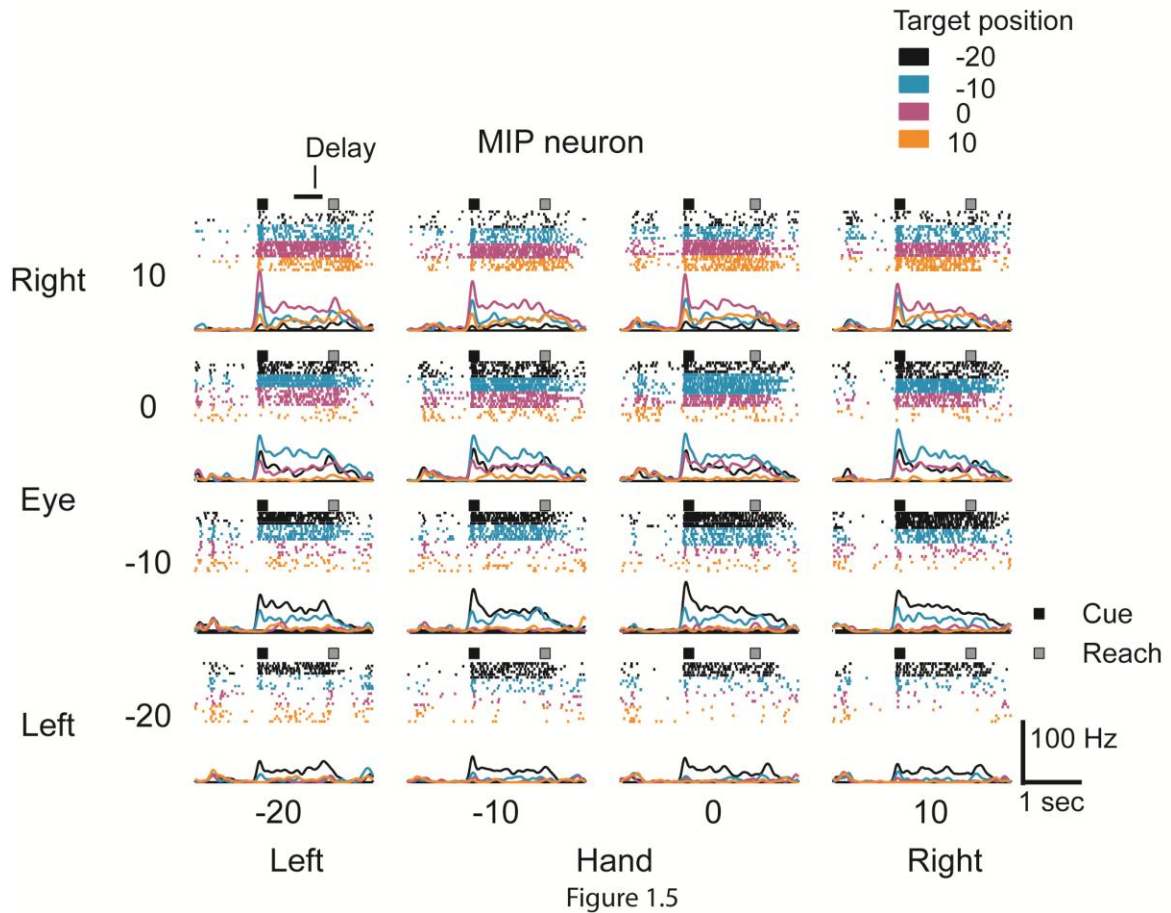
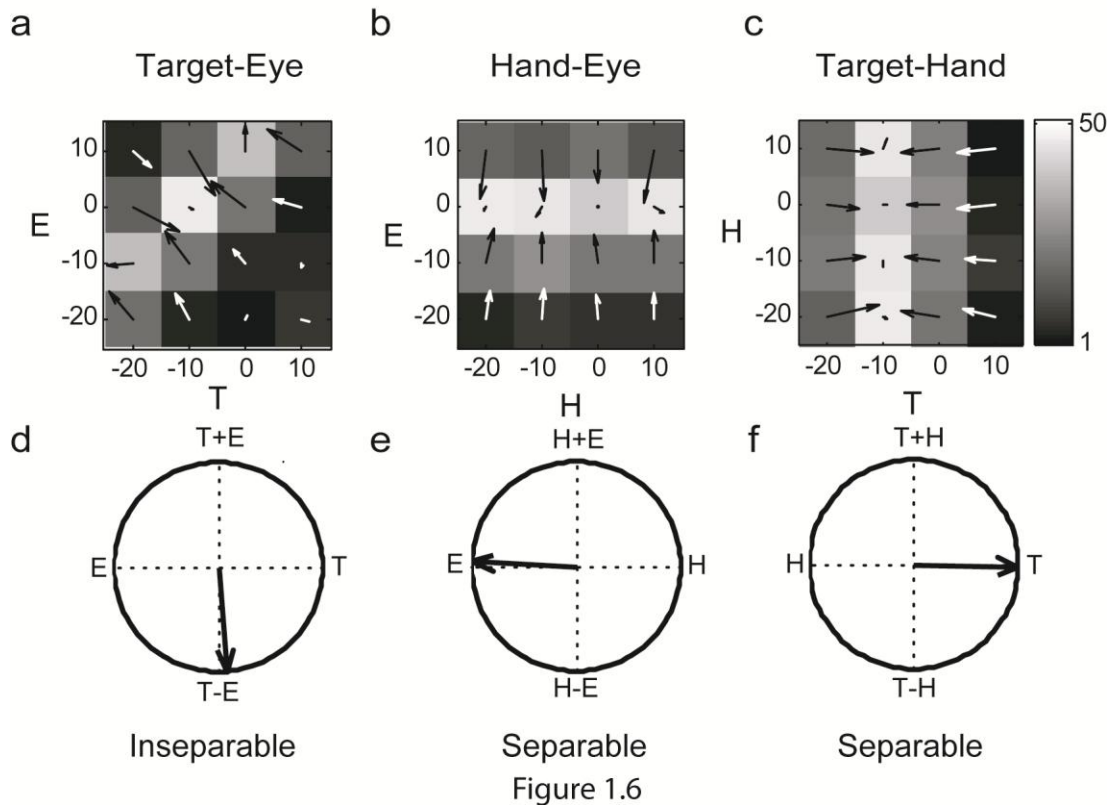


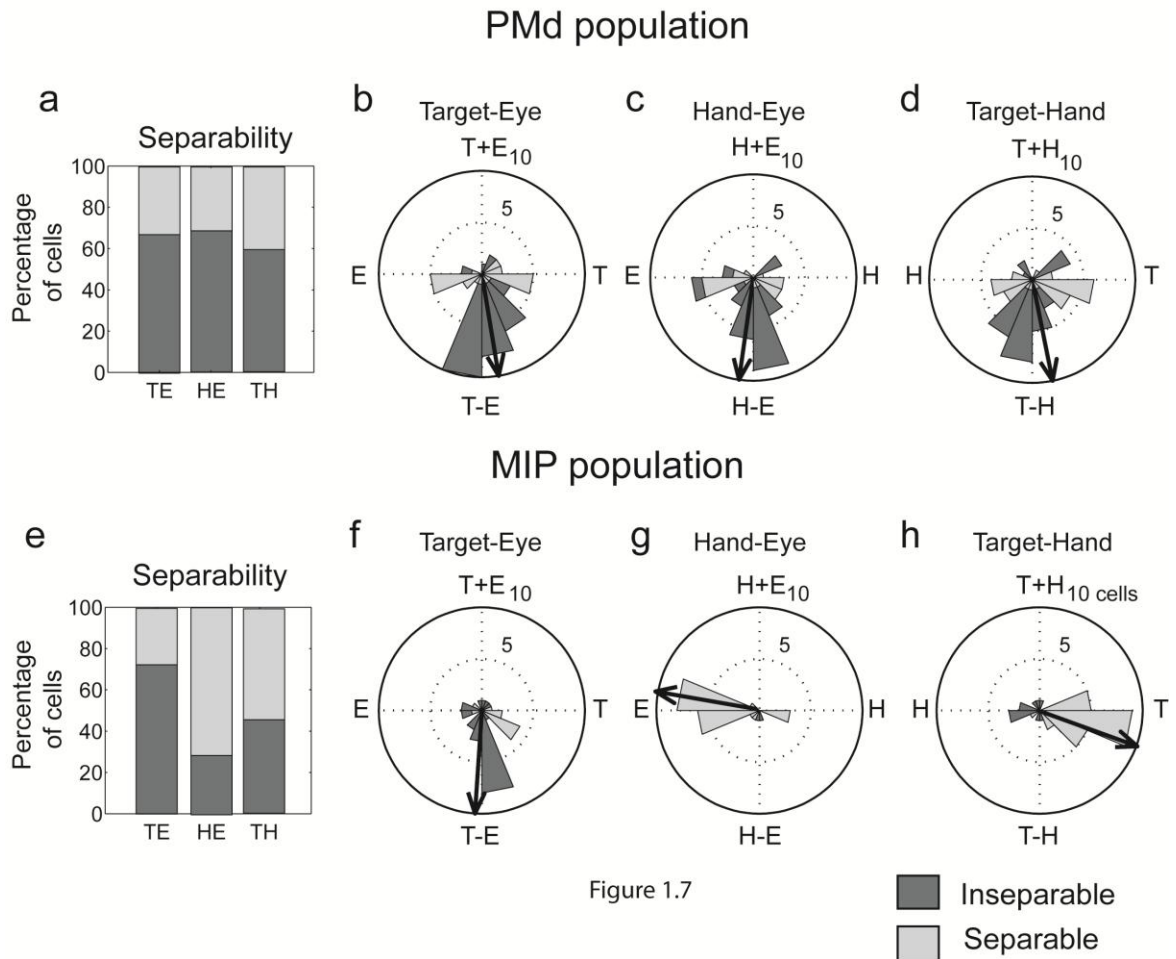
Figure 1.5 shows the response of an example MIP neuron to the reference frame dissociation task. Unlike the PMd cell, large changes in firing are only present when changing eye position for a given target position, visible by comparing rasters of the same color across panels in different rows, or target position for a given eye position, visible by comparing rasters of different colors within a row. Changing hand position alone does not result in a large change in firing rate.



The TE, TH and HE response matrices for the example MIP neuron let us analyze this pattern (**Fig 1.6**). Similar to the PMd cell response, the TE response for the example MIP neuron was inseparable (**Fig 1.6a**) with a response field orientation of -86° (**Fig 1.6d**). In contrast, the TH and HE responses for this cell were separable (**Fig 1.6b–c**). The TH response was dominated by target position (TH response field orientation: 0° , **Fig 1.6e**) with little effect of hand position. The HE response was dominated by eye position (HE response field orientation: 177° , **Fig 1.6f**) again with little effect of hand position. Therefore, this cell is an eye-centered cell and represents target position with respect to eye position alone, in agreement with previously published reports (Batista et al., 1999; Buneo et al., 2002).



Analysis of the delay period responses across a population of neurons in each area reinforced the distinction that PMd neurons had a relative position code while MIP neurons had an eye-centered code (**Fig 1.7**). Across the population, a majority of PMd neurons were tuned to the TE variable pair (63/111 (57%), $p < 0.05$, Randomization test (see **Methods**)), as well as the TH variable pair (63/111 (57%)) and the HE variable pair (58/111 (52%)) tuning. The number of cells tuned to each variable pair is different because some cells were tuned to only one of the three variables. Tuned TE, TH and HE responses of PMd neurons were mostly inseparable (**Fig 1.7a**. TE: 42/63 (67%). TH: 38/63 (60%) HE: 40/58 (69%). $p < 0.05$) indicating that a gain field mechanism could not account for the responses of these neurons. Analysis of the response field orientation for these inseparable cells showed that the mean response field orientations pointed down (**Fig 1.7b-d**. TE: -81° . TH: -79° . HE: -98°). This means that response fields almost completely shifted when either of the hand, eye or target was moved with respect one of the other variables.



Across the population of 48 MIP neurons, 33 cells showed TE tuning (69%), 41 cells showed TH tuning (85%), and 28 cells showed HE tuning (58%). The distribution of separable and inseparable responses for these tuned MIP neurons was markedly different than that of PMd neurons (**Fig 1.7e**). Only the TE responses were mainly inseparable (24/33; 73% inseparable) while the HE and TH responses were mainly separable (HE: 20/28 (71%) separable. TH: 22/41 (54%) separable). Similar to the example MIP cell, the average TE response field orientation for tuned MIP neurons was -94° indicating the response fields almost completely shifted when either eye or target was moved (**Fig 1.7f**). HE and TH responses were largely separable and dominated by eye position or target position (**Fig 1.7e,g,h** HE: -173° . TH: -16°).

The population analysis of **Figure 1.7** established that in PMd all three vectors T_E , T_H and H_E are encoded across a population of cells. However, individual PMd neurons will only encode

reach plans in a relative position code if they encode the T_E , T_H and H_E vectors simultaneously. To identify the extent to which individual PMd neurons simultaneously encode these vectors during reach planning, we examined the intersections of tuning properties for cells with a tuned inseparable response to at least one pair of variables. We found 63 PMd cells encoded at least one of the three vectors. Of these 63 cells, 23 (37%) encoded both T_E and T_H . Therefore, individual PMd cells encode target position with respect to the hand as well as with respect to the eye. A substantial fraction of these cells (16/23 (70%)) also encoded H_E indicating that in PMd all three vectors could be encoded inseparably in individual cells. In contrast, only 22 PMd cells (22/63 (35%)) encoded a single vector. This shows that, as illustrated in the example PMd neuron (**Figs 1.3 and 1.4**), many individual PMd cells simultaneously encode multiple vectors in a relative position code.

In contrast to PMd, of the 31 MIP cells that were tuned to at least one vector, 24 cells (77%) encoded T_E and a substantial proportion of these (11/24 (46%)) encoded only that single vector. This reinforces the distinction that PMd cells tend to simultaneously encode multiple vectors while MIP cells tend to only encode one vector, target position with respect to the eye.

Finally, we wanted to establish whether PMd had a stronger representation of T_E , T_H or H_E . To do this, we compared the tuning strength of the response matrices using the length of the resultant of the gradient analysis. We found the strength of TE tuning was not significantly different than TH tuning (t-test, $p > 0.05$) indicating T_E and T_H are represented with equal strength. We also found the strength of TE tuning was not significantly different than HE tuning and also that the strength of TH tuning was not significantly different than HE tuning. Therefore, PMd encodes all three vectors, T_E , T_H and H_E , with equal strength.

DISCUSSION

We found that during the delay period before a reach PMd neurons encode the target, hand and eye in a relative position code. Contrasting results from parietal area MIP confirmed previous work showing cells in this area use an eye-centered code. We propose eye position signals in PMd could play a role in coordinating the hand with the eye by encoding their relative position. Below we discuss this result in the context of hand-eye coordination, consider limitations of our result related to the specific task employed, and examine methodological differences between our study and other work.

Relative position codes for coordination

Overall, temporal issues in coordination have received more attention than spatial ones. Work on synchronized interlimb movements shows that relative phase, obtained by subtracting the phase angles of each limb, is the central concept for characterizing different behavioral coordination modes (Swinnen, 2002). For example, during movements of the arms or legs, in-phase (relative phase = 0°) movements are more stable and accurate than any other phase relationship. Our finding of an explicit neural representation of relative hand-eye position is an exciting spatial complement to this work as relative position codes could provide a general solution to the spatial problem of coordinating different body parts.

Experience with engineered systems shows a major problem for coordination is the accumulation of errors in position estimation (Olfati and Murray, 2002). Errors in estimating relative position are greatest when the positions of the individual body parts are represented in absolute coordinates. When absolute positions are subtracted to calculate relative position, the errors in position estimation can accumulate and do not cancel. Representing body parts directly in terms of relative position helps solve this problem as it reduces the number of position estimates and cancels errors that would otherwise accumulate (Gamini Dissanayake et al., 2001). Computationally relative position codes are also more efficient than those based on absolute

positions (Csorba and Durrant-Whyte, 1997; Newman, 1999). This is because using relative position separates the problem of coordinating two effectors from the larger problem of controlling the whole body. This is a powerful simplification. Whether neurons also represent the relative position of other body parts, such as the left and right hand, and how these encodings depend on coordination requirements will be an interesting area for future work.

Spatial transformations for hand-eye coordination are the subject of a growing body of work (Crawford et al., 2004). The prevailing view is to consider these as feed-forward spatial transformations converting visual information, which enters the brain in eye-centered coordinates, into hand-centered coordinates, and finally muscle commands for the arm and hand. Recent work shows parietal area 5 may play a role in these transformations. Many cells in area 5 encode targets in both hand and eye coordinates (Buneo et al. 2002). In other words, they represent T_E and T_H and thus bear similarities to the findings for PMd. In the Buneo et al. study extensive response maps like those in Figure 2 were made for five initial hand positions and five target positions, but not for a range of eye positions. Thus, this design did not allow the determination of whether area 5 also represents the relative position of the hand and eye, H_E . It will be interesting to determine whether area 5 is similar to PMd and represents all three vectors in a relative position code. One potential difference between area 5 and PMd is that in PMd we find the encoding of the hand in eye coordinates, H_E , is as strongly represented as both the reach vector, T_H , and the target position in eye-coordinates, T_E . This may not be the case for area 5.

Since we find PMd encodes T_E , T_H and H_E with equal strength, a new function for this area is apparent: the relative position code in PMd may be involved in invertible transformations between hand-centered and eye centered representations. **Figure 1.8** shows a schematic of an invertible transformation. Feed-forward transformations convert visual input in eye-centered coordinates into hand-centered movement commands. They can do this directly using the position of the hand in eye coordinates. This transformation is invertible because a feedback

transformation can also be performed that converts hand-centered into eye-centered coordinates. It does this using eye position in hand coordinates. In this way, relative position codes can perform invertible transformations between eye- and hand-centered representations.

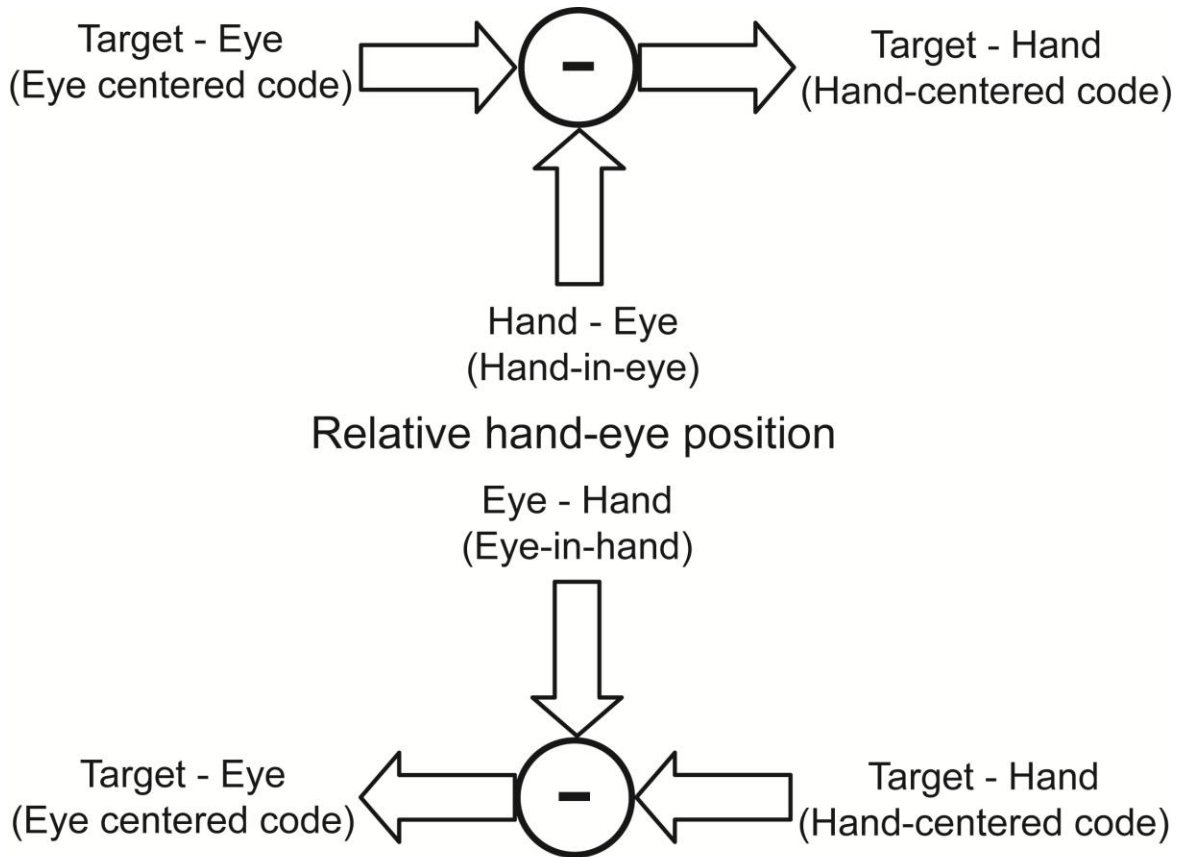


Figure 1.8

How does PMd construct its relative position code? Whereas cells in MIP code targets in eye coordinates, some are gain modulated by limb position (Buneo et al., 2002) and this gain effect also appears to be encoded in eye coordinates (Buneo et al., 1998). These gain modulated MIP neurons can perform the required coordinate transformation to relative position coordinates in PMd by convergence and appropriate weighting of inputs to PMd. The source of this gain signal can be obtained directly from the vision of the hand or from a somatosensory-posture signal. In the latter case this hand-in-body signal could be converted into hand-in-eye coordinates using a gain field related to gaze-in-body (head-in-body plus eye-in-head).

By similar reasoning, H_E can be produced by T_H response fields that are gain modulated by target-in-eye signals. It seems more likely, though, that these vectors can be formed by the same sources as the hand-in-eye gain effects mentioned above. In each case, cortical connections between PMd and other sensory-motor areas are consistent with a role in these invertible transformations (Matelli et al., 1998). Moreover, TMS studies over PMd have been shown to induce temporary disruptions of hand-eye coordination (Van Donkelaar et al., 2002).

Context-dependent reference frames

Movements are made under different constraints and in different behavioral contexts. At present, it is not clear how much the neural encoding of movements is sensitive to these factors. Constraining the position of the hand and eye before and during reaching to certain locations on a screen, as required for the reference frame dissociation task, could elicit specific strategies for doing the task and these strategies in turn could influence neural activity in PMd. For the case of constraining eye position, this issue has been studied for neurons in area MIP by examining them under free-viewing conditions (Cisek and Kalaska, 2002). The conclusion was that the eye-centered encoding is preserved and it will be interesting to determine whether a more complex encoding like a relative position code is also preserved when a subject is freely viewing (see below).

Context also plays an important role as movements may be defensive, aggressive and made outside of a behavioral task altogether. These movements not only differ in their parameters, the speed, endpoint, and trajectory, but also in the affective context in which they are made (Graziano and Cooke, 2006). Recent work examining the role of the expected reward following movements has shown this can exert a powerful influence on neural activity during the plan period before the movement (Musallam et al., 2004; Platt and Glimcher, 1999; Sugrue et al., 2004). This makes it very likely that other changes in context will modulate neural activity. Although it is less

clear how the reference frame of an area itself will change in response to these manipulations, it is important to keep in mind that the class of movements presented here is restricted and overly general conclusions should not be drawn.

Methodological issues with previous work

Other work has investigated eye position signals in PMd without reporting the encoding of relative position. Boussaoud and colleagues (1998) reported significant eye position effects when eye position was varied across three locations on a screen and reaches were made with the hand starting at a button near the body. It is possible these eye position effects reflect the encoding of relative hand-eye position but that it was difficult to observe in this experiment because, unlike our experiments, the hand and eye were not in a common workspace and so the relative positions of the hand and eye were similar across different trial conditions. In addition, they did not independently vary the positions of different effectors across a range of values and apply a combination of SVD and gradient analyses to the resulting matrices. Using this or a similar procedure is important given the potential complexity of the spatial transformations present in the association cortices. The gradient analysis is similar to the cross-correlation method used to measure shifts, but is more sensitive as noise in the response fields cancels instead of accumulates and the method averages across multiple positions instead of just two.

Cisek and Kalaska studied eye position signals during free gaze as a monkey controlled a cursor using a manipulandum from one initial position to different target positions (Cisek and Kalaska, 2002). They reported strong gaze-centered discharge in MIP but modest gaze-related discharge in PMd and argued that eye position signals in PMd, but not MIP, were strongly influenced by controlled fixation. However, their analysis only took into account eye and target position and not initial hand (or cursor) position. Our results indicate that gaze-related activity in PMd neurons depends on hand, eye and target position, not just eye and target position. This

means it is inappropriate to average neuronal responses during fixation periods with, for example, the target above the eye and the eye to the left of the hand with periods with the target above the eye and the eye to the right of the hand as they could have very different firing rates. Since inappropriate averaging of neuronal responses will reduce the strength of an effect, the degree to which eye position responses in PMd are influenced by controlled fixation remains unclear.

EXPERIMENTAL PROCEDURES

Experimental preparation

Two male rhesus monkeys (*Macaca Mulatta*) participated in the experiments. Each animal was first implanted with a head cap and eye coil under general anesthesia. In a second surgery, recording chambers were implanted in frontal and posterior parietal cortex in the right hemisphere of each animal. Structural magnetic resonance imaging was used to identify the position of the arcuate sulcus and intraparietal sulcus and guide placement of the recording chambers to give access to cortex medial to each sulcus (**Fig 1.1c**). At a subset of recording sites in the frontal chamber of each monkey, microstimulation through the recording electrode evoked movements of the hand, arm and occasionally leg with a threshold > 40 uA (330 Hz 400 us monopolar pulse width) consistent with published reports for PMd (Crammond and Kalaska, 1994). At no site was a saccade elicited with a threshold below 80 uA. Single-cell recordings from PPC conformed to previously published reports from MIP (functionally defined as a part of PRR (Calton et al., 2002; Snyder et al., 1997)). All surgical and animal care procedures were done in accordance with National Institute of Health guidelines and were approved by the California Institute of Technology Animal Care and Use Committee.

Neural recordings were made using multiple-electrode microdrives (3- or 5-channel, Thomas Recordings, Germany). During each session neural activity from each electrode was passed through a head stage (x20, Thomas Recordings, Germany), filtered (1 Hz – 10 kHz;

custom), amplified (x500–1000; TDT Electronics, Gainesville, FL), digitized (20 kHz; National Instruments, TX) and continuously recorded to disk for further analysis (custom C and Matlab code).

Behavioral Tasks

Reaches were made with the left arm on a touch-sensitive screen (ELO Touch Systems, CA) while maintaining fixation to isolate reach-related activation from saccade-related activation. Behavior was controlled using custom Labview (National Instruments, TX) code running on a real-time PXI platform. Eye position was monitored with a scleral search coil (CNC Engineering, WA). Visual stimuli were presented on an LCD display (LG Electronics, Korea) placed behind the touch screen. Red circles instructed the animal where to fixate the eye. Green circles instructed the animal where to touch. All trials began with the illumination of a red and green circle which the animal needed to fixate with his eye and touch with his hand, respectively, and hold for a baseline period (~ 1000 ms). A second green circle was then illuminated indicating the target of the reach. A delay period (~ 1000 ms) followed during which the animal had to withhold his response. After this the initial green circle the animal had to touch was extinguished providing the go signal for the animal to reach to the green target while maintaining fixation on the initial red circle. After the reach, the animal had to touch the second green circle while maintaining fixation on the red circle for 300 ms.

The spatial configurations of the initial eye position, initial hand position and target position were independently varied across a range of values. Initial eye position was varied across four locations spaced 10° on a horizontal line, initial hand position was varied across the same four locations and target position was varied across four locations spaced 10° on a horizontal line either above or below the initial hand and eye positions (**Fig 1a**). Targets were placed above or below to best activate the cell(s) being recorded.

Data collection

Cells were first isolated and if stable, recorded during the center-out task for both reaches and saccades. After these initial experiments, if there was a significant response to either task, recordings proceeded to the reference frame task. Occasionally, cells were acquired on additional electrodes and recorded despite the fact they had no task response, or cells were lost during a recording. All cells recorded for an average of at least three trials per condition the reference frame task were included in the database regardless of task response.

Data analysis

Spike events were extracted and classified from the broad-band activity using custom Matlab code (The MathWorks, Natick, MA) during the recording session and resorted offline. To account for nonstationarity in the recordings, spike classification was done on a 100s moving window and clusters were tracked across windows. Occasionally there were periods when clusters were not isolated. Trials during those periods were marked and this data was not subject to further analysis. The delay period was defined as the 500 ms interval starting 500 ms after target onset.

Response matrices were characterized with a combination singular value decomposition (SVD) and orientation analyses (Buneo et al., 2002; Pena and Konishi, 2001). For the eye-hand-target analysis, the response to pairs of variables was determined by holding the third variable constant at the response field peak and analyzing the resulting two-dimensional matrix. The SVD analysis was used to see if each variable was separable or not. Separability was defined by a significantly ($p < 0.05$) large first singular value compared to the first singular value calculated when trial conditions were randomized (randomization test). Thus, instead of referring to the strength of separability, which would be given by the magnitude of the first singular value compared with the others, we classified tuned responses as separable or inseparable according to

the $p=0.05$ threshold. A mean value was subtracted from the response matrix before performing the SVD. Gradient analysis was used to determine the orientation of the response field by computing the two-dimensional gradient of the response (estimated using the MATLAB gradient function), doubling the angles to account for symmetric response fields, and summing the gradient elements. The response to pairs of variables was considered tuned if the resultant gradient length was significantly greater than the length of the resultant gradient when trial conditions were randomized (randomization test). We used a two-way ANOVA to measure tuning and found it gave consistent results. Analyses utilizing all three dimensions of the data simultaneously were carried out by estimating the orientation of the spherical gradient. Unfortunately, symmetry considerations meant that when estimating the orientation of the gradient, the vertical axis had to be treated differently than the horizontal axes. This meant that three gradients were still needed to characterize the data so the more intuitive analyses based on two-dimensional gradients were used instead.

Idealized neuronal responses were created for eye-centered, hand-centered and relative position cells using the following formulae, where E gives eye position on the touch screen, H gives hand position on the touch screen and T gives target position on the touch screen.

$$\begin{aligned}
 \text{Eye-centered cell:} & \quad \frac{1}{1 + \exp\left(\frac{H}{1000}\right)} \exp\left(-\frac{(T - E)^2}{500\pi}\right) \\
 \text{Hand-centered cell:} & \quad \frac{1}{1 + \exp\left(\frac{E}{1000}\right)} \exp\left(-\frac{(T - H)^2}{500\pi}\right) \\
 \text{Relative position cell:} & \quad \exp\left(-\frac{(T - E)^2}{500\pi}\right) \exp\left(-\frac{(T - H)^2}{500\pi}\right) \exp\left(-\frac{(H - E)^2}{500\pi}\right)
 \end{aligned}$$

REFERENCES

- Andersen, R. A., and Buneo, C. A. (2002). Intentional maps in posterior parietal cortex. *Ann Rev Neurosci* 25, 189–220.
- Barash, S., Bracewell, R. M., Fogassi, L., Gnadt, J. W., and Andersen, R. A. (1991b). Saccade related activity in the lateral intraparietal area. II. Spatial properties. *J Neurophysiol* 66, 1109–1124.
- Batista, A. P., Buneo, C. A., Snyder, L. H., and Andersen, R. A. (1999). Reach plans in eye-centered coordinates. *Science* 285, 257–260.
- Boussaoud, D., Jouffrais, C., and Bremmer, F. (1998). Eye position effects on the neuronal activity of dorsal premotor cortex in the macaque monkey. *J Neurophysiol* 80, 1132–1150.
- Buneo, C. A., and Andersen, R. A. (2006). The posterior parietal cortex: Sensorimotor interface for the planning and online control of visually guided movements. *Neuropsychologia*, *in press*.
- Buneo, C. A., Batista, A. P., and Andersen, R. A. (1998). Frames of reference for reach-related activity in two parietal areas. *Society of Neuroscience Abstracts*.
- Buneo, C. A., Jarvis, M. R., Batista, A. P., and Andersen, R. A. (2002). Direct visuomotor transformations for reaching. *Nature* 416, 632–636.
- Calton, J. L., Dickinson, A. R., and Snyder, L. H. (2002). Non-spatial, motor-specific activation in posterior parietal cortex. *Nat Neurosci* 5, 580–588.
- Caminiti, R., Johnson, P. B., Burnod, Y., Galli, C., and Ferraina, S. (1990). Shift of preferred directions of premotor cortical cells with arm movements performed across the workspace. *Exp Brain Res* 83, 228–232.
- Caminiti, R., Johnson, P. B., Galli, C., Ferraina, S., and Burnod, Y. (1991). Making arm movements within different parts of space: the premotor and motor cortical representation of a coordinate system for reaching to visual targets. *J Neurosci* 11, 1182–1197.

- Cisek, P., and Kalaska, J. F. (2002). Modest gaze-related discharge modulation in monkey dorsal premotor cortex during a reaching task performed with free fixation. *J Neurophysiol* 88, 1064–1072.
- Crammond, D. J., and Kalaska, J. F. (1994). Modulation of preparatory neuronal activity in dorsal premotor cortex due to stimulus-response compatibility. *J Neurophysiol* 71, 1281–1284.
- Crawford, J. D., Medendorp, W. P., and Marotta, J. J. (2004). Spatial transformations for eye-hand coordination. *Journal of Neurophysiology* 92, 10–19.
- Csorba, M., and Durrant-Whyte, H. F. (1997). New approach to map building using relative position estimates. Paper presented at: SPIE (Orlando, FL).
- Fogassi, L., Gallese, V., di Pellegrino, G., Fadiga, L., Gentilucci, M., Luppino, G., Matelli, M., Pedotti, A., and Rizzolatti, G. (1992). Space coding by premotor cortex. *Exp Brain Res* 89, 686–690.
- Fu, Q. G., Suarez, J. I., and Ebner, T. J. (1993). Neuronal specification of direction and distance during reaching movements in the superior precentral premotor area and primary motor cortex of monkeys. *J Neurophysiol* 70, 2097–2116.
- Gamini Dissanayake, M. W. M., Newman, P., Clark, S., Durrant-Whyte, H. F., and Csorba, M. (2001). A Solution to the Simultaneous Localization and Map Building (SLAM) Problem. *IEEE Trans Robotics and Automation* 17, 229–241.
- Goldberg, M. E., and Bruce, C. J. (1990). Primate frontal eye fields. III. Maintenance of a spatially accurate saccade signal. *J Neurophysiol* 64, 489–508.
- Graziano, M. S., and Cooke, D. F. (2006). Parieto-frontal interactions, personal space, and defensive behavior. *Neuropsychologia* 44, 845–859.
- Graziano, M. S., and Gross, C. G. (1998). Spatial maps for the control of movement. *Curr Opin Neurobiol* 8, 195–201.

- Graziano, M. S., Yap, G. S., and Gross, C. G. (1994). Coding of visual space by premotor neurons. *Science* 266, 1054–1057.
- Johnson, P. B., Ferraina, S., Bianchi, L., and Caminiti, R. (1996). Cortical networks for visual reaching: physiological and anatomical organization of frontal and parietal lobe arm regions. *Cereb Cortex* 6, 102–119.
- Kakei, S., Hoffman, D. S., and Strick, P. L. (2001). Direction of action is represented in the ventral premotor cortex. *Nat Neurosci* 4, 1020–1025.
- Kalaska, J. F., Scott, S. H., Cisek, P., and Sergio, L. E. (1997). Cortical control of reaching movements. *Curr Opin Neurobiol* 7, 849–859.
- Matelli, M., Govoni, P., Galletti, C., Kutz, D. F., and Luppino, G. (1998). Superior area 6 afferents from the superior parietal lobule in the macaque monkey. *J Comp Neurol* 402, 327–352.
- Mays, L. E., and Sparks, D. L. (1980). Dissociation of visual and saccade-related responses in superior colliculus neurons. *J Neurophysiol* 43, 207–232.
- Musallam, S., Corneil, B. D., Greger, B., Scherberger, H., and Andersen, R. A. (2004). Cognitive control signals for neural prosthetics. *Science* 305, 258–262.
- Newman, P. M. (1999) On the solution to the simultaneous localization and map building problem, University of Sydney, Sydney, Australia.
- Olfati, R., and Murray, R. M. (2002). Distributed cooperative control of multiple vehicle formations using structural potential functions. Paper presented at: Proc of the 15th IFAC World Congress (Barcelona, Elsevier).
- Pena, J. L., and Konishi, M. (2001). Auditory spatial receptive fields created by multiplication. *Science* 292, 249–252.
- Platt, M. L., and Glimcher, P. W. (1999). Neural correlates of decision variables in parietal cortex. *Nature* 400, 233–238.

- Shadmehr, R., and Wise, S. P. (2005). *The computational neurobiology of reaching and pointing* (Cambridge, MA, MIT Press).
- Shen, L., and Alexander, G. E. (1997). Preferential representation of instructed target location versus limb trajectory in dorsal premotor area. *J Neurophysiol* 77, 1195–1212.
- Snyder, L. H., Batista, A. P., and Andersen, R. A. (1997). Coding of intention in the posterior parietal cortex. *Nature* 386, 167–170.
- Sugrue, L. P., Corrado, G. S., and Newsome, W. T. (2004). Matching behavior and the representation of value in the parietal cortex. *Science* 304, 1782–1787.
- Swinnen, S. P. (2002). Intermanual coordination: From behavioral principles to neural-network interactions. *Nat Rev Neurosci* 3, 350–361.
- Van Donkelaar, P., Lee, J.-H., and Drew, A. S. (2002). Eye-hand interactions differ in the human premotor and parietal cortices. *Human Movement Sci* 21, 377–386.

ACKNOWLEDGEMENTS

We would like to acknowledge valuable conversations with Chris Buneo and helpful comments on the manuscript from Alex Gail and Sam Musallam. This work was supported by NIH grants EY05522-21 and MH62528-01, the DARPA BioInfoMicro program and a Career Award in the Biomedical Sciences from the Burroughs Wellcome Fund to BP. We thank Tessa Yao for editorial assistance, Kelsie Pejsa and Leah Martel for animal care and Viktor Shcherbatyuk for technical assistance.

FIGURE LEGENDS

Figure 1.1 The behavioral task and recording sites **(a)** Geometry of hand-eye coordination. Sensory-motor transformations generate movement plans in an extrinsic space and non-linear transformations convert these to an intrinsic space to generate accurate muscle commands. **(b)**

The reference frame dissociation task. A reach without a saccade is made from one of four hand positions on a line to one of four target positions while fixation is maintained at one of four eye positions. (c) Structural magnetic resonance images from one monkey showing recording chamber placement with respect to sulcul landmarks. ‘X’ marks the mean recording location in each chamber.

Figure 1.2 Idealized cell responses with eye-hand-target tuning for cells with three different reference frames. (a) An eye-centered cell whose response is modeled as a gain field of hand position modulating eye-centered tuning. (b) A hand-centered cell whose response is modeled as a gain field of eye position modulating hand-centered tuning. (c) A relative position cell whose response is modeled as a product of eye-centered, hand-centered and relative eye-hand position tuning. The separability, from the SVD, and the response field orientation, from the gradient analysis, (see **Methods**) are shown for each idealized cell. 0° points right and angles increase counter clockwise. White = high firing rate. Black = low firing rate.

Figure 1.3 Example PMd cell. Responses to the reference frame dissociation task are aligned to target onset (black square) as eye position is varied (rows), hand position is varied (columns) and target position is varied (within each panel). Eye (E), hand (H) and target (T) positions are shown above each panel. Spike rasters are shown above the panel color coded for each target position in that panel. Target onset time (black square) and mean movement onset time (grey square) are shown on each panel. The horizontal bar on the top left panel indicates the delay period analysis interval.

Figure 1.4 Example PMd cell eye-hand-target response matrices. (a) Eye-target response matrix during the delay period at the peak of the response field. The hand is at 20° . Arrows show the

two-dimensional gradient elements. **(b–c)** Similar for hand-target and eye-hand response matrices with the eye at 10° and the target at -20° , respectively. **(d)** Overall response field orientation for the TE response matrix, -130° . **(e)** Overall response field orientation for the TH response matrix, -146° . **(f)** Overall response field orientation for the HE response matrix, -77° . 0° points right and angles increase counterclockwise.

Figure 1.5 Example MIP cell. Responses to the reference frame dissociation task are aligned to target onset (black square) as eye position is varied (rows), hand position is varied (columns) and target position is varied (within each panel). Eye (E), hand (H) and target (T) positions are shown above each panel. Spike rasters are shown above the panel color coded for each target position in that panel. Target onset time (black square) and mean movement onset time (grey square) are shown on each panel. The horizontal bar on the top left panel indicates the delay period analysis interval.

Figure 1.6 Example MIP cell eye-hand-target response matrices. **(a)** Eye-target response matrix during the delay period at the peak of the response field. The hand is at -20° . Arrows show the two-dimensional gradient elements. **(b–c)** Similar for hand-target and eye-hand response matrices with the eye at 0° and the target at -10° , respectively. **(d)** Overall response field orientation for the TE response matrix, -86° . **(e)** Overall response field orientation for the TH response matrix, 0° . **(f)** Overall response field orientation for the HE response matrix, 177° . 0° points right and angles increase counter clockwise.

Figure 1.7 Population eye-hand-target analysis during the delay period. **(a)** Population separability for all PMd cells with tuned delay period responses. The percentage of inseparable

cells is shown in dark grey. The percentage of separable cells is shown in light grey. Population histograms for **(b)** Eye-target response field orientation **(c)** eye-hand response field orientation and **(d)** hand-target response field orientation for tuned PMd neurons. Orientations for inseparable cells are shown in dark grey. Orientations for separable cells are shown in light grey. **(e-h)** Same for tuned MIP neurons.

Figure 1.8 Schematic showing how a relative position code performs invertible sensory-motor transformations between eye-centered and hand-centered reference frames.

Chapter 2

A relative position code for saccades in dorsal
premotor cortex

BACKGROUND

Hand-eye coordination allows the fovea to guide skilled manual behavior by coupling two very different mechanical systems. The intrinsic coordinate system of the eye, defined by the six oculomotor muscles, has only rotational degrees of freedom (Westheimer, 1957; Tweed and Vilis, 1987). In contrast, the hand is part of a multi-joint system whose intrinsic coordinates have many rotational and translational degrees of freedom (Soechting and Flanders, 1992; Shadmehr and Wise, 2005). Directly coupling these two systems presents a formidable geometric challenge (Blohm and Crawford, 2007; Henriques and Crawford, 2002). Instead of using intrinsic representations specific to each effector, the brain may use visual representations of space for planning both movements (Crawford et al., 2004). Visual space is extrinsic, defined independently of the musculature and so simplifies the geometry of coordination. As a result, encoding hand-eye coordination in an extrinsic, visual space for both hand and eye movements may be more efficient than coordinating movements using the intrinsic spaces of the hand and eye, although this has yet to be shown and the present work does not directly address this issue.

Recent work investigating reaching in the dorsal premotor area (PMd) of the frontal cortex provides new evidence in support of a role for PMd in coordinating eye and hand movements (Pesaran et al., 2006). Neurons in PMd are responsive to arm movements (Weinrich and Wise, 1982; Weinrich et al., 1984; Caminiti, Johnson, and Urbano, 1990) and encode reach plans in a relative position code that is defined in a coordinate space common to both the hand and eye (Pesaran et al., 2006). This relative position code is different from encodings centered on either the hand or gaze and may reflect an encoding of extrinsic space for both eye and hand movements. Activity depends on the relative position of the hand and gaze and the position of a reach target encoded with respect to both hand and eye position. PMd encodes three vectors: the vector connecting gaze position to the movement target, T_G , the vector connecting hand position to the movement target, T_H , and the relative position of the hand and gaze, H_G . Relative position codes

are evidence of cross-coupling between oculomotor and manual representations and allow direct visual-motor transformations between gaze-centered and hand-centered vectors (Buneo and Andersen, 2006). This makes relative position codes useful for coordinating the hand and eye.

Gaze-related discharge has been previously observed in PMd (Boussaoud et al., 1998; Cisek and Kalaska, 2002; Jouffrais and Boussaoud, 1999; Lebedev and Wise, 2001; Ohbayashi et al., 2003; Fujii et al., 2000), but the spatial properties of saccade-related activity in PMd have not been determined or compared with the spatial properties of reach-related activity and the spatial encoding of saccade discharges in PMd have not been determined. If PMd coordinates reaches with saccades, PMd should have two properties in addition to relative position coding before reaches. First, PMd should be active before saccades as well as reaches. Second, saccade-related activity in PMd should follow a relative position code and encode hand, gaze and target position. We performed two experiments to test these predictions. First, we compared the activity of a population of PMd neurons during a center-out task involving a reach without a saccade and a center-out task involving a saccade without a reach. To compare the strength of saccade-related responses in PMd with those in a reaching area of parietal cortex, we also recorded a population of neurons from the parietal reach region (PRR) under identical conditions. In the second experiment, we determined how activity in PMd encodes saccades using a relative position coding task for saccades. In this task, we varied the position of the hand across a range of positions while systematically instructing saccadic eye movements between several different initial and final gaze positions. Analyzing the pattern of response matrices across all three spatial variables allowed us to identify the spatial encoding of saccade activity in PMd.

METHODS

Experimental preparation

Two male rhesus monkeys (*Macaca Mulatta*) participated in the experiments. Recording chambers were implanted in frontal and posterior parietal cortex in the right hemisphere of each animal. Structural magnetic resonance imaging was used to identify the position of the arcuate sulcus and intraparietal sulcus and guide placement of the recording chambers to give access to cortex medial to each sulcus. Recording sites were the same as those presented in Pesaran et al. (2006). In both animals, PMd recordings were made within the cortical gyrus within 1.5 mm of the cortical surface and PRR recordings were made within the medial bank of the intraparietal sulcus 4–9 mm below the cortical surface. At a subset of recording sites in the frontal chamber of each monkey, microstimulation through the recording electrode evoked movements of the hand, arm and occasionally leg with a threshold > 40 uA (330 Hz, 400 us monopolar pulse width) consistent with published reports for PMd (Crammond and Kalaska, 1994). Low-threshold, < 80 uA, saccades were not evoked at any recording site, consistent with published reports for the caudal portion of PMd (Fujii et al., 2000). All surgical and animal care procedures were done in accordance with National Institute of Health guidelines and were approved by the California Institute of Technology Animal Care and Use Committee.

Neural recordings were made using multiple-electrode microdrives (3- or 5-electrode, Thomas Recordings, Germany). During each session neural activity from each electrode was passed through a head stage (x20, Thomas Recordings, Germany), filtered (1 Hz–10 kHz; custom), amplified (x500–1000; TDT Electronics, Gainesville, FL), digitized (20 kHz; National Instruments, TX) and continuously recorded to disk for further analysis (custom C and Matlab code).

Behavioral Tasks

For all tasks, reaches were made with the left arm on a touch-sensitive screen (ELO Touch Systems, CA) and eye position was monitored with a scleral search coil (CNC Engineering, WA). Visual stimuli were presented on an LCD display (LG Electronics, Korea) placed behind the touch

screen. The eye coil signal was calibrated so that its signal corresponded to the intercept of gaze on the screen. All measures and mathematics were done in screen coordinates. Since we studied relatively small gaze angles, $< 30^\circ$, the difference between calculations in screen coordinates approximate calculations in gaze coordinates. In the following we refer to all spatial coordinates in degrees of visual angle for the cyclopean eye of the subject. Red circles instructed the animal where to fixate the eyes. Green circles instructed the animal where to touch. All trials began with the illumination of a red and green circle which the animal needed to fixate with his eyes and touch with his hand, respectively, and hold for a baseline period (~ 1000 ms). Saccade and reach trials were presented in separate blocks of trials.

In the **saccade tasks (Fig 2.1A,C)**, a second red circle was illuminated after the baseline period indicating the target of the saccade. After a 1–1.5 s delay period, the red circle the animal was fixating was extinguished, providing the go signal for the animal to saccade to the red target while maintaining touch on the initial green circle. After the saccade, the animal had to fixate the second red circle while maintaining a touch on the green circle for 300 ms. In the **reach tasks (Fig 2.1B; Fig S1)**, a second green circle was then illuminated indicating the target of the reach. A 1–1.5 s delay period followed during which the animal had to withhold his response until the initial hand fixation green circle was extinguished, providing the go signal to reach to the green target circle while maintaining eye fixation on the initial red circle. After the reach, the animal had to touch the second green circle while maintaining fixation on the red circle for 300 ms. Reaches needed to be completed within 700 ms of the instruction to move or the trial was aborted. The spatial configurations of the initial gaze position, initial hand position and target position varied between tasks. In the **center-out tasks** the initial hand and gaze position were placed next to each other directly in front of the animal and eight targets were placed on a grid spaced 10° around this point (**Fig 2.1A,B**). In the **relative position coding task** initial gaze position was varied across four locations spaced 10° on a horizontal line, initial hand position was varied across the same four

locations and the position of the saccade target and reach target were varied across four locations spaced 10° on a horizontal line either 10° above or below the initial hand and gaze positions (**Fig 1C; Fig S1**). Targets were placed above or below the initial position to best activate the cell(s) being recorded. The full experimental design for the relative position coding task involved collecting responses during four gaze positions, four hand positions and four target positions for a total of 64 conditions. We obtained a complete data set during the saccade relative position coding task from a total of 116 PMd neurons in two animals.

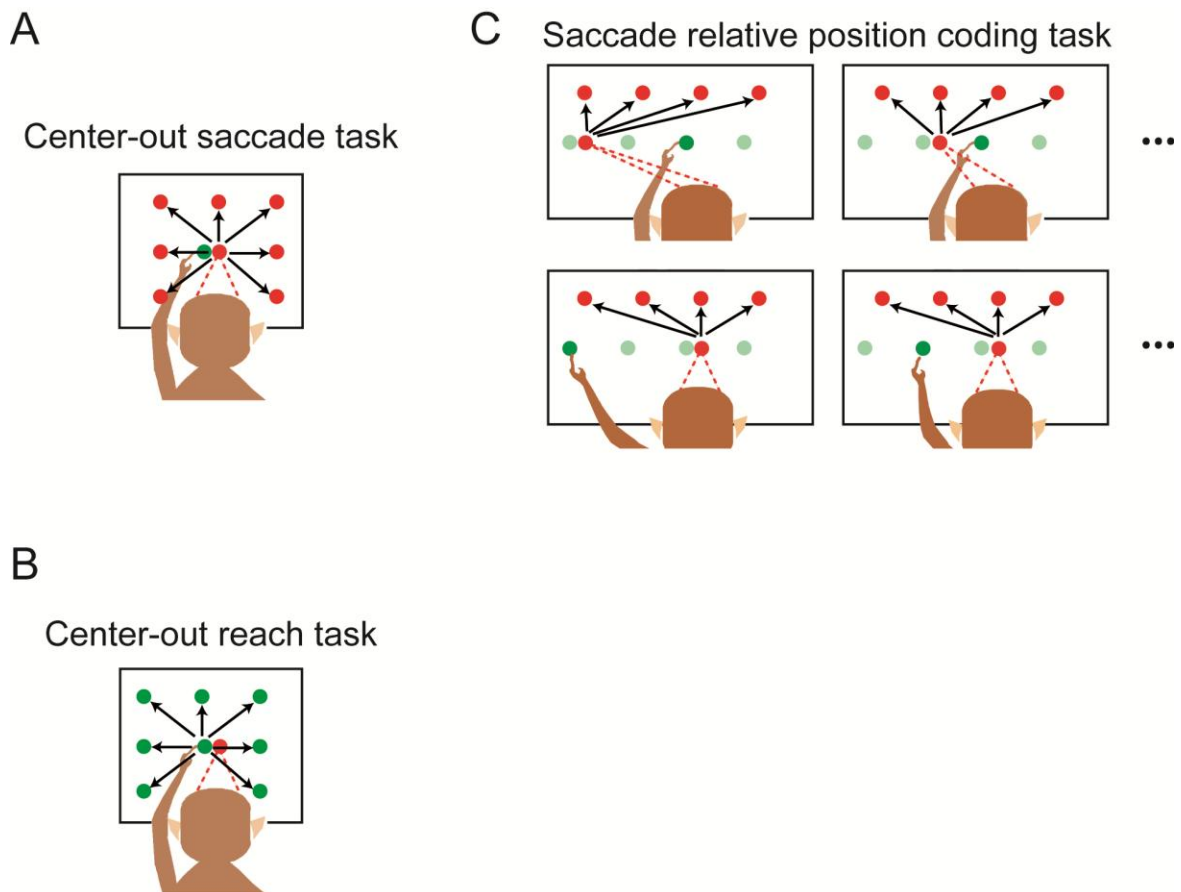


Figure 2.1

The current study forms a companion to Pesaran et al. (2006) which studied the relative position coding task for reaches. In Supplementary Material we present complete data sets from 111 PMd neurons in the same animals recorded during the reach relative position coding task, previously reported in Pesaran et al. (2006). Since the saccade relative position coding task forms

the focus of this study, we present the methodological details of the reach tasks here, but postpone the presentation of results involving the reach tasks to Supplementary Material.

We employed visually guided and not memory-guided movements. As a result, we cannot eliminate the role of visual signals in driving the activity of these neurons. It is worth noting however, that any influence of hand position on the responses we report could not be simply explained by visually driven activity. Moreover, we do not believe the use of visually guided movements contributes to any differences we report between saccade and reach responses. The reason is that we only presented analysis of activity during the delay period of each task and do not include analysis of activity around the time of the visual ‘go’ cue and the subsequent movement, at which time visual conditions between the two tasks differ. During the delay before movement, the visual illumination conditions are essentially the same and differ in terms of the color of the cue, red for saccade and green for reach.

We measure reach end-point time by the time when the touch screen reports a new touch. We measure the time of the saccade by the first time eye velocity exceeds $200^{\circ}/s$ following the visual instruction to make a saccade.

Data collection and analysis

Data collection and analysis were carried out in the manner described in Pesaran et al. (2006). All cells that were recorded for an average of at least 3 trials per condition in either the relative position coding task or center-out tasks were included in the database regardless of task response. Cells were first isolated and, if stable, recorded during the center-out task for both reaches and saccades. Spike waveforms were extracted and classified during the recording session to guide recordings. Waveforms were then resorted offline using a semi-automatic clustering procedure that tracked clusters across time. The baseline period was defined as the 300 ms

interval ending 200 ms before target onset. The delay period was defined as the 500 ms interval starting 500 ms after target onset. Each task was recorded in consecutive separate blocks.

In the center-out task, tuning was significant if the trigonometric moment of the tuning curve was significantly greater than that when the trial conditions were randomized (Crammond and Kalaska, 1996) (randomization test). The trigonometric moment was calculated by taking a vector element given by each movement direction multiplied by the firing rate in that direction and averaging all eight vectors in the tuning curve. The preferred direction was given by the direction of the trigonometric moment of the tuning curve. All randomization tests were done based on at least 10,000 randomizations.

Kuiper's test was used to test the hypothesis that the distribution of preferred directions, or differences, for a population of neurons recorded during the center-out tasks was uniform (Batschelet, 1981). If a population of preferred directions, or differences, was significantly nonuniform, Rayleigh's test was used to test the hypothesis that the distribution of preferred directions, or differences, for a population of neurons was unimodal.

In the relative position coding tasks, response matrices were characterized with a combination singular value decomposition (SVD) and gradient-orientation analyses (Peña and Konishi, 2001; Buneo et al., 2002; Pesaran et al., 2006). For the gaze-hand-target analysis, the response to pairs of variables was determined by holding the third variable constant at the response field peak and analyzing the resulting two-dimensional matrix. This procedure only characterizes spatial coding at the response field peak and not in the flanks of the response field. It is possible that neural coding differs in the response field flanks compared with the response field peak, but since reduced signal-to-noise makes it more difficult to determine the encoding we focus on activity around the response field peak.

The SVD analysis was used to test whether each variable was separable from the others or not. Separability was defined by a significantly ($p < 0.05$) large first singular value compared to the

first singular value calculated when trial conditions were randomized (Randomization test). Thus, instead of referring to the strength of separability, which would be given by the magnitude of the first singular value compared with the others, we classified tuned responses as separable or inseparable according to the $p=0.05$ threshold. A mean value was subtracted from the response matrix before performing the SVD. Gradient analysis was used to determine the orientation of the response field by computing the two-dimensional gradient of the response (estimated using the MATLAB gradient function), doubling the angles to account for symmetric response fields, and summing the gradient elements. The response to pairs of variables was considered tuned if the resultant gradient length was significantly greater than the length of the resultant gradient when trial conditions were randomized (Randomization test).

Intuition on response matrix analysis

To provide intuition on how the matrix analyses distinguish different neural responses, we present activity simulated from idealized neurons encoding gaze and target position either as a vector or using gain fields (**Fig 2.2**). Similar procedures can be used to consider any combination of variables, such as gaze and hand position, instead of gaze and target position. Vector encoding of gaze position and target position was simulated using a Gaussian response field according to the difference between gaze position and target position (**Fig 2.2A**):

$$\text{Vector encoding: } f(G, T) = \exp\left[-\frac{(T - G)^2}{2\pi\sigma^2}\right]$$

Neural firing is represented by $f(G, T)$. Gaze position is represented by G . Target position is represented by T . Altering the weighting of target and gaze position in the argument to the exponential function can give intermediate encodings which are represented mathematically as

$$f(G, T) = f(T - \alpha G) \text{ where } \alpha \neq 1 \left(\alpha = \frac{1}{2}, \text{ Fig 2.2B}; \alpha = 2, \text{ Fig 2.2C}\right):$$

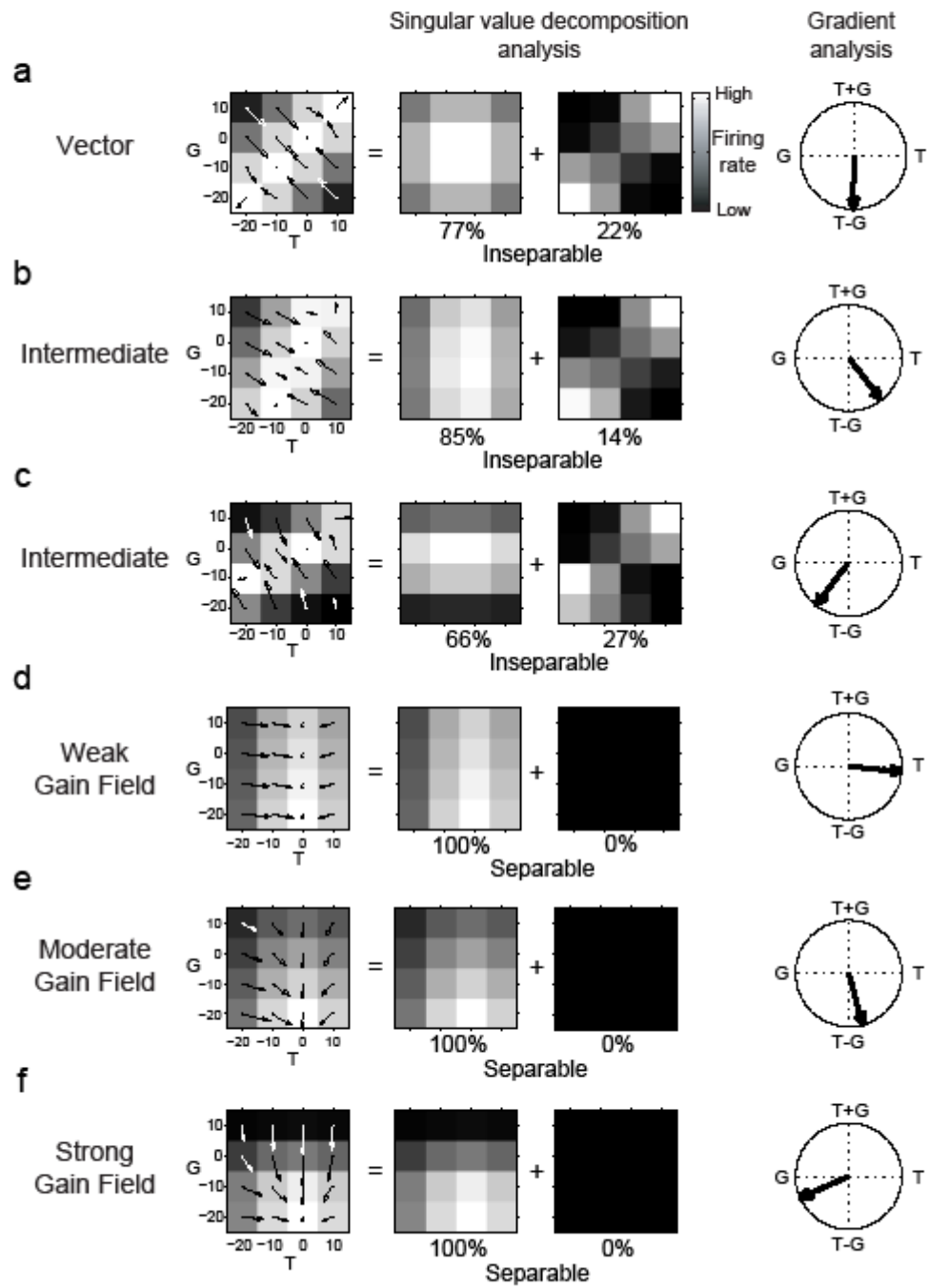
$$\text{Intermediate encoding: } f(G, T) = \exp\left[-\frac{(T - \alpha G)^2}{2\pi\sigma^2}\right]$$

Gain field encoding of gaze position was simulated using a sigmoidal function of gaze position modulating a Gaussian response of target position (**Fig 2.2D–F**):

$$\text{Gain field encoding: } f(G, T) = \frac{1}{1 + \exp[kG]} \exp\left[-\frac{T^2}{2\pi\sigma^2}\right]$$

We varied the strength of the gain field by varying the amplitude of the slope of the sigmoid, k . A weak gain field was simulated with a small value for k ; moderate gain field was simulated with an intermediate value for k ; strong gain field was simulated with a relatively large value for k .

Figure 2 (Andersen)



The primary difference between the response fields is reflected in the functional dependence on G and T. In a vector encoding, G and T appear as arguments to the same function and are inseparable $f(G, T) = f(T - \alpha G)$. In a gain field, G and T appear as arguments to different functions and are multiplicatively separable $f(G, T) = g(G)t(T)$.

We captured separability using a singular value decomposition analysis. Singular value decomposition decomposes the response matrix into a weighted sum of matrices each of which represents G and T as a separable product:

$$f(G, T) = \lambda_1 g_1(G) t_1(T) + \lambda_2 g_2(G) t_2(T) + \dots$$

The weights, λ_i , called singular values, mathematically capture the degree to which the outer product of the corresponding singular vectors (g_i, t_i) contribute to the total energy of the response matrix. If gaze and target position are inseparable, the response matrix cannot be captured with one term and other separable terms are needed to model the inseparable response (**Fig 2.2A–C**). If gaze and target position are separable in the response matrix, the singular value for the first matrix will be large and the matrix decomposition contains only one significant term (**Fig 2.2D–F**). Importantly, the singular value decomposition analysis does not depend on how strongly the response is modulated by the gain field.

We combined the singular value decomposition with a gradient analysis that measured the response field orientation. Intuitively, the response field orientation compares how much neural firing changes with changes in either positional variable. This lets us measure whether neural firing changes more or less when the position of the target is shifted or when the position of gaze is shifted. If the response encodes gaze and target position as a vector with equal influences, the response field orientation points toward T-G (**Fig 2.2A**). Response field orientation also detects intermediate vector response fields. If a vector response field has intermediate encoding with gaze influencing activity less than target position $\alpha < 1$ the response field orientation points away from

T-G toward T (**Fig 2.2B**). Similarly, if a shift of gaze influences the activity more than a shift in target position, $\alpha > 1$, the orientation points away from T-G and toward G (**Fig 2.2C**).

Different gain field effects are also apparent in the response field orientation. When the gain field of gaze position is weak, the response field orientation is directed mainly toward target position (**Fig 2.2D**). As the strength of the gain field increases, the orientation of the response field rotates toward gaze position (**Fig 2.2E**), and can even point near T-G similar to the response field orientation of the vector encoding response. This reflects the fact that changes in gaze and target position have comparable effects on neural firing. When gaze strongly modulates firing, the response field orientation points toward gaze (**Fig 2.2F**).

As the above illustrates, gain fields and vector coding can influence response fields in similar but distinguishable ways. Therefore, we used a combination of both singular value decomposition and gradient analyses rather than either analysis taken alone to correctly identify the encoding of response vectors and gain fields in neural activity.

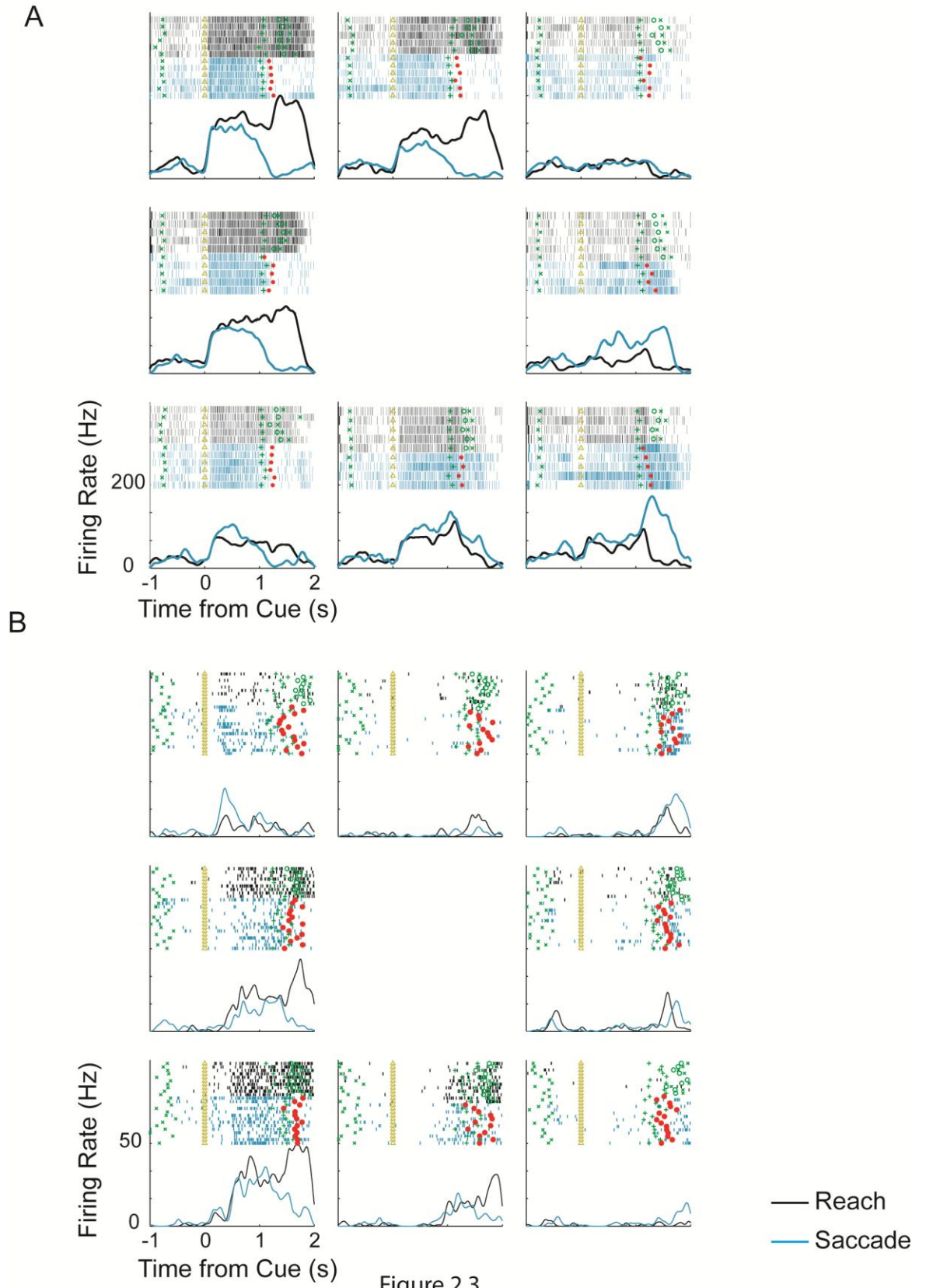
RESULTS

The database for this study consisted of neurons recorded in two experiments. In the first, effector, experiment, 298 PMd neurons (217 in Monkey E, 81 in Monkey Z) were recorded during the saccade and reach center-out tasks. In the second, relative position coding, experiment, 116 PMd neurons (62 in Monkey E, 54 in Monkey Z) were recorded during the saccade relative position coding task.

In Supplementary material, we present results from an additional 140 PRR neurons (91 in Monkey E, 49 in Monkey Z) that were recorded during the center-out tasks under identical conditions as the PMd neurons. We also present results from a population of 111 PMd neurons (38 Monkey in E, 73 in Monkey Z) recorded during the reach relative position coding task that were the focus of an earlier study (Pesaran et al., 2006) in Supplementary Material.

Saccade-related activity in PMd

Responses to the saccade and reach center-out tasks for two example PMd cells are shown in **Fig 2.3A,B**. These example neurons illustrate how cells in PMd responded robustly before both reaches and saccades to their preferred direction ($p < 0.05$, Rank-sum test, both neurons) with delay period activity that was stronger for reaches than saccades ($p < 0.05$, Rank-sum test, both neurons). To assess how strongly the population of neurons in each area responded to each movement, we calculated the firing rate for the preferred direction normalized (divided) by the baseline activity, aligned in time to target onset and averaged over all cells recorded from each area (**Fig 2.4A,B**). As expected, during the delay period before movement, PMd neurons responded more strongly before reaches than saccades (**Fig 2.4A**; $p < 0.05$, Rank-sum test). Surprisingly, PMd showed sustained delay activity before saccades that was nearly as strong and significantly greater than baseline activity (**Fig 2.4A**; $p < 0.001$, Rank-sum test). In comparison, saccade activity in PRR was weaker and barely greater than baseline (**Fig 2.4B**; $p = 0.33$, Rank-sum test).



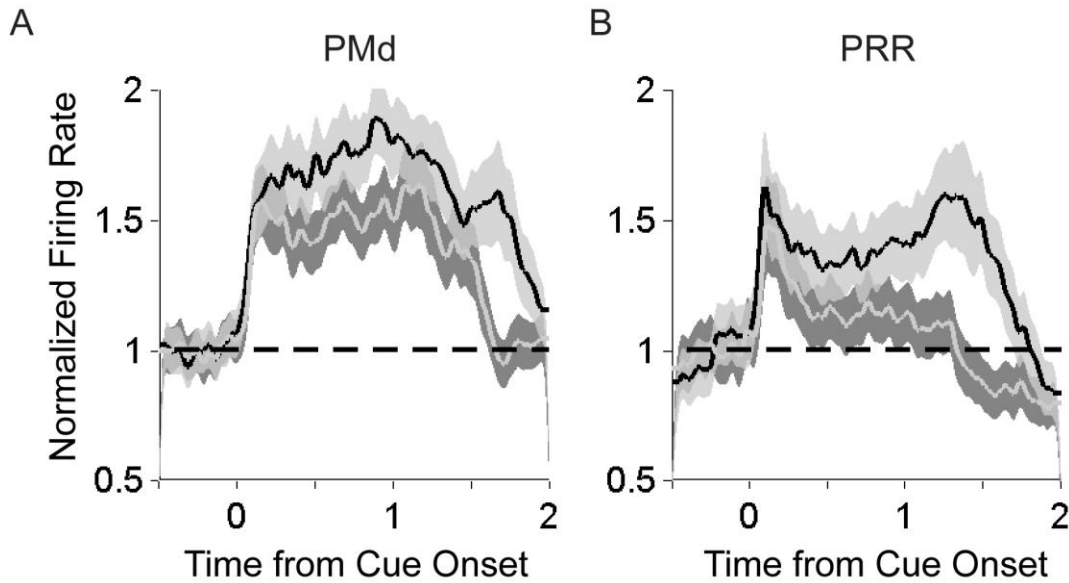


Figure 2.4

The spatial tuning of the PMd response to saccades could be seen on a cell-by-cell basis. Across the population of 298 PMd cells, 174 cells were spatially tuned to either reaches or saccades. As proportions of the 174 spatially tuned cells, 71 cells (71/174; 41%) were exclusively tuned to reaches and not saccades, 37 cells (37/174; 21%) were exclusively tuned to saccades and not reaches and 66 cells (66/174; 38%) were tuned to both reaches and saccades (see Table 2.1).

Table 2.1

PMd neurons (174 tuned cells)			PRR neurons (102 tuned cells)		
Reach only	Saccade only	Reach and Saccade	Reach only	Saccade only	Reach and Saccade
71/174 (41%)	37/174 (21%)	66/174 (38%)	42/102 (41%)	12/102 (12%)	48/102 (47%)

We examined a population of PRR neurons recorded under identical conditions for comparison with the PMd neurons (see **Supplementary Material**). The difference between the proportion of tuned, saccade-only PMd neurons (37/174) and tuned, saccade-only PRR neurons (12/102) was highly significant (Two-sample Binomial test, $p < 0.001$). Thus, PMd contains a larger proportion of exclusively saccade-tuned cells than PRR.

Saccade-related delay activity could coordinate the hand and eye by guiding the eye to the same location as the hand. We examined this by testing whether cells that were tuned to both movements had preferred directions that pointed in the same direction. We recorded 66 PMd neurons (43 in Monkey E; 23 in Monkey Z) that were spatially tuned to both reaches and saccades during the delay period ($p < 0.05$). The distribution of preferred directions for the saccade task was weakly nonuniform ($p = 0.04$; Kuipers test) but not unimodal ($p = 0.64$; Rayleigh test; **Fig 5A**). The distribution of preferred directions for the reach task was not significantly different from uniform (Reach $p = 0.065$, Kuipers test. **Fig 5B**). The difference in preferred directions of PMd neurons to reaches and saccades was unimodal (Rayleigh test; $p < 0.001$) with a mean difference peaked around 19° (**Fig 5C**). This result demonstrates that there is a propensity of cells whose preferred directions align, and that there are also cells whose preferred directions do not align. Cells with responses which do not align are needed for situations where gaze and the hand are decoupled.

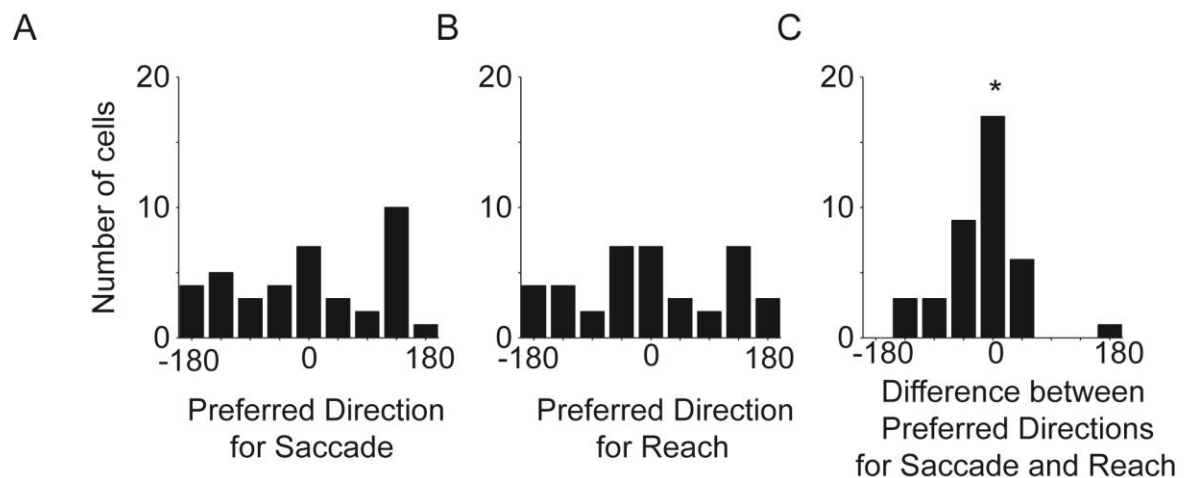


Figure 2.5

A relative position code for saccades

Saccade-related activity in PMd during the center-out task had a similar temporal profile and directional tuning to reach-related activity. This suggests it could serve to coordinate eye and hand movements. To determine whether saccade-related activity could be related to eye-hand coordination, we measured the spatial encoding of a population of PMd neurons by recording their activity during the saccade relative position coding task (**Fig 2.1C**). If this saccade-related activity is involved in spatial coordination, the spatial encoding would follow a relative position code in which changes in gaze position and hand position equally modulate activity. Alternatively, if PMd is exclusively involved in transforming reaches between different coordinates, it would not be expected to represent the vector T_G at all during the saccade relative position coding task. As another alternative, if saccade-related activity in PMd is exclusively involved in the execution of saccade motor plans, spatial encoding will more exclusively represent the saccade target relative to gaze position (vector T_G) and will be relatively insensitive to changes in hand position.

Figure 2.6 presents the hypotheses and formal models of relative position coding and gaze-centered coding and demonstrates how they can be distinguished using response matrix analysis. Response matrix analysis analyzes the spatial encoding of neural activity and was previously developed and applied to determine the spatial encoding of reach-related activity in PMd. Responses are represented as three two-dimensional matrices at the response field peak consisting of the firing rate at each of four target and gaze positions (target-gaze, TG), hand and gaze positions (hand-gaze, HG) and target and hand positions (target-hand, TH). Matrix representations let us distinguish between gaze-centered and relative position codes by assessing the separability, determined from a singular value decomposition, and response field orientation, determined from a gradient analysis, for each of the three response matrices.

If the response follows a gaze-centered code, the TG response matrix will be inseparable with a response orientation directed toward T-G, while the HG and TH response matrices will be

separable (**Fig 2.6A**). **Figure 2.6A** shows a gaze-centered response with relatively little hand position modulation. Other cases with gain fields that modulate the activity more strongly and preserve the essential gaze-centered property of the response are possible (see **Fig 2.2D–F**). If the response follows a relative position code, TG, HG and TH response matrices will all be inseparable (**Fig 2.6B**). **Figure 2.6B** shows the responses as vectors in which gaze, hand and target position modulate the response with equal strength. Intermediate responses in which changes in position could affect firing differently do not alter the essential relative position coding property of the response (see **Fig 2.2A-C**). Our analyses can distinguish between alternatives like the gaze-centered coding model and the general form of the relative position model, in which the expression of a cell's firing rate is an unspecified function of the three relative position vectors. For any response matrix, the possibility that it was created by gain fields alone can be ruled out by the separability analysis while the gradient analysis can show that the combination of the two variables that is encoded is the relative position between the two variables. However, to accurately distinguish between different forms of the general relative position model, like the additive or multiplicative versions shown in **Figure 2.6B**, would require a different analysis and data using a larger range of gaze, hand and target positions.

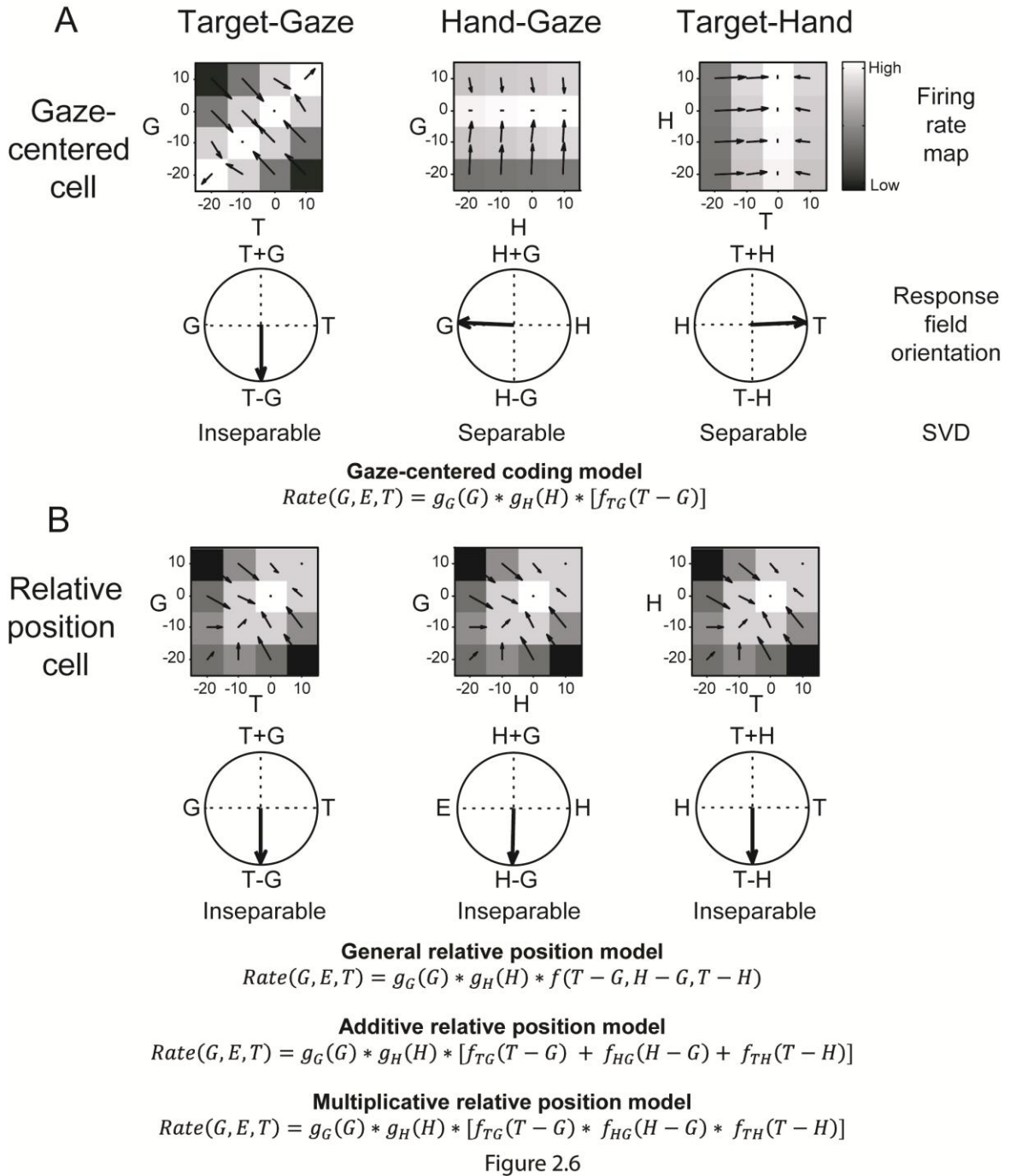


Figure 2.7 shows the response of an example cell to the saccade relative position coding task. This cell responded very strongly to saccades with peak firing in excess of 100 Hz. The influence of changing either hand or gaze position can be seen by comparing rasters of the same color within either rows or columns, respectively. The influence of changing target position can

be seen by comparing rasters of different colors within a panel. Changes in all three variables resulted in robust changes in neural firing.

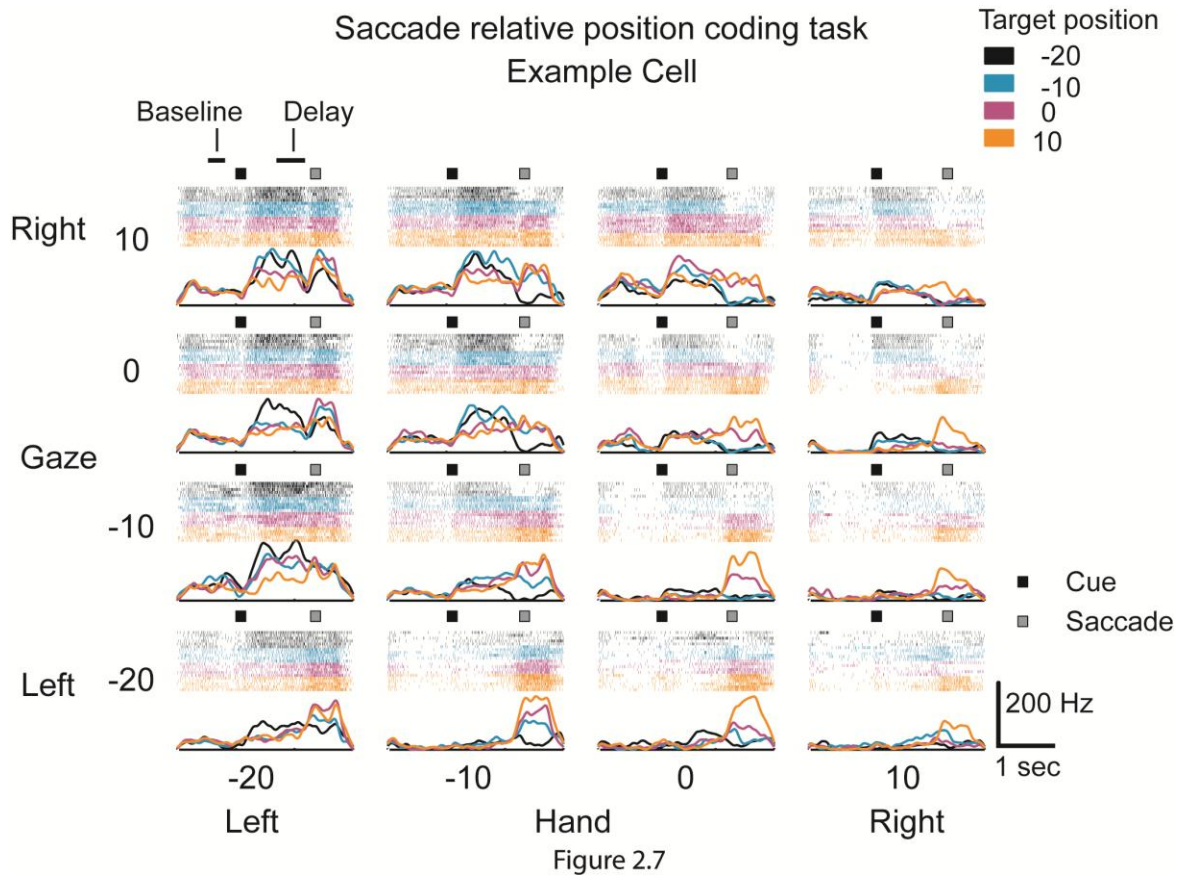


Figure 2.8A–C plots the TG, HG and TH response matrices for the example cell in **Fig 7** during the delay period. The TG response is suppressed for the target to the right of the eye and increases as the target is moved further to the left of the eye. Similar effects are present for HG and TH responses. The TG, HG and TH response matrices were inseparable for this cell and their orientations revealed a dominance of eye and hand position over target position (TG response field orientation: -144° , **Fig 8D**; HG response field orientation -56° , **Fig 8E**; TH response field orientation: -101° , **Fig 8F**).

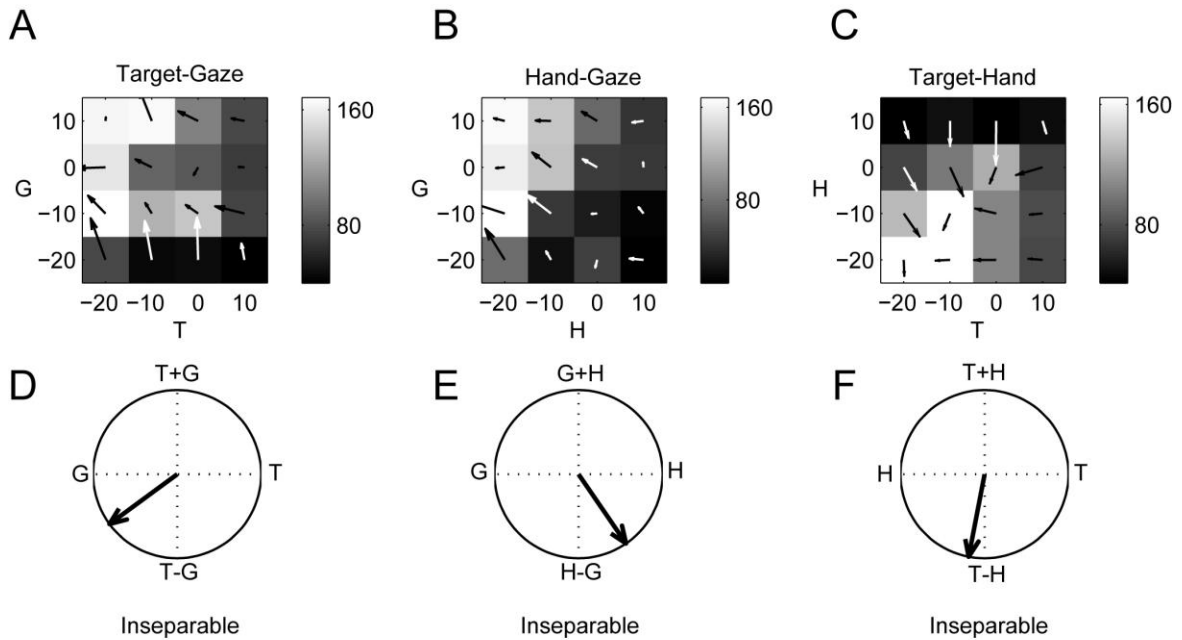


Figure 2.8

We found that a relative position code was present across the population of saccade-responsive PMd cells (**Fig 2.9**). A significant number of neurons were tuned to the TG variable pair (36/116; 31%, $p < 0.05$, randomization test), the HG variable pair (44/116; 38%) and the TH variable pair (53/116; 46%). A majority of the tuned TG, HG and TH responses of PMd neurons were inseparable (**Fig 2.9A**. TG: 28/36; 78%. HG: 32/44; 73%. TH: 39/53; 74%. $p < 0.05$). The response field orientation for these inseparable cells showed that the mean response field orientations pointed down (**Fig 9B-D**. TG: -118° . HG: -63° . TH: -74°). This means that response fields almost completely shifted when either of the hand, gaze or target was moved with respect to one of the other variables. Taken together, these findings mean that the spatial encoding of saccade-related activity in PMd does not just encode the target relative to gaze position. Instead, the population of PMd neurons simultaneously encoded the target with respect to gaze, T_G , the target with respect to the hand, T_H , and relative hand-gaze position, H_G .

Saccade relative position coding task

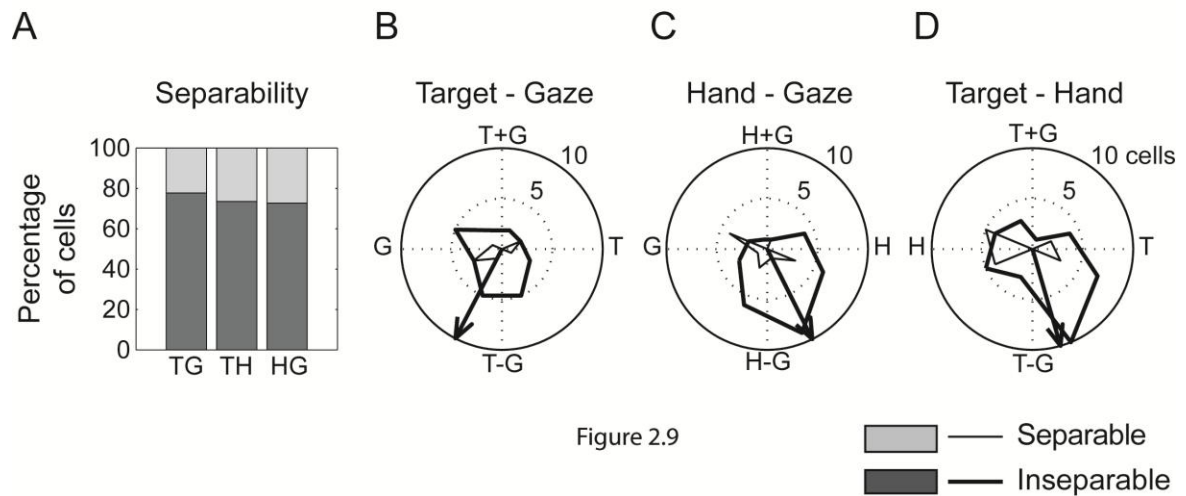


Figure 2.9

Comparing the spatial encoding for saccades and reaches

We then examined the relative position code for saccadic activity in more detail.

Examining the proportion of cells that encoded the different vectors in the saccade relative position coding task, we found that some single cells showed a mixture of inseparable tuning to more than one vector but the overall tendency was that individual cells encoded only one of the vectors (**Fig 2.10A**). Of the 70 cells that encoded any single vector, 28 cells (28/70; 50%) encoded T_G , 32 cells (32/70; 46%) encoded H_G and 39 cells (39/70; 56%) encoded T_H . The sum of these proportions is greater than 1 because a minority of cells simultaneously coded more than one of these vectors. We found 49 cells encoded either T_G or H_G but only 11 cells (11/49; 22%) encoded them both. Similarly, we found 57 cells encoded either T_H or H_G but only 14 cells (14/57; 25%) encoded them both. We also found 57 cells encoded either T_G or T_H but only 10 cells (8/57; 18%) encoded them both. Of the 70 cells that encoded any one vector, only 6 cells encoded all three vectors (6/70; 9%).

Saccade Relative Position Coding

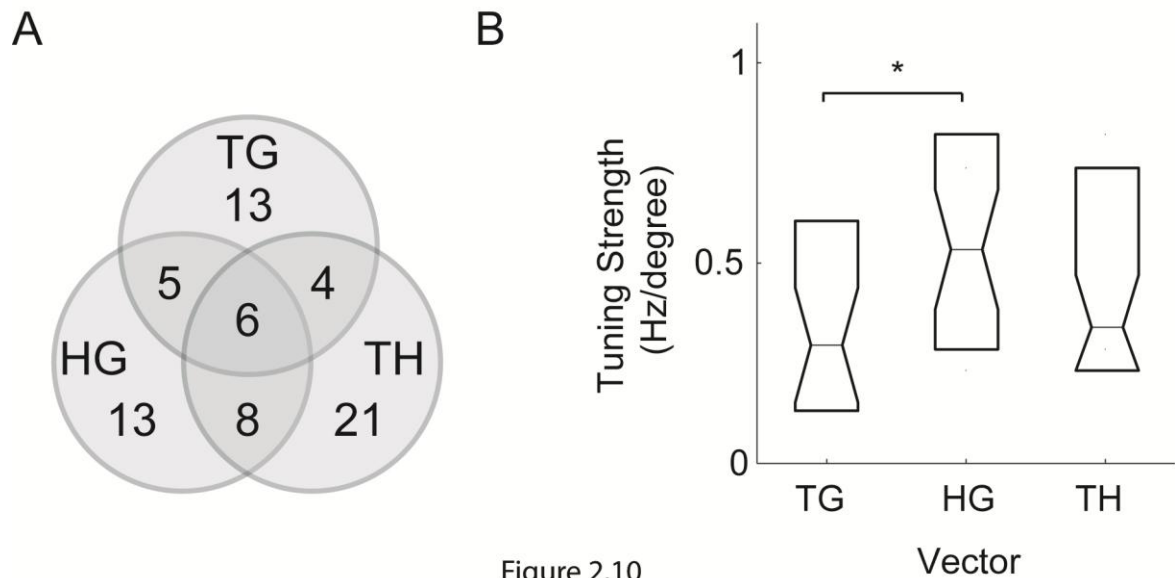


Figure 2.10

The tuning strength of the saccade response matrices, determined by the magnitude of the resultant vector in the gradient analysis, revealed that the representations of T_G , T_H and H_G in PMd were different from each other (**Fig 2.10B**). H_G tuning was the greatest, followed by T_H and then T_G . The difference between H_G and T_G tuning was statistically significant (Rank test; $p < 0.05$). The relatively weak encoding of T_G indicates that saccade-related responses may not be simply related to retinotopic processes. The strength of H_G tuning is consistent with a role for this activity in coordinating the hand with gaze.

Overall, these results show that at the population level saccade-related activity in PMd shares a similar relative position code to reach-related activity in this area, with some differences (see **Supplementary Material** and Pesaran et al. (2006) for details of the reach-related activity). Individual PMd cells do not combine information about T_G , T_H and H_G before saccades to the same extent as they do before reaches. Instead, PMd cells most strongly represent H_G before saccades.

DISCUSSION

In this study, we found PMd neurons respond before saccades in a strong and sustained manner while neurons in parietal area PRR responded transiently. The activity of PMd and PRR neurons tends to have the same preferred direction for reaches and saccades. We also found more exclusively saccade-tuned neurons in PMd than in PRR. Using a saccade relative position coding task, we then showed that saccade responses in PMd follow a relative position code in which the relative position of the hand and gaze, H_G , is represented and the position of the target of the saccade is encoded with respect to both the hand, T_H , and gaze, T_G . Comparison of this relative position code before saccades with the relative position code before reaches reported in Pesaran et al (2006) revealed that before saccades, all three vectors are encoded in the population and that the encoding is strongest for H_G , intermediate for T_H , and weakest for T_G . We also observe hand-gaze coding in PMd during a baseline hold period without movement planning (see **Supplementary Material, Fig S4**). These results demonstrate that combined hand-gaze coding is a reliable feature in the response of PMd neurons. Altogether these results provide important new evidence that saccade and gaze position signals in PMd provide spatial information that could link the control of eye and arm movements.

Common representations for coordination

We propose that a relative position code that is common to both reaches and saccades can guide coordinated eye-hand movements. This code allows eye movements and reaching movements to be planned in the same spatial coordinate system. An advantage of this common spatial coordinate system is that eye movement plans can be directly accessed to guide arm movement plans. Similarly, arm movement plans can be directly accessed to guide eye movement plans. Since hand and eye movements are typically directed toward the same locations during natural movements (Land and Hayhoe, 2001; Johansson et al., 2001), it is efficient to encode hand and eye movements in a common spatial representation (Gielen et al., 1984; van Donkelaar, 1997).

Earlier work studying neurons in frontal and parietal cortex that are involved in guiding eye and arm movements has shown neurons often have common tuning properties for different types of movements (Battaglia-Mayer et al., 2001, 2007). These "global tuning fields" are consistent with the overlap in the alignment of response fields we have observed in the center-out reach and saccade tasks (**Fig 2.4**) and demonstrate the formation of common spatial representations for different movement modalities. Our work complements these findings relating to the alignment of response fields. We find that neurons in PMd exhibit the same spatial representation irrespective of whether a saccade or a reach is being prepared, by considering the spatial encoding of response fields with respect to both gaze and hand position. The common theme that emerges is that neurons across frontal and parietal cortex can share selectivity for different movement modalities.

The broad range of preferred directions that we observe for PMd neurons (**Fig 5**) is also consistent with earlier work that shows that neurons in PMd do not show a preference in response for arm movements to directions contralateral to the reaching arm (Caminiti, Johnson, Burnod, et al., 1990; Caminiti, Johnson, and Urbano, 1990). In contrast, our finding of strong lateralization of the preferred directions of PRR neurons (Supplementary Material) differs from earlier work studying the reach tuning of parietal neurons that shows a more uniform tiling of the workspace (Lacquaniti et al., 1995). The difference in results may be due to two factors. First, we recorded from PRR in the bank of the intraparietal sulcus, while earlier work has recorded from more superficial cortical regions on the gyrus of Brodmann's Area 5. Activity in the bank of the sulcus in the superior parietal lobule is more visual in nature than activity on the surface (Colby and Duhamel, 1991; Buneo et al., 2006) and appears to be similar to area LIP on the lateral bank of the intraparietal sulcus, which shows strong lateralization of activity before saccades (Qian-Quiroga et al., 2006). Second, we made our recordings under enforced fixation while earlier recordings from Area 5 were done during free-gaze. The activity of parietal neurons is centered on the orientation

of gaze (Batista et al., 1999; Buneo et al., 2002; Pesaran et al., 2006), so changes in eye position during freely made eye movements affects the responses of parietal neurons (Cisek et al., 2002).

A relative position code is a suitable representation for coordinating eye and arm movements because it provides a particular encoding that allows signals to be transformed between representations within a common extrinsic coordinate frame. This spatial representation allows signals to be transformed from gaze-centered to hand-centered representations frames and to be transformed from hand-centered to gaze-centered representations. This is because relative hand-gaze position links the representation of movement goals centered on the hand and eye. This linkage means that the reference frames are invertible by treating gaze and hand position on equal terms and encoding them as a difference. Visual gaze-centered coordinates can be converted into visual hand-centered coordinates by subtracting relative hand-gaze position. Visual hand-centered coordinates can be converted into visual gaze-centered coordinates by subtracting relative gaze-hand position (Pesaran et al., 2006; Buneo et al., 2002). Since we observe a similar encoding before saccades and reaches, the same transformations may be activated by both movements. This suggests that a representation of visual space linked to the hand may also be useful for saccades. Consistent with this idea, evidence from human psychophysical experiments shows that gaze-centered representations may guide reaching (Henriques and Crawford, 2001; Henriques and Crawford 1998) and that the saccade system can transform hand-centered somatosensory signals into oculomotor coordinates (Ren et al., 2006). Other studies demonstrate that hand position modulates saccadic reaction times and FEF activity during a purely saccadic task (Thura, Hadj-Bouziane, et al., 2008; Thura, Boussaoud, et al., 2008).

When considering a relative position code, it is important, however, to keep in mind the geometry of rotations in which retinal projections at different eye positions are different for the same saccade vectors (Crawford and Guitton, 1997; Klier and Crawford, 1998; Blohm et al., 2007). Therefore, the extrinsic, visual space in which spatial computations may be performed will

introduce systematic errors between eye and hand positions dependent on the angle of gaze. These effects are small in our experiment since we use a rather limited range of gaze and target positions. In order to strictly distinguish between visual and intrinsic frames of reference for relative position codes, one needs to use a larger range of gaze, target and hand positions and/or systematically vary the torsional tilt of the eye and hand. If the nervous system does use visual coordinates, it must correct for the errors in visual coordinates in order to guide accurate movements. These corrections may be performed by the nonlinear transformations to the corresponding intrinsic coordinate frames (Blohm et al., 2009; Crawford et al., 1997; Klier et al., 1998).

Saccade responses in premotor cortex

What is the relationship between saccade responses in premotor cortex and other cortical regions? The presence of stronger saccade planning activity in PMd than in PRR demonstrates that the PMd saccade response is not likely to result from input from PRR. Saccade signals in PMd may originate in frontal cortex. The frontal eye fields (FEF) and the supplementary eye fields (SEF) are the main oculomotor control centers in the frontal cortex (Goldberg and Bruce, 1990; Schlag and Schlag-Rey, 1987; Schall and Thompson, 1999; Russo and Bruce, 2000). These areas have anatomical connections with nearby regions of frontal cortex involved in skeletomotor control, including the dorsal and ventral premotor cortices and the supplementary motor area (Huerta and Kaas, 1990; Huerta et al., 1987). Consequently, input from FEF and/or SEF may be reflected in the PMd response to saccades.

While the premotor cortices are principally implicated in the control of visually-guided limb movements (Mushiake et al., 1991; Wise et al., 1997), microstimulation elicits saccades from regions in both PMd and PMv and neurons in both these areas are active before saccades as well as reaches (Fujii et al., 1998, 2000; Mitz and Godschalk, 1989). The functional significance of these saccade responses, however, has remained unclear. Convergent evidence suggests that saccade

responses in PMd are not directly involved in the control of eye movements, and may link the control of eye movements with the control of arm movements as part of a distributed cortical network including SEF and FEF.

Evidence from microstimulation suggests that the saccade responses we observe are not closely associated with saccade commands because we evoked muscle twitches and not saccades with electrical microstimulation at those sites. In contrast, microstimulation of SEF and FEF elicits eye movements. In the FEF, microstimulation elicits eye movements with currents below 50 μ A and as low as 10 μ A (Bruce et al., 1985). In the SEF microstimulation also elicits saccades at current levels as low as 20 μ A (Schlag et al., 1987), but at higher current levels than FEF (Russo and Bruce, 1993).

The anatomical projections of PMd also suggest that PMd plays a direct role in reaching and not saccades. PMd neurons have a relatively minor projection to the superior colliculus (Fries, 1985) and hence to downstream oculomotor structures, and they have a much more substantial projection to the spinal cord (Dum and Strick, 2002; He et al., 1993).

Single-unit recordings also show that instead of having overlapping responsibilities with PMd, SEF and FEF are more directly involved in saccade control and PMd is more directly involved in reach control. The spatial encoding of PMd neurons for saccades that we have demonstrated appears distinct from the encoding in SEF and FEF. Saccade responses in PMd are predominantly not retinotopic and there is a strong dependence of the response on the relative position of the hand and gaze. Hand position influences saccade signals in FEF (Thura, Hadj-Bouziane, et al., 2008) with a strong dependence on the orientation of eye and head. An influence of hand position on saccade responses in SEF has not been previously shown although SEF neurons have been shown to selectively respond to reaches made with saccades (Mushiake et al., 1996). Additional work is needed to measure hand position signals in FEF and SEF before saccades to more directly compare with the representation of PMd neurons for saccades.

Instead of playing a direct role in saccadic eye movement generation, as has been proposed for FEF and SEF, we propose that saccade signals in PMd provide spatial information that links the control of eye and arm movements in a distributed cortical network.

Sensitivity issues in reference frame analyses

How neural activity encodes space is fundamental to understanding the relationship between brain and behavior. The neural encoding of multiple spatial variables, such as the orientation of the arm, orbital eye position and the position of parts of the body, has been the subject of much work (e.g., Andersen and Mountcastle, 1983; Andersen et al., 1985; Graziano, 2001; Graziano et al., 1994; Van Opstal et al., 1995; Stricanne et al., 1996). When many spatial variables are encoded, neural response patterns are complex and individual variables typically do not dominate the response. Here, using an identical set of matrix analysis procedures, we have uncovered how activity in PMd before both reaches and saccades encodes multiple spatial variables in a relative position code.

Studies have found gain fields and intermediate response fields are common coding schemes for multiple spatial variables (Andersen et al., 1985; Avillac et al., 2005; Stricanne et al., 1996). In typical experimental designs, neural responses are measured for many different target positions but the positions of individual effectors are varied across fewer locations, typically two or three (Batista et al., 2007; Mullette-Gillman et al., 2009; Avillac et al., 2005). The resulting response curves are then analyzed across pairs of effector positions to identify the neural code. While potentially effective at identifying responses that depend on one effector, pair-wise comparisons often cannot distinguish between gain fields and intermediate responses and may lead to the conclusion that the neuronal response inconsistently encodes spatial variables.

Consider gain-modulated responses in which gain effects vary with changes in position to give a gain field of response modulations. The gain field can lead simple pair-wise comparisons, such as correlation measures, to the incorrect conclusion that the response curve does not shift with the position of that effector. This problem is most pronounced for open response curves, where the peak of the response field is not sampled on both sides. Another problem is that pair-wise measures such as distance metrics accumulate noise across the tuning curves instead of cancelling noise (Batista et al., 2007). Lack of robustness to noise reduces the sensitivity of these tests.

To demonstrate a relative position code, more sophisticated matrix analyses methods are necessary. Matrix analysis compares multiple spatial comparisons, and so extends approaches involving pair-wise comparisons, explicitly distinguishing between gain fields and vector or intermediate responses. There are still limitations to these analysis methods, however. For example, one principal limitation of matrix analysis is that the analysis is performed collectively across the entire response matrix. This could be misleading when neurons have responses that vary across space within the response matrix or when neurons have bimodal response fields.

ACKNOWLEDGEMENTS

This work was supported by NIH grants EY05522-21, MH62528-01, the Boswell Foundation, the Sloan-Swartz Center for Theoretical Neurobiology at Caltech, and the DARPA BioInfoMicro program. BP was supported by a Career Award in the Biomedical Sciences from the Burroughs Wellcome Fund, a Watson Program Investigator Award from NYSTAR, a McKnight Scholar Award and a Sloan Research Fellowship. We thank Tessa Yao for editorial assistance, Kelsie Pejisa and Leah Martel for animal care and Viktor Shcherbatyuk for technical assistance.

REFERENCES

- Andersen, R. A., Essick, G. K., and Siegel, R. M. (1985). Encoding of spatial location by posterior parietal neurons. *Science* *230*, 456–458.
- Andersen, R. A., and Mountcastle, V. B. (1983). The influence of the angle of gaze upon the excitability of the light-sensitive neurons of the posterior parietal cortex. *J. Neurosci* *3*, 532–548.
- Avillac, M., Denève, S., Olivier, E., Pouget, A., and Duhamel, J. (2005). Reference frames for representing visual and tactile locations in parietal cortex. *Nat. Neurosci* *8*, 941–949.
- Batista, A. P., Buneo, C. A., Snyder, L. H., and Andersen, R. A. (1999). Reach plans in eye-centered coordinates. *Science* *285*, 257–260.
- Batista, A. P., Santhanam, G., Yu, B. M., Ryu, S. I., Afshar, A., and Shenoy, K. V. (2007). Reference frames for reach planning in macaque dorsal premotor cortex. *J. Neurophysiol* *98*, 966–983.
- Batschelet, E. (1981). *Circular Statistics in Biology*, Academic Press, Inc.
- Battaglia-Mayer, A., Ferraina, S., Genovesio, A., Marconi, B., Squatrito, S., Molinari, M., Lacquaniti, F., and Caminiti, R. (2001). Eye-hand coordination during reaching. II. An analysis of the relationships between visuomanual signals in parietal cortex and parieto-frontal association projections. *Cereb. Cortex* *11*, 528–544.
- Battaglia-Mayer, A., Mascarò, M., and Caminiti, R. (2007). Temporal evolution and strength of neural activity in parietal cortex during eye and hand movements. *Cereb. Cortex* *17*, 1350–1363.
- Blohm, G., and Crawford, J. D. (2007). Computations for geometrically accurate visually guided reaching in 3-D space. *J Vis* *7*, 4.1–22.
- Blohm, G., Keith, G. P., and Crawford, J. D. (2009). Decoding the cortical transformations for visually guided reaching in 3D space. *Cereb. Cortex* *19*, 1372–1393.
- Boussaoud, D., Joffrais, C., and Bremmer, F. (1998). Eye position effects on the neuronal activity of dorsal premotor cortex in the macaque monkey. *J. Neurophysiol* *80*, 1132–1150.
- Bruce, C. J., Goldberg, M. E., Bushnell, M. C., and Stanton, G. B. (1985). Primate frontal eye fields. II. Physiological and anatomical correlates of electrically evoked eye movements. *J. Neurophysiol* *54*, 714–734.
- Buneo, C. A., and Andersen, R. A. (2006). The posterior parietal cortex: sensorimotor interface for the planning and online control of visually guided movements. *Neuropsychologia* *44*, 2594–2606.
- Buneo, C. A., Jarvis, M. R., Batista, A. P., and Andersen, R. A. (2002). Direct visuomotor transformations for reaching. *Nature* *416*, 632–636.

- Caminiti, R., Johnson, P. B., Burnod, Y., Galli, C., and Ferraina, S. (1990). Shift of preferred directions of premotor cortical cells with arm movements performed across the workspace. *Exp Brain Res* 83, 228–232.
- Caminiti, R., Johnson, P. B., and Urbano, A. (1990). Making arm movements within different parts of space: dynamic aspects in the primate motor cortex. *J. Neurosci* 10, 2039–2058.
- Cisek, P., and Kalaska, J. F. (2002). Modest gaze-related discharge modulation in monkey dorsal premotor cortex during a reaching task performed with free fixation. *J. Neurophysiol* 88, 1064–1072.
- Colby, C. L., and Duhamel, J. R. (1991). Heterogeneity of extrastriate visual areas and multiple parietal areas in the macaque monkey. *Neuropsychologia* 29, 517–537.
- Crammond, D. J., and Kalaska, J. F. (1996). Differential relation of discharge in primary motor cortex and premotor cortex to movements versus actively maintained postures during a reaching task. *Exp Brain Res* 108, 45–61.
- Crawford, J. D., and Guitton, D. (1997). Visual-motor transformations required for accurate and kinematically correct saccades. *J. Neurophysiol* 78, 1447–1467.
- Crawford, J. D., Medendorp, W. P., and Marotta, J. J. (2004). Spatial transformations for eye-hand coordination. *Journal of Neurophysiology* 92, 10–19.
- van Donkelaar, P. (1997). Eye-hand interactions during goal-directed pointing movements. *Neuroreport* 8, 2139.
- Dum, R. P., and Strick, P. L. (2002). Motor areas in the frontal lobe of the primate. *Physiol. Behav* 77, 677–682.
- Fries, W. (1985). Inputs from motor and premotor cortex to the superior colliculus of the macaque monkey. *Behav. Brain Res* 18, 95–105.
- Fujii, N., Mushiake, H., and Tanji, J. (1998). An oculomotor representation area within the ventral premotor cortex. *Proc. Natl. Acad. Sci. U.S.A* 95, 12034–12037.
- Fujii, N., Mushiake, H., and Tanji, J. (2000). Rostrocaudal distinction of the dorsal premotor area based on oculomotor involvement. *J. Neurophysiol* 83, 1764–1769.
- Gielen, C. C., van den Heuvel, P. J., and van Gisbergen, J. A. (1984). Coordination of fast eye and arm movements in a tracking task. *Exp Brain Res* 56, 154–161.
- Goldberg, M. E., and Bruce, C. J. (1990). Primate frontal eye fields. III. Maintenance of a spatially accurate saccade signal. *J. Neurophysiol* 64, 489–508.
- Graziano, M. S. (2001). Is reaching eye-centered, body-centered, hand-centered, or a combination? *Rev Neurosci* 12, 175–185.
- Graziano, M. S., Yap, G. S., and Gross, C. G. (1994). Coding of visual space by premotor neurons. *Science* 266, 1054–1057.

- He, S. Q., Dum, R. P., and Strick, P. L. (1993). Topographic organization of corticospinal projections from the frontal lobe: motor areas on the lateral surface of the hemisphere. *J. Neurosci* *13*, 952–980.
- Henriques, D. Y. P., and Crawford, J. D. (2002). Role of eye, head, and shoulder geometry in the planning of accurate arm movements. *J. Neurophysiol* *87*, 1677–1685.
- Huerta, M. F., and Kaas, J. H. (1990). Supplementary eye field as defined by intracortical microstimulation: connections in macaques. *J. Comp. Neurol* *293*, 299–330.
- Huerta, M. F., Krubitzer, L. A., and Kaas, J. H. (1987). Frontal eye field as defined by intracortical microstimulation in squirrel monkeys, owl monkeys, and macaque monkeys. II. Cortical connections. *J. Comp. Neurol* *265*, 332–361.
- Johansson, R. S., Westling, G., Bäckström, A., and Flanagan, J. R. (2001). Eye-hand coordination in object manipulation. *J. Neurosci* *21*, 6917–6932.
- Jouffrais, C., and Boussaoud, D. (1999). Neuronal activity related to eye-hand coordination in the primate premotor cortex. *Exp Brain Res* *128*, 205–209.
- Klier, E. M., and Crawford, J. D. (1998). Human oculomotor system accounts for 3-D eye orientation in the visual-motor transformation for saccades. *J. Neurophysiol* *80*, 2274–2294.
- Lacquaniti, F., Guigon, E., Bianchi, L., Ferraina, S., and Caminiti, R. (1995). Representing spatial information for limb movement: role of area 5 in the monkey. *Cereb. Cortex* *5*, 391–409.
- Land, M. F., and Hayhoe, M. (2001). In what ways do eye movements contribute to everyday activities? *Vision Res* *41*, 3559–3565.
- Lebedev, M. A., and Wise, S. P. (2001). Tuning for the orientation of spatial attention in dorsal premotor cortex. *Eur. J. Neurosci* *13*, 1002–1008.
- Mitz, A. R., and Godschalk, M. (1989). Eye-movement representation in the frontal lobe of rhesus monkeys. *Neurosci. Lett* *106*, 157–162.
- Mullette-Gillman, O. A., Cohen, Y. E., and Groh, J. M. (2009). Motor-related signals in the intraparietal cortex encode locations in a hybrid, rather than eye-centered reference frame. *Cereb. Cortex* *19*, 1761–1775.
- Mushiake, H., Fujii, N., and Tanji, J. (1996). Visually guided saccade versus eye-hand reach: contrasting neuronal activity in the cortical supplementary and frontal eye fields. *J. Neurophysiol* *75*, 2187–2191.
- Mushiake, H., Inase, M., and Tanji, J. (1991). Neuronal activity in the primate premotor, supplementary, and precentral motor cortex during visually guided and internally determined sequential movements. *J. Neurophysiol* *66*, 705–718.

- Ohbayashi, M., Ohki, K., and Miyashita, Y. (2003). Conversion of working memory to motor sequence in the monkey premotor cortex. *Science* 301, 233–236.
- Peña, J. L., and Konishi, M. (2001). Auditory spatial receptive fields created by multiplication. *Science* 292, 249–252.
- Pesaran, B., Nelson, M. J., and Andersen, R. A. (2006). Dorsal premotor neurons encode the relative position of the hand, eye, and goal during reach planning. *Neuron* 51, 125–134.
- Russo, G. S., and Bruce, C. J. (1993). Effect of eye position within the orbit on electrically elicited saccadic eye movements: a comparison of the macaque monkey's frontal and supplementary eye fields. *J. Neurophysiol* 69, 800–818.
- Russo, G. S., and Bruce, C. J. (2000). Supplementary eye field: representation of saccades and relationship between neural response fields and elicited eye movements. *J. Neurophysiol* 84, 2605–2621.
- Schall, J. D., and Thompson, K. G. (1999). Neural selection and control of visually guided eye movements. *Annu. Rev. Neurosci* 22, 241–259.
- Schlag, J., and Schlag-Rey, M. (1987). Evidence for a supplementary eye field. *J. Neurophysiol* 57, 179–200.
- Shadmehr, R., and Wise, S. P. (2005). *The Computational Neurobiology of Reaching and Pointing: A Foundation for Motor Learning* illustrated edition. (The MIT Press).
- Soechting, J. F., and Flanders, M. (1992). Moving in three-dimensional space: frames of reference, vectors, and coordinate systems. *Annu. Rev. Neurosci* 15, 167–191.
- Stricanne, B., Andersen, R. A., and Mazzoni, P. (1996). Eye-centered, head-centered, and intermediate coding of remembered sound locations in area LIP. *J. Neurophysiol* 76, 2071–2076.
- Thura, D., Boussaoud, D., and Meunier, M. (2008). Hand position affects saccadic reaction times in monkeys and humans. *J. Neurophysiol* 99, 2194–2202.
- Thura, D., Hadj-Bouziane, F., Meunier, M., and Boussaoud, D. (2008). Hand position modulates saccadic activity in the frontal eye field. *Behav. Brain Res* 186, 148–153.
- Tweed, D., and Vilis, T. (1987). Implications of rotational kinematics for the oculomotor system in three dimensions. *J. Neurophysiol* 58, 832–849.
- Van Opstal, A. J., Hepp, K., Suzuki, Y., and Henn, V. (1995). Influence of eye position on activity in monkey superior colliculus. *J. Neurophysiol* 74, 1593–1610.
- Weinrich, M., and Wise, S. P. (1982). The premotor cortex of the monkey. *J. Neurosci* 2, 1329–1345.
- Weinrich, M., Wise, S. P., and Mauritz, K. H. (1984). A neurophysiological study of the premotor cortex in the rhesus monkey. *Brain* 107 (Pt 2), 385–414.

Westheimer, G. (1957). Kinematics of the eye. *J Opt Soc Am* 47, 967–974.

Wise, S. P., Boussaoud, D., Johnson, P. B., and Caminiti, R. (1997). Premotor and parietal cortex: corticocortical connectivity and combinatorial computations. *Annu. Rev. Neurosci* 20, 25–42.

FIGURE LEGENDS

Figure 2.1 Behavioral tasks. **(a)** Center-out task for saccades involved the monkey touching a central target while making a saccade from an adjacent location to one of eight peripheral targets arranged on a square spaced 10° . The lower target is not shown for clarity. **(b)** Center-out task for reaches involved the monkey fixating a central target while making a reach from an adjacent location. **(c)** Saccade relative position coding task. A saccade is made from one of four initial gaze positions on a line to one of four target positions while a touch is maintained at one of four hand positions on a touch screen. Hand positions and reach targets are shown in green, gaze positions and saccade targets are shown in red.

Figure 2.2 Example simulated responses and analysis. **(a)** Vector response field (i.e. $f(G,T)=f(T-G)$) decomposed by singular value decomposition analysis and gradient analysis. The first two matrix responses in the singular value decomposition are shown. The fraction of the total energy they capture is given beneath each matrix. The response field orientation from the gradient analysis is shown on the right-most column. **(b)** Intermediate response field.

$f(G,T) = f\left(T - \frac{G}{2}\right)$ **(c)** Intermediate response field. $f(G,T) = f(T - 2G)$ **(d)** Weak gain field of eye position modulating target position coding. **(e)** Moderate eye position gain field. **(f)** Strong eye position gain field. White = high firing rate. Black = low firing rate. For the response field orientation, 0° points right and angles increase counter clockwise.

Figure 2.3 Example PMd cell responses. **(a)** Rasters and peri-stimulus time histograms for activity of an example cell to a reach without a saccade (blue) and a saccade without a reach (black). Time of the cue onset (triangle), end of delay period (green cross) mean saccade time (red square) and mean reach end time () are shown. **(b)** Same as **(a)** for another PMd cell.

Figure 2.4 Comparison of saccade- and reach-related activity during the center-out tasks. **(a)** Population average normalized histograms aligned to target onset for reaches (black) and saccades (grey) to the preferred direction. Mean time of saccade (square). Mean time of reach endpoint (triangle). **(b)** Same for PRR.

Figure 2.5 Population histograms preferred directions of PMd neurons. **(a)** Histogram of preferred direction of activity during delay period before saccades. **(b)** Histogram of preferred direction of activity during delay period before reaches. **(c)** Histogram of difference in preferred directions during delay periods before saccades and reaches. Asterisk marks the mean preferred direction difference. Preferred directions before a reach and saccade point in similar directions.

Figure 2.6 Idealized cell responses and formal models for **(a)** gaze-centered and **(b)** relative position coding cells. The idealized gaze-centered cell response shown is modeled as a gain field of hand position modulating gaze-target vector coding. In the formal model, an additional gain field of gaze position can affect the cell's firing rate as well. The idealized relative position coding cell response shown is modeled as hand-gaze, target-gaze and target-hand position tuning. In the formal model, gain fields of gaze position and hand position can also affect the cell's firing rate as well. The response field orientation from the gradient analysis (see Results and Methods) is shown for each idealized cell. 0° points right and angles increase counter clockwise. White = high firing rate. Black = low firing rate.

Figure 2.7 PMd example cell responses to the saccade relative position coding task. Activity is aligned to target onset (black square) as gaze position is varied (rows), hand position is varied (columns) and target position is varied (within each panel). Gaze (G), hand (H) and target (T) positions are shown above each panel. Spike rasters are shown above the panel color coded for each target position in that panel. Target onset time (black square) and mean saccade time (grey square) are shown on each panel. Horizontal bars on the top left panel indicate the delay and movement period analysis intervals.

Figure 2.8 PMd example cell response matrices during the saccade relative position coding task. **(a)** Target-gaze response matrix during the delay period at the peak of the response field. The hand is at -20° . Arrows show the two-dimensional gradient elements. **(b-c)** Similar for hand-gaze and hand-target response matrices with the target at -20° and gaze at 10° , respectively. **(d)** Overall response field orientation for the TG response matrix, -144° . **(e)** Overall response field orientation for the HG response matrix, -56° . **(f)** Overall response field orientation for the TH response matrix, -101° . 0° points right and angles increase counter clockwise.

Figure 2.9 Population gaze-hand-target analysis during the delay period. **(a)** Population separability for all PMd cells with tuned delay or movement period responses. The percentage of inseparable cells is shown in dark grey. The percentage of separable cells is shown in light grey. **(b)** Target-gaze response field orientation **(c)** target response field orientation and **(d)** eye-hand response field orientation for tuned PMd neurons. Orientations for separable cells are shown in dark grey. Orientations for inseparable cells are shown in light grey.

Figure 2.10 PMd delay period responses during the saccade relative position coding task. **(a)**

Venn diagram of the number of neurons with tuned inseparable TG, TH and HG responses during

the saccade relative position coding task. **(b)** Tuning strength of the saccade response matrices. *

denotes significant difference ($p < 0.05$).

Chapter 3

Free choice activates a decision circuit between
frontal and parietal cortex

We often face alternatives which we are free to choose between. Planning movements to select an alternative involves a number of areas in frontal and parietal cortex¹⁻¹¹ that are anatomically connected into long-range circuits¹². These areas must coordinate their activity to select a common movement goal, but how neural circuits make decisions remains poorly understood. Here we simultaneously record from the dorsal premotor area (PMd) in frontal cortex and the parietal reach region (PRR) in parietal cortex to investigate neural circuit mechanisms for decision making. We find that correlations in spike and local field potential (LFP) activity between these areas are greater when monkeys are freely making choices than when they are following instructions. We propose that a decision circuit featuring a subpopulation of cells in frontal and parietal cortex may exchange information to coordinate activity between these areas. Cells participating in this decision circuit may influence movement choices by providing a common bias to the selection of movement goals.

According to theories of decision making, we make choices by selecting the alternative that is most valuable to us¹³. How much we value each alternative is revealed by our choices. If we value swimming as much as running, we will choose to do both instead of always choosing one over the other. Although actions with similar values can lead to different choices, only one choice can be made at a time. Planning a movement to select an alternative activates many areas of the brain. How does the brain decide what to do? PMd and PRR plan reaching arm movements¹⁴ and are directly connected¹². We therefore studied these areas to identify a neural circuit for deciding where to reach.

We trained two monkeys to do a free search task and an instructed search task (Fig 3.1a,b). In both tasks, monkeys made a sequence of reaches to visual targets for juice rewards. The key manipulation was that, in the free search task, the three targets were visually identical circles, and the monkey could search in any sequence (Fig. 3.1a) while in the instructed search task, the three targets were a circle, a square and a triangle, and the monkey had to search in a fixed sequence (Fig. 3.1b). To control other sensory, motor and reward-related factors, we carefully matched the

two tasks by yoking the sequences presented in the instructed task to the monkey's choices in the free search task (see Online Methods, Supplementary Results and Supplementary Fig 2).

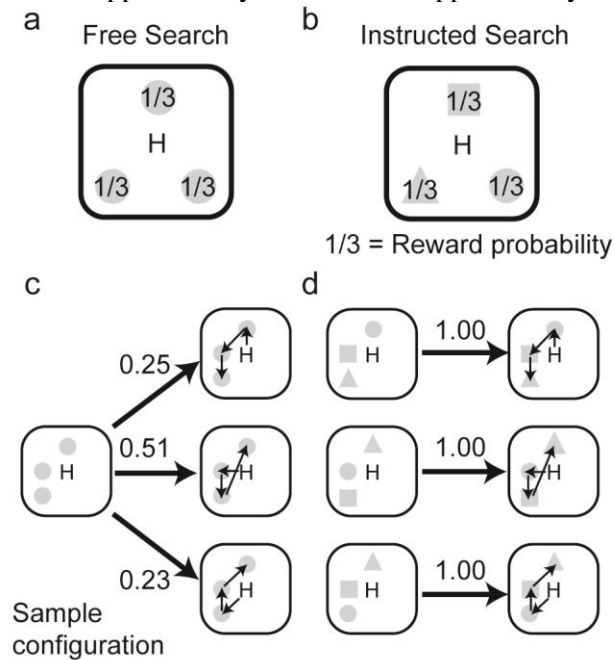


Figure 3.1

We designed the free search task to allow choices by simply releasing constraints. During free search, each monkey's choices varied, even for identical stimuli (Fig. 3.1c). In contrast, instructed search movement sequences did not vary (Fig. 3.1d). Overall, each monkey developed a free search strategy and chose between two or three different movement sequences for most search arrays (see Supplementary Fig. 3).

While the tasks we studied could differ in other aspects, like reward expectancy, attention, or overall effort, analysis of each animal's behavior indicates that the major difference involves decision making (see Supplementary Results). Free and instructed search involve different decisions because the alternatives have different values. Free search involves choosing between movement sequences with similar values so choices vary from trial to trial (Fig 3.1c). Since we reward only one movement sequence, instructed search involves alternatives with very different values. Consequently, each monkey repeatedly makes the same choices (Fig 3.1d).

When movement choices vary from trial to trial, PMd and PRR must coordinate their activity. Analyzing spiking and LFP activity may resolve neural coordination between these areas. Spiking activity measures action potentials from individual neurons. LFP activity predominantly measures synaptic potentials in a population of neurons near the recording electrode¹⁵. Spike-field coherency directly relates these two signals by measuring how well LFP activity is predicted by action potentials. We therefore measured spike-field coherency to characterize neural coordination between PMd and PRR and identify the neurons involved in this coordination.

We made 314 PMd spike-PRR field and 187 PRR spike-PMd field recordings in two animals during both free and instructed search tasks (see Supplementary Materials). We estimated spike-field coherency between spiking in PMd and LFP activity in PRR using a ± 150 ms analysis window that was stepped through the trial every 10 ms from before the onset of the search array to the time of the first reach. A highly significant, transient increase in 15 Hz coherence following search array onset was clearly present in an example recording (Fig 3.2a). Coherence was significant during both tasks but stronger during free search (Fig. 3.2b; $p < 0.05$, t-test). Similarly, coherence between spiking in PRR and LFP activity in PMd was weaker but revealed the same pattern (Fig. 3.2c,d). In this recording, coherence was only significant during free search and not during instructed search (Fig. 3.2d).

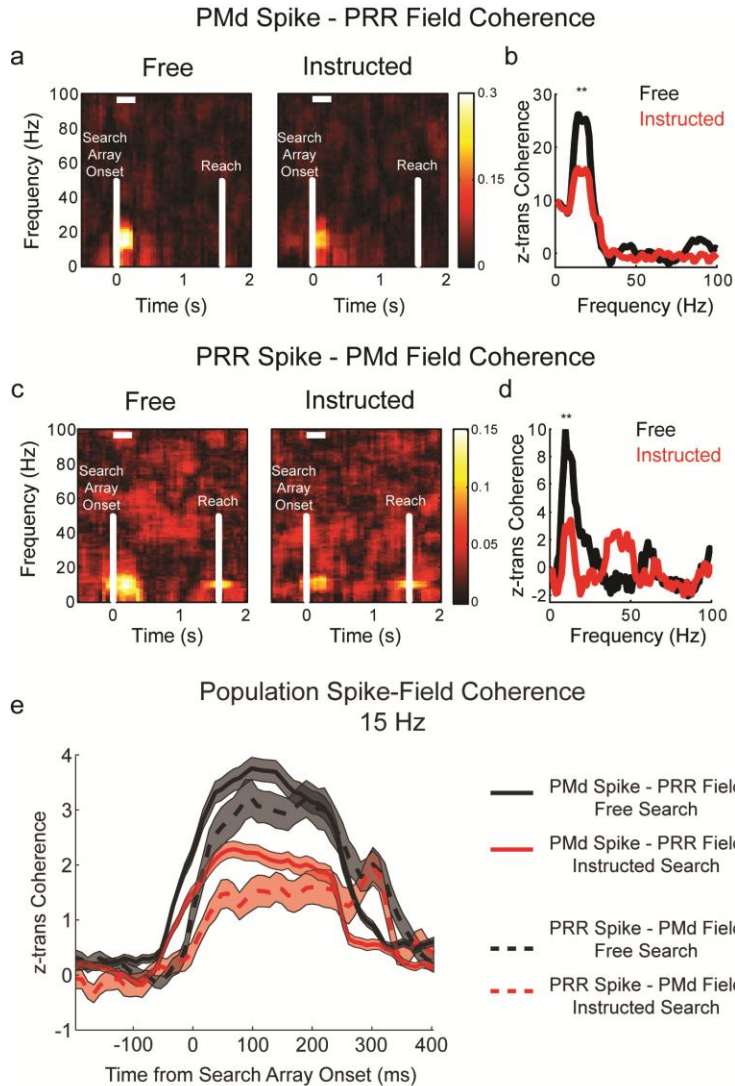


Figure 3.2

Significant coherence at 15 Hz implies that the timing of action potentials is correlated with fluctuations in LFP activity. Analyzing the relative phase of activity in PMd and PRR supported this and revealed correlations in the timing of activity in each area that were not simply time-locked to search array onset (see Supplementary Results and Supplementary Fig 4). Interestingly, the amplitude of spike and LFP activity, as opposed to their relative timing, did not predict PMd-PRR coherence. We correlated the strength of the coherence immediately following search array onset with LFP power and did not observe a significant correlation ($p=0.45$; F-test). Linear regression of spike-field coherence against the change in firing rate immediately following search array onset revealed that coherence was not simply related to the firing rate as well ($r^2=0.06$,

$p=0.14$). Cells with an increase in firing rate generally had the greatest coherence. However, coherence also increased for some cells whose firing rate decreased or did not change.

Spike-field correlations were present only between select pairs of recording sites. Across the population, 74 PMd spike-PRR field recordings (74/314, 24%) contained statistically significant coherence at 15 Hz following search array onset during either task ($p<0.05$; t-test. see Table 3.1). A similar proportion of PRR spike-PMd field recordings (43/187 23%; $p<0.05$) were significant (see Table 3.2). In both cases, spike-field coherence was most prevalent during free search. The fraction of correlated recordings significantly increased between sites with overlapping ($< 20^\circ$) response fields ($p<0.05$; Binomial test; 54 % of PMd spike – PRR field recordings, 45% of PRR spike - PMd field recordings).

Table 3.1: Population PMd spike-PRR field coherence

PMd Spike-PRR Field Coherence			
Center-out	Free or Instructed		
23/221 (10%)	74/314 (24%)		
	Free only	Instructed only	Free and instructed
	31/74 (42%)	20/74 (27%)	22/74 (22%)

Table 3.2: Population PRR spike-PMd field coherence

PRR Spike-PMd Field Coherence			
Center-out	Free or Instructed		
13/138 (9%)	43/187 (23%)		
	Free only	Instructed only	Free and instructed
	21/43 (49%)	12/43 (28%)	9/43 (21%)

To test whether spike-field coherence between PMd and PRR is specific to decision making, we measured coherence during two control experiments. First, we measured spike-field coherence during a single target center-out task instructing monkeys to move to a single peripheral target. In this task, the monkey did not choose between targets. The proportions of recordings with significant spike-field coherence fell dramatically (see Tables 3.1 and 3.2). Only 10% (23/221) of PMd spike-PRR field recordings and 9% (13/138) of PRR spike-PMd field recordings had significant coherence. Second, during both search tasks, we found that saccades are reliably made following search array onset (see Supplementary Results). To test whether spike-field coherence was due to these eye movements, we measured coherence in one animal during a variant of the search tasks that involved enforced fixation. Even during fixation, spike-field coherence was significant following search array onset and was strongest during free search (see Supplementary Results, Supplementary Fig. 5 and Supplementary Tables 1 and 2). The population average spike-field coherence across all cells recorded during each task reinforced the selectivity for the search tasks (see Supplementary Fig. 6). These control experiments demonstrate that spike-field coherence between PMd and PRR is associated with making a decision.

LFP activity was not only correlated with spiking activity in the other area. Within-area spike-field coherence was also significant (see Supplementary Results and Supplementary Figs 7 and 8). Since spiking was coherent with locally recorded LFP activity, LFP activity may capture the correlation we observe between areas. Partial spike-field coherence analysis¹⁶ addresses this concern (see Supplementary Methods and Supplementary Fig. 9). In each example case, partial spike-field coherence remained significant after accounting for local LFP activity ($p < 0.05$, t-test). Significant partial spike-field coherence was also present across the population (74% of PMd spike-PRR field partial coherence and 70% of PRR spike-PMd field partial coherence; see Supplementary Results). Therefore, spike-field coherence between PMd and PRR directly relates correlations across the circuit to the activity of individual neurons.

Spike-field coherence gives two independent measures of the neuronal coordination between PRR and PMd. This may indicate how activity flows across the circuit. We estimated the population average coherence for each of the populations that showed coherence at 15 Hz in either search task and compared them (Fig. 3.2e). Across each population, PMd-PRR spike-field z-score coherence (see Methods and Supplementary Methods) was stronger during free search than during instructed search ($p < 0.01$, Bonferroni-corrected t-test). Importantly, PMd spike-PRR field coherence started ~ 30 ms earlier than PRR spike-PMd field coherence.

Assuming that LFP activity is predominantly synaptic, this suggests that PMd is activated before PRR during search and that PMd spiking is reflected in PRR LFP activity before PRR spiking is reflected in PMd LFP activity (see Supplementary Discussion). The activity is at a relatively low frequency, ~ 15 Hz, and is transient, ~ 350 ms. Our time resolution is limited, but the correlation can involve only a few 15 Hz cycles. Since action potentials are propagated between areas, one attractive possibility is that spike-field coherence measures signals in a subpopulation of neurons that travel across this circuit first from PMd to PRR and then back from PRR to PMd in a “handshake”. Consistent with this, the 30 ms latency between the spike-field coherence measurements (Fig 3.2e) is a half-cycle at 15 Hz.

PMd and PRR spiking activity let us examine when each area becomes active. We recorded 115 PMd and 39 PRR neurons responsive to search array onset to measure response latency in each area. PMd spiking responded significantly earlier than PRR spiking in both tasks (PMd instructed search = 64 ± 6 ms; Free search = 79 ± 5 ms. PRR instructed search = 90 ± 10 ms; Free search = 109 ± 11 ms. Mean \pm s.e.m.; Fig 3.3). We then estimated response latency for 110 PMd neurons and 120 PRR neurons recorded in both animals during the center-out task. PRR cue response latencies were significantly shorter in this task than in either of the search tasks ($p < 0.05$; Permutation test) and PMd and PRR response latencies did not differ (PMd = 63 ± 5 ms; PRR = 70 ± 6 ms; $p = 0.51$, Wilcoxon test; Fig 3.3e). This suggests that the response latency difference between PRR and PMd is specific to making a decision.

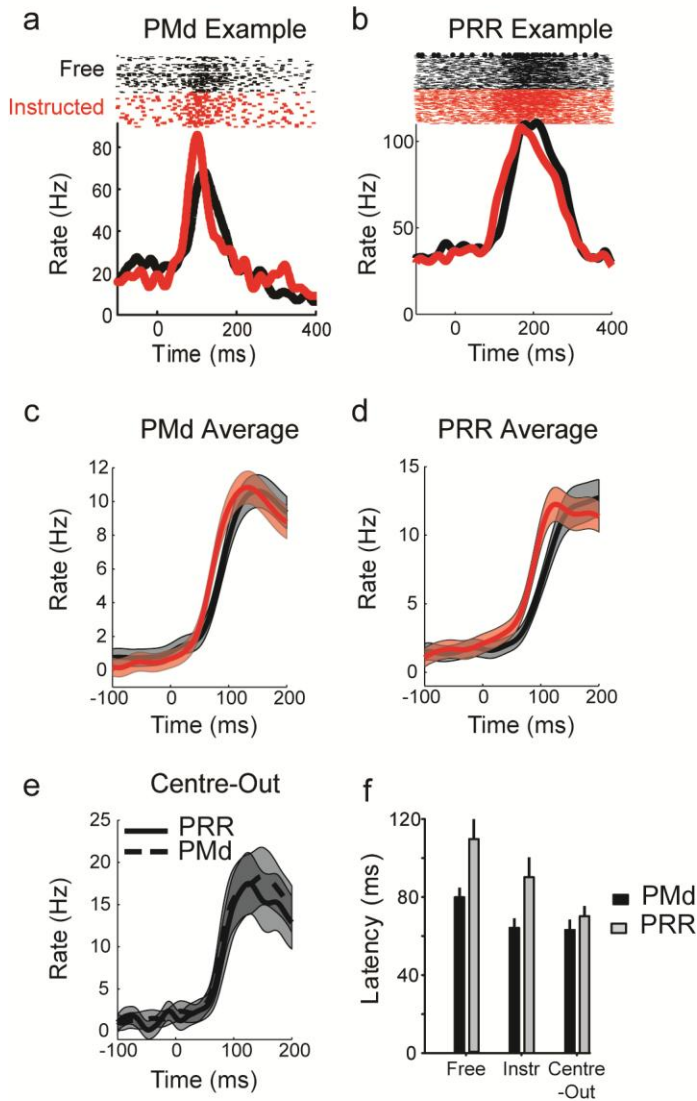


Figure 3.3

Since spike-field correlations are strongest during decision making, the sub-population of coherent neurons may encode the upcoming movement choice. If so, cells with significant spike-field correlations should predict the movement choice earlier than cells which do not. We investigated this with a receiver-operating characteristic (ROC) analysis of the firing rate during free search (see Supplementary Methods). We calculated the average choice probability separately for correlated and uncorrelated PRR and PMd neurons. In both areas, correlated neurons predict the movement choice after search array onset during the period of greatest spike-field coherence (Fig. 3.4a,b, see also Fig 3.2e). Later in the trial, uncorrelated cells predict the movement choice

as accurately as correlated cells. Neurons with long-range correlations may, therefore, exchange information about movement choice between PMd and PRR.

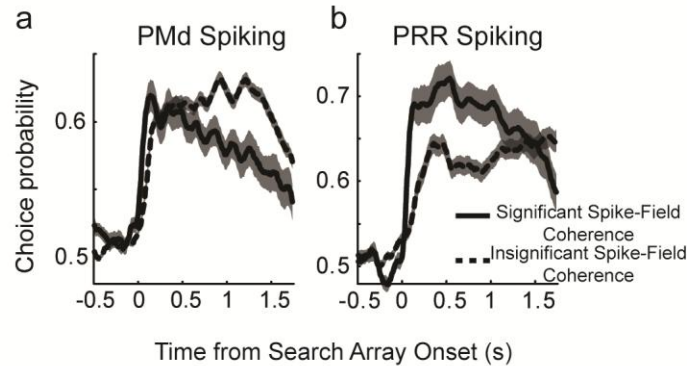


Figure 3.4

In summary, correlations between PMd and PRR are activated by decision making. Coherence is strongest during free search and is weaker during instructed search. Far less coherence is present during a simpler center-out task, and the pattern of coherence is unaffected by freely made eye movements. This shows that decision making is distributed across a frontal-parietal circuit and that top-down signals from PMd influence decisions in this circuit.

Why is coherence stronger during free search? This could be due to the nature of the decision. Choices were variable during free search. In contrast, the same choices were made repeatedly during instructed search (Fig 3.1). Decision making can be modelled by races underlying the selection of each alternative¹⁷. These races must be closer during free search because choices are more variable. Therefore, the difficulty of the decision may underlie coherence between PMd and PRR. Cognitive control mechanisms are activated to select between alternative actions. Prefrontal, medial frontal and cingulate cortex are involved in these mechanisms¹⁸⁻²⁰ and could modulate frontal-parietal coherence during decision making.

During search, the flow of activity across frontal and parietal cortex may reflect the process of deciding. Information rises fastest in PMd (Fig 3.3f), so it cannot be driven by PRR¹⁴, and must take alternative routes possibly through the thalamus, superior colliculus and frontal eye

fields²¹. Information may go from frontal to parietal cortex²² and then back in a “hand shake” of increased communication (Fig 3.2e) that reflects the decision. This transient coordination may reflect how long the decision takes. Subsequent activity may reflect movement planning following the decision (see Supplementary Discussion). Oscillations and synchronization in frontal and parietal cortex exist during attention and movement preparation^{2, 23–28}. Correlations at specific frequencies could be a signature of these cognitive processes²⁹. We have identified a decision circuit in which frontal-parietal communication occurs at relatively low frequencies. The neurons participating in this circuit predict the movement choice earliest and could play an important role in deciding where to reach.

METHODS SUMMARY

Two male rhesus monkeys (*Macaca Mulatta*) participated in the experiments. We recorded single-unit and LFP activity from PMd and PRR using Pt/Ir electrodes controlled by multiple-electrode microdrives (Thomas Recordings, Germany). Each monkey was trained to perform a reach search for juice rewards either by freely making choices or by following instructions. Correlations between spiking and LFP activity within and between PMd and PRR were estimated using multitaper spectral methods^{2, 30}. All surgical and animal care procedures were done in accordance with National Institute of Health guidelines and were approved by the California Institute of Technology Animal Care and Use Committee.

ACKNOWLEDGEMENTS

This work was supported by NIH grants, EY 07492, EY05522 and MH62528, the DARPA BioInfoMicro program as well as a Career Award in the Biomedical Sciences from the Burroughs Wellcome Fund (BP), a James D. Watson Investigator Program Award from NYSTAR (BP), and a Sloan Research Fellowship (BP). We thank David Heeger and Heather Dean for comments on the

manuscript, Nathaniel Daw for helpful conversations, Tessa Yao for editorial assistance, Kelsie Pejsa and Nicole Sammons for animal care and Viktor Shcherbatyuk and Mike Walsh for technical assistance. The authors have no competing interests.

AUTHOR CONTRIBUTIONS

BP, MJN and RAA designed the experiment and wrote the paper. BP and MJN collected the data and BP performed the data analysis.

FIGURE LEGENDS

Figure 3.1: Task and behavior. **a**, Free search task. Three circular targets presented at eight potential locations spaced 10° apart around the central hand position, H. **b**, Instructed search task. Targets in the instructed search task were a circle, square and triangle and the monkey had to reach to them in that order. Each target had an equal, $1/3$, probability of being the rewarded target. **c**, The most frequent movement sequences made in response to an example configuration during the free search task. The same configuration elicits three different sequences. **d**, Instructed search configurations elicit the same sequence. Probability shown above each arrow

Figure 3.2: PMd-PRR spike-field coherence. **a–b**, Example PMd spike-PRR field coherence: **a**) Time-frequency coherence every 50 ms during free and instructed search. Amplitude is color coded. Activity is aligned to search array onset (First vertical white bar). Average time of the 1st reach (Second vertical white bar). White horizontal bar shows analysis window for **b**. **b**, Coherence line plot for free (black) and instructed (red) search tasks. Coherence is z-transformed. Significant difference at 15 Hz (**, $p < 0.05$; t-test). **c–d**, Example PRR spike-PMd field coherence. **e** .Population average 15 Hz PMd-PRR spike-field coherence every 10 ms. PMd spike-PRR field coherence (solid). PRR spike-PMd field coherence (dashed). Free search (black).

Instructed search (red). Coherence is z-transformed before averaging. 95% confidence intervals, Bonferroni corrected, (shaded).

Figure 3.3: Spike response latencies. **a**, Example PMd neuron response to free search (black) and instructed search (red). Activity is aligned to search array onset. Movement to the cell's preferred direction. **b**, Population average PMd spike response for cells. Activity is baseline subtracted. Standard error of the mean (shaded). **c**, Example PRR neuron. **d**, Population average PRR spike response. **e**, Population average PRR and PMd spike responses during center-out task to the preferred direction. **f**, Population response latencies for PMd and PRR during free search, instructed search and the centre-out task. Error bars indicate 95% confidence intervals.

Figure 3.4: ROC choice probability estimated from the firing rate for neurons with and without significant PMd-PRR spike-field coherence. **a**, Population average choice probability for correlated (solid) and uncorrelated (dashed) PMd neurons. 95% confidence intervals (shaded). **b** Same for PRR neurons

REFERENCES

1. Scherberger, H. & Andersen, R. A. Target selection signals for arm reaching in the posterior parietal cortex. *J Neurosci* 27, 2001–12 (2007).
2. Pesaran, B., Pezaris, J. S., Sahani, M., Mitra, P. P. & Andersen, R. A. Temporal structure in neuronal activity during working memory in macaque parietal cortex. *Nat Neurosci* 5, 805–811 (2002).
3. Gold, J. I. & Shadlen, M. N. Representation of a perceptual decision in developing oculomotor commands. *Nature* 404, 390–394 (2000).

4. Shadlen, M. N. & Newsome, W. T. Motion perception: seeing and deciding. *Proc Natl Acad Sci U S A* 93, 628–33. (1996).
5. Pesaran, B., Nelson, M. J. & Andersen, R. A. Dorsal premotor neurons encode the relative position of the hand, eye, and goal during reach planning. *Neuron* 51, 125–34 (2006).
6. Cisek, P. & Kalaska, J. F. Neural correlates of reaching decisions in dorsal premotor cortex: specification of multiple direction choices and final selection of action. *Neuron* 45, 801–14 (2005).
7. Sugrue, L. P., Corrado, G. S. & Newsome, W. T. Matching behavior and the representation of value in the parietal cortex. *Science* 304, 1782–1787 (2004).
8. Gail, A. & Andersen, R. A. Neural dynamics in monkey parietal reach region reflect context-specific sensorimotor transformations. *J Neurosci* 26, 9376–84 (2006).
9. Quiñero, R., Snyder, L. H., Batista, A. P., Cui, H. & Andersen, R. A. Movement intention is better predicted than attention in the posterior parietal cortex. *J Neurosci* 26, 3615–20 (2006).
10. Romo, R. & Schultz, W. Neuronal activity preceding self-initiated or externally timed arm movements in area 6 of monkey cortex. *Exp Brain Res* 67, 656–62 (1987).
11. Platt, M. L. & Glimcher, P. W. Neural correlates of decision variables in parietal cortex. *Nature* 400, 233–8. (1999).
12. Johnson, P. B., Ferraina, S., Bianchi, L. & Caminiti, R. Cortical networks for visual reaching: physiological and anatomical organization of frontal and parietal lobe arm regions. *Cereb Cortex* 6, 102–19. (1996).
13. Kreps, D. M. *A course in microeconomic theory* (Princeton University Press, Princeton, 1990).

14. Wise, S. P., Boussaoud, D., Johnson, P. B. & Caminiti, R. Premotor and parietal cortex: corticocortical connectivity and combinatorial computations. *Annu Rev Neurosci* 20, 25–42 (1997).
15. Mitzdorf, U. Current source-density method and application in cat cerebral cortex: investigation of evoked potentials and EEG phenomena. *Physiol Rev* 65, 37–100 (1985).
16. Halliday, D. M. et al. A framework for the analysis of mixed time series/point process data--theory and application to the study of physiological tremor, single motor unit discharges and electromyograms. *Prog Biophys Mol Biol* 64, 237–78 (1995).
17. Bogacz, R., Brown, E., Moehlis, J., Holmes, P. & Cohen, J. D. The physics of optimal decision making: a formal analysis of models of performance in two-alternative forced-choice tasks. *Psychol Rev* 113, 700–65 (2006).
18. Kerns, J. G. et al. Anterior cingulate conflict monitoring and adjustments in control. *Science* 303, 1023–6 (2004).
19. Daw, N. D. & Doya, K. The computational neurobiology of learning and reward. *Curr Opin Neurobiol* 16, 199–204 (2006).
20. Goldberg, G. Supplementary motor area structure and function: review and hypotheses. *Behav Brain Sci* 8, 567–616 (1985).
21. Schmolesky, M. T. et al. Signal timing across the macaque visual system. *J Neurophysiol* 79, 3272–8 (1998).
22. Cisek, P. Integrated neural processes for defining potential actions and deciding between them: a computational model. *J Neurosci* 26, 9761–70 (2006).
23. Scherberger, H., Jarvis, M. J. R. & Andersen, R. A. Cortical local field potential encodes movement intentions. *Neuron* 46, 347–354 (2005).

24. Murthy, V. N. & Fetz, E. E. Synchronization of neurons during local field potential oscillations in sensorimotor cortex of awake monkeys. *J Neurophysiol* 76, 3968–82. (1996).
25. Bressler, S. L., R. Coppola and R. Nakamura. Episodic multiregional cortical coherence at multiple frequencies during visual task-performance. *Nature* 366, 153–156 (1993).
26. Rickert, J. et al. Encoding of movement direction in different frequency ranges of motor cortical local field potentials. *J. Neurosci.* 25, 8815–8824 (2005).
27. Riehle, A., Grun, S., Diesmann, M. & Aertsen, A. Spike synchronization and rate modulation differentially involved in motor cortical function. *Science* 278, 1950–3 (1997).
28. Buschman, T. J. & Miller, E. K. Top-down versus bottom-up control of attention in the prefrontal and posterior parietal cortices. *Science* 315, 1860–2 (2007).
29. Fries, P. A mechanism for cognitive dynamics: neuronal communication through neuronal coherence. *Trends Cogn Sci* 9, 474–80 (2005).
30. Mitra, P. P. & Pesaran, B. Analysis of dynamic brain imaging data. *Biophys J* 76, 691–708 (1999).

ONLINE METHODS

Experimental preparation

Two male rhesus monkeys (*Macaca Mulatta*) participated in the experiments. Each animal was first implanted with a head cap and eye coil under general anaesthesia. In a second surgery, recording chambers were implanted in frontal and posterior parietal cortex in the right hemisphere of each animal. Structural magnetic resonance imaging was used to identify the position of the arcuate sulcus and intraparietal sulcus and guide placement of the recording chambers to give access to cortex medial to each sulcus. In both animals, PMd recordings were

made within the cortical gyrus within 1.5 mm of the cortical surface and PRR recordings were made within the intraparietal sulcus 4 – 9 mm below the cortical surface.

Behavioral Tasks

For all tasks, reaches were made with the left arm on a touch-sensitive screen (ELO Touch Systems, CA). Visual stimuli were presented on an LCD display (LG Electronics, Korea) placed behind the touch screen. All trials began with the illumination of a central circle which the animal needed to touch with his hand and hold for a baseline period (~ 500 ms).

In the **search tasks**, after a baseline hold period (0.5–1 s), three targets were presented on a 3x3 grid (spaced 10°) of eight possible locations around the start point. After a delay period (1–1.5 s) the monkey was given a go signal to reach to one of the three targets. Only one of the three targets triggered a juice reward when touched. If the monkey did not reach to the target that gave the reward, he was allowed to make additional reaches to targets following subsequent hold periods (0.5–1 s). Additional reaches were permitted until the reward was received. Targets were extinguished once they were touched. An auditory tone signalled the go signal for each reach. A different set of three targets from the eight possible locations appeared each trial, and the target that gave the reward was chosen from these three targets with equal probability. This stimulus-reward configuration set ensured that the monkey didn't repeatedly perform the same stereotyped sequence of movements. This elicited choices by releasing constraints instead of intensively training the subject to overcome biases and avoid stereotyped choices. If the animal reached to the wrong shape in the instructed search task, the trial was aborted. The animal first knew it was in a free search or instructed search trial when the search array was illuminated.

The free and instructed search tasks were yoked in an interleaved design to match the sensory-, motor- and reward-related contingencies. We did this by initially requiring the monkey to perform an initial set of free search trials in a block (typically 50). The search array

configurations were selected at random from the set of 56 possible configurations. We counted the number of times each search array configuration was presented and the number of times each possible movement sequence was made during the free search task. After the initial set of free search trials was performed, we began to randomly interleave instructed search trials. During this phase of the session, the probability of a given trial being a free search or instructed search task was balanced so that after 200 total trials an equal number of trials from each task would be successfully completed. Search array configurations for the free search task continued to be selected at random. Search array configurations for the instructed search task were drawn from the probability distribution defined by the set of search configurations presented in the preceding free search trials that were successfully completed. To match the motor contingencies in the instructed search trials to the free search trials, the order of the movement sequences instructed by the search array was drawn from a probability distribution defined by the set of movement choices made in the preceding free search trials. To reduce the number of trials needed to estimate these movement sequence probabilities and to prevent the generation of stereotyped movement sequences, we matched only the first element of the instructed movement sequence with the monkey's choices and allowed potential mismatch for the second and third elements of the instructed movement sequence. All probability distributions were updated after each successful trial. Eye movements were unconstrained and, on a subset of experimental sessions (53 sessions in Monkey E, 15 sessions in Monkey Z), were monitored using a scleral search coil (CNC Engineering, WA).

A variant of the **search tasks with enforced fixation** was also tested in one animal (Monkey E). In this variant, the search tasks were identical except that the monkey needed to maintain fixation at the current touch location throughout the trial. As a result, the only eye movements that were allowed were made at the time of a reach movement.

In the **center-out task**, a single target was presented at one of eight peripheral locations on a 3x3 grid (spaced 10°) of eight possible locations around the start point. After a delay period (1–

1.5 s) the monkey reached to the target and was then given a juice reward. Fixation was enforced during the period following acquisition of the start point through the end of the delay period. At this time gaze was unconstrained and both monkeys made a coordinated saccade to the target of the reach movement.

Section II: Investigations of analytical methodology for
awake, behaving extracellular recording data

Chapter 4

Analysis of per-trial correlations of ensemble spike- spike coherence

BACKGROUND

Comparisons of the means of neural and behavioral data across repeated trials in different experimental conditions have proven useful in furthering our understanding of cognition and other functions of the brain. But merely demonstrating simultaneous effects on the central tendency of two or more measured quantities when the experimental condition changes only demonstrates each quantity's relation to the changed experimental condition. Going beyond this to investigate trial-by-trial correlations can be a useful tool to validly draw stronger conclusions of some direct relationship between the two measured quantities. For most data metrics these correlations can be investigated in a straightforward manner. However, trial-by-trial correlations can present a challenge for an estimate such as neural coherence, which typically requires multiple trials for the estimate itself to be made.

Neural coherence has been a metric of particular interest in neuroscience in the past decade, being used as a measure of neural synchronization in a range of studies (for example, Buschman and Miller 2007; Chalk et al., 2010; Fries et al., 2001, 2008; Gregoriou et al., 2009; Pesaran et al., 2002, 2008; Rutishauser et al., 2010; Scherberger, 2005). These investigations rely on the mean coherence over trials, typically being compared between different experimental conditions. One notable study that did look at the correlation of coherence with other parameters across trials was Womelsdorf, et al. (2006). Here the authors devised and applied a novel leave-one-trial-out method for estimating the coherence for each individual trial, which they then correlated with behavioral reaction times to conclude that increased gamma coherence during the trial predicted faster reaction times. This clearly presented a solution to the problem, although there are other viable methods to accomplish this correlation that were not explored in this study, such as using groups of multiple trial estimates or multiple taper estimates within a single trial (Thompson and Chave, 1991; Jarvis and Mitra, 2001). Additionally, this per-trial analysis has only been applied to single pairs of spikes and fields, but in the literature has not to our knowledge yet

been extended to an ensemble of multiple simultaneously recorded signals. It is of interest to know to what extent analysis of these ensembles holds a potential for revealing possible increased and synergistic information beyond what is present in individual signal pairs.

Here we compare these different methods of measuring per-trial neural coherence for the purpose of comparing neural coherence correlations with other data metrics. Investigating these correlations is of interest as they could identify possible direct functional roles of coherent neural activity during the performance of behavioral tasks. We investigated this for individual pairs of recorded spike trains as well as for entire ensembles of simultaneously recorded spike trains using data recorded from granular and supragranular layers of rat barrel cortex in response to a paired auditory and whisker stimulus. All of the techniques we describe here apply to analyses of continuous data series as well, including LFP, EEG and MEG data.

MATERIALS AND METHODS

Data collection:

All of the experiments in this report were approved by the Vanderbilt University Animal Care Committee (IACUC), carried out in an AAALAC approved animal facility, and were in accordance with the guidelines of the NIH and the Society for Neuroscience. 5 Long-Evans rats (2 males and 3 females; 250–350 g, 2–3 months old at the time of recording) were used for this study.

Each rat was anesthetized with urethane (1.5 g/kg, 30% aqueous solution, i.p.) and the surgical procedure to expose the barrel cortex was performed as previously described (Popescu and Ebner 2010). Commercial quartz glass insulated, platinum/iridium microelectrodes were used, having 2–6 M Ω resistance (Thomas Recording, Giessen, Germany). The electrodes were advanced into the brain using an Eckhorn microdrive system (Thomas Recordings, Giessen, Germany). Analog waveform signals were amplified by Thomas preamps and collected by a Plexon MAP system (Plexon Inc., Texas) in which the waveforms were digitized at 40 kHz. Multiunit activity

viewed online using Sort Client and PeriEvent Client software (Plexon Inc., Texas) was used to identify the whisker that evoked the largest amplitude response in a multi-unit poststimulus time histogram (PSTH), which was designated as the “principal whisker” (PW). Principal component analysis and template matching were used in Offline Sorter (Plexon Inc.) for assigning spike waveforms to separate single units from the multiunit stream. Typically 2–3 units per electrode could be isolated for further analysis from each electrode recording position. Further data analysis was then carried out in Matlab (MathWorks).

Three blocks of stimuli consisting of 100 trials each (ISI of 1 or 0.5 Hz within each block) were presented in the following order: first, a block of 4-ms-duration principal whisker deflections (Wi); second, a block of condition-test stimuli in which an auditory click stimulus (10 ms duration) preceded a 4 ms whisker stimulus by 10 ms ($Au+Wi$); and finally, a block of auditory click stimuli alone (Au) (Fig. 1a). For the novel analyses of this article, we only analyze the $Au+Wi$ condition-test condition, though for background information we present some results from the other conditions that were part of the analysis of the original study. Multiple recording sessions at different depths traversing S1 were made for each rat. The dataset included a total of 27 recording sessions with 86 isolated cells, and 97 spike pairs.

Prior to recording, the whiskers were trimmed to 5 mm beyond the fur to keep the whisker angle of deflection uniform. During the recordings, whiskers were stimulated using a piezoelectric bimetal wafer as described in Popescu and Ebner (2010). The piezo stimulator delivered 100 stimuli to a whisker in a caudal direction (1 Hz, 600 μ m amplitude, 4 ms duration, 2 ms rise time). The auditory stimulus was generated by a second channel on an 8 channel DS8000 stimulator, which was controlled by a Spike 2 script to activate a speaker (Kenwood, 20–20,000 Hz response range). The speaker was positioned 20 mm away from the ear of the rat on the same side as the whisker stimulus (both right side). Auditory stimuli were delivered at 1 Hz (75 db spl, 10 ms duration square wave either alone or 10 ms prior to a whisker stimulus in the $Au+Wi$ condition).

The Au+Wi stimulus was presented at 0.5 Hz. The onset of the Wi stimulus was considered to be the onset time of the trial.

Spike timing metrics:

We analyzed two direct measures of the spiking response to the stimulus. To measure the spike latency for a given spike train, we took the average time of the first spikes in each trial appearing within a time window from 3 to 150 ms. To measure the spike latency mean standard error (MSE), we average the square of the deviation of these first spike times of each trial from the average spike latency.

Spike-spike Coherence:

We analyzed spectral coherency between pairs of spike trains using procedures described in Jarvis and Mitra (2001). Spike trains were converted into a continuous signal discretely sampled at 1 kHz with values of 1 or 0 depending on whether or not a spike was present in the corresponding 1 ms time bin for the given trial. In addition, we applied the point process finite sample size correction for spike spectral estimators described in Jarvis and Mitra (2001).

To construct the coherograms shown in Figure 4.1, we used a 200 ms time window sliding across the time during a trial with a 10 ms step size. Data were windowed with the first in the series of discrete prolate spheroidal sequences (Jarvis and Mitra, 2001; Slepian, 1983), which provides optimum frequency localization for a finite temporal window. A frequency bandwidth of 5 Hz was used. Further analyses of coherence were conducted on two specific individual time periods: a poststimulus period spanning from 0 to 150 milliseconds after stimulus delivery that we refer to as the response period, and a longer period spanning from 150 to 1000 milliseconds after the stimulus that we refer to as the baseline period. Before further analyses, coherence values were

z-transformed to an unbiased and approximately Gaussian distribution using the procedure following from Thompson and Chave (1991) and described in Bokil et al. (2007).

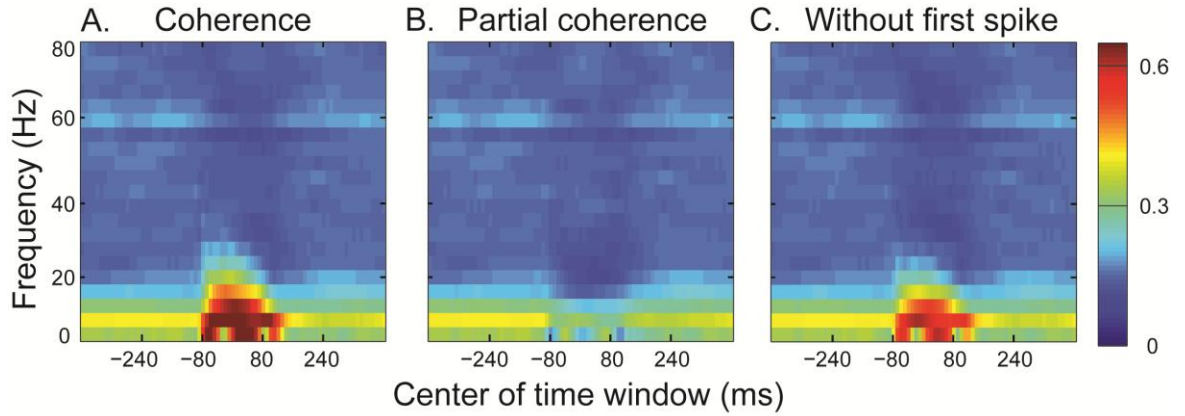


Figure 4.1. Coherence patterns averaged across all spike pairs in the sample. (A) Coherence. (B) Partial coherence. (C) Coherence with the first spike following the stimulus removed.

In order to investigate to what extent the coherence observed results from the consistent response of both neurons to the stimulus rather than from their unique relationship to each other, for Figure 1B we calculated the coherence of Fourier residuals, which we refer to as the partial coherence, following the terminology of Srinivasan (2004). Specifically, the Fourier coefficient for each trial ($\hat{x}_n(f)$) is transformed into a residual Fourier coefficient ($p\hat{x}_n(f)$) by subtracting the mean Fourier coefficient across trials. Partial spectra, partial cross spectra, and partial coherence are then calculated using these residual Fourier coefficient in the same manner that their ordinary values are calculated using the original Fourier coefficients.

$$\hat{x}_n(f) = \sum h(t)x_n(t)e^{-2\pi ift}$$

Above, $\hat{x}_n(f)$ denotes the Fourier component of trial n for a given frequency f , $x_n(t)$ denotes the signal for that trial as function of time t (i.e., a sequence of 0s and 1s representing the presence

or absence of a spike in every millisecond bin), and $h(t)$ describes the windowing function used as a function of time. Then,

$$p\hat{x}_n(f) = \hat{x}_n(f) - \langle \hat{x}_n(f) \rangle$$

$$pS_{xx}(f) = \frac{1}{N_T} \sum_{n=1}^{N_T} p\hat{x}_n(f) p\hat{x}_n(f)^*$$

$$pS_{yy}(f) = \frac{1}{N_T} \sum_{n=1}^{N_T} p\hat{y}_n(f) p\hat{y}_n(f)^*$$

$$pS_{xy}(f) = \frac{1}{N_T} \sum_{n=1}^{N_T} p\hat{x}_n(f) p\hat{y}_n(f)^*$$

$$pC_{xy}(f) = \frac{pS_{xy}(f)}{\sqrt{pS_{xx}(f) pS_{yy}(f)}}$$

Above, $pC_{xy}(f)$ denotes the partial coherence, N_T denotes the number of spectral estimates, and

* denotes the complex conjugate.

Methods of measuring coherence per trial:

As described in the equations above, multiple spectral estimates are necessary for the calculation of coherence or partial coherence. In neuroscience experiments, these multiple estimates can commonly be acquired through repeated trials of a stimulus or a behavior.

Additionally, multi-taper spectral analysis allows for the use of multiple orthogonal data windows,

or tapers, to provide independent estimates of spectra and coherence from a single period of time during a trial (Thompson and Chave, 1991). For a given window length duration of N seconds, as a rule of thumb, $2*N*W - 1$ tapers provide reliable estimates of the spectrum (Slepian, 1983; Thompson and Chave, 1991), where W is the desired frequency bandwidth of the estimate. Thus for a given fixed window duration, a tradeoff exists between the number of tapers used, and the specificity of the frequency resolution desired. For all methods we describe below, the results that we present in this article were generally robust across a range of values for parameters such as the number of tapers, the value for W or the particular frequencies averaged.

5 Trials method. Here the sample of trials was broken down into groups of 5 trials, with the coherence calculated in each group across those 5 trials and 1 taper used for each trial. To correlate other measures with these coherence estimates, the other measures were averaged across the same 5 trial groups with the correlation performed across the resulting 20 groups. Any number of trials per group could be used in this procedure. However we did not find that the results were particularly sensitive to the precise number used and chose 5 to provide a reasonable balance between the size of the group and the number of groups. The resulting frequency resolution was 6.7 Hz for the response window analysis, and 1.2 Hz for the baseline period. Before further analyses, we averaged the resulting response period coherence estimates between 0 to 6.7 Hz and the resulting baseline coherence estimates between 0 and 4 Hz. We found that the results were not appreciably changed when we averaged the response period from 0 to 20 Hz as was done in the other methods.

5 Tapers method. In this method, we utilized the ability of the multi-taper methods to provide multiple spectral estimates for a single trial to calculate coherence within each trial. Because the coherence result that we were investigating is present over a wide frequency range (0

to 20 Hz, see Figure 1), even the short window lengths that we applied here allowed for the use of multiple tapers to estimate the coherence, as described above. The resulting frequency resolution was 20 Hz for the response window analysis, and 3.5 Hz for the baseline analysis. Before further analyses, we averaged the resulting response period coherence estimates between 0 to 20 Hz and the resulting baseline coherence estimates between 0 and 4 Hz.

Leave-One-Trial-Out method. We calculated the coherence for each trial following procedures described in Womelsdorf et al. (2006) which we refer to as the Leave-One-Trial-Out method. To briefly reiterate the procedure here: The z-transformed coherence is first calculated across all trials (below: $C(S)$). Then for each trial i , the z-transformed coherence is calculated across all trials but with that trial left out (below: $C(S_{(i)})$). The coherence for trial i (C_i) is then estimated according to the equation:

$$C_i = N * C(S) - (N - 1) * C(S_{(i)})$$

where N is the number of trials. For further details, see Womelsdorf et al. (2006). All parameters for the individual coherence calculations were set to the same as those used in the 5 Tapers method described above.

Correlations:

Correlations involving the per-trial coherence estimates were carried out using matlab's `corrcoef.m` function. The p -values we report have been Bonferroni-corrected within each family of hypothesis tested, which we defined as the 3 pairwise comparisons between the 3 methods for each test (i.e. the p -values we report have been multiplied by 3 from their single comparison values).

Correlations between coherence and spike-metrics were performed once for each spike in the pair (which we refer to as spike-pairs), and thus twice for each pair of spikes overall.

Canonical correlation:

We performed a canonical correlation analysis to determine the relationship between baseline coherence and the combination of behavioral coherence and stimulus response properties of all spikes and pairs of spikes simultaneously recorded in each session. For each per-trial coherence estimate method, the trial-by-trial (or group-by-group) coherence estimates for all possible pairs of simultaneously recorded neurons during the baseline period were used as the set of independent variables. The set of dependent variables was comprised of the response window coherence for each pair, as well as the spike latency and spike latency MSE for each individual neuron recorded. Trials with no spikes in a given spike train during any of the windows analyzed result in an undefined coherence for pairs involving that trial, and those trials were removed from the canonical correlation analysis. We used the `canoncorr.m` function in the Matlab stats toolbox to carry out the analyses. The p -values used to assess significance of the first canonical correlation for each session reflect Lawley's modification to Bartlett's chi-squared statistic. For more details about the canonical correlation analyses and hypothesis testing, see Krzanowski (1988) and Seber (1984).

RESULTS

Pattern of coherence:

In this dataset, we had previously observed that the whisker stimulus elicits strong low-frequency-coherent neural activity among pairs of neurons (Figure 4.1A). This coherence could

result from both neurons in each pair coherently responding to the same stimuli rather than from a direct coherent relationship between the neurons themselves at that time. To investigate this, we looked at a partial coherence estimate that measures the coherence among residual Fourier components (Figure 4.1B). Here the low-frequency coherence is conspicuously absent, and actually decreases following the stimulus. This indicates that the coherence shown in Figure 4.1A resulted from the timing of the spikes of both neurons in each pair that were time-locked to the same stimulus. The timing of the first spike might be of particular importance to this coherence. To investigate this we plotted the ordinary coherence after removing the first spike in the response to the stimulus from each spike train (Figure 4.1C). Though much of the coherence during the response to the stimulus remains, the coherence does decrease considerably when the first spike in the response is removed, indicating some importance for the timing of the first spike in contributing to this coherence.

Comparing the 3 methods:

While this pattern of partial coherence and coherence could prove troubling for conclusions about the importance of interactions between neurons at the time of the stimulus, it does provide a unique opportunity to test parameters of this data that would be expected to correlate with the ordinary coherence but not partial coherence that we observe. The coherence patterns suggest that the response period coherence results from a pair of spike trains that are time-locked to the stimulus and not each other. Given this and the importance of the first spike in contributing to this coherence, the consistency of the timing of the first spike would be expected to correlate with this coherence. Moreover, shorter first spike latencies would also be expected to correlate with this coherence, in part because of the correlation between shorter latencies and more consistent timing and in part because of the steep shape of the mean spike rate response increase (Figure 4.3B). Thus, the performance of the various techniques used for estimating trial-

by-trial coherence that we investigate here (see Materials and Methods) can be reasonably compared through the trial-by-trial correlation of the response period coherence with these metrics.

Figure 4.2 shows histograms of the correlation coefficients across spike-pairs for each method, measuring the trial-by-trial correlation of the response period coherence with the spike latency (Figure 4.2A) and the spike latency MSE (Figure 4.2B). As expected, there is an overall negative correlation in both cases. For the correlation between the coherence and the latency of the first spike, the mean coefficient for the 5 tapers method was significantly less than the leave-one-trial-out method (t-test, $p < 0.05$), while other differences were not significant. For the correlation with the spike latency MSE, the mean coefficient for the 5 trials method was significantly less than the 5 tapers method (t-test, $p < 0.05$), while other differences were not significant.

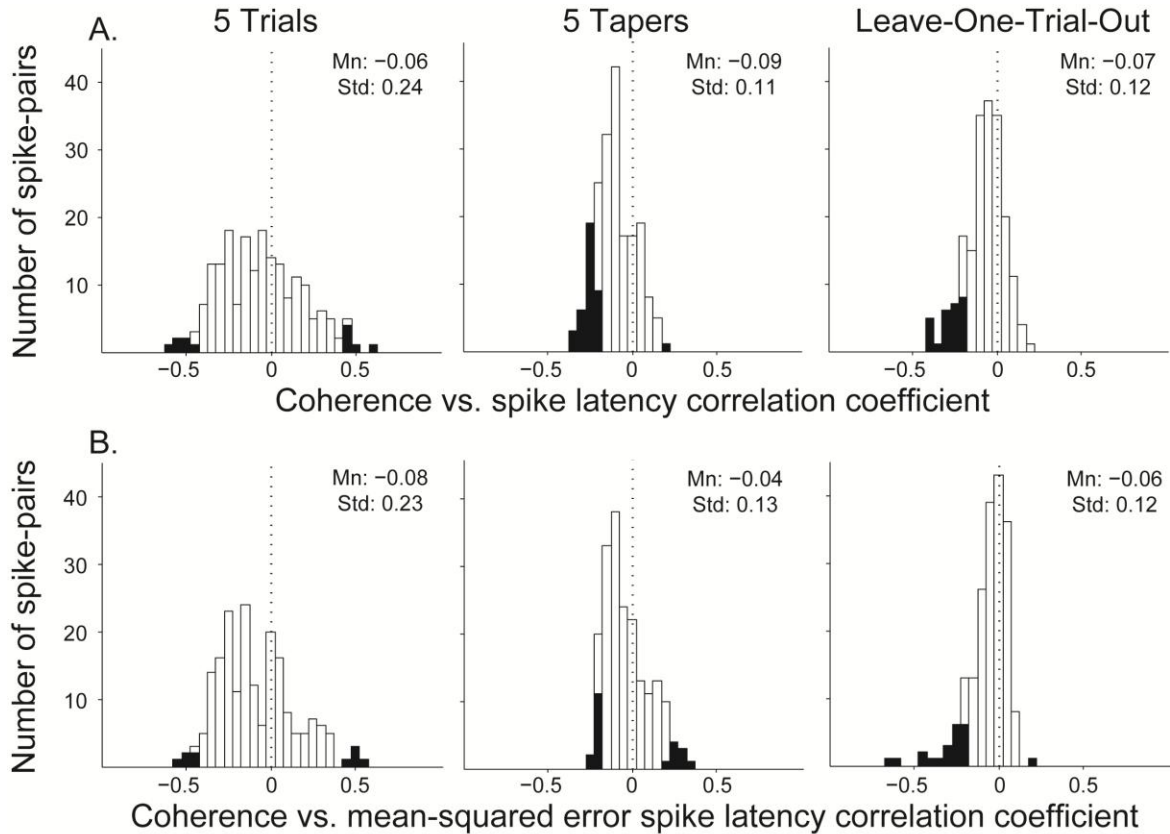


Figure 4.2. Histograms of correlation coefficients between response period coherence and direct measures of spike timing for all spike-pairs. Left column: 5 Trials method; middle column: 5 Tapers method; right column: Leave-One-Trial-Out method. Correlations that are individually significant at the 0.05 level are filled in on the histogram. (A) Response period coherence vs. spike latency. (B) Response period coherence vs. spike latency MSE.

Visually apparent from Figure 2 is that the 5 trials method was much less consistent, with much more spread-out distributions than either the 5 tapers or leave-one-trial-out methods. This was confirmed statistically (Levene's test of variances, $p < 0.001$ for both spike latency and spike latency MSE), while the 5 tapers and leave-one-trial-out methods' variances were not different from each other. The larger variance resulting from the 5 trials method is likely a result of the smaller number of points entered into the correlation, which is inherent to the 5 trials method that breaks up the data up into groups of trials. The leave-one-trial-out method appeared to be the most consistent and robust method of the 3, as reflected by the number and sign of the correlation coefficients that were individually significant at the uncorrected 0.05 threshold within each spike-

pair. The leave-one-trial-out method had a significantly larger proportion of negative to positive significant correlation coefficients than the 5 trials method with respect to spike latency and spike latency MSE (Pearson's chi-squared test, $p < 0.001$ and $p < 0.01$, respectively), and than the 5 tapers method with respect to spike latency MSE (Pearson's chi-squared test, $p < 0.05$). The 5 tapers method also had a proportion of negative to positive significant correlation coefficients that was significantly larger than that of the 5 trials method with respect to spike latency only (Pearson's chi-squared test, $p < 0.001$).

Example application: Absence of an anticipated trial-by-trial correlation

In other work (Ghoshal et al., submitted) we had found that when comparing across conditions, the mean-low frequency coherence during a baseline period preceding each stimulus increased with the introduction of an auditory stimulus (Au) as compared to a whisker only stimulus (Wi) (Figure 4.3A). This occurred in the absence of a stimulus-locked change in firing rate (Figure 4.3B,C). Additionally, the paired auditory and whisker stimulus (Au+Wi) elicited a response with decreased latency and variability of the first spike time as compared to the Wi stimulus (Figure 4.3C).

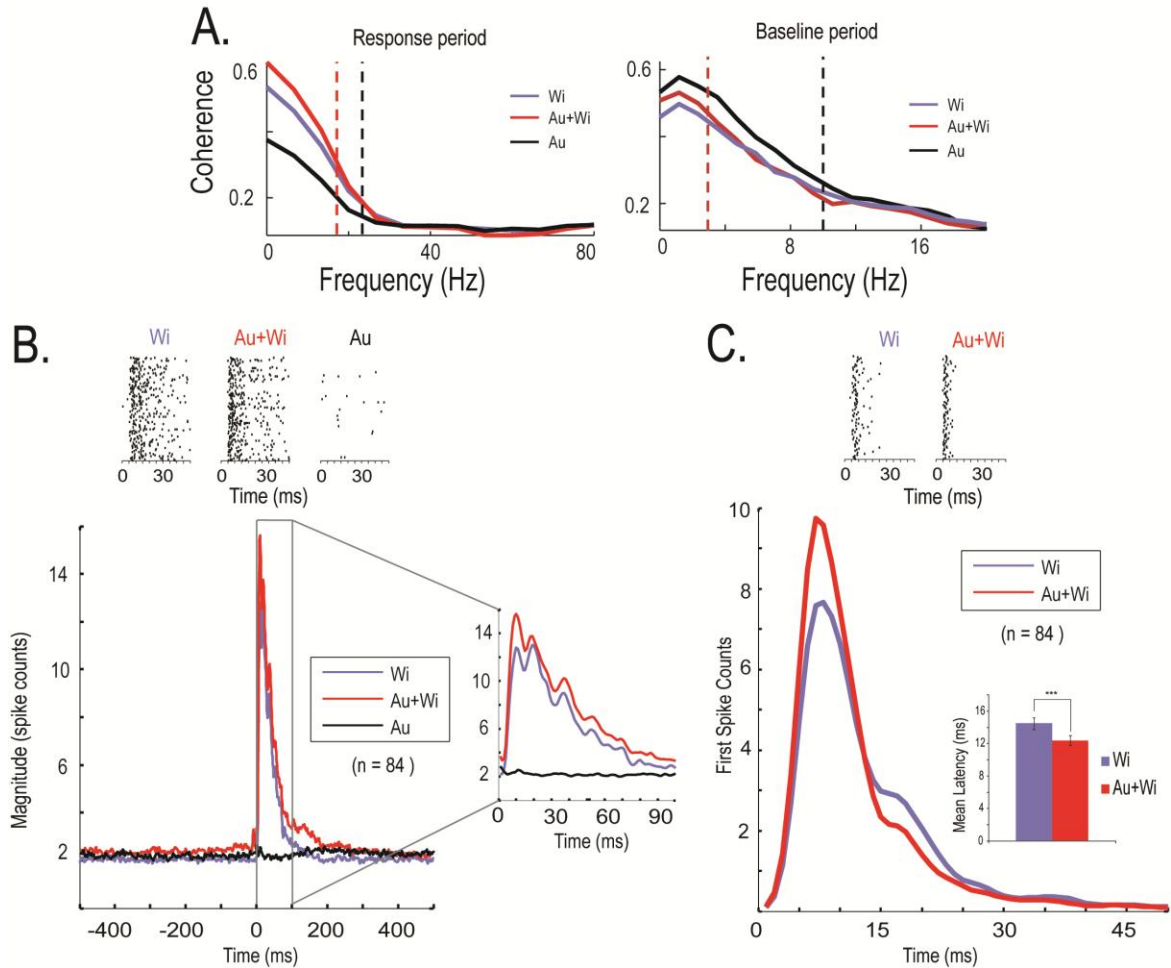


Figure 4.3. Mean coherence, firing rate and latency effects across conditions. Wi = whisker only stimulus; Au = Auditory only stimulus; Au + Wi = Auditory and whisker stimulus. Reproduced from Ghoshal et al. (Submitted). (A) Coherence during the response period (left) and baseline period (right). Colored vertical dashed lines denote the extent of frequency bands extending from 0 Hz that were found to be significantly different than the Wi stimulus alone for the corresponding stimulus type as indicated in the figure. (B) Raster plots of a single neuron (upper row) and the population PSTHs (lower row), with the period from 0 to 100 ms expanded to the right. (C) First spike raster plots (see Materials and Methods) of the same single neuron as in B (upper row) and population first spike latency histograms (lower row) for the Wi and Au+Wi conditions. Raster plots show that this neuron has earlier and more consistent first spike times across trials to Au+Wi stimuli, while the latency histogram shows an increased number of average first spike times in the population in the first 15 ms. The bar graph shows that the overall mean onset latency is significantly shorter in Au+Wi than the Wi alone.

Taken alone, these results are consistent with the conclusion that the increase in baseline coherence caused by the auditory stimulus “primed” the neural network in S1 to respond more quickly and regularly to the whisker stimulus. However, if this conclusion were true, a trial-by-trial positive correlation between baseline and response period coherence, and a negative

correlation between baseline coherence and spike latency and variability would be observed. We investigated this using all 3 per-trial coherence estimation methods. As shown in Figure 4.4, the mean correlations in all cases are near zero. Thus, this trial-by-trial analysis indicates that one cannot reach the stronger conclusion about baseline coherence directly leading to a less variable stimulus response, and this apparent conclusion from an analysis of the mean coherence alone (Figure 4.3) may have been misleading.

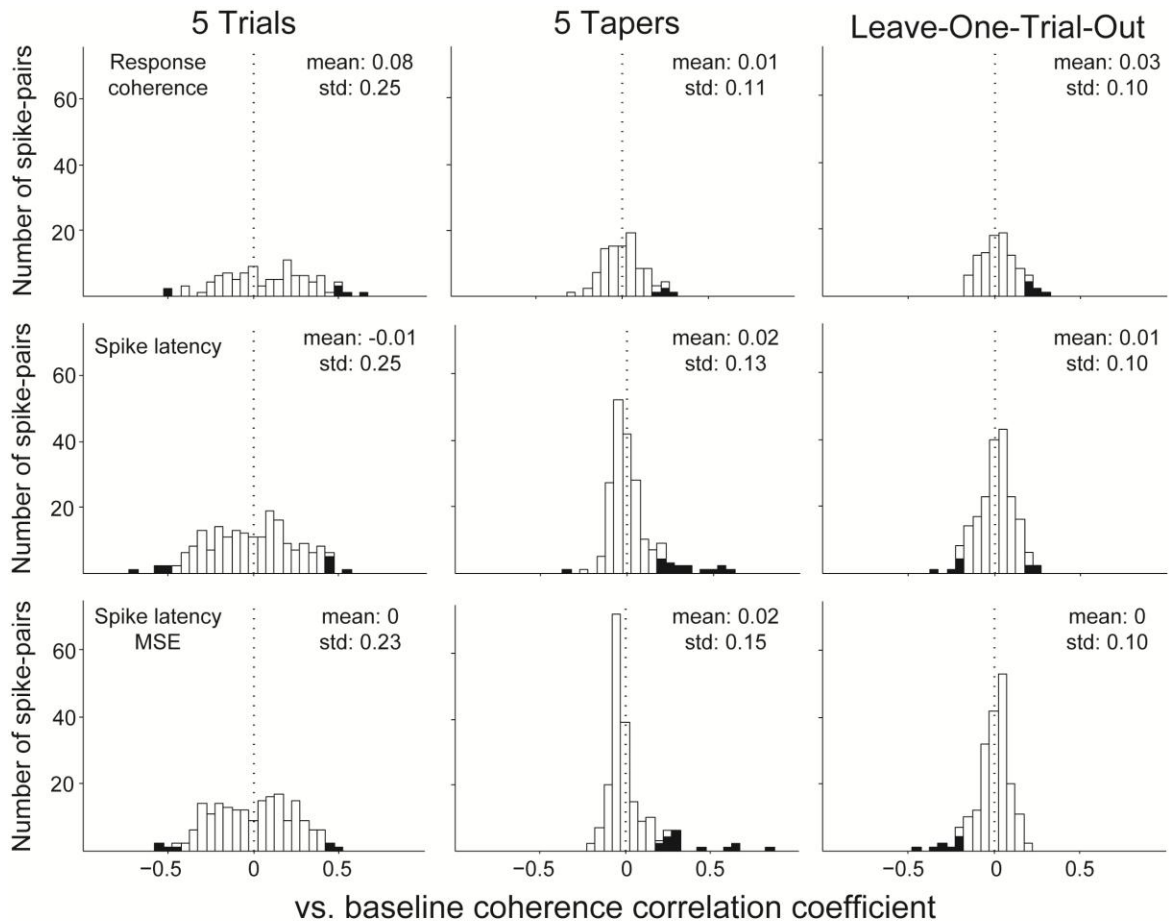


Figure 4.4. Histograms of correlation coefficients with baseline period coherence. Left column: 5 trials method; middle column: 5 tapers method; right column: leave-one-trial-out method. Correlations that are individually significant at the 0.05 level are filled in on the histogram. Top row: Baseline period coherence vs. response period coherence. Middle row: Baseline period coherence vs. spike latency. Bottom row: Baseline period coherence vs. spike latency MSE.

Canonical correlation across an ensemble of all simultaneously recorded spikes

In addition to exploring single-pair trial-by-trial coherence analyses, we investigated a framework for their application to an ensemble of simultaneously recorded neurons. Specifically, we wanted to see to what extent the coherence of all recorded neurons in an ensemble during the baseline period of a trial could predict their coherence and the spike timing characteristics of their stimulus responses later in the trial. To investigate this, we performed a canonical correlation analysis with the baseline coherence of all simultaneously recorded pairs of spikes as independent variables, and the response period coherence for the same pairs, as well as the spike latency and the spike latency MSE for all neurons as dependent variables. The histograms of the resulting first canonical variant correlation coefficients across sessions are shown in Figure 4.5. If this coefficient is significant, it suggests that there is indeed significant explanatory power between the independent and dependent variables. Significant portions of sessions had significant first canonical variants at the 0.05 level for the 5 trials and 5 tapers method (9/27 and 7/27 respectively, binomial test, $p < 0.001$ in both cases), but not the leave-one-trial-out method (3/27, binomial test, $p > 0.05$). Thus, it appears that there may be some predictive power between the coherence and spike timing metrics at different points in time during the trial, although this is not completely clear given the disagreement between the methods.

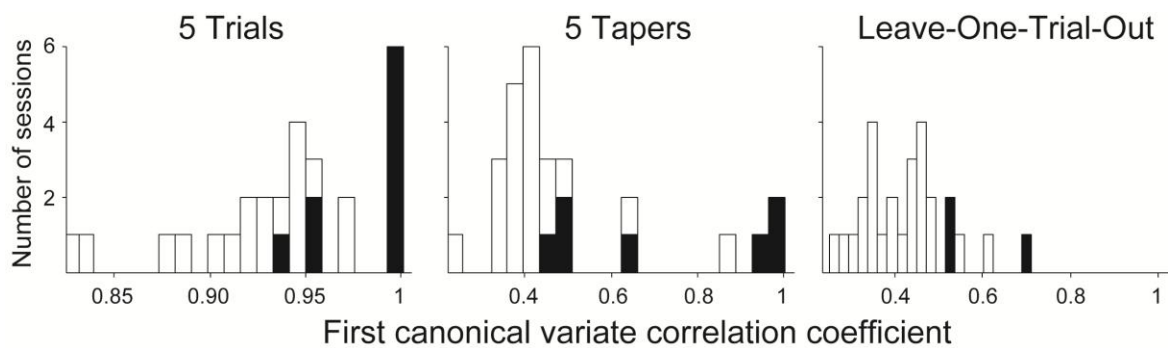


Figure 4.5. Histograms of the first canonical variate correlation coefficient across sessions. Left column: 5 Trials method; middle column: 5 Tapers method; right column: Leave-One-Trial-Out method. Correlations that are individually significant at the 0.05 level are filled in on the histogram.

Average absolute value per pair or neuron

5 Trials

5 Tapers

Leave-One-Trial-Out

Baseline coherence	0.5081	0.5074	0.4816
Response coherence	0.2660	0.2598	0.2698
Spike Latency	0.2571	0.2589	0.2576
Spike Latency MSE	0.2368	0.2659	0.2486

Average absolute value per session

	5 Trials	5 Tapers	Leave-One-Trial- Out
Baseline coherence	0.3571	0.3995	0.3846
Response coherence	0.1622	0.1407	0.1876
Spike Latency	0.1482	0.1646	0.1502
Spike Latency MSE	0.1266	0.1973	0.1278

Table 4.1. Mean correlation coefficients between the first canonical variate and various estimates across simultaneously recorded pairs and spikes. For the upper table, we took the absolute value of each correlation for every spike or every pair of spikes within each session before averaging across sessions. For the lower table, we took the raw average within each individual session and then the absolute value when averaging across sessions.

Interpretation of the canonical variants themselves can prove challenging, though one noticeable pattern in particular emerges when investigating them across our sample of sessions. Table 1 shows the average correlation coefficients between the first canonical variant and the corresponding dependent or independent variables. The average is calculated in 2 different ways: by taking the absolute value of the correlation coefficient for each pair or individual neuron within each session before averaging across sessions, or by taking the raw average of the correlation

coefficients within each session before taking the absolute value and averaging across all sessions. Between sessions, the sign of a variable's correlation with a canonical variant is arbitrary and meaningless, and thus we take the absolute value before averaging across sessions in both cases. However, within a session the sign difference between, for example, the correlation with the baseline coherence of one pair and the baseline coherence of another pair with the canonical variant is meaningful. If, for example, the only meaningful information from the baseline coherence that was being exploited in the canonical correlation for a given session was the mean across all the pairs, the signs for all pairs within that session would be the same. Taking the absolute value before or after averaging across sessions in this case would not affect the resulting average. Instead, we find that when taking the absolute value for each pair or spike within a session, the average correlation coefficients are noticeably higher for all metrics. This suggests that the signs of the correlation coefficients tend to differ within a session, and suggests that there may be information available in the idiosyncrasies of each neuron or pair or spikes in the ensemble, beyond just their mean values.

Discussion

We found that the leave-one-trial-out method for calculating spike-spike coherence on a per-trial basis more consistently and robustly showed a negative correlation with measures of spike timing variability. Other multi-taper estimates however also perform reasonably well and tend to yield roughly similar conclusions, if with less precision. We provided an example use of these techniques in investigating the relationship between spike-spike coherence and other spike metrics at different times during a trial. We found an absence of an otherwise anticipated correlation of coherence, which highlights the need for performing trial-by-trial coherence analyses. We then presented a framework for the analysis of trial-by-trial coherence and other

metrics in an ensemble of simultaneously recorded spike trains. The application of this framework in our data and suggested that predictive power between these values at different times during a trial may exist in a manner that makes use of the information beyond just the mean values across pairs and cells.

Our primary comparison between the different methods for estimating per-trial coherence used a short 150 ms time window with coherent activity that was known to be stimulus locked and not uniquely phase-locked between the neurons in the pair. Though it may seem unusual to use 5 tapers in time windows as short as this, it is possible to do so when averaging across a large frequency band as we do here. Perhaps one surprise in our results is how well this 5 tapers method performs and how similar its results are to the other methods we tested through all of the analyses that we compared. That being said, the leave-one-trial-out method may perform slightly better for the reasons of consistence and robustness as we've stated above. The basic principle behind the leave-one-trial-out method of calculating a per-trial estimate based on the difference from the estimate when using all trials and the estimate when the given trial is left out could likely also be fruitfully applied to other metrics that like coherence typically require multiple trials, such as JPSTH measures of synchrony, for example.

From our results alone, which use time-locked activity within the short time period window, it may not be entirely certain that the higher consistency of the leave-one-trial-out method carries over to nonstimulus locked coherence, or coherence in longer time windows. That being said, there is no reason to expect that the leave-one-trial-out method should perform any worse than other methods in those different situations, and we have at least suggested that it performs better in the specific situation we tested. Additionally, Figure 4.4 does suggest that when comparing non-stimulus locked coherence in a longer time window, the leave-one-trial-out method gives similar overall results and still with slightly better precision than the other metrics, further suggesting that it performs better under those circumstances as well. In this situation though, it is

not as clear what the “correct” answer should be in terms of what we should expect the mean of this correlation to be. Since we are correlating the coherence with spike timing metrics completely outside the window used to calculate the coherence, the results are not constrained by anything but the true pattern in the data itself. This pattern can’t be known *a priori* and unlike our other tests is unrelated to the mathematical determination of coherence. For these reasons, simulations where the underlying trial-by-trial coherence is manipulated would indeed be the best manner for comparing these three metrics. To address this, one would have to face the challenge of creating data with coherence that changes on a trial by trial basis, which we are not attempting to address in this study.

The contribution of our canonical correlation analyses is primarily to lay out a framework in which one could investigate this in other datasets. Canonical correlations have been more commonly used in psychological research, though we show here their applicability to neural data. The conclusions specific to our dataset are not entirely clear as in this situation the procedure using the leave-one-trial-out method disagrees with the procedures using the other methods. It is worth noting that the leave-one-trial-out method is moderately close to significance (Binomial test of 0.05 significance level across sessions, 3/27, $p=0.15$), so perhaps with more data or in other datasets the results from the different methods would agree. Still, the results with the other methods as well as the differences in the signs of the correlations with the first canonical variants for each individual variable within a session for all methods are suggestive that additional predictive information is added by the idiosyncratic directions of trial-by-trial fluctuations of coherence in each pair in an ensemble.

CONFLICT OF INTEREST

This research was conducted in the absence of any commercial or financial relationships that could be construed as a potential conflict of interest.

ACKNOWLEDGEMENTS

Matthew Nelson was supported by the Programme de bourses d'excellence Eiffel.

REFERENCES

Bokil, H., Purpura, K., Schoffelen, J.-M., Thomson, D., and Mitra, P. (2007). Comparing spectra and coherences for groups of unequal size. *J Neurosci Methods* 159, 337–345.

Buschman, T.J., and Miller, E.K. (2007). Top-down versus bottom-up control of attention in the prefrontal and posterior parietal cortices. *Science* 315, 1860–1862.

Chalk, M., Herrero, J. L., Gieselmann, M. A., Delicato, L. S., Gotthardt, S., and Thiele, A. (2010). Attention reduces stimulus-driven gamma frequency oscillations and spike field coherence in V1. *Neuron* 66, 114–125.

Fries, P., Reynolds, J.H., Rorie, A.E., and Desimone, R. (2001). Modulation of oscillatory neuronal synchronization by selective visual attention. *Science* 291, 1560–1563.

Fries, P., Womelsdorf, T., Oostenveld, R., and Desimone, R. (2008). The effects of visual stimulation and selective visual attention on rhythmic neuronal synchronization in macaque area V4. *J. Neurosci.* 28, 4823–4835.

Gregoriou, G.G., Gotts, S.J., Zhou, H.H., and Desimone, R. (2009). High-frequency, long-range coupling between prefrontal and visual cortex during attention. *Science* 324, 1207–1210.

Jarvis, M.R., and Mitra, P.P. (2001). Sampling properties of the spectrum and coherency of sequences of action potentials. *Neural computation* 13, 717–749.

Krzanowski, W. J. (1988). *Principles of Multivariate Analysis*. Oxford: Oxford University Press.

Pesaran, B., Pezaris, J.S., Sahani, M., Mitra, P.P., and Andersen, R.A. (2002). Temporal structure in neuronal activity during working memory in macaque parietal cortex. *Nat Neurosci* 5, 805–811.

Pesaran, B., Nelson, M.J., and Andersen, R. A. (2008). Free choice activates a decision circuit between frontal and parietal cortex. *Nature* 453, 406–409.

Popescu, M. V., and Ebner, F. F. (2010). Neonatal sensory deprivation and the development of cortical function: Unilateral and bilateral sensory deprivation result in different functional outcomes. *J. Neurophysiol.* 104, 98–107.

Rutishauser, U., Ross, I. B., Mamelak, A. N., and Schuman, E. M. (2010). Human memory strength is predicted by theta-frequency phase-locking of single neurons. *Nature* 464, 903–907.

Scherberger, H., Jarvis, M. R., and Andersen, R. A. (2005). Cortical local field potential encodes movement intentions in the posterior parietal cortex. *Neuron* 46, 347–354.

Seber, G. A. F. (1984). *Multivariate Observations*. New York: Wiley.

Slepian, D. (1983). Some comments on fourier analysis, uncertainty and modeling. *Society for Industrial and Applied Mathematics* 25, 379–393.

Srinivasan, R. (2004). Internal and external neural synchronization during conscious perception. *International journal of Bifurcation and Chaos in Applied Sciences and Engineering* 14, 825–842.

Thompson, D.J., and Chave, A.D. (1991). “Jackknifed error estimates for spectra, coherences, and transfer functions” in *Advances in spectrum analysis and array processing*, ed. Haykin, S. (Englewood Cliffs, NJ: Prentice-Hall, Inc.), 58–113

Womelsdorf, T., Fries, P., Mitra, P.P., and Desimone, R. (2006). Gamma-band synchronization in visual cortex predicts speed of change detection. *Nature* 439, 733–736.

FIGURE LEGENDS

Figure 4.1. Coherence patterns averaged across all spike pairs in the sample. **(A)** Coherence. **(B)** Partial coherence. **(C)** Coherence with the first spike following the stimulus removed

Figure 4.2. Histograms of correlation coefficients between response period coherence and direct measures of spike timing for all spike-pairs. Left column: 5 trials method; middle column: 5 tapers method; right column: leave-one-trial-out method. Correlations that are individually significant at the 0.05 level are filled in on the histogram. **(A)** Response period coherence vs. spike latency. **(B)** Response period coherence vs. spike latency MSE

Figure 4.3. Mean coherence, firing rate and latency effects across conditions. Wi = whisker only stimulus; Au = Auditory-only stimulus; Au + Wi = Auditory and whisker stimulus. Reproduced from Ghoshal et al. (Submitted). **(A)** Coherence during the response period (left) and baseline period (right). Colored vertical dashed lines denote the extent of frequency bands extending from 0

Hz that were found to be significantly different than the W_i stimulus alone for the corresponding stimulus type as indicated in the figure. **(B)** Raster plots of a single neuron (upper row) and the population PSTHs (lower row), with the period from 0 to 100 ms expanded to the right. **(C)** First spike raster plots (see Materials and Methods) of the same single neuron as in B (upper row) and population first spike latency histograms (lower row) for the W_i and $Au+W_i$ conditions. Raster plots show that this neuron has earlier and more consistent first spike times across trials to $Au+W_i$ stimuli, while the latency histogram shows an increased number of average first spike times in the population in the first 15 ms. The bar graph shows that the overall mean onset latency is significantly shorter in $Au+W_i$ than the W_i alone.

Figure 4.4. Histograms of correlation coefficients with baseline period coherence. Left column: 5 trials method; middle column: 5 tapers method; right column: leave-one-trial-out method.

Correlations that are individually significant at the 0.05 level are filled in on the histogram. Top row: Baseline period coherence vs. response period coherence. Middle row: Baseline period coherence vs. spike latency. Bottom row: Baseline period coherence vs. spike latency MSE

Figure 4.5. Histograms of the first canonical variate correlation coefficient across sessions. Left column: 5 trials method; middle column: 5 tapers method; right column: leave-one-trial-out method. Correlations that are individually significant at the 0.05 level are filled in on the histogram.

Chapter 5

Nonindependent and nonstationary response times in
stopping stepping saccade tasks

BACKGROUND

Cognitive control is revealed in experiments that require subjects to change their performance in response to changes in their environment (e.g., Logan, 1985). The stop-signal task (Logan, 1994; Verbruggen & Logan, 2008b) and the target-step task (Camalier et al., 2007; Murthy, Ray, Shorter, Schall, & Thompson, 2009) have been used to examine executive control of saccadic eye movements in humans and macaque monkeys (Camalier et al., 2007; Hanes & Schall, 1995). These tasks present a target for an eye movement and then present either a stop signal, which indicates that the eye movement should be withheld, or a “stepped” target, which indicates that the eye movement should be directed to a new location. Performance on these tasks can be understood as the outcome of a race between a GO process that makes the initial saccade and a STOP process that inhibits the initial saccade to maintain fixation or to allow a new saccade to the new location (Camalier et al., 2007; Logan & Cowan, 1984; see also Boucher, Palmeri, Logan, & Schall, 2007). The race model assumes that the finish times for the GO and STOP processes as a function of trial number are stationary stochastic processes with independence between trials. This article reports data that challenge those assumptions and explores the consequences of those violations for analyses based on the race model. Our goal is not to evaluate the causes of nonindependence and nonstationarity but rather to document them in stopping and stepping tasks, and evaluate their effects on race-model and trial history analyses.

Nonstationarity refers to a stochastic process described by a mean or variance that changes over time. Response times (RTs) gradually becoming slower from the beginning to the end of an experimental session is one example of nonstationarity. *Nonindependence* refers to statistical dependence across samples in a time series. A correlation in RT between successive trials is one example of nonindependence. A time series that is nonstationary must be nonindependent, but the reverse is not necessarily true (e.g., autoregressive and moving average models, Wagenmakers, Farrell, & Ratcliff, 2004).

The fact that RTs are often nonstationary and nonindependent is well established (e.g., Gilden, 2001; Wagenmakers et al., 2004). For instance, RT on a given trial can vary with the stimulus and response that occurred on the preceding trial (e.g., Fecteau & Munoz, 2003; Luce, 1986). Furthermore, RT can change with arousal, fatigue, learning, and motivation throughout a session (Broadbent, 1971; Freeman, 1933; Welford, 1968, 1980). Several investigators have documented apparently systematic changes in RT during performance of the stop signal task (Cabel, Armstrong, Reingold & Munoz, 2000; Emeric et al., 2007; Kornyló, Dill, Saenz, & Krauelis, 2003; Li, Krystal, & Mathalon, 2005; Özyurt, Colonius, & Arndt, 2003; Rieger & Gauggel, 1999; Schachar et al., 2004; Verbruggen & Logan, 2008b; Verbruggen, Logan, Liefoghe & Vandierendonck, 2008). For example, the RT decreases after no stop signal trials and increases after stop signal trials.

Race-model analyses of stopping and stepping tasks focus on two measures of performance. First is the *inhibition function*, the probability of failing to cancel the response to the initial stimulus on a stop or step trial as a function of the interval between the onset of the initial stimulus and the stop or step signal (*stop-signal delay*, SSD, or *target-step delay*, TSD). Second is the RT on trials with and without a stop (step) signal. From these quantities can be derived a measure of the time needed to interrupt the initial response. This measure is referred to as the *stop-signal RT* (SSRT) in stopping tasks and the *target-step RT* (TSRT) in stepping tasks.

Here we first explore whether RT is nonindependent and nonstationary, and how this impacts estimates of SSRT and TSRT derived from the race model. We also explore how nonindependence and nonstationarity might impact measures of trials-to-trial adaptations of RT. To address these issues, we measured the extent to which RTs were nonindependent and nonstationary across trials during performance of saccade stopping and stepping tasks by humans and macaque monkeys, and assessed the impact of this on conventional analyses of these data.

METHODS

With the exception of search step data from monkey T, all the data presented here have formed the basis of previous publications (Boucher, Palmeri, Logan & Schall, 2007; Boucher, Stuphorn, Logan, Schall & Palmeri, 2007; Camalier et al., 2007; Hanes, Patterson, & Schall, 1998; Paré & Hanes, 2003). Here we reanalyze these data with a focus on the magnitude and impact of nonindependence and nonstationarity of RT.

Stop-signal task

In the stop-signal task, no-signal and stop-signal trials were randomly interleaved (Figure 5.1). On no-signal trials, subjects fixated a central point until it disappeared whereupon a peripheral target appeared without any distractors. Subjects were then required to shift gaze to that location. On stop-signal trials, the central fixation point reappeared following a variable delay after the appearance of the target. We refer to this variable delay as the *stop-signal delay* (SSD). On these trials, subjects were instructed to cancel any impending saccade and maintain fixation on the initial fixation position. We refer to these trials as *cancelled trials* (they are also called “signal-inhibit” trials in the literature). Monkeys were rewarded following both the cancelled stop-signal trials and correct no-signal trials. Because the occurrence and timing of the stop signal was unpredictable, on some trials subjects could not cancel their movement but instead made a saccade to the target. We refer to these error trials as *noncancelled trials* (they are also called “signal-respond” trials in the literature). Monkeys were not rewarded following these trials.

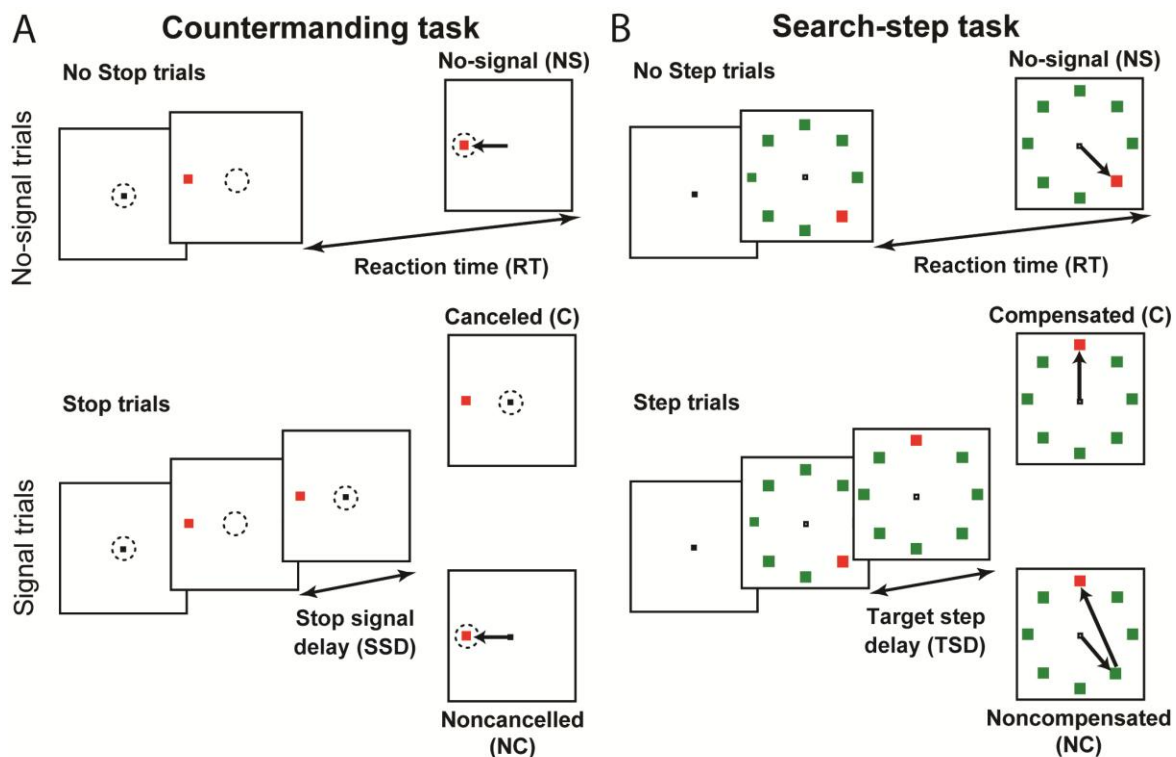


Figure 5.1

In this paper, we consider data collected for this task from five monkeys (*Macaca mulatta* and *Macaca radiata*) (Hanes et al., 1998; Paré & Hanes, 2003) and five human participants (Boucher, Stuphorn, et al., 2007). For the monkeys, the target could appear in one of two locations: either to the left or the right of the fixation point, positioned in the receptive field or movement field of a neuron.

For the human participants, the target could appear in one of four locations: in the upper or lower left, or the upper and lower right, relative to the fixation point. The proportion of stop trials varied from 10 to 70% for monkeys (typically 25%), and was 30% for humans. The mean elapsed time between the start of consecutive trials was ~ 4 seconds for monkeys and humans. Target eccentricities were 8.5 degrees for humans, and varied between 4 and 16 degrees for monkeys, according to receptive field location for the neuron recorded as part of the neurophysiological experiment. More task details are available in the cited publications.

Search-step task

In the search-step task, no-signal and target-step trials were randomly interleaved (Figure 5.1). On no-signal trials, subjects were required to shift gaze to a color singleton, either a red target among green distractors or a green target among red distractors. The color of the singleton varied across sessions. On target-step trials, the target stepped to a different location in the array after a variable delay after its appearance in its initial location. We refer to this variable delay as the target-step delay (TSD). On these trials subjects were instructed to cancel their response to the initial location and shift their gaze directly to the new location (i.e., to compensate for the target step). We refer to these trials as *compensated trials*. Monkeys were rewarded following both compensated target-step trials and correct no-signal trials. Because the occurrence, timing, and location of the steps were unpredictable, on some trials subjects could not compensate for the step but instead made a saccade to the initial target location. We refer to these error trials as *noncompensated trials*. Monkeys were not rewarded following these trials.

In this paper, we consider data collected for this task from four monkeys (Murthy et al., 2007; Murthy et al., 2009) and three human participants (Camalier et al., 2007). For the majority of the sessions in which the monkey data were collected, the target appeared with 7 distractors (set size of 8). The target and distractors were evenly spaced in a circle around the central fixation point at the eccentricity of the receptive field of the neurons (4–16 degrees). For the human data, 1, 3, or 7 distractors appeared with the target randomly from trial to trial for most sessions at a fixed eccentricity of 9.5 degrees. On a subset of sessions with monkeys and a subset of blocks within sessions with humans, the target appeared without any distractors. This condition is equivalent to the familiar double-step task (e.g., Becker & Jürgens, 1979). For both humans and monkeys, the effects described here did not vary between the double-step and search-step tasks with different set sizes, so we combined data from the two tasks. The proportion of step trials varied from 25 to 50%

for monkeys and was 40% for humans. The mean elapsed time between the start of consecutive trials was ~ 3 seconds for monkeys and ~ 5 seconds for humans.

Manipulation of stop signal or target step delay

In the stopping and stepping tasks, SSD and TSD are independent variables. When the delay is short, subjects are more likely to cancel the impending saccade. When the delay is long, subjects are more likely to make a saccade to the initial target location. For some sessions presented here, the values of SSD (TSD) were predetermined and presented randomly throughout the session independent of the subject's behavior. We refer to these as *randomized* SSD (TSDs). In other sessions, a 1-up/1-down staircase was used to adjust SSD (TSD) on each trial based on the subject's behavior. In this procedure, the delay was increased by a predetermined amount (50 ms for humans in both tasks, 17 to 50 ms in monkeys) following each cancelled or compensated trial and was decreased by the same amount following each noncancelled or noncompensated trial. The goal of this procedure is to ensure that subjects respond successfully to the stop signal or target step on around 50% of the trials (Logan, Schachar, & Tannock, 1997; Osman, Kornblum, & Meyer, 1990). We refer to these as *stair-cased* SSDs (TSDs). Most of the data for the stopping task were recorded using randomized SSDs, with the exception of data from monkeys H and N, which was primarily recorded using a staircase procedure. All of the search step data were recorded using the staircase procedure. For certain analyses pertinent to the manner of SSD or TSD selection, subsets of data are grouped and analyzed based on whether or not the staircase procedure was used.

Stop task SSDs ranged from 25 to 275 ms for humans, and 25 to 450 ms for monkeys for both stair-cased and non-staircased data. Step task TSDs ranged from 50 to 250 ms for humans and from 33 to 250 ms for monkeys. Monitor refresh rates varied between subjects and tasks but were either 60 or 80 Hz, depending on the experimental equipment used.

Race model accounts of performance in stopping and stepping

Performance in the stop-signal task can be understood as the outcome of a race between two stochastic processes, a GO process and a STOP process (Logan, 1994; Logan & Cowan, 1984; see also Boucher, Palmeri et al., 2007). The process that finishes first determines which behavior is produced. Recently this model has been extended to the search-step and double-step task with the addition of a second GO process to produce the compensated saccade (Camalier et al., 2007; see also Verbruggen, Schneider, & Logan, 2008). The race model formulation affords the ability to calculate the correct time needed to interrupt preparation of the initial movement (Logan & Cowan, 1984). This time is referred to as *stop signal reaction time* (SSRT) for the stop-signal task and *target step reaction time* (TSRT) for the search-step task.

We used two methods to estimate SSRT and TSRT (Figure 5.2). With the *integration method*, SSRT or TSRT can be calculated for each SSD or TSD by integrating the no-signal RT distribution until the proportion of RTs is equal to the proportion of noncancelled or noncompensation trials on the inhibition or compensation function for a particular SSD or TSD. The SSRT or TSRT is then given by that point in time minus the SSD or TSD. Using this method, an estimate of SSRT or TSRT is determined for each SSD or TSD, with the overall measure typically averaged across SSDs or TSDs. With the *difference method*, the mean of the inhibition (compensation) function is calculated by treating the function as a cumulative distribution function. The SSRT or TSRT is then equal to the mean of the no-signal RT distribution minus this value. SSRTs and TSRTs we report in this article are the average of the values from these two methods.

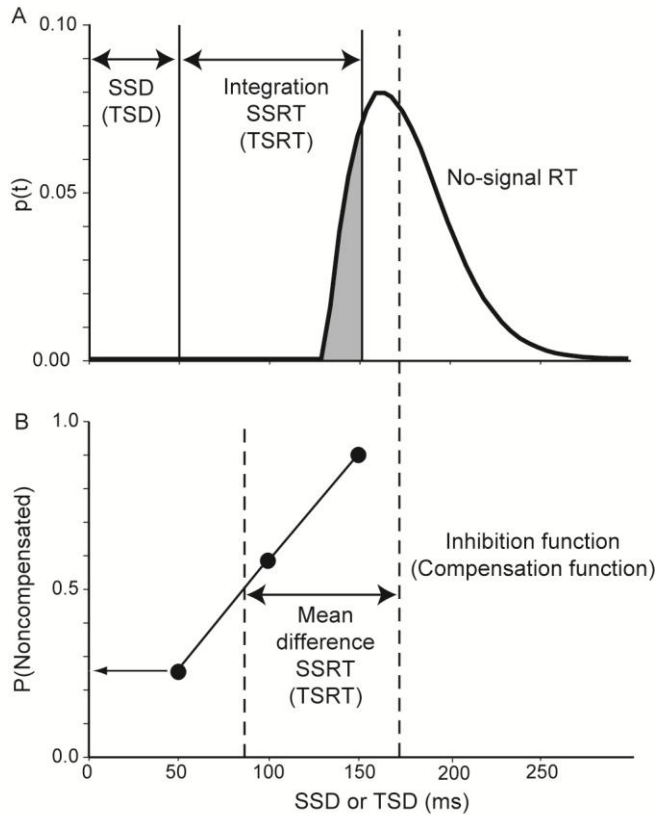


Figure 5.2

Response time spectra

Power spectra quantify trial-by-trial nonindependence in RT data (Gilden, 2001; Wagenmakers et al., 2004). If the processes producing RTs in a time series are independent across trials (which also requires stationarity), the spectrum of the data series will be flat, like the spectrum of white noise sampled with the same frequency. To test whether RT data deviate from this prediction, we estimated the power spectra of RT series and averaged them across sessions for each subject. Power spectra of RTs on no-signal trials were estimated using the Lomb-Scargle method for unevenly sampled data (Lomb, 1976; Scargle, 1982) with stop or step trials treated as missing data. For each session, this produced a spectral estimate with frequency step sizes equal to the reciprocal of the number of trials in the session. The resulting frequencies ranged from one such step up to the Nyquist limit. Adjacent frequency components were averaged into bins spaced evenly on a logarithmic scale, and then averaged across each session to give a spectral estimate for

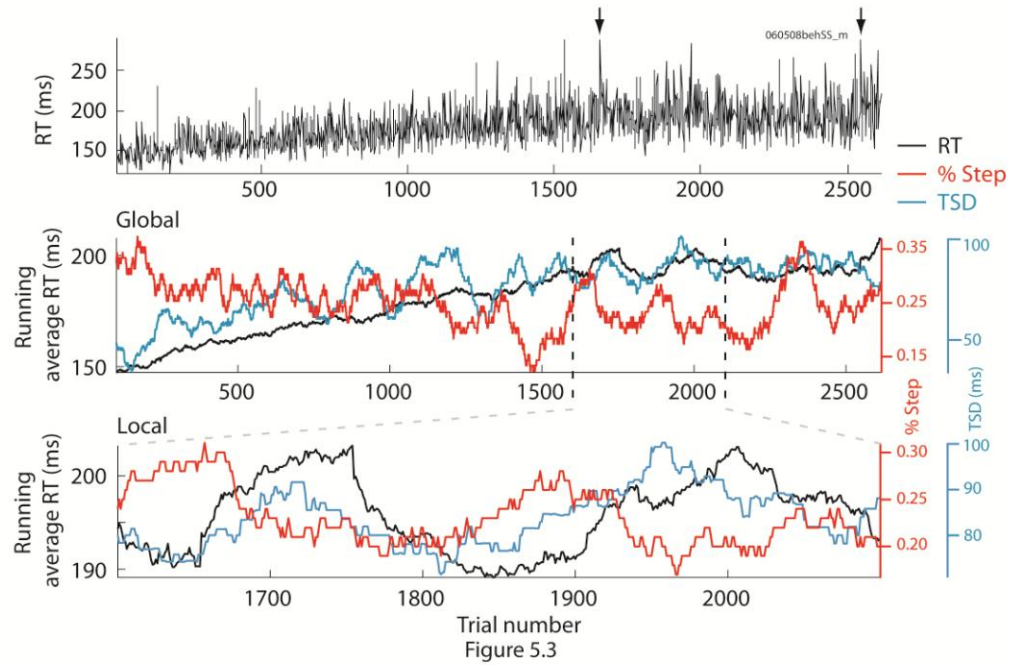
each subject. Confidence intervals were calculated using the assumption that the spectral density estimates follow a chi-square distribution with degrees of freedom equal to twice the number of averaged estimates (Jarvis & Mitra, 2001). We considered this to be the number of sessions for each subject. For comparison, we randomly permuted the trial order once for each session and estimated the trial-shuffled spectrum by the same procedure used for the original data. For more details on these methods, please see Appendix C.

RESULTS

Data were obtained from humans and macaque monkeys performing a stop signal task and a search-step task with saccadic eye movements. All statistical tests were performed at a 0.05 significance level.

Nonindependent and nonstationary response times

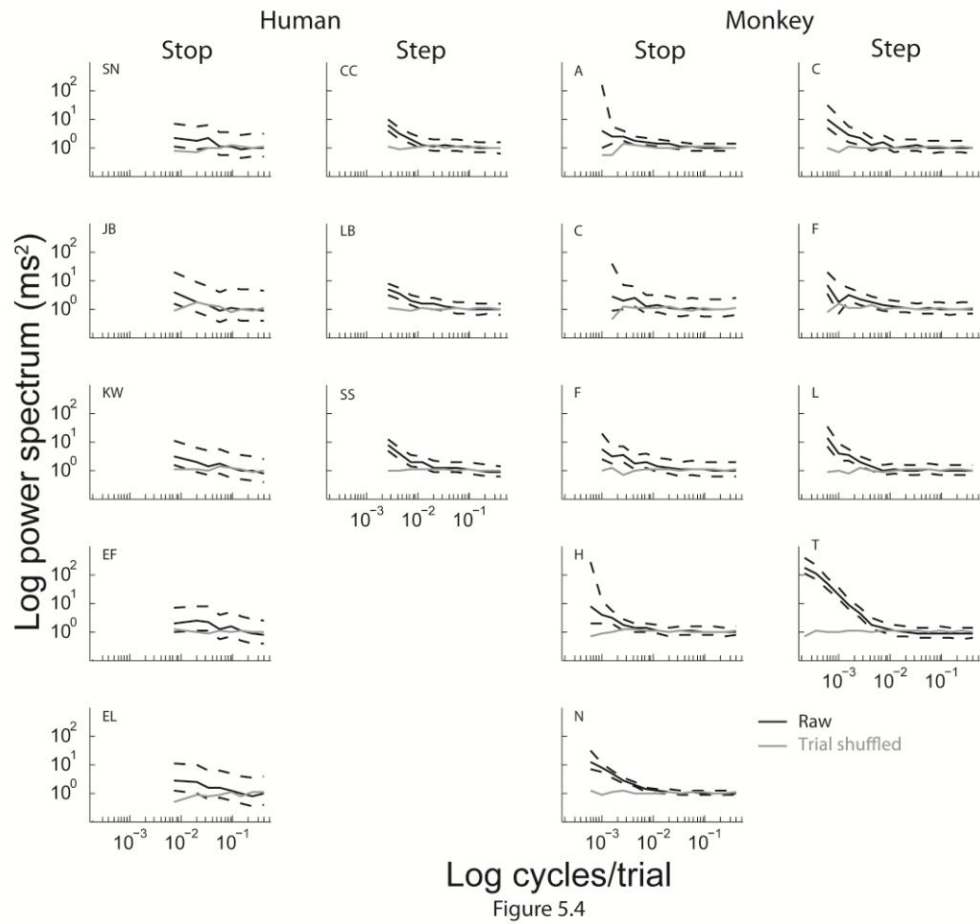
We observed fluctuations in RT during the course of a session occurring on *immediate* (1 trial), *local* (~ 10 to 100 trials), and *global* (~ 1000 trials) time scales. Fluctuations on all of these scales can be seen in Figure 5.3, which shows a representative session of a monkey performing the step task. The raw RTs are presented in the top panel and the 100-trial running averages of RT, TSD, and percentage of step trials are shown in the middle and lower panels. Immediate variability can be attributed to the irreducible randomness of RT or adaptive control across successive trials. Local variation of RT often coincided with gradual changes of the running fraction of step trials or average target step delay (see also Emeric et al., 2007). Global variation could be expressed as a gradual slowing (or speeding) of RT across a session, probably resulting from extraneous factors not controlled or manipulated by the experiment such as fatigue or motivation fluctuations.



A gradual increase of RT mean and variance is evident in Figure 5.3. To assess this for all of the sessions, we divided each session into thirds by trial number and compared the mean and

variance between the initial and final thirds of each session. Table 5.1 summarizes the trends, indicating the numbers and percentages of sessions with significant increases or decreases of RT mean and variance (ranksum for mean, Levene's nonparametric test for variance, both two tailed; the expected chance level is 2.5% for each cell in the table). More sessions than would be expected by chance had significant changes in RT mean and variance, although across subjects and sessions both decreases and increases of RT mean and variance were observed. Thus, RTs were nonstationary.

To quantify the degree of independence of RTs across trials, we calculated the frequency spectrum of RTs for each subject. Figure 5.4 shows the power spectra for the successive RTs produced by each subject with confidence intervals compared to the power spectra derived from a shuffled sequence of the same RTs. For both humans and monkeys in both the stepping and stopping tasks, spectral power was elevated at low frequencies. Across subjects, the power at the lowest frequency was at least twice the power at the highest frequencies. We observed the same pattern when calculating the RT spectra after removing any linear trends from the data. Thus, RTs show significant slow fluctuations beyond a linear trend occur during performance of these tasks. The higher power at low trial frequencies indicates that RTs within immediate and local time scales are expected to be positively correlated. We verified that this was the case for pairs of consecutive no-signal trials.



Impact of nonindependent and nonstationary RTs on inhibition functions

Performance in stopping or stepping tasks is characterized by the probability of failing to cancel the initial movement as a function of the delay of the stop or step signal. The relationship of this inhibition (or compensation) function to the distribution of RTs is used to calculate SSRT (or TSRT). Having already demonstrated the nonindependence and nonstationarity of RT, in this section we consider the impact these have on the form of the inhibition (or compensation) function.

We plotted inhibition functions from different chronological epochs within sessions. Figure 5.5 displays data from a representative session in which a monkey performed the stop-signal task with the SSD adjusted through the staircase procedure. Figure 5.5A shows that RT increased gradually over the course of the session, coincident with a gradual increase in SSD. Figure 5.5B compares the inhibition function derived over the entire session to inhibition functions derived from an early epoch (during which RT and SSD were shorter) and a later epoch (during which RT and SSD were longer). The inhibition function over the entire session had a shallower slope than the inhibition functions from either epoch. Many sessions across species and tasks showed similar differences between session-level and epoch-level inhibition functions or compensation functions.

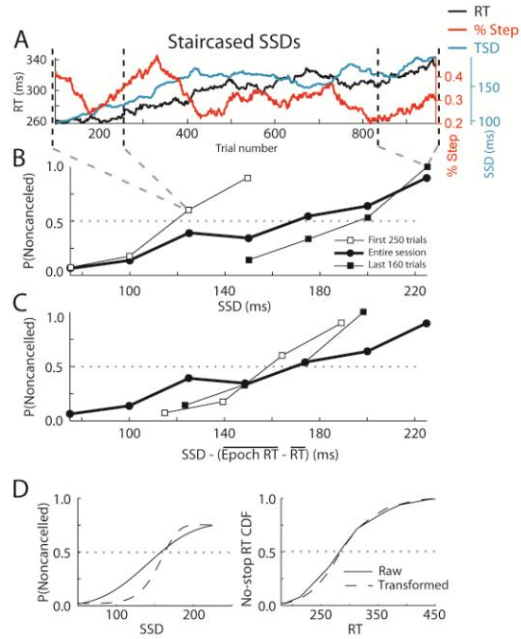


Figure 5.5

To compare inhibition functions across sessions, it has been shown previously that the abscissa of the inhibition function can be transformed to represent the relative finishing time of the

STOP and GO processes by subtracting SSD and SSRT from the mean RT for each epoch (Logan & Cowan, 1984). The logic of this transformation follows from the race model claim that the probability of inhibiting depends on the relative finishing time of these processes, not on the absolute finishing time of either process alone. Specifically, as illustrated in Figure 5.5C, we produced a transformed SSD (referred to as SSD') by subtracting the difference between the mean RT in each epoch and the mean RT over the entire session from the original SSD:

$$SSD' = SSD - (\overline{Epoch RT} - \overline{RT}).$$

This translates the inhibition functions from an epoch when a subject responds more quickly to higher values of SSD' and translates the inhibition function from an epoch when a subject responds more slowly to lower values of SSD'. The transformed inhibition functions overlap each other as well as the inhibition function from the entire session. Note that this procedure does not change the slopes. We extended this epoch-by-epoch transformation procedure to a trial-by-trial transformation according to

$$SSD'_i = SSD_i - (Local RT_i - \overline{RT}).$$

The SSD_i (TSD_i) for the i th stop (step) trial was transformed to SSD'_i (or TSD'_i) by subtracting the difference between the average RT on no-signal trials in the 101-trial interval centered on that trial (represented by $Local RT_i$ above) and the session average RT (\overline{RT} above). The length of the averaging window was truncated as necessary near the start or end of a session. Resulting SSD' (TSD') values were binned, and the proportion of stop (step) trials in which the subject failed to cancel the initial responses in each bin was determined. The transformed inhibition (compensation) functions, which plot this proportion against the SSD' (TSD') values, allows us to probe the impact of nonindependence and nonstationarity on inhibition functions by providing an example of what the data would look like if fluctuations of mean RT were removed. The forms of these transformed inhibition (compensation) functions were characterized by cumulative Weibull function fits to the values. The slopes of the transformed inhibition

(compensation) function were tested statistically as follows. We performed a permutation test comparing the median slopes of the transformed inhibition function to the slopes when trial order was randomly permuted 1000 times before applying the transformation procedure.

The left panel of Figure 5.5D shows the fitted cumulative Weibull distributions for the original and transformed inhibition functions for this sample session. The number and proportion of sessions in which the transformed inhibition function was significantly steeper than the original inhibition function is shown in the first column of Table 5.2. Across the population, the transformed inhibition function is significantly steeper in most sessions. In the human search step data this effect was less prevalent.

The foregoing analyses focused on data from sessions in which SSD (TSD) was adjusted on a staircase according to subjects' performance. With the stair-case procedure, a different range of SSD (TSD) values is presented within different epochs of an experimental session due to differences in RTs across epochs. To determine if the underestimation of the inhibition function slope is specific to the use of stair-casing, we performed the same analyses on data from a monkey performing the stop-signal task with a set of SSD's randomly presented with equal probability. Figure 5.6A shows a 100-trial running mean of the RTs and the probability of not canceling on stop trials, with two epochs highlighted. Clearly, the probability of not canceling varied inversely with RT. For the same SSD values, subjects are more likely to inhibit the initial movement during an epoch of slower responding.

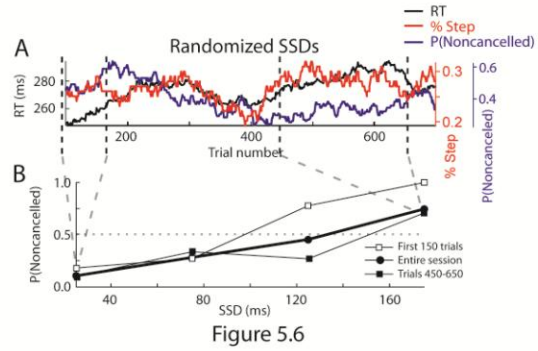


Figure 5.6

Figure 5.6B compares the inhibition functions from each epoch with that from the entire session. We compared the heights and slopes of these inhibition functions. The inhibition function

from the epoch when the subject was responding more quickly lies above that from the epoch when the subject was responding more slowly. The inhibition function slopes between these particular epochs and the overall session were not noticeably different. However, when the same transformation applied to staircased sessions was applied to this session, the transformed inhibition function was again found to be significantly steeper than the original. This procedure was applied to each session with fixed SSD (TSD). The number and proportion of sessions of non-stair-cased data for each subject in which the transformed inhibition function was significantly steeper than the original is shown in the first column of Table 5.3. Across the population this was significant for many non-stair-cased sessions. Thus a shallower slope of the inhibition function from an entire session seems to be a general consequence of nonindependence and not due to adapting SSD (TSD) to performance via stair-casing.

Estimating SSRT or TSRT

The transformation procedure was also used to calculate a transformed SSRT (TSRT) (designated SSRT' (TSRT')). To do so, RTs were transformed as follows:

$$RT'_i = RT_i - (Local\ RT_i - \overline{RT}).$$

The RT_i for the i th trial with no stop (step) signal was transformed to RT'_i by subtracting the difference between the local average RT and the session average RT as described above.

Naturally, the distribution of RT' is centered on the session mean but with less variance, as shown in the right panel of Figure 5.5D. Although modest, the significance of the reduction of variance for this session was verified statistically using another 1000 shuffle permutation test comparing the standard deviation of the RT' distribution. For the session illustrated in Figure 6, the reduction of no-signal RT variance by the transformation approached significance ($p = 0.055$). For each subject, the number and proportion of sessions in which the transformation significantly reduced the RT standard deviation is shown in the second column of Tables 5.1 and 5.2 for stair-

cased and non-stair-cased data, respectively. Adjusting for RT nonindependence and nonstationarity by this transformation procedure significantly reduced the variance of no-signal RT distributions in many sessions for all subjects.

Using the SSD' (TSD') and RT' values from which slow fluctuations in RT have been removed, we obtained a transformed SSRT' (TSRT'). SSRT' and SSRT values were not significantly different for the session illustrated in Figure 5 (SSRT = 141 ms, SSRT' = 136 ms, permutation test) or Figure 5.6 (SSRT = 153 ms, SSRT' = 152 ms, permutation test). The distributions of differences of SSRT' (TSRT') and SSRT (TSRT) across subjects and conditions are illustrated in Figure 5.7. Overall, accounting for the nonindependence and nonstationarity of RT had very little effect on the estimate of stop process duration SSRT (TSRT). The third columns of Tables 5.1 and 5.2 display for each subject the numbers and proportions of sessions in which SSRT' (TSRT') was significantly different from SSRT (TSRT). Adjusting for RT nonindependence and nonstationarity by this transformation rarely changed significantly the SSRT (TSRT). The only exception was monkey T performing the search step task, for whom 14 of 42 sessions showed a significant difference between TSRT and TSRT'.

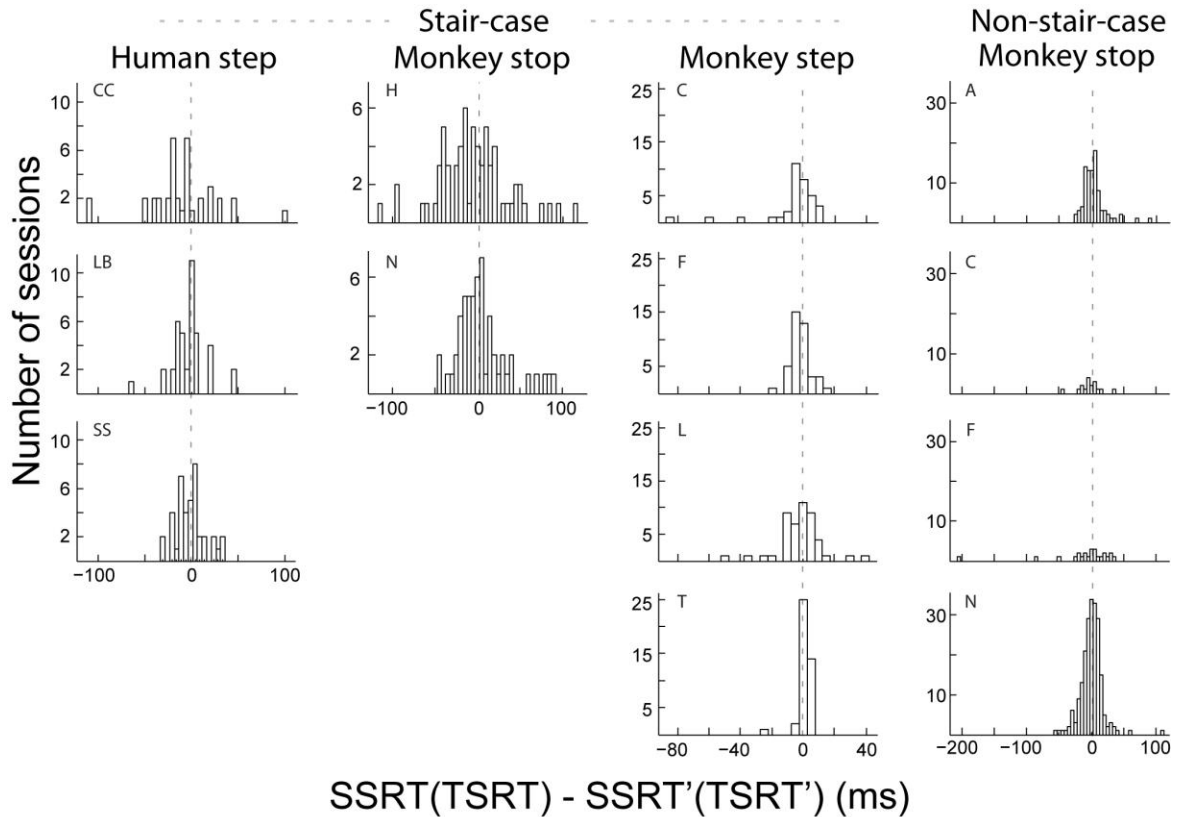


Figure 5.7

Furthermore, we found no systematic bias in the distributions of $SSRT'(TSRT')$ relative to $SSRT(TSRT)$ (paired t-tests). Only subject CC performing the step task exhibited a significant difference between $TSRT'$ than $TSRT$ (12.5 ms slower, $t(37) = 3.3$, $p < 0.05$). In spite of these idiosyncrasies we conclude that the estimation of $SSRT(TSRT)$ is robust against nonstationarity or nonindependence of RT. Moreover, in Appendix A we show mathematically that with fluctuating GO and STOP process finish time distributions, one method of measuring $SSRT(TSRT)$ provides a time-weighted average of the $SSRT(TSRT)$ value over the entire session. This suggests that even as a subject's RT fluctuates, the value of $SSRT$ remains stable.

Trial-by-trial RT adjustments during stopping and stepping

A hallmark of executive control is the ability to change behavior based on past stimuli, responses, and outcomes. Many studies have shown that subjects adjust their RT based on the

previous trial's stimulus parameters (e.g., Verbruggen & Logan, 2008a) or their behavior on the previous trial (e.g., Emeric et al., 2007). These and related studies implicitly assume independence and stationarity in RT when examining RTs on trial $n+1$ based on the stimuli or responses in trial n . However, if the occurrence of the stop (step) response on trial n varies with fluctuations of RT alone, then conclusions drawn from an examination of RTs on trial $n+1$ alone may be misleading.

A change in RT on trial $n+1$ could be due to an executive control signal influencing behavior based on the outcome of trial n . Alternatively, relationships between performance on trials n and $n+1$ could simply be consequence of nonindependence and nonstationarity of RT. Hence, a change in RT on trial $n+1$ may not be due to an executive control signal. One way to account for the effects of nonindependence and nonstationarity is to consider what happened on the $n-1$ trial.

Figure 5.8 shows the RTs on no-signal trials before ($n-1$) and after ($n+1$) all three trial types for the stop task (no-signal, cancelled, and noncancelled) and the step task (no-signal, compensated, and noncompensated). Colors for each subject are indicated, and the horizontal dotted lines denote the grand mean no signal RT for each subject for comparison. We restricted this analysis to 3-trial sequences for noncancelled and cancelled trial types to those triplets in which the $n-1$ and $n+1$ trial were both no-signal trials. For the no-signal trial type we just required that the $n-1$ trial type was a no-signal trial. As shown previously, RTs appear slower following cancelled trials as opposed to noncancelled trials (e.g., Emeric et al., 2007). The current analysis shows that RT was also slower before noncancelled trials. Appendix B demonstrates mathematically that these differences in RT with trial history are a simple consequence of fluctuations in RT. The proof relies on the fact that for a given SSD more cancelled trials will tend to occur when the subject is responding slowly, while more noncancelled trials will tend to occur when the subject is responding quickly. Thus, the incidence of successful or unsuccessful

inhibition varies with RT fluctuations, which is manifest in the RTs of trials before and after the alternative responses.

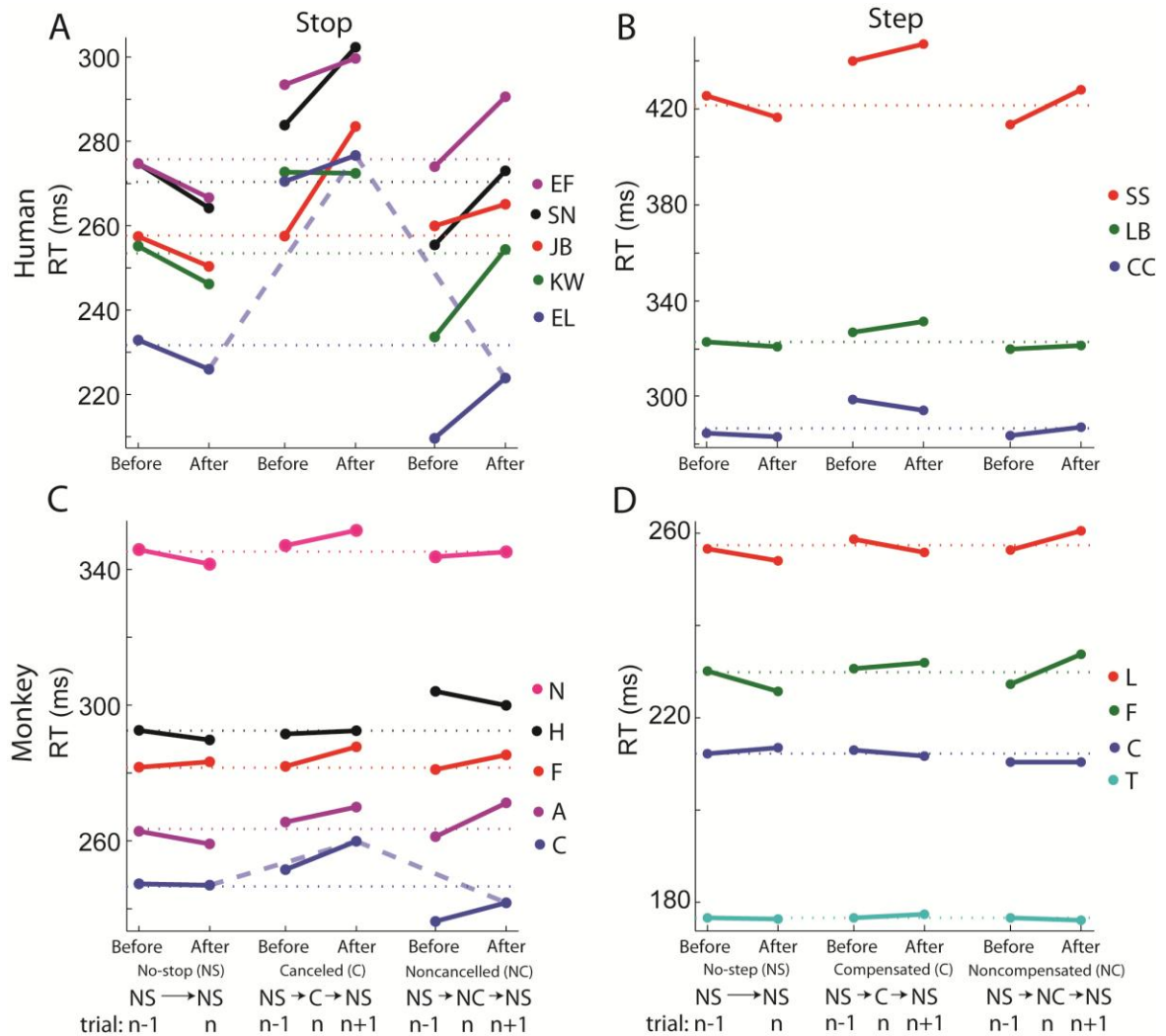


Figure 5.8

To determine if the variation of RT after different types of trials exceeds what can be explained by nonindependence and nonstationarity of RT, we performed a pair of planned interaction contrasts of RT for each combination of species and task in a 3x2 design with trial type (no-signal, canceled/compensated, noncanceled/noncompensated) and trial sequence (RT before or after the target trial type) as within-subject factors. An interaction in this design will reveal trial history effects independent of effects of RT fluctuations. A repeated measures omnibus ANOVA using Greenhouse-Geisser adjusted degrees of freedom revealed a significant interaction of trial

type and sequence in the stop task for both humans ($F(1.3, 5.2) = 11.7$) and monkeys ($F(1.5, 6.0) = 7.1$) but not in the step task (humans: $F(2.0, 4.0) = 1.7$; monkeys: $F(2.0, 6.0) = 2.5$).

We investigated the omnibus interaction in the stop task further. To determine if the magnitude of RT changes following cancelled trials differs from that following noncancelled trials, we performed a paired t-test of the differences in RTs before and after cancelled trials to the differences in RTs before and after noncancelled trials. No significant difference was found for either humans ($t(4) = -0.5$) or monkeys ($t(4) = 0.8$). To investigate whether subjects slow their responses following cancelled or noncancelled stop signal trials relative to responses following a no-signal trial, we performed paired t-test of the differences in RTs of consecutive no-signal trials compared to the average difference in RTs before and after cancelled or noncancelled trials. RTs were significantly faster following a no-signal trial as compared to following a cancelled or noncancelled trial (humans - 21.7 ms, $t(4) = -11.0$; monkeys - 6.0 ms, $t(4) = -3.6$). Taken together, these results show that both humans and monkeys are slower following a stop trial as opposed to following a no-signal trial, but the amount of slowing is comparable between cancelled and noncancelled trials. In the step task, generalized slowing following step trials was not observed.

DISCUSSION

We have shown that RTs in humans and monkeys performing the saccade stop-signal and search-step tasks are nonindependent and nonstationary across trials. However, we have shown empirically and mathematically that methods used to estimate SSRT (TSRT) are robust to such RT fluctuations. Nevertheless, nonindependence and nonstationarity of RT can result in an underestimate of the slope of the inhibition (compensation) function across a session. We have also shown how nonindependence and nonstationarity of RT influences analyses of trial history.

We propose that examining the RT on trials both before and after a trial of interest can help account for changes in RT due only to nonindependence and nonstationarity. We found that RT was relatively slower both before and after cancelled stop signal trials compared to before and after noncancelled trials and RT was not specifically slowed after cancelled as compared to noncancelled trials.

Nonstationarity of the STOP process

We have shown that no-signal RTs in the saccade stop-signal and target-step tasks are nonindependent and nonstationary. Within the race model, this would be modeled as a GO process that slowly varies throughout a session and that is subject to trial-to-trial correlations. The stop process also could vary throughout a session (see Appendix A). However, because measurement of the SSRT (TSRT) requires 100 or more trials to produce a stable estimate, it is difficult to demonstrate the nonstationarity of SSRT (TSRT). Thus, we have not explicitly shown the nonstationarity of the stop process.

Race model implications

An important contribution of this work has been to show that the calculations of SSRT (TSRT) are largely unaffected by RT fluctuations. Calculations using the mean difference method will yield a time-weighted average of the SSRT (TSRT) over the session. Validating the measurement of SSRT (TSRT) is important because of its utility as a measure of impulsivity in clinical and developmental studies (e.g., Schachar et al., 2004).

While fluctuations in RT do not affect SSRT or TSRT calculations, we did demonstrate that it results in shallower inhibition functions. Because the slope of the inhibition function can be used to derive a measure of the variability of SSRT (Band et al., 2003; Colonius, 1990; Logan &

Cowan, 1984), these new results suggest that fluctuations in RT can result in an overestimate of the variability of SSRT.

Choice of staircased or versus randomized SSDs

A subject of methodological interest for investigators using stopping or stepping tasks is whether to adjust the SSD (TSD) by a staircase procedure or randomly select from preset values. RT fluctuations occur in both staircased and nonstaircased sessions, but as we have shown, fluctuating RTs manifest some of their effects differently depending on how the SSDs are selected. For example, whether SSDs are staircased or randomized will affect how strongly RT fluctuations impact the trial history analyses. As RT varies during a session, a greater concentration of noncancelled trials will occur when a subject is responding quickly, while a greater concentration of cancelled trials will occur when a subject is responding slowly. This imbalance will be particularly prevalent when the SSDs are randomized. When using the staircase procedure, however, the proportion of canceled stop trials will be stabilized over global RT fluctuations, though there will still be some remaining bias because of local fluctuations in RT. All of the human and most of the monkey stopping data analyzed here and in Emeric et al. (2007) used randomized SSDs, which likely contributed to the magnitude of the RT shifts between the trials before cancelled and noncancelled trials.

Additionally, when staircasing is used, SSDs fluctuate in response to RT fluctuations, which creates a correlation of RT with SSD. We have found this correlation to be significant in most individual staircased sessions across species and tasks. One practical consequence of this is that this correlation should be taken into account when comparing noncancelled RTs to no-signal RTs. To verify that behavior conforms to the race model, investigators often compare the distribution of noncancelled RTs at each SSD to the distribution of no-signal RTs over the whole session. If at any SSD the noncancelled distribution exceeds the no-signal distribution, this is seen

as a violation of the independence premise of the race model. However, when staircasing is used, this may not be a valid comparison because this correlation dictates that the overall no-signal RT distribution will be different from the RT distribution at each SSD, (TSD) particularly at the highest and lowest SSD (TSD). Instead it may be preferable to compare the noncancelled RT distribution at each SSD (TSD) to the RT distribution on no-signal trials when that same SSD (TSD) was expected.

In contrast to when staircased, when randomized SSD (TSD) is used, the values remain constant despite the RT fluctuations. Instead of a positive correlation between SSD (TSD) and RT there is a negative correlation between the probability of responding on a stop (step) trial and RT, as one would expect from the race model.

Stopping trial history

We have shown that inferences about the effect that events on trial n has on performance on trial $n+1$ must control for the nonindependence and nonstationarity of RT. We suggest using the no-signal trials on trial $n-1$ as a simple control comparison (since events on trial n cannot affect events on prior trial $n-1$). Of course, one could argue that trial $n-1$ is preceded by other trial types that would influence its RT, which in turn are influenced by other preceding trials, and so on. However, in practice, the numbers of equivalent trials preceding $n-1$ or following $n+1$ and beyond in these tasks are too few for sufficient statistical power.

Cabel et al. (2000) and Emeric et al. (2007) found greater slowing of RTs following canceled as compared to following noncancelled trials. Emeric et al. (2007) also reported no systematic slowing of RTs following noncancelled trials. This apparent lack of post-error slowing following a missed stop signal was surprising given the apparent ubiquity of post-error slowing in

a range of tasks (e.g., Hajcak, McDonald & Simons, 2003; Rabbit, 1966). However, when we accounted for RT nonindependence and nonstationarity by examining trial n-1, we found that subjects are indeed slower to respond on trials following noncancelled (error) trials. Of note, however, subjects slowed their RTs to the same degree following cancelled (correct) trials. Thus, current results indicate a general slowing of RT following any stop signal trial. Clearly, accounting for RT nonindependence and nonstationarity has important implications for understanding alternative mechanisms whereby trial history affects performance (e.g., Botvinick, Braver, Barch, Carter, & Cohen, 2001; Schall & Boucher, 2007; Verbruggen, Logan, et al. 2008).

ACKNOWLEDGEMENTS

We thank Doug Hanes, Veit Stuphorn, Alex Gotler, Adi Murthy, and Kirk Thompson for their efforts in the original data collection, Corrie Camalier and Erik Emeric for assistance working with the datasets as well as original data collection, Courtney Segovis for assistance with the manuscript, and Pierre Pouget for helpful discussions. This work was supported by NIH R01-MH55806, NIH RO1-EY08890, NIH F32-EY016679, AFOSR FA 9550-07-1-0192, NSF SBE-0542013, NIH P30-EY08126, NIH P30-HD015052, the Temporal Dynamics of Learning Center SBE-0542013, an NSF Science of Learning Center, and Robin and Richard Patton through the E. Bronson Ingram Chair of Neuroscience.

REFERENCES

Band, G. P., van der Molen, M. W., & Logan, G. D. (2003). Horse-race model simulations of the stop-signal procedure. *Acta Psychologica (Amsterdam)*, **112**, 105–142.

- Becker, W. & Jürgens, R. (1979). An analysis of the saccadic system by means of double step stimuli. *Vision Research*, **19**, 967–983.
- Botvinick, M. M., Braver, T. S., Barch, D. M., Carter, C. S., & Cohen, J. D. (2001). Conflict monitoring and cognitive control. *Psychological Review*, **108**, 624–652.
- Boucher, L., Palmeri, T. J., Logan, G. D., & Schall, J. D. (2007). Inhibitory control in mind and brain: An interactive race model of countermanding saccades. *Psychological Review*, **114**, 376–397.
- Boucher, L., Stuphorn, V., Logan, G. D., Schall, J. D., & Palmeri, T. J. (2007). Stopping eye and hand movements: Are the processes independent? *Perceptual Psychophysics*, **69**, 785–801.
- Broadbent, D. E. (1971). *Decision and Stress*. London: Academic Press.
- Cabel, D. W., Armstrong, I. T., Reingold, E., & Munoz, D. P. (2000). Control of saccade initiation in a countermanding task using visual and auditory stop signals. *Experimental Brain Research*, **133**, 431–441.
- Camalier, C. R., Gotler, A., Murthy, A., Thompson, K. G., Logan, G. D., Palmeri, T. J., ET AL. (2007). Dynamics of saccade target selection: Race model analysis of double step and search step saccade production in human and macaque. *Vision Research*, **47**, 2187–2211.
- Colonus, H. (1990). A note on the stop-signal paradigm or how to observe the unobservable. *Psychological Review*, **97**, 309–312.
- Emeric, E. E., Brown, J. W., Boucher, L., Carpenter, R. H., Hanes, D. P., Harris, R., ET AL. (2007). Influence of history on saccade countermanding performance in humans and macaque monkeys. *Vision Research*, **47**, 35–49.
- Fecteau, J. H., & Munoz, D. P. (2003). Exploring the consequences of the previous trial. *Nature Reviews Neuroscience*, **4**, 435–443.
- Freeman, G. L. (1933). The facilitative and inhibitory effects of muscular tension upon performance. *American Journal of Psychology*, **26**, 602–608.

- Gilden, D. L. (2001). Cognitive emissions of 1/f noise. *Psychological Review*, **108**, 33–56.
- Hajcak G., McDonald, N., & Simons R.F. (2003). To err is autonomic: Error-related brain potentials, ANS activity and post-error compensatory behavior. *Psychophysiology*, **40**, 895–903.
- Hanes, D.P., Patterson W.F., & Schall J.D. (1998). The role of frontal eye field in countermanding saccades: Visual, movement and fixation activity. *Journal of Neurophysiology*, **79**, 817–834.
- Hanes, D. P., & Schall, J. D. (1995). Countermanding saccades in macaque. *Visual Neuroscience*, **12**, 929–937.
- Kornylo, K., Dill, N., Saenz, M., & Krauzlis, R. J. (2003). Canceling of pursuit and saccadic eye movements in human and monkeys. *Journal of Neurophysiology*, **89**, 2984–2999.
- Jarvis, M. R. & Mitra P. P. (2001). Sampling properties of the spectrum and coherency of sequences of action potentials. *Neural Computation*, **13**, 717–749.
- Li, C. S., Krystal, J. H., & Mathalon, D. H. (2005). Fore-period effect and stop-signal reaction time. *Experimental Brain Research*, **167**, 305–309.
- Logan, G. D. (1985). Skill and automaticity: Relations, implications and future directions. *Canadian Journal of Psychology*. **39**, 367–386.
- Logan, G. D. (1994). On the ability to inhibit thought and action: A user's guide to the stop signal paradigm. In D. Dagenbach, & T. Carr (Eds.), *Inhibitory processes in attention, memory, and language*. (pp. 189-239). San Diego: Academic Press.
- Logan, G. D., & Cowan, W. B. (1984). On the ability to inhibit simple and choice reaction time responses: A theory of an act of control. *Psychological Review*, **91**, 295–327.
- Logan, G. D., Schachar, R. J., & Tannock, R. (1997). Impulsivity and inhibitory control. *Psychological Science*, **8**, 60–64.

- Lomb, N. R. (1976). Least-squares frequency analysis of unequally spaced data, *Astrophysical and Space Science*, **39**, 447–462.
- Luce, R. D. (1986). *Response Times: Their Role in Inferring Elementary Mental Organization*. New York: Oxford University Press.
- Murthy, A., Ray, S., Shorter, S. M., Priddy, E. G., Schall, J. D., & Thompson, K. G. (2007). Frontal eye field contributions to rapid corrective saccades. *Journal of Neurophysiology*, **97**, 1457–1469.
- Murthy, A., Ray, S., Shorter, S. M., Schall, J. D., & Thompson K. G. (2009). Neural control of visual search by frontal eye field: Effects of unexpected target displacement on visual selection and saccade preparation. *Journal of Neurophysiology*, **101**, 2485–2506.
- Osman, A., Kornblum, S., & Meyer, D. E. (1990). Does motor programming necessitate response execution? *Journal of Experimental Psychology: Human Perception and Performance*, **16**, 183–198.
- Özyurt, J., Colonius, H., & Arndt, P. A. (2003). Countermanding saccades: Evidence against independent processing of go and stop signals. *Perception & Psychophysics*, **65**, 420–428.
- Paré, M., & Hanes, D. P. (2003). Saccadic reaction time in the monkey: Advanced preparation of oculomotor programs is primarily responsible for express saccade occurrence. *Journal of Neurophysiology*, **76**, 3666–3681.
- Percival, D. B., & Walden, A. T. (1993). *Spectral analysis for physical applications*. Cambridge: Cambridge University Press.
- Rabbitt, P. M. (1966). Error correction time without external error signals. *Nature*, **212**, 438.
- Rieger, M., & Gauggel, S. (1999). Inhibitory after-effects in the stop signal paradigm. *British Journal of Psychology*, **90**, 509–518.
- Scargle J.D. (1982). Studies in astronomical time series analysis. II. Statistical aspects of spectral analysis of unevenly spaced data. *Astrophysical Journal*, **263**, 835–853.

- Schachar, R. J., Chen, S., Logan, G. D., Ornstein, T. J., Crosbie, J., Ickowicz, A., & Pakulak, A. (2004). Evidence for an error monitoring deficit in attention deficit hyperactivity disorder. *Journal of Abnormal Child Psychology*, **32**, 285–293.
- Schall, J. D., & Boucher, L. (2007). Executive control of gaze by the frontal lobes. *Cognitive Affective and Behavioral Neuroscience*, **7**, 396–412.
- Verbruggen, F., & Logan, G. D. (2008a). Long-term aftereffects of response inhibition: Memory retrieval, task goals, and cognitive control. *Journal of Experimental Psychology: Human Perception and Performance*, **34**, 1229–1235.
- Verbruggen, F., & Logan, G. D. (2008b). Response inhibition in the stop-signal paradigm. *Trends in Cognitive Sciences*, **12**, 418–424.
- Verbruggen, F., Logan, G. D., Liefvooghe, B., & Vandierendonck, A. (2008). Short-term aftereffects of response inhibition: repetition priming or between-trial control adjustments. *Journal of Experimental Psychology: Human Perception and Performance*, **34**, 413–426.
- Verbruggen, F., Schneider, D. W., & Logan, G. D. (2008). How to stop and change a response: The role of goal activation in multi-tasking. *Journal of Experimental Psychology: Human Perception and Performance*, **34**, 1212–1228.
- Wagenmakers, E. J., Farrell, S., & Ratcliff, R. (2004). Estimation and interpretation of $1/f^{\alpha}$ noise in human cognition. *Psychonomic Bulletin & Review*, **11**, 579–615.
- Welford, A. T. (1968). *Fundamentals of Skill*. London: Methuen.
- Welford, A. T. (1980). Choice reaction time: Basic concepts. In A. T. Welford (Ed.), *Reaction Times*. (pp. 73-128). New York: Academic Press.

FIGURE LEGENDS

Figure 5.1. The experimental tasks. A: Stopping. The dotted circle indicates the subject's gaze within each frame. A one-sided arrow indicates a saccade. A majority of trials are no-signal trials

in which the subject fixates centrally and responds to a peripheral target that appears by making a saccade to it. A minority of trials are stop trials in which following some delay after the presentation of the target, the central fixation point reappears, directing the subject to maintain central fixation. If they are able to successfully withhold the impending saccade, the trial is labeled as a cancelled trial. If the subject errantly makes a saccade to the target, the trial is labeled as a noncancelled trial. B: Search-step. A one-sided arrow indicates a saccade the subject makes. A majority of trials are no-signal trials in which the subject fixates centrally and responds to an array of stimuli that appears by making a saccade to the oddball target. A minority of trials are step trials in which following some delay after the presentation of the target, the location of the oddball singleton moves to a different location on the array through two isoluminant color changes, directing the subject to make a saccade to the new location of the target. If they are able to successfully make a saccade to the new target location, the trial is labeled as a compensated trial. If the subject errantly makes a saccade to the target, the trial is labeled as a noncompensated trial.

Figure 5.2. Illustration of how SSRT and TSRT are calculated according to the race model. A: Probability density of response times in trials with no stop signal. Mean of distribution indicated by vertical dashed line. Duration of SSD (TSD) and of SSRT (TSRT) indicated by horizontal arrows. Shaded portion of the function indicates proportion of trials in which response would have occurred before the critical time of $SSD + SSRT$ ($TSD + TSRT$) for a given SSD (TSD). B: Inhibition function plots the probability of responding on trials calling for a stop (step) response as a function of SSD (TSD). Lower horizontal arrow highlights the fraction of failures for the shortest SSD (TSD) which corresponds to shaded area in A. SSRT (TSRT) determined from difference between mean RT on no-signal trials and the midpoint of the inhibition function indicated by upper horizontal arrow

Figure 5.3. Immediate, local, and global variation of RT, TSD and the percentage of step trials in a sample session of a monkey performing the search-step task with TSDs determined by a 1-up/1-down stair-case procedure. The top plot shows unfiltered no-signal RTs. Arrows indicate two trials with RTs that exceeded the scale of the plot (left 431 ms, right 556 ms). The middle plot shows 100 trial running average of the RT (black), TSD (blue) and the percentage of step trials (red) for the same set of trials. The lower plot shows the same for a portion of the session.

Figure 5.4. Spectrum of RTs. The panels show RT mean-square power spectra plotted against frequency in units of cycles per trial, averaged across sessions for each subject. For each panel, the solid black line shows the power spectrum, with 95% confidence intervals shown in the dashed lines. The grey line in each panel shows the spectral estimate of the same data when the trial order within each session is randomly permuted. Plots are collected in each column based on the species and task for each subject as indicated. Across species and tasks RT spectra are significantly not flat for most subjects, with increased power at low frequencies and decreased power at high frequencies compared to that of the independent trial-shuffled spectrum.

Figure 5.5. Effects of nonindependent and nonstationary RTs on inhibition functions for staircased data. A: 100 trial running average of the RT (black), SSD (blue) and the percentage of step trials (red) for a sample session of a monkey performing the stopping task. SSDs for this session were determined by a 1-up/1-down stair-case procedure. B: Comparison of inhibition function for an entire session with inhibition functions within two epochs. C: Transformation of inhibition functions by subtracting from the SSD the difference between the mean no-signal RT in an epoch and the mean no-signal RT over the entire session. D: Transformation of the inhibition function and of no-signal RT distribution resulting from subtracting from each SSD and RT the difference between the mean local RT and the mean overall RT. Left panel shows original and transformed

inhibition functions. Right panel shows original and transformed no-signal RT distributions. SSRT calculated from original and transformed distributions were 141 and 136 ms, respectively.

Figure 5.6. Effects of nonindependent and nonstationary RTs on inhibition functions when SSD is not adaptively staircased. Conventions are as in Figure 5.

Figure 5.7. Effects of nonindependent and nonstationary RTs on estimations of SSRT or TSRT. Each panel show histograms of the original SSRT or TSRT values minus the transformed value (SSRT' or TSRT') for each session for a given subject, with plots arranged by species, task, and stair-case condition as indicated.

Figure 5.8. Trial triplet analysis. As indicated in the schematics below panels C and D, the data included here are taken from occurrences of sequences of (from left to right) two consecutive no-signal trials, a cancelled (compensated) trial with a no-signal trial before and after it, and a noncancelled (noncompensated) trial with a no-signal trial before and after it during the stop (step) task. The mean RT on the no-signal trials from each sequence are plotted as indicated for each subject with colors corresponding to each subject as indicated beside each plot. The horizontal dotted lines show the overall mean no-signal RT for each subject. The thick dashed lines in A and C show for one human participant and one monkey the comparison that was made in Emeric et al. (2007) with these data. A and C show data for human participants and monkeys, respectively, performing the stop task, and panels B and D show data for human subjects and monkeys respectively performing the step task. For each condition, the monkey data in C and D plot the mean of all the session mean values for each subject, and the human data in A and B plot the aggregate mean value for all the trials pooled from all sessions.

Table 5.1.

Numbers and proportions of sessions for each subject with significant increases and decreases to the mean and standard deviation of RT when comparing the first and last of three evenly sized epochs in a session. Means were tested using a nonparametric rank sum test, and variances were tested using Levene's nonparametric test. Both tests were two-tailed. The expected chance level is 2.5% for each cell in the table.

Human stop

Subject	Mean increase	Mean decrease	Standard	Standard
			deviation increase	deviation decrease
SN	1/10 (10%)	1/10 (10%)	0/10 (0%)	1/10 (10%)
JB	2/6 (33%)	0/6 (0%)	0/6 (0%)	0/6 (0%)
KW	3/9 (33%)	1/9 (11%)	0/9 (0%)	0/9 (0%)
EF	2/9 (22%)	1/9 (11%)	0/9 (0%)	0/9 (0%)
EL	1/7 (14%)	1/7 (14%)	1/7 (14%)	0/7 (0%)

Human step

CC	9/38 (24%)	24/38 (63%)	2/38 (5%)	5/38 (13%)
LB	5/40 (13%)	16/40 (40%)	0/40 (0%)	3/40 (8%)
SS	14/40 (35%)	15/40 (38%)	4/40 (10%)	2/40 (5%)

Monkey stop

A	4/89 (4%)	3/89 (3%)	10/89 (11%)	3/89 (3%)
C	2/17 (12%)	2/17 (12%)	1/17 (6%)	2/17 (12%)
F	1/24 (4%)	3/24 (13%)	2/24 (8%)	1/24 (4%)

H	8/67 (12%)	6/67 (9%)	3/67 (4%)	1/67 (1%)
N	50/269 (19%)	45/269 (17%)	30/269 (11%)	21/269 (8%)

Monkey step

C	12/34 (35%)	2/34 (6%)	12/34 (35%)	1/34 (3%)
F	13/41 (32%)	8/41 (20%)	4/41 (10%)	5/41 (12%)
L	21/47 (45%)	3/47 (6%)	9/47 (19%)	4/47 (9%)
T	42/42 (100%)	0/42 (0%)	28/42 (67%)	1/42 (2%)

Table 5.2.

Numbers and proportions of stair-cased sessions for each subject in which a transformation to remove RT fluctuations significantly affected indicated values at a $p < 0.05$ level

Human step

Subject	Inhibition function slope	No-signal RT	
		standard deviation	TSRT
CC	2/38 (5%)	31/38 (82%)	0/38 (0%)
LB	0/40 (0%)	34/40 (85%)	0/40 (0%)
SS	1/40 (3%)	28/40 (70%)	0/40 (0%)

Monkey stop (stair-case)

H	34/67 (51%)	18/67 (27%)	0/67 (0%)
N	25/56 (45%)	20/56 (36%)	0/56 (0%)

Monkey step

C	28/34 (82%)	16/34 (47%)	2/34 (6%)
F	30/41 (73%)	18/41 (44%)	0/41 (0%)
L	38/47 (81%)	22/47 (47%)	0/47 (0%)
T	27/42 (64%)	42/42 (100%)	14/42 (33%)

Table 5.3.

Numbers and proportions of non-stair-cased sessions for each subject in which a transformation to remove RT fluctuations significantly affected indicated values at a $p < 0.05$ level

Subject	Inhibition function slope	No-signal RT	
		standard deviation	SSRT
A	25/89 (28%)	31/89 (35%)	1/89 (1%)
C	2/17 (12%)	6/17 (35%)	0/17 (0%)
F	12/24 (50%)	13/24 (54%)	1/24 (4%)
N	43/213 (20%)	106/213 (50%)	0/213 (0%)

APPENDIX A

Effect of nonindependence and nonstationarity on SSRT calculation with the mean-difference method

Here we will show that one common measurement of SSRT is robust to the nonindependent and nonstationary fluctuations that we have shown to exist in RT data. This holds provided that the proportion of stop trials presented to the subject remains constant through the RT changes. In particular, here we consider SSRT calculation using the mean-difference method (see Methods, Logan & Cowan, 1984).

For simplification, in the following formulation we consider the STOP and GO processes in discrete epochs of arbitrary numbers of trials with each process being stationary within an epoch. In the extreme case these epochs of stationarity can be as short as one trial, which makes no assumption of stationarity between any trials. The logic of the formulation would remain the same in this case, with two minor differences. The epoch means we describe would instead be considered to be the expected value of a single trial's RT rather than the mean RT across an epoch, and the value of w_i for all i could be simplified to $1/N$ where N is the number of trials in the session.

Using conventions from Logan and Cowan (1984), let $f(t)$ denote the probability density function of the distribution of GO process finish times as measured by the RTs on no-signal trials over the entire session. Let w_i denote the proportion of the total number of no-signal trials over the entire session that is contained within epoch i , and let $f_i(t)$ denote the distribution of GO process finish times within that epoch. Thus we define that

$$f(t) = \sum_i w_i f_i(t) \quad (1)$$

The mean GO process finish time \bar{T} is thus

$$\bar{T} = \int_{-\infty}^{\infty} t f(t) dt = \int_{-\infty}^{\infty} t [\sum_i w_i f_i(t)] dt = \sum_i w_i \int_{-\infty}^{\infty} t f_i(t) dt = \sum_i w_i \bar{T}_i \quad (2)$$

where \bar{T}_i is the mean GO process finish time for epoch i .

As described in Logan and Cowan (1984) the inhibition function, which is the probability of not canceling an initial saccade on a stop trial with a given SSD, can be treated as the cumulative distribution of some random function T_d . Let T_d be distributed as the function $\phi(t_d)$ such that

$$\phi(t_d) = \frac{dP_r(t_d)}{dt} \quad (3)$$

Where $P_r(t_d)$ is the probability of responding on a stop trial with an SSD of t_d . For simplicity, we will assume that the duration of the ballistic component of the movement is zero, although that can be added to the model for completeness without affecting these results. Let $f_{si}(t)$ denote the distribution of STOP process finish times within each epoch. Thus for epoch i , the distribution of T_d is given by

$$\phi_i(t_d) = \int_{-\infty}^{\infty} f_{si}(u) f_i(u + t_d) du \quad (4)$$

For the entire session,

$$\phi(t_d) = \sum_i w_i \phi_i(t_d) = \sum_i w_i \int_{-\infty}^{\infty} f_{si}(u) f_i(u + t_d) du \quad (5)$$

Importantly, if the ratio of stop trials is identical in each epoch, then each w_i here will correspond to the w_i for the no-signal distribution in equation 1 as the weight of each epoch's contribution to the entire session's inhibition function and the no-signal distribution will be the same.

We can then calculate the mean of this distribution as

$$\bar{T}_d = \int_{-\infty}^{\infty} t_d \phi(t_d) dt_d = \sum_i w_i \int_{-\infty}^{\infty} t_d \int_{-\infty}^{\infty} f_{si}(u) f_i(u + t_d) du dt_d \quad (6)$$

With the observation that $\int_{-\infty}^{\infty} t_d \int_{-\infty}^{\infty} f_{si}(u) f_i(u + t_d) du dt_d = \bar{T}_i - \bar{T}_{si}$, where \bar{T}_{si} is the mean

STOP process finish time for epoch I, equation 6 can be rewritten as

$$\bar{T}_d = \sum_i w_i (\bar{T}_i - \bar{T}_{si}) = \sum_i w_i \bar{T}_i - \sum_i w_i \bar{T}_{si} \quad (7)$$

The difference-of-means method presented in Logan and Cowan (1984) suggests that one method to estimate SSRT for a given dataset is to subtract the mean of the inhibition function from the mean of the no-signal RT distribution for the entire session. Applying equations 2 and 7 we see that if the distributions of the GO and STOP process that vary across epochs within a session, this measurement would still amount to a weighted average of the SSRT in each epoch.

$$\bar{T} - \bar{T}_d = \sum_i w_i \bar{T}_{si} \quad (8)$$

This would be the measurement of interest in most cases even if the SSRT distribution does vary within a session, and so this measurement of SSRT is robust to fluctuations in RT and SSRT during a session, given that the assumptions in the analysis hold.

One assumption that would not hold strictly true is that the fraction of stop trials is constant in every epoch simply due to randomness in the determination of stop trials and the timing of changes in RT. If this happens, it would bias the measurement of SSRT to some extent. For example, if during a given epoch in which the subject is responding faster than normal the subject was also presented with more stop trials than normal, that epoch would have a disproportionate effect in determining the inhibition function for the overall session than it would in determining the no-signal RT distribution for the entire session. This would shift the inhibition function earlier in time so that the no-signal RT distribution and resulting measurements of SSRT for the entire session would overestimate SSRT.

It is also worth noting that a change in the proportion of stop trials arising by chance can induce changes in RT (Emeric et al., 2007). This would suggest that these spontaneously occurring epochs could serve to bias the calculation of SSRT, resulting in some degree of underestimation of SSRT following the logic described above. For this reason it may be wise for experimenters to follow the common practice of pseudorandomizing the presentation of stop trials to prevent long stretches of too few or too many stop trials locally to mitigate this effect.

This would also suggest that a session with rapidly fluctuating RTs would result in more noise being added to the estimation of SSRT, but that measurements made from longer sessions should be more robust to the effects of this noise.

APPENDIX B

Effect of RT nonindependence and nonstationarity during stopping or stepping tasks on measurements of response times before and after cancelled and noncancelled trials

Here we will show that fluctuations in RT will cause the mean RT on no-signal trials before and after cancelled trials to be higher than the mean RT on no-signal trials before and after noncancelled trials even when the presence of a cancelled or noncancelled trial does not have any effect on the distribution of no-signal RTs on any trial. The proof below explicitly shows this for trials following a cancelled or noncancelled trial, but the same logic applies to trials preceding a cancelled or noncancelled trial.

For the sake of simplicity, we will consider the case in which an experimental session consists of two epochs of equal size and the SSDs are randomized such that each SSD is presented with the same probability in the two epochs. In epoch 1, suppose that the cumulative distribution function of the GO process finish times are given by some function $F(t)$ with an expected value of \bar{T} , and that the finish time distribution in epoch 2 is the same but slowed by a constant amount, t_{slow} . Thus, in epoch 2 the cumulative distribution function of GO finish times is given by $F(t - t_{slow})$ with an expected value of $\bar{T} + t_{slow}$.

Let RT_{NC1i} and RT_{NC2i} denote the i th RT on a no-signal trial following a noncancelled trial in the first and second epochs, respectively, and likewise let RT_{C1i} and RT_{C2i} denote the i th RT on a no-signal trial following a cancelled trial in the first and second epochs, respectively. Let the mean RT on no-signal trials following noncancelled and cancelled trials be given by \bar{T}_{NC} and \bar{T}_C , respectively. Then,

$$\bar{T}_{NC} = \frac{1}{N_{1NC} + N_{2NC}} * \left(\sum_i^{N_{1NC}} RT_{NC1i} + \sum_i^{N_{2NC}} RT_{NC2i} \right) \quad (1)$$

$$\bar{T}_C = \frac{1}{N_{1C} + N_{2C}} * \left(\sum_i^{N_{1C}} RT_{C1i} + \sum_i^{N_{2C}} RT_{C2i} \right)$$

Where N_{1NC} and N_{2NC} are the total numbers of no-signal trials following noncancelled trials in the first and second epochs, respectively, and N_{1C} and N_{2C} are the total numbers of no-signal trials following cancelled trials in the first and second epochs, respectively. Focusing on noncancelled trials, because RT_{NC1i} and RT_{NC2i} are determined from independent identically distributed samples of the GO process's finish time distribution, this means that:

$$E(\bar{T}_{NC}) = \frac{E(N_{1NC}) * \bar{T} + E(N_{2NC}) * (\bar{T} + t_{slow})}{E(N_{1NC}) + E(N_{2NC})} \quad (2)$$

For the sake of simplicity, let SSRT be the same constant value between epochs, \bar{T}_s . Let the variable N_{tdj} denote the number of stop trials in an epoch at a given SSD value t_{dj} . By the logic of the race model,

$$E(N_{1NC}) = \sum_j F(\bar{T}_s + t_{dj}) * E(N_{tdj}) \quad (3)$$

$$E(N_{2NC}) = \sum_j F(\bar{T}_s + t_{dj} - t_{slow}) * E(N_{tdj})$$

Note that when a staircase procedure is not used and the SSD is randomized as we consider here, the expectation of N_{tdj} is the same for both epochs. Similarly, for cancelled trials:

$$E(N_{1C}) = \sum_j [1 - F(\bar{T}_s + t_{dj})] * E(N_{tdj}) \quad (4)$$

$$E(N_{2C}) = \sum_j [1 - F(\bar{T}_s + t_{dj} - t_{slow})] * E(N_{tdj})$$

The function F is a monotonically increasing cumulative distribution, so for any t_{dj} :

$$F(\bar{T}_s + t_{dj} - t_{slow}) \leq F(\bar{T}_s + t_{dj}) \quad (5)$$

where the limit of equality is reached only if the value of F does not change anywhere in the range from $\bar{T}_s + t_{dj} - t_{slow}$ to $\bar{T}_s + t_{dj}$. Thus:

$$E(N_{1NC}) \geq E(N_{2NC}) \quad (6) \quad \text{and} \quad E(n_{1C}) \leq E(n_{2C}) \quad (7)$$

Equation 2 can be rewritten as:

$$E(\bar{T}_{NC}) = (1 - w_{2NC}) * \bar{T} + w_{2NC} * (\bar{T} + t_{slow}) = \bar{T} + w_{2NC} * t_{slow} \quad (8)$$

$$\text{where } w_{2NC} = \frac{E(N_{2NC})}{E(N_{1NC}) + E(N_{2NC})}$$

$$\text{Similarly, it can be shown that:} \quad E(\bar{T}_C) = \bar{T} + w_{2C} * t_{slow} \quad (9)$$

$$\text{where } w_{2C} = \frac{E(N_{2C})}{E(N_{1C}) + E(N_{2C})}$$

Using equations 6 and 7, we see that $w_{2C} \geq 0.5 \geq w_{2NC}$ and thus

$$E(\bar{T}_C) \geq E(\bar{T}_{NC}) \quad (10)$$

even though there is no direct effect of any cancelled or noncancelled trial slowing the response on the following trial.

APPENDIX C

Spectral Methods

Here we provide background to the spectral analyses we used to test whether our RT data display power spectra that deviate from the flat spectrum associated with an independent time series.

For a given discretely sampled time series $x[t]$ with a constant interval between samples, a direct estimate of its power spectrum can be obtained through the conventional periodogram. As shown below, the periodogram reflects a normalized square of a correlation of the time series with sinusoidal signals at a given frequency across all time points in the sample.

$$P_x[f] = \frac{1}{N_o} \left| \sum_{t=1}^{N_o} x[t] e^{-2\pi i f t} \right|^2$$

or equivalently

$$P_x[f] = \frac{1}{N_o} \left[\left(\sum_{t=1}^{N_o} x[t] \cos(2\pi f t) \right)^2 + \left(\sum_{t=1}^{N_o} x[t] \sin(2\pi f t) \right)^2 \right]$$

where N_o refers to the number of time points in the sample.

Such computations are often performed on signals that are digital samples over time of some underlying temporally continuous value. Examples from electrophysiology research include a local field potential or an electroencephalogram channel. Here we consider RT spectra analyses that are analogous to these signals, but with differences in the underlying implications. The unit of ‘time’ in these analyses is an ultimately discrete unit of trial numbers rather than a precise unit of time like seconds or ms. We thus consider frequency in units of inverse trial numbers rather than Hertz. However, in this analysis the concept of frequency may be more easily conceptualized by considering the corresponding period of a given frequency, which has units of trials. For the dependent variable of the time series, instead of volts (or indeed microvolts) we measure RT in units of ms and measure power in units of ms^2 . The maximum possible sampling rate is fixed at 1

sample per trial, which results in a Nyquist frequency limit of 0.5 inverse trials that we can meaningfully consider.

The spectral analysis associated with the stopping and stepping tasks we consider in this paper come with an additional caveat. We are interested in the spectrum of the GO process, which can be directly measured from the RTs of no-signal trials only (Logan & Cowan, 1984). This means that we can only include these trials' RTs in our spectral analysis which results in a missing datum for every stop or step trial. Importantly, it would be incorrect to ignore these missing data and analyze the sequence of no-signal trials only using techniques that assume regularly spaced data samples. Instead to accurately measure the RT power spectra, we must take into account the specific trial position of every no-signal RT. To do so we used techniques described in Lomb (1976) and Scargle (1982) for the spectral analysis of irregularly spaced data which we briefly review below.

Scargle (1982) presents the use of a modified periodogram:

$$P(f) = \frac{1}{2} \left\{ \frac{[\sum_j X(t_j) * \cos(2\pi f(t_j - \tau))]^2}{\sum_j \cos^2(2\pi f(t_j - \tau))} + \frac{[\sum_j X(t_j) * \sin(2\pi f(t_j - \tau))]^2}{\sum_j \sin^2(2\pi f(t_j - \tau))} \right\}$$

where τ is defined as:

$$\tau = \frac{1}{2 * 2\pi f} \tan^{-1} \left[\frac{\sum_j \sin(2 * 2\pi f t_j)}{\sum_j \cos(2 * 2\pi f t_j)} \right]$$

Using the details described in Lomb (1976), Scargle (1982) demonstrates that this is the equivalent of a least-squares fit of sine waves to irregularly spaced data. Indeed regularly spaced data can be seen as a special case of this more-general measure, as Scargle shows that in this case these expressions reduce to the conventional expressions for periodograms. The effect of the parameter τ is to maintain the invariance of the estimate to a time-shift in the input time series, as well as to preserve the accurate relative phases between different frequencies. For the special case of

regularly spaced data, τ will equal zero. As Scargle shows, the other modifications of the periodogram serve to produce resulting estimates of spectral power that have the same statistical properties as the conventional periodogram with regularly spaced data. Based on this, we use statistical techniques that are described in Jarvis & Mitra (2001), and developed in Percival & Walden(1993). Specifically, a 95% confidence interval for the population spectral power at a given frequency, $P_{pop}(f)$, given the estimated spectral power, $P(f)$, is given by:

$$\frac{v_o P(f)}{q_2} \leq P_{pop}(f) \leq \frac{v_o P(f)}{q_1}$$

q_1 and q_2 , respectively, refer to the 2.5th and 97.5th percentiles of the chi-square distribution with degrees of freedom of v_o . In our case the degrees of freedom are equal to twice the number of sessions averaged across. Before averaging across sessions, we also averaged spectral estimates in adjacent frequency bins within each session, but we did not add these estimates to our total degrees of freedom since some of these adjacent estimates would not be totally independent.

Section III: Investigations of the acquisition of extracellular recordings in awake behaving animals: Understanding how the recorded voltage relates to neural activity

Chapter 6

Review of signal distortion through metal
microelectrode recording circuits and filters

BACKGROUND

Various metal microelectrodes have been designed to isolate spikes (Green, 1958; Hubel, 1957; Levick and Cleland, 1974; Merrill and Ainsworth, 1972; Wolbarsht et al., 1960; reviewed by Lemon, 1984), and different metals and insulations are in use today. An equivalent circuit model of a metal microelectrode in tissue has been proposed that has important theoretical implications about frequency-dependent amplitude attenuation (Lemon, 1984; Robinson, 1968) and phase shifts (Geddes, 1972) of recorded signals. Such consideration in past neurophysiological literature has been primarily given only to the recording of spiking activity. Filtering applied during data acquisition or offline further distorts recorded signals (Oppenheim and Schaefer, 1998). If not prevented or accounted for, such distortions can introduce uncertainty into analyses of LFPs or spike shapes. Many recent studies have described LFP phase (Bragin et al., 1995; Haslinger et al., 2006; Lee et al., 2005; Lin et al., 2006; Murthy and Fetz, 1996; O'Keefe and Recce, 1993; Skaggs et al., 1996), spike-field phase relationships (Haslinger et al., 2006; Lee et al., 2005; Lin et al., 2006; Murthy and Fetz, 1996; O'Keefe and Recce, 1993; Skaggs et al., 1996), event-triggered potentials (Krieman et al., 2006; Fries et al., 2001a,b) and LFP power or coherence comparisons across frequencies (Fries et al. 2001a,b; Liu and Newsome, 2006; Rickert et al., 2005; Womelsdorf et al., 2006). However, phase distortion caused by the recording system is rarely considered (but see O'Keefe and Recce, 1993) and electrode-induced effects have been overlooked. Therefore, we performed systematic measurements to verify that the equivalent circuit model applies to commercial electrodes (FHC) and a data acquisition system (Plexon) in common use by neurophysiologists, and to demonstrate the signal distortions that can occur.

MATERIALS AND METHODS

Equivalent circuit model

Figure 6.1 illustrates a modified version of a commonly cited equivalent circuit model of a metal microelectrode recording in the brain (Robinson, 1968). The effective electrode impedance (Z_e') is the sum of impedances due to the resistance of the electrolyte (R_s), the resistance of the electrode metal (R_m) and, most importantly, the resistance and capacitance at the double layer that forms at the electrode/electrolyte interface at the uninsulated electrode tip (R_e and C_e). The effective amplifier input impedance (Z_a') is the total impedance to ground past the electrode; this includes a path through the first amplifier, or head stage (Z_a), and shunting routes to ground outside the amplifier (R_{sh} and C_{sh}) which are typically capacitive. This shunt capacitance arises mainly from the capacitance across the insulation between the electrode shaft and the surrounding electrolyte as well as the cumulative capacitance along cables and connectors between the electrode and head stage amplifier (Robinson, 1968). These routes to ground parallel to the amplifier reduce the effective amplifier impedance, and being capacitive, this effect increases with signal frequency.

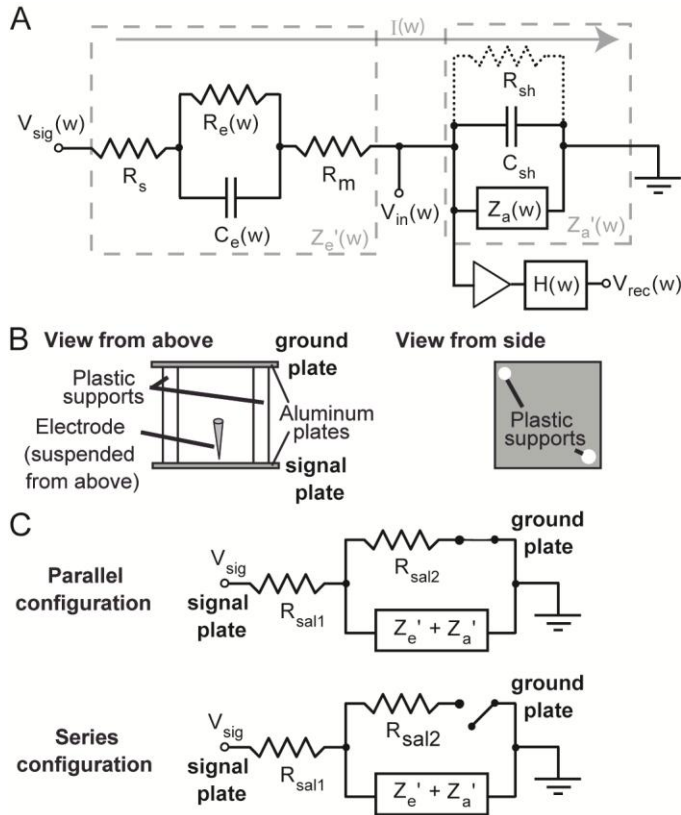


Figure 6.1

Signals at the tip of the electrode (V_{sig}) generate currents (I) that flow to ground through the series combination of the effective electrode impedance and the effective amplifier input impedance:

$$I(\omega) = \frac{V_{sig}(\omega)}{Z_a'(\omega) + Z_e'(\omega)} \quad (1)$$

The voltage at the input of the amplifier (V_{in}) is given by

$$V_{in}(\omega) = V_{sig}(\omega) - I(\omega) \cdot Z_e'(\omega) = \frac{V_{sig}(\omega) \cdot Z_a'(\omega)}{Z_a'(\omega) + Z_e'(\omega)}$$

(2)

Equation 2 shows that Z_a' and Z_e' form a voltage divider so that when Z_a' is not substantially larger than Z_e' , V_{in} will be less than V_{sig} . This signal attenuation will be accompanied by a phase shift between V_{sig} and V_{in} because Z_a' and Z_e' are complex values with phases and magnitudes. When multiplying and dividing complex numbers, phases are, respectively, added and subtracted independently of the numbers' magnitudes, while the phase of a complex sum is the phase of the separately summed real and imaginary fractions weighted by the magnitudes of each number, so that larger numbers contribute more to the phase of the resulting sum. Therefore the phase difference between V_{sig} and V_{in} equals the phase of the effective input impedance Z_a' minus the phase of the combined impedance $Z_a' + Z_e'$. When Z_a' is much larger than Z_e' the phase of the combined impedance is dominated by the phase of Z_a' , so the resulting phase shift will be negligible. When this is not the case, potentially noticeable phase shifts will occur and will increase in size as both the relative magnitude of Z_e' to Z_a' increases and the overall phase difference between Z_e' and Z_a' increases. The direction of the phase shift will depend on whether Z_e' is more or less capacitive than Z_a' , resulting in positive or negative going phase shifts, respectively. For example, if Z_e' were purely capacitive (phase = -90) and Z_a' were purely resistive (phase = 0), then when the magnitudes of Z_a' and Z_e' are approximately equal, the phase of V_{in} relative to V_{sig} would be about 45 degrees, indicating that V_{in} would lead V_{sig} by this amount. This phase shift would increase towards an asymptote of 90 degrees as Z_e' becomes larger than Z_a' . Note that because Z_a' and Z_e' are functions of frequency, the magnitude and phase relationship between V_{sig} and V_{in} will be frequency dependent.

It is worth noting that only the first amplifier's input impedance is critical for the measurement, as this is the only amplifier that interacts with the electrode and affects the possibly considerable voltage drop that may occur across it. At this stage, the initial amplifier sets its voltage using its electrical power source based on its gain and the signal input to it, with the limitation that it cannot set a voltage larger than the voltage of its power source. That signal is then sent to following amplifiers and/or recording equipment, and at each stage an additional possible voltage divider is created involving the output impedance of the preceding stage and the input impedance of the following stage. However, no further signal distortion typically occurs at these stages as the input impedance of these stages can usually easily be set well above the output impedance of the preceding stage.

Filtering effects

Physiological data acquisition systems include filters that will affect signals in a manner described by the transfer function of the system ($H(\omega)$) such that:

$$V_{\text{rec}}(\omega) = H(\omega) \cdot V_{\text{in}}(\omega) = H(\omega) \cdot \frac{V_{\text{sig}}(\omega) \cdot Z_a'(\omega)}{Z_a'(\omega) + Z_e'(\omega)} \quad (3)$$

Any filter, analog or digital, that could be applied in real time during data acquisition would necessarily introduce some frequency-dependent phase shifts that become large near the filter's pass-band edges. However, once data acquisition has stopped it becomes possible to re-apply the same filter to time reversed data which imposes exactly the same phase shifts introduced during acquisition but in the opposite direction, thus correcting the phase shifts applied during acquisition. This forms the basis for phase-shift free filters that may be applied in post-acquisition processing (Mitra 2001).

Data collection procedures

Signals were recorded using a MAP system (Plexon Inc., Dallas, TX) in which signals were passed through a first and second amplifier, which we refer to as a head stage and a preamplifier, respectively, following the convention of the company that constructed it. After the amplifiers, signals are passed to a multichannel acquisition processor (MAP) for A to D conversion and recording. At the stage of the preamplifier, each input channel is separated into two output channels that undergo different analog filtering, with one channel designed to record higher frequency spikes and one designed to record lower frequency field potentials, which we refer to as the spike and LFP channels, respectively. In this article, when the outputs from both channels are not overlaid, values shown in plots at and below 175 Hz were obtained from the LFP channel data, and values at and above that were obtained from spike channel data as indicated on the plots. Taken together, the two outputs enabled us to perform measurements across the entire frequency range of interest, and for those frequencies that could be measured through either channel (~ 80 Hz to 300 Hz), the results from each channel were the same.

Most of the data presented in this study was recorded with a HST/8 o50-G20 (Rev 3.0) head stage (Plexon Inc., Dallas, TX) with a gain of 20, which we refer to as the low-input impedance head stage (38 M Ω input resistance with 3 pF of parallel capacitance and 10 pF of series capacitance acting on the input before amplification). This was used with a following preamplifier with a gain of 50 (Plexon Inc., Dallas, TX). The preamplifier was configured as a PBX2/16sp/16fp preamplifier with two cascaded 1-pole low-cut Butterworth filters and a 4-pole high-cut Butterworth filter for each of 16 spike channels (100 Hz – 8 kHz) and 16 field potential channels (0.7 Hz – 170 Hz). Additional filtering by the MAP system's SIG board causes the effective low-cut frequency of the recorded spike channels to be ~ 250 Hz. Unless otherwise specified, all data presented in this study was recorded with this equipment.

Different head-stages and preamps were used in some recordings to determine the effects of different equipment. We tested a second head stage (Plexon Inc., Dallas, TX) with a gain of 1, HST/8o50-G1-GR, which we refer to as the high input impedance head-stage ($> 1 \text{ G}\Omega$ input resistance with $\sim 2 \text{ pF}$ of parallel input capacitance and no series capacitance). This was primarily used with a PBX2/16 sp/16 fp preamplifier (Plexon Inc., Dallas, TX) with a gain of 1000 but with the same LFP and spike channel filters as the primary preamplifier mentioned above. We also obtained the phase response of the LFP channel of a second preamplifier for signals up to 300 Hz passed directly to the high input impedance head stage across no resistance. This preamplifier was configured as a PBX/16sp-r-G50/16fp-G50 preamplifier (Plexon Inc., Dallas, TX) with 16 spike channels (spike data not shown) and 16 field potential channels (1-pole Butterworth filters, cutoffs of 3.3 – 88 Hz). Because this configuration resulted in an overall gain of 50 between the head-stage and preamp instead of an overall gain of 1000 that occurred with all other recordings, larger voltage signals were tested with this combination of equipment to compensate, though all other equipment and procedures were kept the same. The resulting data from this test is shown in the grey line in Figure 6.7.

The MAP unit can also record additional analog signals via BNC inputs on a separate card (National Instruments, TX). This was used to record the actual non-attenuated voltage signal as well as the spike channel data as a continuous signal using the OUT board of the MAP unit. The LFP channel was automatically recorded by this same equipment, and thus all three signals for analysis in this study (actual signal, spike channel, and LFP channel) were time-stamped and recorded simultaneously by the same equipment. The sampling rate used for all recordings was 20 kHz. Channel 1 was used for all recordings, and the inputs to unused channels were grounded.

Most voltage signals used in this study were generated by clipping onto the audio output pin of a computer playing Matlab-generated .wav files. This allowed us to present arbitrary signals to the system and to reproduce with ease precisely the same signal at many frequencies

across different conditions. Distortions introduced by the audio card of the computer qualitatively seemed small for most signals, and were unimportant to the conclusions of the study as we were able to record the actual output signal in all cases. In order to generate signals of the appropriate amplitudes for use with the neural recording equipment, signals were first attenuated by a factor of about 100 by being passed through a voltage divider constructed by connecting a 100 Ω and 1 Ω resistor in series, with the exception of the few tests that were performed with the secondary preamplifier using larger and unattenuated voltages. Some later tests were performed using sinusoidal signals created by a function generator (33220A function/arbitrary waveform generator, Agilent Technologies, Santa Clara, CA). Output signals from this were still initially routed through the same voltage divider.

To verify amplifier input impedance, the attenuated signal was passed directly to the head-stage connector or passed across resistors with impedances varying from 11.5 to 88 M Ω for the low-input impedance head stage. For the high-input impedance head stage, low-frequency signals were passed across very high metallic resistances ranging from .5 to 2.5 G Ω , while moderate-to-higher-frequency signals were passed across moderate resistances ranging from 1.2 to 66.0 M Ω . See the impedance calculations subsection in this methods section for a description of how the amplifier input impedance was assessed using this data.

For the electrode data, an apparatus was constructed consisting of two square 7 x 7 inch aluminum plates connected together by two plastic supporting rods causing a plate separation of 7 inches. A coarse schematic of the apparatus can be seen in Figure 6.1B. The plates were connected with their broad sides facing each other and they stood on their thin edge in a large plastic tub filled with either dilute saline with a concentration of 0.225% by weight or physiological saline with a concentration of 0.9% by weight. By passing current between the plates, a one-dimensional voltage gradient was created in the dimension normal to the plates' broad sides. Voltage changed with the horizontal position between the two plates but was

approximately uniform in the two directions orthogonal to this: the vertical direction and the horizontal direction parallel to the plates. The dilute saline was initially chosen as its higher resistivity allowed for a better control of this gradient. Later recordings were made with both saline concentrations to investigate potential effects of saline concentration on the electrode tip impedance.

To provide a verification of the equivalent circuit model, data was collected under two configurations. In the *parallel configuration*, the attenuated signal was connected to one plate, which we define as the signal plate, with the other plate connected to ground, which we call the ground plate. In this case, when the electrode tip is immersed in the saline it provides a high impedance route to ground from the signal plate that is parallel to a lower impedance route through the ground plate. The actual voltage gradient in the saline will primarily be unaffected by the presence or the position of the electrode. This is generally analogous to the case of neural recording. In the *series configuration*, the ground plate is disconnected from everything, so that the electrode would be the only series connection between the signal plate and ground and thus all current in the signal passing through the aluminum plate must pass through the electrode and amplifier circuit as well. Resistance between the two plates was measured before and after each recording session and found to be around 100 to 200 Ω . At the start of a session the resistance was occasionally larger than this, in which case we sanded down both plates' surfaces which served to lower the impedance to the appropriate level, most likely by removing aluminum oxide or possibly solid sodium chloride that had formed on the plates.

The electrodes used for data collection solely in the dilute saline with the low input impedance head-stage were 5 tungsten microelectrodes, (FHC, Bowdoinham, ME) 3 insulated with glass and 2 with epoxyite, with varying impedances ranging from .5 to 9.8 M Ω at 1 kHz per the manufacturer specifications. We tested an additional epoxyite insulated electrode with a manufacturer specified impedance of 8.4 M Ω at 1 kHz using only the high-input impedance head

stage in dilute saline. The FHC catalog numbers for the 5 electrodes used with the low-input impedance head stage were: UEWLGASEBN1E, UEWLGASEFN1E, UEWLGASGBN4E, UEWLGASGDN4E, and UEWLGASGFN4E, and the catalog number for the electrode used with only the high-input impedance head stage in dilute saline was UEWLGASEFN1E. We later tested 3 additional epoxyite insulated electrodes with manufacturer specified 1 kHz impedances ranging from .5 to 10 M Ω with both head-stages and in dilute and/or physiological saline. The catalog numbers for these electrodes are: UEWLGASEBN1E, UEWLGASEDN1E and UEWLGASEFN1E. The order in which the tests were performed for both head-stages and saline concentrations was varied for each of these electrodes. Through the course of the experiment the impedance of each electrode was independently measured (see Figures 6.3C, 6.4C, and 6.6B), and the tests conducted in physiological saline matched reasonably well with the manufacturer specified values (see Figure 6.6B). The tip geometry was not varied across electrodes.

Using a surgical micromanipulator clamping onto a single-channel microdrive, (FHC, Bowdoinham, ME) electrodes were suspended from above and lowered to a vertical position 100 microns below the saline surface at a horizontal position between the two plates 3 mm away from the signal plate. The horizontal distance from the signal plate was set by using the surgical micromanipulator to very carefully touch the side of the electrode to the plate as determined by careful visual inspection, then advancing it 3 mm away from the plate. The depth of the saline surface was determined through online viewing of the signals recorded by the amplifier while adjusting the electrode depth with the microdrive to determine when electrical contact was consistently first made between the electrode and the saline. The electrode was then lowered with the microdrive 100 microns beyond that point for data collection. We compared the data recorded from each electrode to data recorded from a specially constructed steel pin reference electrode with 0.5 mms of uninsulated tip and negligible tip impedance. This reference electrode was suspended 600 microns below the saline surface, with the horizontal position and other conditions

kept the same to obtain an estimate of the actual voltage presented to each electrode, accounting for any effects of the aluminum plates and saline. Data was collected close to the signal plate so that the recorded voltages would be as large as possible while maintaining a small voltage gradient which resulted from the small output voltages used along with the large horizontal separation between the plates. The small voltage gradients were desired to help diminish the effects of variables that could not be reproduced between electrodes with exact precision, such as the orientation and horizontal position of the electrode. Recordings of sinusoidal voltages at a few frequencies were conducted after each recording session for each electrode to ensure that the electrode's impedance was not affected by the signals applied during the session. Only small apparent impedance drops were noticed on occasion.

During data collection with the electrodes and the low-impedance head stage, Z_a' was manipulated by clipping onto the connection between the electrode and the head stage and connecting that to ground through different metallic resistors with known impedances (R_{sh} in Figure 6.1A). This created an additional parallel route to ground downstream of the electrode tip and lowered Z_a' by a known amount. This was done in both the parallel and series configurations to create the additional 10 Hz Z_a' values of approximately 2, 8, and 14 M Ω , in addition to the unmanipulated value of 38 M Ω .

For the electrodes tested in both concentrations of saline, additional impedance measurements were made using a commercially available LCR meter (E4980A, Agilent Technologies, Santa Clara, CA), which is an instrument that can measure inductance (L), capacitance (C) and resistance (R). Measurements were made in the 4 terminal paired configuration with the high potential and current leads ultimately connected to the plate near the electrode, and the low potential and current leads ultimately connected to the top of the electrode. All other leads to the aluminum plates were disconnected while this measurement was made. In

addition to these tests, a corroborating impedance measurement at 1 kHz was made using a 1 kHz metal electrode impedance tester (Model Imp-1, Bak Electronics, Mount Airy, MD)

Signals used

The bulk of the data for this study was gathered using sinusoidal voltages with frequencies varying from 0.5 Hz to 9 kHz. The exact frequencies (in Hz) tested that underly the data shown in each figure are: .5, 1, 2.5, 5, 10, 15, 20, 25, 30, 40, 50, 60, 70, 80, 90, 100, 125, 150, 175, 200, 250, 300, 500, 1000, 1500, 2000, 2500, 3000, 3500, 4000, 4500, 5000, 6000, 7000, 8000 and 9000. The amplitudes of most of the un-attenuated signals were kept approximately constant with a peak amplitude of ~ 320 mV for the metallic resistor data and ~ 200 mV for the electrode data. For situations in which the resulting signals were too small to record reliably because of the combined effects of filters and resistors or electrodes, signal amplitudes were increased to improve the signal-to-noise ratio in order to better determine the recorded phases and amplitudes. Every data point analyzed however was considered only in terms of the gain relative to the applied voltage which was also recorded, so the absolute voltage of the signals was unimportant.

The amplitudes used to record electrode data thus corresponded to voltages of less than 2 mV at the electrode tip. Evoked potentials recorded in cortex with microelectrodes have been published with maxima that exceed this (Kandel and Buzsaki, 1997), although physiological values at higher frequencies resulting from action potentials typically do not reach this level. Current density is known to affect electrode impedance when the current density exceeds a certain level (Geddes et al., 1971), but our estimations suggest that with the equipment and signals we used, current densities were well below this level. Additionally, we verified at a few frequencies that electrode and amplifier impedance do not appreciably change with current amplitude for the signals and equipment we used (data not shown). This suggests that for physiological recordings

with any reasonable equipment, any distortions that occur will not depend on signal amplitude appreciably.

The amplitude and phase of the digitized recorded signals were measured in two ways, each using 50 cycles of the data. For most recordings, the *nlinfit* function in Matlab (MathWorks, v. 2007b) was used to find the best sine-wave fit given the known frequency of the sinusoid. In some cases the Hilbert transform was used instead, defining the amplitude as the average magnitude of the Hilbert transform and defining the phase as the phase of the first sample resulting from a linear fit of the complex phase of the Hilbert transform. The code used for each method is provided in the Supplementary Materials. Amplitude ratios and phase comparisons between the recorded and actual signals were always made using the same method for each signal. For more details, see the Supplementary Methods online.

For the verification of group delay with data, passband filtered pulse signals with different center frequencies were used, similar to what is shown in example 5.1 of (Oppenheim and Schaefer, 1998). A few examples of signals used are shown in Figure 6.9 (see Supplementary Materials online). The center frequencies of the filters used also varied from 0.5 to 9 kHz while the duration of the signal itself decreased with frequency to allow for more-precise temporal localization of the smaller group delays at higher frequencies. The filter and duration specifications were determined to provide the best frequency localization for each signal, given that the amplitude envelope varied sharply enough over time to determine the delay between the two envelopes at each frequency. The filtered pulses used were obtained by windowing sinusoids of the given carrier frequency with the first of the discrete prolate spheroidal sequences with a time-bandwidth product of 1 for a given duration. The maximum voltages of the filtered pulses used for each recording session approximately matched the voltage amplitude of the sinusoidal signal used for each frequency in the same session. For these signals, we used the magnitude of the Hilbert transform, which can be thought of as the instantaneous amplitude of a time series

(Marple 1999a), as an estimation of the amplitude envelope for both the recorded and actual signal. We then determined the amplitude envelope delay to be the time delay at which the cross-correlation between the actual and recorded envelope estimates was maximal. For our data this gave the exact same results to a previously published method of estimating group delay that we later found (Marple 1999b) in which the order in which the cross-correlation and Hilbert transform were applied was reversed from what we have presented here.

For the shape distortion data, we used a voltage shape obtained from a single neuron's recorded waveform, as well as a frequency-modulated version of the same waveform with signal power concentrated in the LFP frequency ranges. The original waveform had a duration of 1 ms, which was temporally modulated to have a duration of about 25 ms in the lower-frequency version. Properties of the computer's audio card did distort the lower-frequency waveform somewhat, but, again, because we were able to record the actual voltage applied this was unimportant as to our purpose of demonstrating shape distortion by the recording equipment. The insets of Figure 6.10 A and B show an estimate of the power spectral density of the actual signals sent using a Fourier Transform windowed with the first of the discrete prolate spheroidal sequences with a time-bandwidth product of 1 for the duration of the signal. Also, to demonstrate a recording of high-frequency spikes recorded simultaneously with lower-frequency field potentials, we also used the same passband filtered pulse signals that were used to verify the group delay, but with the high-frequency spike waveform added at the highest central peak of the signal. These signals were recorded using one electrode with a 1 kHz impedance verified to be 3.3 M Ω using the 1 kHz metal electrode impedance tester. For the presentation of this recorded data, the system's LFP channel output is displayed with the Spike channel added to it around the time of the spike.

The variance of all the measurements performed in this study was negligible, provided that all electrical connections were adequately made and left undisturbed between measurements and that the signal amplitudes used for measurements with electrodes were kept sufficiently low to

avoid affecting electrode impedance. To estimate the variance that occurs while changing electrical connections, we performed measurements with one low impedance electrode at 50 Hz several times while alternating connections between the low- and high-input impedance head stages and the corresponding following amplifiers between each measurement. There was somewhat more variance in the high-input impedance head stage measurements than the low-input impedance head stage. High-input impedance head stage measurements had a range of the raw gain spanning 5.3% of the maximal value, while the low-input impedance head stage measurements had a range of the raw gain spanning only .3% of the maximal value. There was no systematic trend in the value of the impedance across these measurements, suggesting the electrode impedance was not altered by them.

Impedance calculations

To determine the effective amplifier input impedance, calculations were made using the amplitude ratio (V_{rec}/V_{sig}), which we refer to as the gain, observed in the metallic resistor data across all frequencies. To remove the effects of analog filters, the gain for each recording was divided by the same signal's gain in the reference recording where the signal was applied directly to the head stage using no resistors at all. We refer to this value as the normalized gain, or here as V_{rat}' . V_{rat}' along with the magnitude of the known metallic resistance the signal was sent across, which in this case is Z_e' , can be used to calculate the effective input impedance of the head-stage as $Z_a' = (V_{rat}' \cdot Z_e') / (1 - V_{rat}')$. This is a rewritten version of equation 2 using V_{rat}' in place of V_{rec}/V_{sig} , and considering V_{rec} and V_{sig} to be the raw gain of the metallic resistor and reference recording respectively.

To determine the effective electrode impedance, this same procedure was followed with electrode recordings to obtain V_{rat}' , using the gain of the steel pin recordings as the reference recording to remove any effects caused by the saline or aluminum plates in addition to removing

effects caused by the analog filtering. This along with the known magnitude of Z_a' was used to calculate the effective electrode impedance at each frequency as $Z_e' = Z_a' \cdot (1/V_{rat}' - 1)$, which is again a rewritten version of equation 2 and the equation above.

We report the value calculated for all the individual Z_a' values tested for one electrode, (Figure 6.3) in addition to the averages for the parallel and series configurations across the 4 tested values of Z_a' for several electrodes (Figure 6.4). In reporting averages of electrode impedance measurements in each configuration, a few outlying recordings were discounted for some electrodes.

Phase calculations

The measured phase shift for each recording was defined as the phase of the recorded signal minus the phase of the actual signal, so that a positive phase referred to the recorded signal leading the actual signal. The phases were plotted using the unwrap function in matlab to provide a seemingly continuous phase response across frequencies. Since the precise value of the phase is ambiguous since a phase curve is equivalent to the same curve shifted by any multiple of 360 degrees, 0 degrees was defined so that the phases for the most frequencies within the passband of each channel's filters were closest to 0 degrees. For the presentation of electrode-amplifier circuit induced phase shifts in Figure 6.5 and 6.6, the filter-induced reference phase shown in black in Figure 6.7 was subtracted from the raw recorded phase shift with each electrode to remove the common filter-induced phase effects and leave only the phase shifts resulting from the electrode-amplifier circuit. The filter-induced reference phase was obtained from the recorded phase shifts of signals sent directly into the head stage and was comprised of data collected from both the low- and high-input impedance head stages as both were used with following preamplifiers with identical specified filter properties. The data above 10 Hz were recorded using the low impedance head stage, and the data at and below 10 Hz were recorded with the high impedance head stage

which has no series capacitance acting before amplification that introduces additional phase shifts in this frequency band. For the electrode data collected with the high-input impedance head stage, the high-input impedance reference phase data was subtracted over the entire frequency range recorded to produce the orange curves in Figure 6.5.

To calculate group delay, the derivative of the phase with respect to frequency is approximated using the change in phase and frequency between each pair of consecutive frequency points explicitly measured. Group delay was then calculated according to the equation below:

$$\text{Group Delay}\left(\frac{f_1 + f_2}{2}\right) = -\left[\frac{\Delta Ph}{360}\right] / \Delta f \quad (4)$$

ΔPh is the difference in phase between adjacent frequencies measured in units of degrees, Δf is the difference in frequency in units of Hz, f_1 and f_2 are the frequencies of the consecutive measurements used in the calculation, and group delay is given in units of seconds. The group delay measurement using each pair of consecutive frequencies is defined as pertaining to the group delay observed at the mean of the two frequencies.

RESULTS

Determination of amplifier input impedance

To verify that the equivalent circuit model applies to microelectrode recordings, we measured the input impedance for two head stages, one with lower- and one with higher- input

impedance. To do this we measured V_{rec} with V_{sig} consisting of sine wave voltages (0.5 to 9 kHz) applied to the head stage across different metallic resistances. Figure 6.2 plots measurements made with the lower-input impedance head stage through a range of metallic resistors. The variation of gain ($V_{\text{rec}}/V_{\text{sig}}$) through the LFP and spike channels as a function of frequency and resistance is clear (Figure 6.2A). By normalizing the gain for each resistor by the gain for signals applied directly to the head stage, the filter properties of the system were removed (Figure 6.2B). The normalized gain allows us to calculate the effective input impedance of the head stage for each resistor (Figure 6.2C). The input impedance we measured corresponds to the specifications of this head stage. The parallel input capacitance of the head stage causes the input impedance to decrease at high frequencies; the series capacitance causes it to rise at very low frequencies. The impedance measurements are largely independent of the resistive load and match well with the specified values, except at high frequencies where our measurements are consistently low, suggesting an added voltage drop across these resistors. However, this is expected given the presence of the capacitance shunting the amplifier, C_{sh} . These deviations from the specified input impedance at high frequency permit an estimation of C_{sh} which measured ~ 2.7 pF in our recording setup. It is important to note that this value can change for the same equipment according to its physical arrangement.

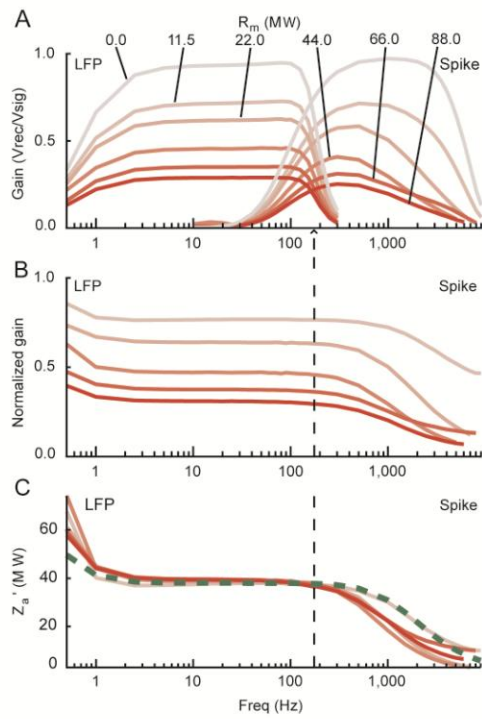


Figure 6.2

We also tested a head stage with a higher-input impedance which we empirically verified in a similar fashion. Due to the very high input resistance, the effective input impedance for this

head stage was largely determined by the capacitance within and outside the amplifier for most frequencies. For low frequencies, we verified there was little voltage drop over very high metallic resistances, while for moderate to higher frequencies we verified that there was little voltage drop over moderate resistances.

Equivalent circuit verification and signal attenuation

After determining the input impedance of the amplifier (Z_a'), we determined whether the equivalent circuit describes signals recorded through metal microelectrodes immersed in dilute saline, using the apparatus depicted in Figure 6.1B. This was done in a *parallel configuration* and a *series configuration* (Figure 6.1C, see Methods). If the equivalent circuit model is correct, then measurements of electrode impedance should be independent of both the configuration and the value of Z_a' .

Figure 6.3 plots measurements made with the lower-input impedance head-stage through a representative high-impedance, glass-insulated electrode. Systematic variation of raw (Figure 6.3A) and normalized (Figure 6.3B) gain (V_{rec}/V_{sig}) through the LFP and spike channels was observed as a function of frequency and Z_a' with slightly higher gain in the series than in the parallel configuration. This is to be expected because more total current travels through the saline in the parallel configuration, resulting in a larger voltage drop from the signal plate to the electrode tip. The normalized gain at the various values of Z_a' afforded calculation of the effective electrode impedance as a function of frequency (Figure 6.3C). Electrode impedance measured across signal frequencies did not vary with Z_a' for either parallel or series configurations. This constancy was found for all electrodes tested. Thus, the equivalent circuit was verified.

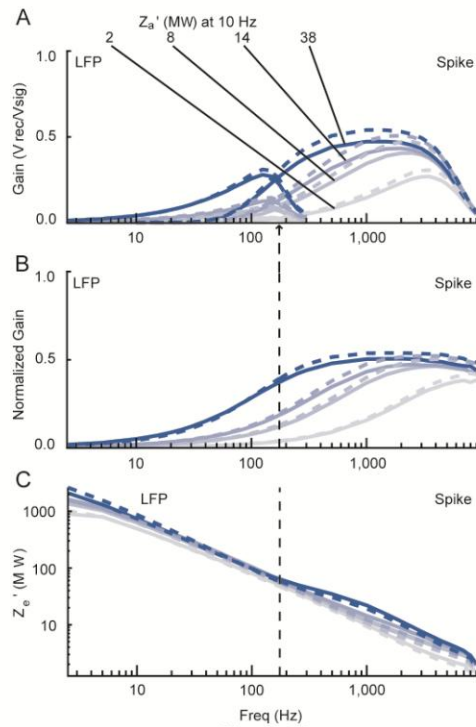


Figure 6.3

The same pattern of results was obtained for electrodes spanning impedance values from .5 to 9.8 MΩ (manufacturer specified at 1 kHz) (Figure 6.4). Beyond extending the verification of the equivalent circuit, it is also clear that electrode impedance increased substantially with

decreasing frequency, and was 10 to 45 times higher at 10 Hz than 1 KHz, consistent with previous reports (Merrill and Ainsworth, 1972; Lemon, 1984). Note that the rise in electrode impedance at low frequencies is not just a result of a constant capacitance across frequencies since R_e and C_e are generally considered to be frequency dependent themselves (Robinson, 1968; Ferris 1974), which is supported by our calculations of R_e and C_e (Figure S1, see Supplementary Results online) that rely on the recorded amplitudes and phase shifts with each electrode and our estimation of Z_a' . As a consequence of the frequency dependence of the electrode impedance, the effective amplifier gain was much less at the lower frequencies. We have also confirmed this in the brain with simultaneous recordings of electrodes with different impedances in the same approximate brain location (Nelson et al., 2006). Tungsten microelectrodes commonly used for isolating single spikes are typically 2 to 3 M Ω at 1 KHz. Thus, considerable attenuation of LFP frequency signals can occur when such electrodes are used with this lower impedance head stage.

The orange lines in Figure 6.4 show results using the higher impedance head-stage with one high-impedance electrode, with a manufacturer specified impedance of 8.4 M Ω . We can see that no considerable attenuation occurs with this electrode, as the normalized gain (Figure 6.4B) is close to one over the entire frequency range tested.

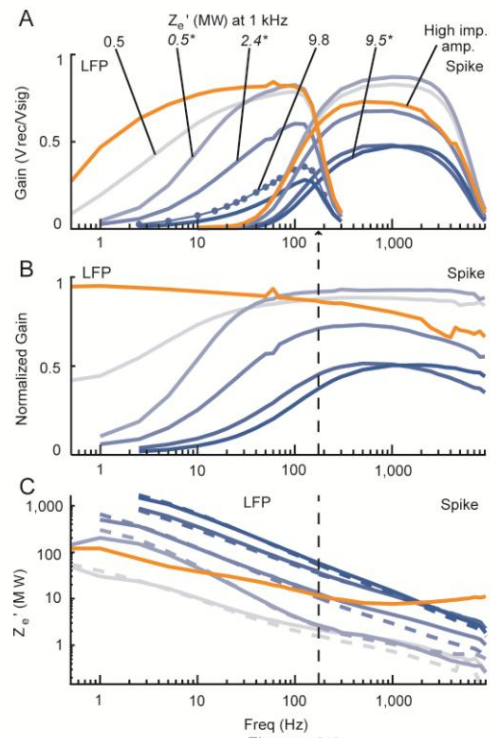
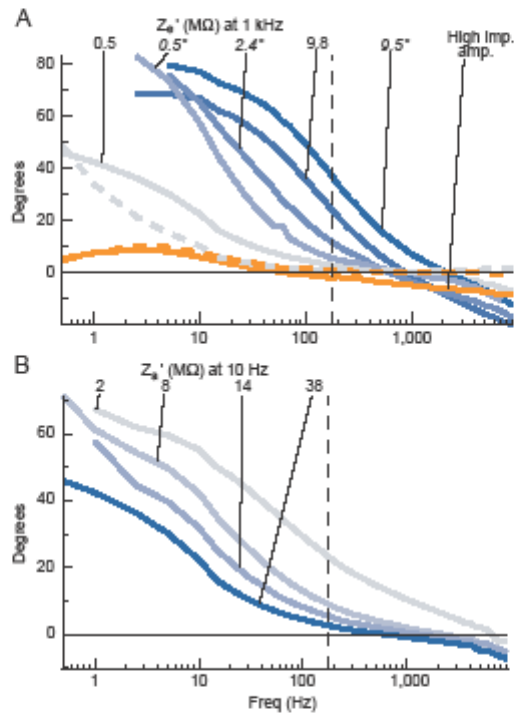


Figure 6.4

Electrode-amplifier circuit induced phase shifts

Besides amplitude attenuation, the equivalent circuit of microelectrode recordings shows that signals will also be distorted through frequency-dependent phase shifts. We measured the phase of V_{in} relative to the phase of V_{sig} as a function of frequency for signals sent across electrodes of different impedances by subtracting the phase-shifts induced by the acquisition system's filters alone from the phase shifts of the same sinusoidal signals recorded with electrodes (Figure 6.5A). Marked phase shifts occurred when using the lower impedance head stage for signals below 100 Hz where electrode impedance was higher, and were greater overall for higher impedance electrodes. These phase shifts are positive in direction at lower frequencies and exceed 80 degrees in our data, which in conjunction with the estimated electrode impedance magnitudes suggest that the phase angle of the electrode impedances are nearly a full -90 degrees over these frequencies for some electrodes (Figure S1). At higher frequencies the phase shifts shown in Figure 6.5 reverse in direction, becoming slightly negative, suggesting that Z_a' is more capacitive than Z_e' at these frequencies because of the shunt and parallel amplifier input capacitance. The phase shifts recorded with the steel pin reference electrode shown by the dashed grey line for this head stage are sizeable below 10 Hz, primarily resulting from the series capacitance within the head stage acting on the input before amplification. This would thus partly contribute to the phase shifts recorded with other electrodes at those frequencies, though for most electrodes these phase shifts would be large even without this contribution. The phase shifts also increase in magnitude as Z_a' decreases (Figure 6.6B) as described above, following the predictions of the equivalent circuit.



Nelson, et al.
Figure 5

The orange lines in Figure 6.5A again shows results using the higher impedance head stage with one high-impedance electrode, demonstrating that like the attenuation, no electrode-amplifier circuit induced phase shifts occur with this head stage.

Saline concentration effects

After recording data in dilute saline, we were interested in determining if the effects we have shown are qualitatively or quantitatively different in physiological (0.9 % by weight) saline. From a careful inspection of Figures 6.3 and 6.4, it is apparent that though our measurements are consistent with each other, they are noticeably higher than the manufacturer specified impedance values. To reconcile this, we made independent impedance measurements using a commercially available LCR meter and a 1 kHz metal electrode impedance tester (see Methods) for several electrodes in both saline concentrations. This was done in addition to performing the same sinusoidal recordings with both head-stages as we had done before, but without the additional manipulations of the value of Z_a' .

The results are shown in Figure 6.6. The resulting normalized gains (Figure 6.6A) show that there was less voltage attenuation in the physiological saline for both head-stages, though considerable low-frequency voltage drops still occurred with the low impedance head stage for all tests performed. Interestingly, at high frequencies some attenuation does consistently occur for the high-input impedance head stage, and the gains are similar to what is observed with the low-input impedance head stage for the same electrodes and saline conditions. This suggests that effects from shunt capacitance (C_{sh}) in this recording setup dominate the value of Z_a' over this frequency range and demonstrates that even when using a high input impedance head-stage, investigators may want to take care to minimize this capacitance to avoid minor to moderate spiking signal loss and shape distortion. The electrode-amplifier circuit induced phase shifts for the same conditions are shown in Figure 6.6C. This again shows that the phase shifts co-occur with amplitude attenuation which can both be quite large at low frequencies with the low impedance head stage in either saline concentration. This also shows high frequency phase shifts that are largely independent of the head stage, as was found with the high frequency amplitude effects.

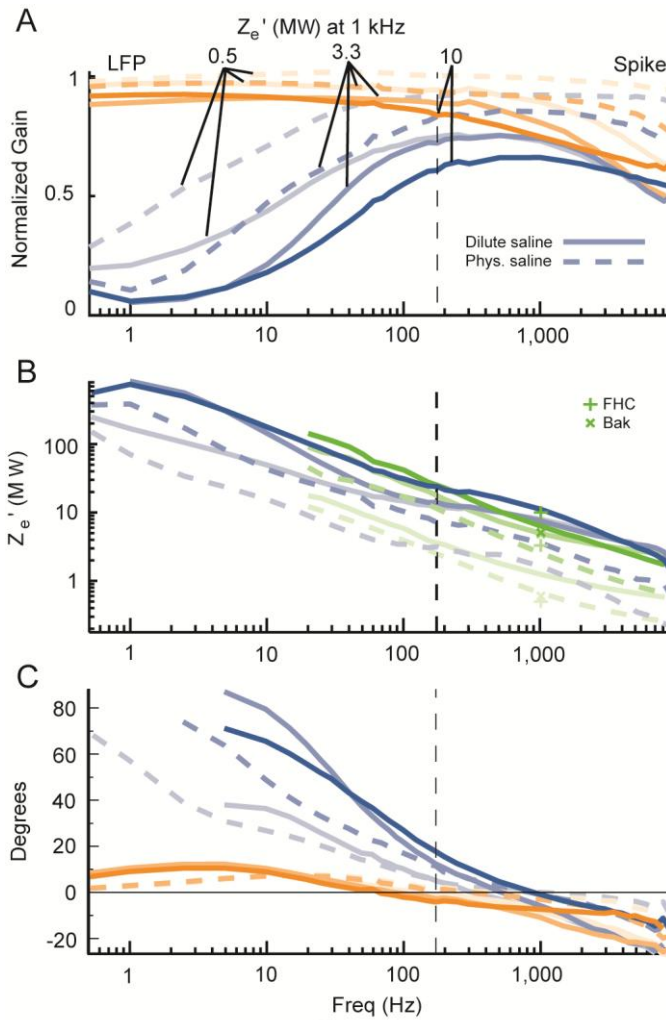


Figure 6.6

Figure 6.6B shows the resulting electrode impedances predicted by the model based on the low impedance amplifier data in addition to other corroborating measurements. As before, we see that the impedance values resulting from the normalized gains in dilute saline are consistently larger than the value specified by the manufacturer. However, when performed in physiological saline, we see that there is a decrease in impedance measurements that is roughly twofold across all frequencies. This occurred in both the sinusoidal recordings and the measurements of the Agilent LCR meter. The resulting impedance measurements in physiological saline values match well with the manufacturer specified impedances, suggesting the saline concentration was the

primary cause of the mismatch between the manufacturer specified impedance values and our earlier recordings.

It is important to note that this change in impedance across different saline concentrations is not a result of the changed resistance through the solution itself, but instead reflects an effect on the impedance across the electrode/electrolyte interface at the electrode tip. First, the data in each case is compared to the steel pin reference electrode data recorded under the same conditions to account for changes in the actual voltage at the tip between conditions. The change in saline concentration would however affect the value of R_s resulting from the resistance encountered to reach the small electrode tip. This has been estimated before to be largely negligible in physiological saline compared to the impedance across the electrode tip (Robinson, 1968). The dilute saline would be expected to have a fourfold increase in resistivity compared to physiological saline (Grimnes and Martinsen, 2000), but the value of R_s would still remain largely negligible. Finally, the value of R_s would not change with frequency. Since the absolute impedance differences between saline concentrations are clearly frequency dependent, it further suggests that this results from a change in the impedance across the electrode tip (R_e and C_e).

Filter-induced phase shifts

Filters used in the data acquisition system ($H(\square)$) can cause substantial phase shifts between V_{in} and V_{rec} that would add to the phase shifts induced by the electrode-amplifier circuit. To isolate this, we measured directly the phase of V_{rec} relative to the phase of V_{sig} as a function of frequency for signals sent directly to the head stage ($V_{in} = V_{sig}$), shown in black (Figure 6.7) for the filters used in the rest of this study with both head stages. These phase shifts become large near the edges of the filters' passbands, although the raw phase shift within the passbands of these filters is considerable as well.

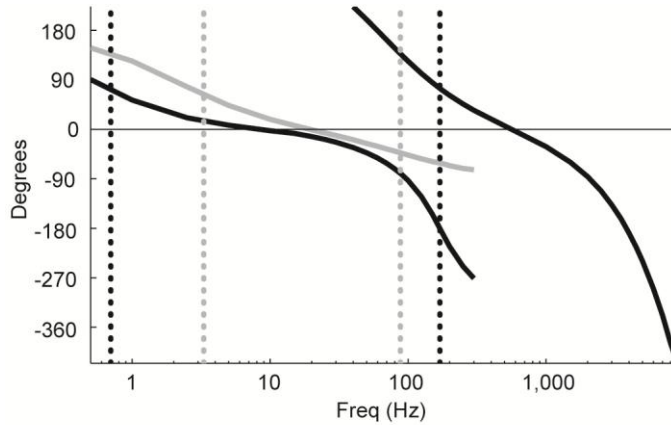


Figure 6.7

Figure 6.7 shows another characteristic of filter-induced phase shifts. Over the narrow frequency range where a given signal can be recorded simultaneously through both the spike and the LFP channels, the outputs of the two channels are out of phase with each other. While expected, this result clearly demonstrates that different phase shifts arise from the different filter properties of the two channels. To further illustrate this, we used a second LFP preamplifier with different filter properties to record signals up to 300 Hz, with results shown in grey on Figure 6.7. Even in the region where the passbands of the two LFP amplifiers overlap, considerable differences in the phase response occurs, with each LFP preamplifier inducing characteristic shifts from the phase of the input signal. We have also found that phase shifts near the filter passband edges can vary from channel to channel for a given preamplifier (Figure S2). Thus, equipment-specific filtering properties must be accounted for to report accurately the phase of LFP data, especially at frequencies near the passband edges of analog filters.

Group delay

The phase shift at a given frequency can be translated into a time delay for a pure sinusoid at that frequency. If the phase shift were constant across frequencies, this would correspond to a progressively decreasing time shift as the frequency increases. On the other hand, if the phase shifts of a system were the result of a pure time delay of the signal, then the phase response would

be a linear function of frequency, with the magnitude of the slope reflecting the magnitude of the delay. The negative derivative of the phase with respect to frequency, called the *group delay*, is a useful measure of delay even when the phase response is nonlinear. For a narrow bandwidth around a given frequency where the variation of phase with frequency is approximately linear, the group delay measures the delay of the amplitude envelope for all components of signals within this narrowband “group” of sinusoids (Oppenheim and Schaefer 1998; Smith 2006). Note that at any particular frequency, the group delay need not equal the time shift calculated directly from the phase shift (i.e., the phase shift in fractions of a cycle divided by the frequency), which is called the *phase delay*. The two delays will differ over at least some part of the spectrum if the system’s phase response is not entirely linear. When the group delay and phase delay are not equal, the system will necessarily distort the shapes of signals in the time-domain (Smith 2006).

Figure 6.8A shows the group delay for the electrode data; this is just the negative derivative of the low-input impedance head stage phase data from Figure 6.5 (in units of cycles) with respect to frequency (see Equation 4, Methods) without the subtraction of the filter-induced reference phase. Group delay varies modestly with electrode impedance and generally decreases with increasing frequency. For comparison, the group delay calculated from the filter-induced phase shifts of the black line in Figure 6.7 is shown here, and the group delay for the metallic resistor data is shown in Figure 6.8B. The filter-induced group delay through the LFP channel is relatively constant from 25 to 85 Hz at ~ 3 ms, and the group delay through the spike channel above 1 kHz is constant at ~ 0.15 ms. The electrode-amplifier-circuit-induced phase shifts in the microelectrode data resulted in added delays in the LFP frequency range that varied on average from an additional 0.35 ms at 85 Hz to 1.10 ms at 35 Hz. Over lower frequencies, the additional delays were even larger for some electrodes, with the series capacitance within the low impedance head stage partly contributing to this. Recall that the purely filter-induced group delays from either head stage will be the same as both use the same filters with the same phase response. To

summarize, the group delay in the spike-related frequency range will not distort spike timing appreciably, but the group delay in the LFP frequency range will introduce a systematic delay that can become quite large at lower frequencies.

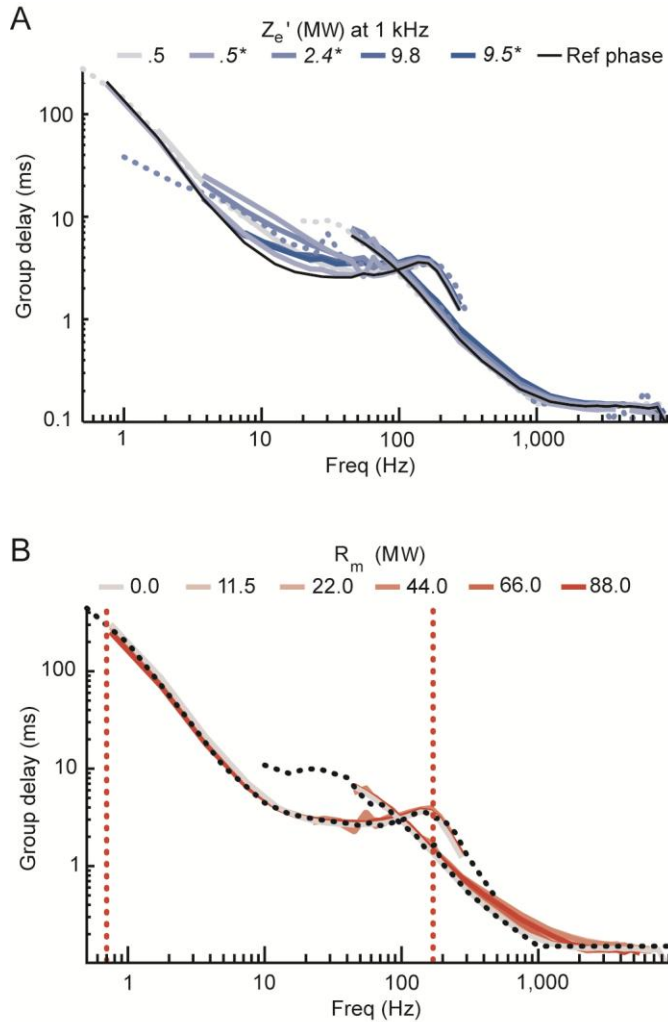
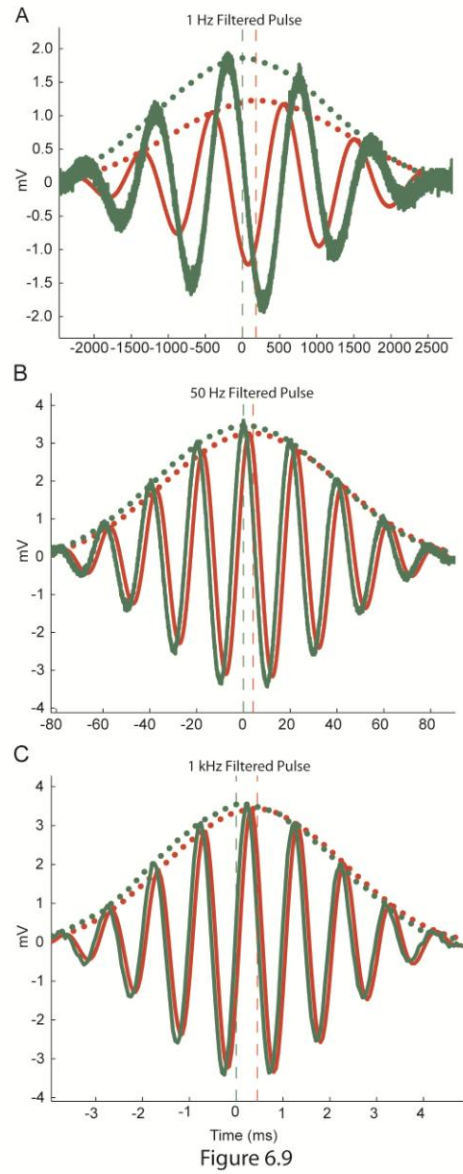


Figure 6.8

These conclusions depend on the quality of the group delay function derived from the phase shift measurements. To obtain a more direct measurement of group delay, we sent narrowband filtered pulses (see Methods for description, Figure 6.9 for examples) and measured the time delay at which the cross-correlation between the actual and recorded envelope estimates was maximal. The dotted traces in Figure 6.8A show the results for two of the electrodes color-coded for the electrode's impedance. Each of these traces matches very well the electrode's

calculated group delay. Other electrodes tested in this manner also showed good matches with their group delays, as did the metallic resistor data (Figure 6.8B). This confirms that the group delay measured for this system actually measures the delay of the amplitude envelope of a signal at a given frequency, which differs from the phase delay of the signal directly calculated from the phase shift of the carrier frequency.



Distortion of field potential and spike waveforms

Because the group delay and phase delay are not equal over many frequencies, and because of the amplitude attenuation by analog filters and the electrode itself, we expect distortion of recorded waveform shapes in the time domain to occur. To view this, we recorded with and without microelectrodes a voltage shape obtained from a single neuron's recorded waveform as well as a frequency-modulated version of the same waveform with the signal power concentrated in the LFP frequency ranges (Figure 6.10). Figure 6.10A shows the results for the LFP frequency range waveform, in which the delay in the recorded signal of about 3 to 4 ms can be clearly seen, matching the group delay for the relevant frequency ranges comprising this waveform. Electrode-impedance-dependent distortion of the recorded shapes can also clearly be seen, probably resulting largely from the amplitude attenuation properties of the electrode, with more of the lower frequencies of the signal being filtered out as electrode impedance increases.

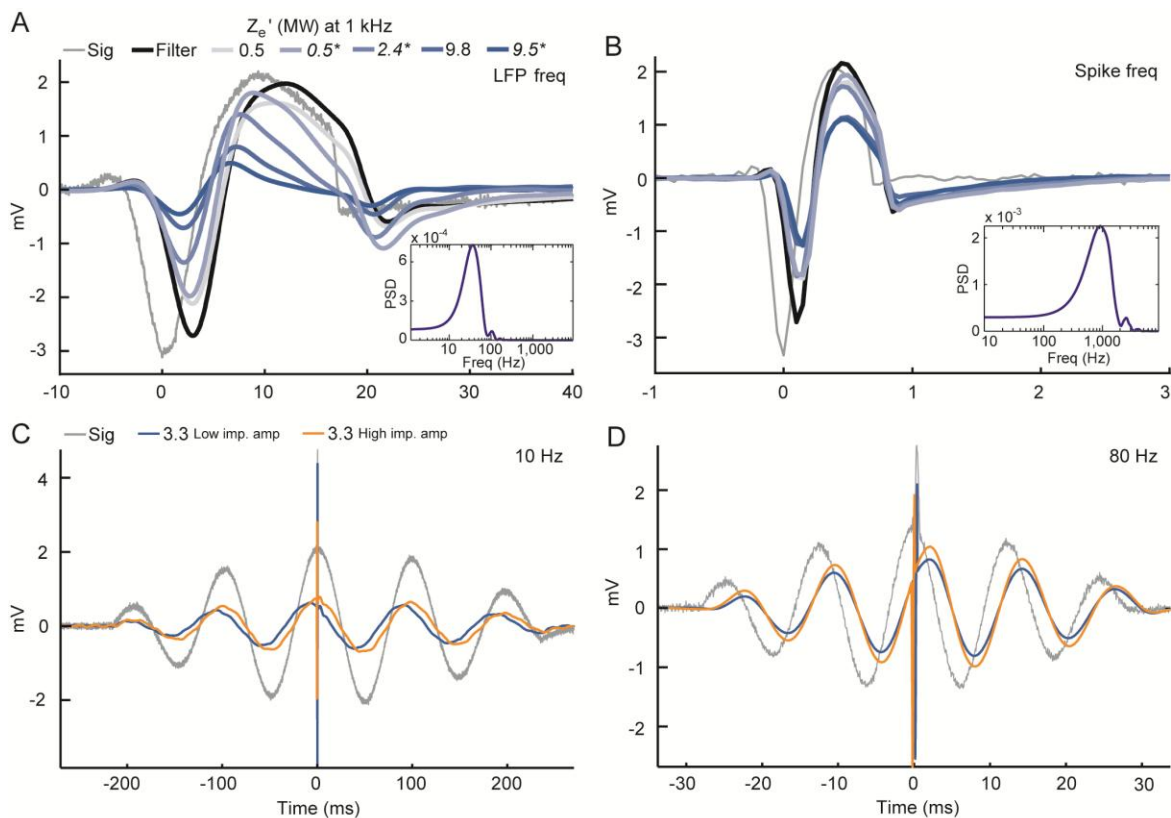


Figure 6.10

Figure 6.10B shows the results for the raw waveform in the spike frequency range, in which the shorter (~ 0.1 ms) delay can also clearly be seen. The effect of electrode impedance can be seen in the progressive attenuation of the amplitude of the recorded waveform, with a tendency for both the electrode and non electrode data to attenuate the first large negative trough more so than the following large positive peak. The most conspicuous shape distortion though, is the phantom after-hyperpolarization that is not present in the input signal. Of course the sub-ms delay in the overall timing of the spike will have little appreciable impact since the precision of spike timing is rarely important to that degree. However, the amplitude attenuation of the spikes could potentially make it more difficult to record and isolate spikes among noise, particularly with higher impedance electrodes. As we showed earlier, this cannot be avoided with higher impedance amplifiers since Z_a in this frequency range is dominated by the shunt capacitance, at least for our experimental setup. The filter-induced phantom after-hyperpolarization suggests that any inferences made about this portion of the action potential in particular without adjusting for the distortion would be misleading.

Finally, to demonstrate the effects of these distortions on simultaneously recorded spikes and LFPs, we used frequency pulses with the high-frequency spike from Figure 6.10B added to the signal at the maximum of the highest central peak. The results from one medium impedance electrode in physiological saline using either head-stage are shown in Figure 6.10C and D. For the 10 Hz signal, the filter-induced phase shift happens to be near zero at this frequency (see Figure 6.8), resulting in a near-zero phase shift observed with the high impedance head stage. However, electrode-amplifier-circuit-induced phase shifts with the low impedance amplifier cause the carrier wave of the recorded signal to lead the actual signal causing the recorded spike to appear on the falling edge of the recorded LFP oscillation instead of at its true position at the peak. For the 80 Hz signal, the direction of the filter-induced and electrode-amplifier-circuit-induced phase shifts counteract each other, with the filter-induced phase shifts dominating and causing the recorded

spike to appear well on the rising edge of the recorded LFP oscillation instead of at its true position at the peak. It is worth noting that this considerable filter-induced phase shift occurs at this frequency even though based solely on the high-frequency cutoff of 170 Hz one might superficially expect the phase shift to be negligible at 80 Hz.

DISCUSSION

Summary

We have shown that signals recorded with tungsten microelectrodes and an acquisition system commonly used in neurophysiology can be distorted substantially from the actual signals at the electrode tip. This distortion consists of frequency-dependent phase shifts and amplitude attenuation. The system filters imposed noticeable phase shifts even within their passbands. The observed phase shifts were dependent on the exact specifications of the pre-amplifier selected for use in a given system. When the electrode impedance was high with respect to the effective input impedance of the head stage amplifier, both attenuation and additional phase shifts of the recorded signal occurred. Of the two head stages we tested, this occurred with the lower input impedance head stage and primarily at lower frequencies because of the oft-overlooked fact that microelectrode impedance becomes much higher as frequency decreases. As such, equipment designed primarily to record spiking activity may not be able to record LFP activity without distorting the signal. We demonstrated that the distortions decrease with increasing saline concentration, but are still considerable with the low-input impedance headstage in physiological saline. Thus, these effects are of particular importance when gathering and interpreting LFP data. We showed that phase effects from both sources lead to amplitude envelope delays that differ from the direct time equivalent of the phase shift at a given frequency. We have also demonstrated shape distortion effects on recorded lower-frequency event-triggered potentials and spike shapes.

Impact of distortions

If the distortions demonstrated in this study occur and are not accounted for, any analysis using such LFP or spike shape data would be affected, and in certain cases this may lead to incorrect conclusions. Negative results at lower frequencies in LFP power or coherence (Fries et al., 2001a; Liu and Newsome, 2006), particularly at subgamma frequencies (<40 Hz) become difficult to interpret as are direct comparisons of these measures across frequencies (Fries et al., 2001b; Rickert et al., 2005; Womelsdorf et al., 2006). Measures of absolute LFP phase in relation to an event or spikes will be shifted (Bragin et al., 1995; Haslinger et al., 2006; Lee et al., 2005; Lin et al., 2006; Murthy and Fetz, 1996; Skaggs et al., 1996) meaning that any mappings of potentials onto the times when neurons locally are excited and inhibited (Fries et al., 2001a; Haslinger et al., 2006; Lin et al., 2006) will be incorrect. Because of the amplitude envelope delays, there will be subtle delays imposed on the timing of changes in frequency power or coherence (Womelsdorf et al., 2006). And finally, theoretical interpretations of spike shapes (Barthó et al., 2004; Gold et al., 2006; Nowak et al., 2003, Mitchell et. al., 2007) and event-triggered LFPs (Fries et al., 2001a,b; Krieman et al., 2006) may be incorrect, and techniques using waveforms as classification data (Fries et al., 2001a, Krieman et al., 2006) will be affected as well.

We would like to clearly indicate that we are not claiming that the results of any of the articles we mention above are necessarily distorted or that all of their conclusions should be questioned even if some signal distortion did occur. Indeed different equipment than what we have tested was often used, and such studies may or may not be susceptible to such distortions to a similar degree. However, due to past and current standards in the literature regarding methodological documentation it is not possible for a reader to determine the extent to which LFP data in a given publication may have been affected or to be certain that such distortions are negligible. In a qualitative review of the LFP literature, we found that though cutoff frequencies for filter passbands are usually mentioned, the filter phase response is rarely mentioned. The filter

specifications that are given are typically insufficient for the reader to be sure that the phase response will be near zero for the frequency ranges in question, even in cases where this would affect some of the conclusions of the article. Electrode impedance ranges measured at 1 kHz are only occasionally mentioned. The names of companies providing the amplification and recording equipment are also occasionally mentioned, but importantly, specific model numbers or relevant input impedances of amplifiers are never mentioned. This additional information should be included as well, as we have shown that different products provided by the same company can be susceptible to different levels of distortions. Indication of accounting for all the signal distortions we have shown is also never given.

Additionally, though some conclusions from analyses we have mentioned may be rendered incorrect as result of distortions that were not considered, this will not be true of conclusions from all analyses of such data. Most notably, comparisons within a given frequency band across different conditions using the same equipment should remain valid, though such comparisons at lower frequencies may be subject to a lower signal-to-noise ratio. While it is possible that rigorous statistical testing like bootstrapping and other methods could alleviate this to a certain extent, if potential distortions are a problem for a given data set, uncertainty regarding negative results at low frequencies would inevitably remain regardless of the statistical procedures employed on the distorted data. If the signal is analyzed in the time domain which combines LFP activity from all frequencies, then if the underlying neural activity between the two conditions differs at all then their frequency content must differ and the distortions will affect the recorded activity under each condition differently. As we have shown, the time-domain waveform shape of the signal can be distorted, which would thus affect such comparisons across conditions, most notably for results involving the precise timing of activity.

However, an impact of unaccounted signal distortion that is much more important than whether or not it may render a given specific analysis to be strictly wrong is that it leads to an

overall distorted view of the underlying neural activity and the state of the brain during experiments. With LFPs in particular, though some progress can be made using recorded activity merely as an arbitrary signal with which to determine when activity in a brain area generally differs between conditions, of critical importance to truly understanding the brain will be to determine what the underlying brain states are that give rise to the recorded neural activity. Signal distortions that are not accounted for will lead such mappings to be incorrect. For example, in one recent study (Lin et al., 2006) the authors note that basal forebrain tonic neurons (BFTNs) synchronize spiking activity just before the troughs of recorded prefrontal cortex (PFC) LFP theta oscillations of about 10 Hz. They interpret this as suggesting that the BFTN synchronization leads and probably contributes to a cortical activity increase that results in the LFP trough. Inferences like these are potentially the most fruitful uses of LFP activity to improve our understanding of the brain. However, if their recordings were distorted, which a reader cannot ascertain, then their general finding that BFTN synchronization occurs phase locked with PFC theta activity would likely still be true, but the reported phase at which this occurs and the theoretical interpretation of this relative to the timing of cortical excitation may need to be adjusted.

Because the distortions we have shown can implicate different underlying neural activity as giving rise to recorded data and can also potentially alter certain direct conclusions, they should be kept in mind when interpreting any LFP result, though we cannot quantify their extent in any given existing article. Our results also emphasize the importance of including methodological details in publications. Of course not every trivial detail of an experiment can be mentioned so a proper balance must be found, but our work illustrates some of the problems that can result from reporting too little. In particular, the mindset that a reader should assume that methodological details not mentioned in the article were done correctly by the experimenters without any verification of that has obvious negative consequences for the advancement of science. Particularly with the advent of web-based supplemental materials there is ample room to put full

details of the experimental apparatus in publications. We also encourage instrument providers to post more complete information on their web sites. However, we feel it is most appropriate for the specific equipment used in a study to be documented in the article text or supplemental information, rather than solely in an external source like a lab website. This avoids confusion as the equipment used often varies between projects in a lab and it allows the reader to more easily find the information they need.

While we hope that our results will lead readers to view existing LFP literature in a somewhat different light, our primary concern is that those performing future neurophysiology experiments will be more aware of these distortions and either avoid them entirely or account for them properly. Additionally, it is important for authors themselves to understand how this recording circuit works, which reveals in what instances and in what ways electrode characteristics like impedance will affect recorded signals. Investigators should not solely rely on equipment providers to ensure that their recordings are done correctly. Among other reasons, the way that equipment is arranged in a particular experiment independently of how it is built affects the shunt capacitance. We have shown that even with the best of equipment, this could lead to degradation of recorded spiking activity, making isolating single-cell activity in the brain more difficult.

With regards to electrode-amplifier circuit induced distortions, while our results indicate that this will be a problem for a low impedance head stage that has been in use by some for recording LFPs, this is not true of all available amplifiers as we have demonstrated with a higher impedance head stage. Indeed, amplifiers with very high input impedances have been easily obtainable for some time (Purves, 1981). It cannot be our place to test all the equipment used in neurophysiology today, but we hope that in light of what we have shown, prudent labs will determine what distortions arise in their experiments, particularly if their work involves recording LFPs. We cannot say exactly how widely used the 38 M Ω head stage that we tested in this study is, but we do know that some other labs have been using it for recording LFPs with

microelectrodes. Additionally, it seems likely to us that other equipment providers may have additionally distributed equipment that results in at least some degree of low-frequency signal distortion, as problems could easily result from overlooking or being unaware of the large increases in electrode impedance at low frequencies. Considering electrode impedances at 1 kHz as they are often labeled, amplifier input impedances of several tens of M Ω easily seem sufficiently high, though we have shown that indeed they are not for the recording of LFPs.

With regards to filter-induced distortions, provided that analog filters are used before digitizing and recording potentials, which is for all practical purposes a requirement for most recording systems, phase distortions will necessarily occur as they are a property of any causal filter. These distortions are therefore far more prevalent, though they are seldom accounted for in existing LFP studies. Sensitivity to this issue should also be present when considering the use of postrecording digital filters, as many of these may introduce phase shifts as well but carefully implemented ones may not. Potential filter-induced phase shifts should always be kept in mind when interpreting existing and future results reporting the absolute phases of field potentials (Bragin et al., 1995; Haslinger et al., 2006; Lee et al., 2005; Lin et al., 2006; Murthy and Fetz, 1996; Skaggs et al., 1996), shapes of spikes (Barthó et al., 2004; Gold et al., 2006; Nowak et al., 2003, Mitchell et al., 2007) and evoked potentials (Fries et al., 2001a,b; Krieman et al., 2006).

Correction techniques

An easy way to avoid the electrode-amplifier-circuit-induced portion of the effects that we have shown is through hardware adjustments with the use of a head-stage with a much higher input impedance than the 38 M Ω head stage tested for most of this study. As we have shown, amplifiers with low frequency input impedances of 1 G Ω are sufficient to eliminate this distortion

for all practical purposes with the use of most metal microelectrodes under reasonable conditions. It should also be noted that shunt capacitance can compromise even the highest amplifier input impedances, so care must always be taken to minimize this, for example with the use of minimal-length cables between the electrode and head stage, negative capacitance injection, driven shield arrangements or other techniques (Purves, 1981 pp. 45–49).

Care should also be taken to select filter properties appropriate for the intended analyses, another useful hardware adjustment. Passband edges should be placed as far off as possible from the frequency ranges of interest since the region of negligible phase shift is somewhat narrower than the region of negligible amplitude attenuation. The number of poles and type of filter can be selected to achieve the proper balance between phase distortions and amplitude response fluctuations in the passband, both of which form tradeoffs with each other.

For any of the effects we have shown that could not be avoided during data acquisition, software adjustments involving *ex post facto* correction routines using de-convolutions are possible to account for them once the transfer function of all the elements in the circuit are known. This is easily obtainable for the recording system itself by recording sine wave voltages spanning the frequency spectrum of interest with a desired resolution as we have done in this study, though other techniques like the use of a chirp signal may be possible, which would only require the use of one test signal. Signals can be generated using a function generator or a computer's audio output as was done in this study. If additional electrode-amplifier-circuit-induced effects could not be sufficiently mitigated with an appropriate head-stage, measurements of the system transfer function including the electrode would need to be performed as well. Preferably, this should be done within the brain before and after a recording session to get the best estimate of the transfer function resulting from the electrode's impedance at the time of recording. Available online in the Supplementary Note is a text file containing Matlab code to generate .wav files for signal generation, interpret the recorded data to obtain the transfer function, and apply the correction

techniques given the empirically obtained transfer function. For Plexon users, a software tool provided by Plexon for correcting preamplifier phase distortions can be downloaded from www.plexoninc.com/support/phase.html.

Other electrode variables

There is no indication that the nature of the equivalent circuit described in this article will depend on electrode characteristics, though the value of specific model parameters may. For example, insulation material may affect the shunt capacitance to ground, as glass insulation for example has been known to be more capacitive than epoxylite (Robinson, 1968), but with recordings at a negligible depth we found that results with different insulation materials were not qualitatively different. The physical properties of an electrode, which we have not investigated here, may also considerably affect the signals recorded by an electrode in a complicated physical environment like the brain (Lemon, 1984).

The basic equivalent circuit we present applies to other types of microelectrodes as well, including glass micropipette, carbon fiber and microwire electrodes. These typically have much higher impedances than metal microelectrodes and it has been suggested that with such electrodes experimenters have typically used appropriately high-input impedance amplifiers (Geddes et al., 1967), though we feel documentation of this is still warranted in articles presenting such data.

SUPPLEMENTARY MATERIALS

Supplementary materials for this article can be found online.

ACKNOWLEDGEMENTS

We would like to thank Justin Crouse at FHC for valuable discussions, Bruce Williams for construction of and assistance with the design of the electrode testing apparatus, and AB Bonds for

valuable discussions and comments regarding the manuscript. This work was supported by RO1-EY08890, Robin and Richard Patton through the E. Bronson Ingram Chair of Neuroscience and center grants P30-EY08126 and P30-HD015052.

DISCLOSURES

The authors affiliated with Vanderbilt University have no competing interests. The authors affiliated with Plexon have competing interests.

REFERENCES

- Barthó P, Hirase H, Monconduit L, Zugaro M, Harris KD, Buzsáki G.** Characterization of neocortical principal cells and interneurons by network interactions and extracellular features. *J Neurophysiol* 92: 600–608, 2004.
- Bragin A, Jando G, Nadasdy Z, Hetke J, Wise K, Buzsaki G.** Gamma (40-100 Hz) oscillation in the hippocampus of the behaving rat. *J Neurosci* 15: 47–60, 1995.
- Ferris CD.** *Introduction to Bioelectrodes*. New York: Plenum Press, 1974.
- Fries P, Neuenschwander S, Engel AK, Goebel R, Singer W.** Rapid feature selective neuronal synchronization through correlated latency shifting. *Nat Neurosci* 4: 194–200, 2001a.
- Fries P, Reynolds JH, Rorie AE, Desimone R.** Modulation of oscillatory neuronal synchronization by selective visual attention. *Science* 291: 1560–1563, 2001b.
- Geddes LA.** *Electrodes and the measurement of bioelectric events*. Wiley-Interscience: New York 1972: 3–43
- Geddes LA, Baker LE, McGoodwin, M.** The relationship between electrode area and amplifier input impedance in recording muscle action potentials. *Med Biol Eng* 5: 561–569, 1967.

- Geddes LA, DaCosta CP, Wise, G.** The impedance of stainless steel electrodes. *Med Biol Eng* 9: 511–521, 1971.
- Gold C, Henze DA, Koch C, Buzsáki, G.** On the origin of the extracellular action potential waveform: A modeling study. *J Neurophysiol* 95: 3113–3128, 2006.
- Green JD.** A simple microelectrode for recording from the central nervous system. *Nature* 182: 962, 1958.
- Grimnes S, Martinsen OG.** *Bioimpedance & bioelectricity basics*. Academic Press: London, UK, 2000: 15.
- Haslinger R, Ulbert I, Moore CI, Brown EN, Devor A.** Analysis of LFP phase predicts sensory response of barrel cortex. *J Neurophysiol* 96: 1658–1663, 2006.
- Hubel DH.** Tungsten microelectrode for recording from single units. *Science* 125: 549–550, 1957.
- Kandel A Buzsáki, G.** Cellular-synaptic generation of sleep spindles, spike-and-wave discharges, and evoked thalamocortical responses in the neocortex of the rat. *Journal of Neuroscience* 17: 6783–6797, 2007
- Kreiman G, Hung CP, Kraskov A, Quiroga RQ, Poggio T, DiCarlo JJ.** Object selectivity of local field potentials and spikes in the macaques inferior temporal cortex. *Neuron* 49: 433–445, 2006.
- Lee H, Simpson GV, Logothetis NK, Rainer G.** Phase locking of single neuron activity to theta oscillations during working memory in monkey extrastriate visual cortex. *Neuron* 45: 147–156, 2005.
- Lemon R.** *Methods for neuronal recording in conscious animals*. Chichester: Wiley-Interscience, 1984.
- Levick WR, Cleland BG.** Selectivity of microelectrodes in recordings from cat retinal ganglion cells. *J Neurophysiol* 37: 1387–1393, 1974.

- Lin SC, Gervasoni D, Nicolelis MA.** Fast modulation of prefrontal cortex activity by basal forebrain non-cholinergic neuronal ensembles. *J Neurophysiol* 96: 3209–3219, 2006.
- Liu J, Newsome WT.** Local field potential in cortical area MT: stimulus tuning and behavioral correlations. *J Neurosci* 26: 7779–7790, 2006.
- Marple SL.** Computing the discrete-time analytic signal via FFT. *IEEE transactions on signal processing* 47: 2600–2603, 1999a.
- Marple SL.** Estimating group delay and phase delay via discrete-time “analytic” cross-correlation. *IEEE transactions on signal processing* 47: 2604–2607, 1999b.
- Merrill EG, Ainsworth A.** Glass-coated platinum-plated tungsten microelectrode. *Med Biol Eng* 10: 662–672, 1972.
- Mitchell JF, Sundberg KA, Reynolds, JH.** Differential attention-dependent response modulation across cell classes in macaque visual area V4. *Neuron* 55: 131–141, 2007.
- Mitra SK.** *Digital signal processing, second ed.* Mc-Graw-Hill, 2001
- Murthy VN, Fetz EE.** Synchronization of neurons during local field potential oscillations in sensorimotor cortex of awake monkeys. *J Neurophysiol* 76: 3968–3982, 1996.
- Nelson MJ, Pouget P, Schall JD.** Effect of electrode impedance on measurement of local field potentials in the supplementary eye field. *Soc Neurosci Abstr* 32: 835, 2006.
- Nowak L, Azouz R, Sanchez-Vives M, Gray C, McCormick D.** Electrophysiological classes of cat primary visual cortical neurons in vivo as revealed by quantitative analyses. *J Neurophysiol* 89: 1541–1566, 2003.
- O’Keefe J, Recce ML.** Phase-relationship between hippocampal place units and the EEG theta rhythm. *Hippocampus* 3: 317–330, 1993.
- Oppenheim AV, Schaffer RW.** *Discrete-time signal processing, second ed.* Englewood Cliffs, NJ: Prentice-Hall, 1998.

- Purves RD.** *Microelectrode methods for intracellular recording and iontophoresis*. London: Academic Press, 1981.
- Rickert J, de Oliveira SC, Vaadia E.** Encoding of movement direction in different frequency ranges of motor cortical local field potentials. *J Neurosci* 25: 8815–8824, 2005.
- Robinson DA.** The electrical properties of metal microelectrodes. *Proc IEEE* 56: 1065–1071, 1968.
- Skaggs WE, McNaughton BL, Wilson MA, Barnes CA.** Theta phase precession in hippocampal neuronal populations and the compression of temporal sequences. *Hippocampus* 6: 149–172, 1996.
- Smith JO.** Introduction to digital filters [Online]. Stanford University. <http://ccrma.stanford.edu/~jos/filters06/> [2006].
- Wolbarsht ML, MacNichol EF, Wagner HG.** Glass insulated platinum microelectrode. *Science* 132: 1309–1310, 1960.
- Womelsdorf T, Fries P, Mitra PP, Desimone R.** Gamma-band synchronization in visual cortex predicts speed of change detection. *Nature* 439: 733–736, 2006.

FIGURE LEGENDS

Figure 6.1. Equivalent circuit model and methods. A: Equivalent circuit model of a metal microelectrode in the brain adapted from Robinson 1968. The entire circuit is comprised of the electrode in the brain and the amplifier with a filter. The effective impedance of the electrode (Z_e) is comprised of the resistance of the electrolyte solution (R_s), the resistance and capacitance at the double layer interface of the electrolyte and the uninsulated electrode tip (R_e and C_e) and the (negligible) resistance of the metal electrode (R_m). The effective input impedance of the amplifier (Z_a') is comprised of the input impedance of the head-stage amplifier (Z_a) and the shunt resistance and capacitance to ground from the tip of the electrode to the input of the amplifier (R_{sh} and C_{sh}).

The triangle represents an ideal amplifier that draws no current. The nonideal aspects of the amplifier have been accounted for in Z_a . Given the frequency-dependent potential at the electrode tip ($V_{\text{sig}}(\omega)$), a current ($I(\omega)$) is drawn towards ground through the electrode and effective amplifier circuit, creating the potential ($V_{\text{in}}(\omega)$) at the input of the amplifier which is subject to the frequency response of analog filters ($H(\omega)$) before being recorded ($V_{\text{rec}}(\omega)$), all according to the equation: $V_{\text{rec}}(\omega) = H(\omega)[(V_{\text{sig}}(\omega) \cdot Z_a'(\omega)) / (Z_e'(\omega) + Z_a'(\omega))]$. Thus, the microelectrode recording circuit corresponds to a voltage divider with a frequency-dependent gain due to the filtering of $H(\omega)$ and the frequency dependence of the impedances Z_e' and Z_a' . B: diagram of microelectrode testing apparatus. Two aluminum plates were connected and separated from each by nonconducting plastic supports, shown here from a top and side view. The apparatus was immersed in dilute saline with voltage signals applied to the signal plate with an electrode suspended from above 3 mm away. See the Methods section for more details. C: equivalent circuits for the parallel and series configuration. R_{sal1} is the resistance for current to travel from the signal plate to the electrode tip in the saline, and R_{sal2} is the remaining resistance for current to reach the ground plate.

Figure 6.2. Measurement of effective amplifier input impedance. Plots show amplitude data from signals sent directly to the low-input impedance head stage across different metallic resistors (R_m). Line colors are coded from grey to red based on the magnitude of R_m , with the precise values for each line indicated in A. Spike and LFP channel data (see Methods) are shown overlapping in A, but in B and C the vertical dashed line denotes the point where data to the left corresponds to the LFP channel data only, and data to the right corresponds to the spike channel data only. Frequency is shown on a log scale. For a list of the exact frequencies tested, please see the Signals used subsection in the Methods section. A: raw gain of the recorded over the actual signal. B: normalized gain showing the voltage attenuation across the resistor. This plot shows the raw gains

in A for each recording with a greater than zero resistance divided by the raw gain of the reference recording, which was the recording in which R_m was zero. C: effective amplifier input impedance calculations derived from the above data for each trace. The green dashed line represents the reported value of the amplifier alone.

Figure 6.3. Measurement of effective electrode impedance for one electrode. Plots show amplitude data from signals recorded with one high impedance glass-insulated electrode in dilute saline using different manipulated values of Z_a' with the low-input impedance head stage. Line colors are coded from grey to blue based on the value of Z_a' at 10 Hz, with the precise values for each line indicated in A. Parallel configuration data is shown with solid lines, series configuration data is shown with dashed lines. Spike and LFP channel data (see Methods) are shown overlapping in A, but in B and C the vertical dashed line denotes the point where data to the left corresponds to the LFP channel data only, and data to the right corresponds to the spike channel data only. Frequency is shown on a log scale. For a list of the exact frequencies tested, please see the Signals used subsection in the Methods section. A: raw gain of the recorded over the actual signal. B: normalized gain showing the voltage attenuation across the electrode, given by the value in A for each recording divided by the raw gain of the reference recording, which was done with a steel pin with negligible impedance. C: effective electrode impedance (Z_e') calculations derived from the above data for each trace. Z_e' is shown on a log scale.

Figure 6.4. Voltage attenuation and impedance measurements for several electrodes. Plots show amplitude data from signals recorded with electrodes in dilute saline. Grey-to-blue lines show data recorded using the low-input impedance head stage for electrodes with low-to-high measured impedance values at 10 Hz. The manufacturer specified 1 kHz impedance value for each electrode is indicated in A. Values in italics and followed by an asterisk denote data from a glass insulated

electrode. Orange lines show data recorded with the higher-input impedance head stage for one electrode with a large specified 1 kHz impedance of 8.4 M Ω . Parallel configuration data is shown with solid lines, series configuration data is shown with dashed lines. A and B denote parallel configuration recordings with no Z_a' manipulations, and C shows the average parallel and series configuration values across 4 different values of Z_a' . Spike and LFP channel data (see Methods) are shown overlapping in A, but in B and C the vertical dashed line denotes the point where data to the left corresponds to the LFP channel data only, and data to the right corresponds to the spike channel data only. Frequency is shown on a log scale. For a list of the exact frequencies tested, please see the Signals used subsection in the Methods section. A: raw gain of the recorded over the actual signal. B normalized gain showing voltage attenuation across the electrode, given by the value in A for each recording divided by the raw gain of the reference recording, which was done with a steel pin with negligible impedance. C: Effective electrode impedance (Z_e') calculations derived from the above data for each trace. Z_e' is shown on a log scale.

Figure 6.5. Electrode-amplifier-circuit-induced phase shifts using electrodes. All phase shifts are shown after subtracting the phase shifts induced by the system filters (see Figure 6.8). A positive phase means that the recorded signal leads the actual signal. Frequency is shown on a log scale. For a list of the exact frequencies tested, please see the Signals used subsection in the Methods section. The vertical dashed lines denote the points on each plot where data to the left corresponds to the LFP channel data and data to the right corresponds to the spike channel data. A: phase shifts for signals recorded using different electrodes in the parallel configuration in dilute saline. Grey-to-blue lines show data recorded using the low-input impedance head stage for electrodes with low-to-high measured impedance values at 10 Hz. The manufacturer specified 1 kHz impedance value for each electrode is indicated. Values in italics and followed by an asterisk denote data from a glass insulated electrode. Orange lines show data recorded with the higher-

input impedance head stage for one electrode with large high-frequency impedance. The dashed lines in grey and orange show the phase shifts for the steel pin reference electrode used with the low and high impedance headstages, respectively. B: phase shifts for signals recorded with a low impedance epoxy-lite-insulated electrode in the parallel configuration in dilute saline with the low impedance head stage while manipulating Z_a' . Line colors are coded from grey to blue based on the manipulated value of Z_a' at 10 Hz, with the precise values indicated.

Figure 6.6. Voltage attenuation, phase shifts and impedance measurements with different saline concentrations. In all plots and colors, data recorded in physiological saline is shown with dashed lines, and data recorded in dilute saline is shown in solid lines. The saturation level of all colors reflects electrode impedance, with the strongest colors showing data collected with the highest impedance electrodes. The manufacturer specified 1 kHz impedance value for each electrode is indicated in A. All electrodes were epoxy-lite insulated. Blue lines show data recorded with the low-input impedance head stage in the parallel configuration, orange lines show data recorded with the high-input impedance head stage in the parallel configuration, and green lines show impedance measurements made with the Agilent LCR meter. Frequency is shown on a log scale for all plots. For a list of the exact frequencies tested, please see the Signals used subsection in the Methods section. A: the normalized gain showing voltage attenuation across the electrode, as in figures 6.3B and 6.4B. B: the effective electrode impedance (Z_e') calculations, derived from the low-input impedance head stage data only in A as well as the measurements made by the Agilent LCR meter. A + denotes an electrode's manufacturer specified value at 1 kHz, and a x denotes the value from the Bak metal electrode impedance tester at 1 kHz made in dilute saline. Measurements with the Bak tester in physiological saline were always somewhat lower than the dilute saline values, but these are not shown for clarity. Z_e' is shown on a log scale. C: electrode-amplifier-circuit-induced phase shifts.

Figure 6.7. Filter-induced phase shifts. The recorded phase shifts of signals sent directly into head-stages used with different analog filters are shown, with spike and LFP channel data overlapping. A positive phase means that the recorded signal leads the actual signal. Frequency is shown on a log scale. For a list of the exact frequencies tested, please see the Signals used subsection in the Methods section. Both head-stages were used throughout this study with following preamplifiers with identical specified filter properties, which had resulting phase shifts shown here in black. The data above 10 Hz were recorded using the low-input impedance head stage, and the data at and below 10 Hz were recorded with the high-input impedance head stage which has no series capacitance that introduces additional phase shifts in this frequency band (see Figure 10). This black line was used as the purely filter-induced reference phase and subtracted from other data recorded with this equipment to determine the phase shifts introduced by other sources. The grey line shows the LFP channel phase shifts recorded for a second preamplifier with the high-input impedance head stage. The dotted vertical lines show the cutoff frequencies for the LFP channel filter with its phase response shown in the corresponding color.

Figure 6.8. Group delays. Spike and LFP channel data are shown overlapping. Frequency is shown on a log scale. For a list of the exact frequencies tested, please see the Signals used subsection in the Methods section. The filter-induced phase shifts were not subtracted from any data shown here. A: group delay for electrode data. Grey-to-blue lines show data recorded in dilute saline in the parallel configuration using the low-input impedance head stage for electrodes with low-to-high measured impedance values at 10 Hz. Solid lines show group delays calculated from equation 4 (see methods) using the recorded phase shifts of sine waves at different frequencies, while dotted lines show the measured amplitude envelope delay using narrowband filtered pulse signals recorded with two electrodes. The manufacturer specified values at 1 kHz

are indicated in the color legend above the plot. Values in italics and followed by an asterisk denote data from a glass insulated electrode. The group delays from the filter-induced reference phase response (the black lines from Figure 8) are shown by the black line for comparison. B: group delay for metallic resistor data. Line colors are coded from grey to red based on the value of R_m , with the precise values for each line indicated above the plot. The dotted black line shows the measured amplitude envelope delay using narrowband filtered pulse signals sent directly to the head-stage with no resistors, which corresponds well with the calculated group delay. The dotted vertical lines show the cut-off frequencies for the LFP channel filter used.

Figure 6.9. Examples of filtered frequency pulses used for amplitude envelope and group delay measurements. Actual signals presented directly to the head-stage are shown in green, recorded signals are shown in red. For each signal, the raw values are shown with solid lines and the Hilbert-magnitude estimations of the amplitude envelope with local average smoothing applied are shown with dotted lines. The maximum point of each estimated envelope is shown with vertical dashed lines. Data are presented for bandpass filtered pulses centered around frequencies of A: 1 Hz, B: 50 Hz, and C: 1 kHz. LFP channel data are shown in A and B, spike channel are data shown in C.

Figure 6.10. Recorded waveform shapes. Grey-to-blue lines show waveforms recorded in the parallel configuration in the low-input impedance head stage for electrodes with low-to-high measured impedance values at 10 Hz. The manufacturer specified value at 1 kHz indicated in the color legend above the plot. Values in italics and followed by an asterisk denote data from a glass insulated electrode. The thin grey line shows the actual voltage presented, and the thick black line shows the voltage recorded with the signal voltage applied directly to the same head-stage. Dilute saline was used for the electrode recordings in A and B, and physiological saline was used for the

data in C and D. A: LFP channel data only for a lower-frequency version of the waveform. B: Spike channel data only for a higher-frequency version of the waveform. Beneath each plot is a power-spectral density (PSD) estimation of the actual voltage waveform in each plot, obtained with a windowed Fourier transform. C and D: 10 and 80 Hz frequency pulse waveforms additively combined with the high-frequency spike from B. LFP channel data is displayed with the Spike channel data additively combined to it at the time of the recorded spike.

Chapter 7

Do electrode properties create a problem in interpreting local field potential recordings?

Local field potential (LFP) recordings within the brain have become an important tool used by neuroscientists to make inferences about the activity of a population of cells near an electrode. Each passing year analysis of LFPs in neuroscience seems to bring important new insights on the possible workings of networks in the brain to produce behavior (Buschman and Miller, 2007; Canolty, et al., 2006; Gregoriou et al., 2009; Liu and Newsome, 2006; Lubenov and Siapas, 2009; Pesaran et al., 2008; Womelsdorf et al., 2006). Indeed LFPs have become a near-ubiquitous tool in neurophysiology seemingly in use anywhere extracellular spikes are also recorded.

One issue that often comes up among those who interpret LFP data is uncertainty about how electrode impedance and other electrode parameters affect LFP recordings, which presents a potential problem in their interpretation. Indeed this is a complex question, as current flow in the brain depends on a multitude of factors and extracellular recordings cannot uncover the precise neural events giving rise to a specific LFP voltage. Amidst this uncertainty, one commonly mentioned idea that exists today is the notion that microelectrodes of different impedances or geometries might integrate signals across space differently which could lead to differing results between experiments that use electrodes of different impedances to collect LFP data. This notion has been frequently expressed verbally by many, though direct discussions of it in the literature (Pesaran, 2009) have been more rare. Literature discussing how these electrode parameters affect spike recordings (Andersen et al. 2010; Moxon, 1999; Paik et al., 2003; Ward et al., 2009) is more commonly found however. Despite the relative prevalence of this question in the field, research investigating it has been lacking and no definitive answer to it has been proposed. However, we believe that the answer to this question can be found from information gleaned from a range of existing literature and published data, though most in the field are not presently aware of this. The uncertainty surrounding this issue is important to address as it creates a potential barrier for the comparison of LFP data across experiments and laboratories. Furthermore, as the interpretation of

LFPs continues to move beyond its infancy further into the territory of a standard neuroscience technique, such comparisons will be increasingly common and important for building consensus in the field.

As we will describe here, we believe this issue presents one of the rare cases in neuroscience in which the answer that would make the work of trying to understand the brain easier also happens to be true. That is to say, provided that the proper recording equipment is used, the impedance and geometry of microelectrode recording sites in the ranges typically used in extracellular experiments do not appreciably affect LFP recordings. Scientists in fact do not need to attend to this issue when interpreting LFP data or comparing such results across experiments and laboratories.

To defend this claim, the first point to *a priori* clarify is that an electrode can be considered to report the average voltage present at its uninsulated tip or recording site (Nunez and Srinivasan, 2006; Robinson, 1968). Indeed using metal microelectrodes suspended in saline, we have verified that this was the case and that this model presented years ago by David Robinson does hold true (Nelson et al., 2008). Thus, the only sense in which an electrode integrates a signal across space is by determining this average voltage. The shape and size of an electrode's recording site will not, for example, affect the way in which it responds to distant as opposed to nearby voltage sources.

Second, if the proper recording equipment is used, the voltage that is ultimately amplified and recorded will not be appreciably electrically affected by the electrode's impedance. Indeed in previous work we demonstrated this to be the case (Nelson et al., 2008). Recorded voltages in saline using electrode impedances spanning the range typically used in extracellular experiments were independent of the electrode's impedance when using a head stage with a high ($> 1 \text{ G}\Omega$) input impedance. This does require some attention from neurophysiologists though, as another commercially available head stage we tested had a lower input impedance which led to electrode

impedance-dependent signal distortions. Fortunately, when they occur these distortions can be corrected *post hoc* (Nelson et al., 2008) as has been done for several recent publications (Gregoriou et al., 2009; Siegel et al., 2009).

A separate question from whether the impedance of an electrode electrically impacts the recorded voltage is the question of whether the size and geometry of the recording site impacts the recorded LFPs. Within the framework that we have described here, one can conceive how during a recording these parameters could affect the average voltage present over the whole uninsulated site, and thus affect the recorded values.

An electrode's impedance is of course highly dependent on the size of its uninsulated surface area. Indeed impedance, which is more easily measured, is essentially used only as a proxy to describe an electrode's uninsulated surface area, which is of more interest to neuroscientists. For spike recordings, for example, the general viewpoints in the field tend to be that larger recording sites spanning more of the extracellular space will record more neurons at a given time (Andersen et al., 2010; Moxon, 1999; Paik et al., 2003; Ward et al., 2009) while smaller recording sites will have more specificity and record individual neurons that are better isolated (Moxon, 1999; Paik et al., 2003). These views are not established facts however, and there is at least some contrary evidence in the literature (Suner et al., 2005).

The impact on spike recording set aside, it may be tempting for one to make the claim that LFPs are affected by recording site size and geometry. However a closer look reveals that current estimates of the spread of LFP signals suggest that these potentials in the brain vary on a spatial scale larger than the size of uninsulated electrode recording sites used in extracellular recordings. For instance, Katzner and colleagues (Katzner et al., 2009) recently showed that LFPs are more local than previously thought, but even their newly lowered estimate still suggests that LFPs primarily originate from sources within 100 μm of a given point with noticeable contributions coming from up to within 250 μm . Meanwhile, even a 300 k Ω at 1 kHz tungsten electrode, which

is a very low impedance by extracellular recording standards and thus has a very large recording site, corresponds to a surface area of only $1850 \mu\text{m}^2$ (Yaeli et al., 2009). For a conical electrode at even an extreme angle of 10 degrees, this would result in an uninsulated height near $80 \mu\text{m}$, as illustrated in Figure 7.1. Similar data published for platinum-iridium electrodes (Lemon, 1984; Tielen et al., 1971) ultimately yields the same conclusion and further suggests that this will hold true for other metals as well. Changing the size and shape of a recording site within this range would not likely appreciably affect the average potential found over the site based on current estimates of the spread of LFPs.

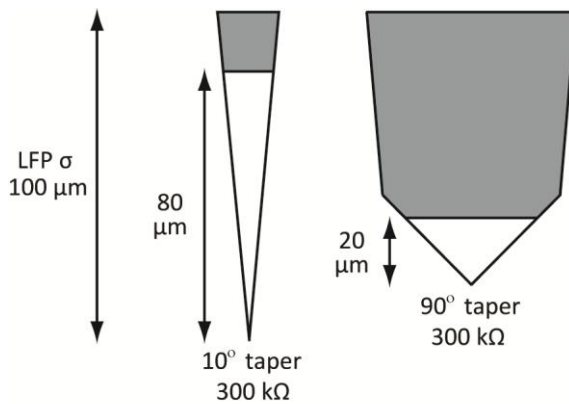


Figure 7.1

Thus we feel that evidence available in the literature suggests that the impedance, size and shape of the recording sites of microelectrodes will not affect the recording of LFPs. This holds for microelectrodes spanning the range of impedances typically used in extracellular recording experiments, provided that head stages of the proper input impedance are used (Nelson et al., 2008). Of course it would be possible to produce an extremely low impedance microelectrode that may indeed report different voltages than typical microelectrodes, but it is not clear that anything would be gained by the use of such an electrode. Indeed larger electrode recording sites essentially only serve as low-pass spatial filter (Nunez and Srinivasan, 2006), and it would seem that the more-precise spatial measurement provided by microelectrodes currently in use would be preferred in any reasonable scientific application.

Those who might disagree with the claim we have presented here should be clear in their reasons for doing so. The framework that we have presented describing the circuit properties of microelectrode recordings is generally accepted, though many neuroscientists may be unaware of it. Assuming one then does not disagree with this framework, disagreeing with our claim amounts to the counterclaim that LFP voltage profiles in the brain change appreciably on a spatial scale smaller than a few tens of microns, which is the scale of microelectrode recording sites in use today. Thus, for this counterclaim to be true, it is important to note that current beliefs about the spread of LFPs must then be wrong. Even if hypothetically LFPs did vary on such a small spatial scale, the very precise placement of an electrode within the brain would then likely be of more importance than the size and geometry of its recording sites. In such a case it is unclear that it would even be possible or desirable to attempt to capitalize on such a fine spatial structure of the local field potential.

Although the electrode parameters of impedance and recording site size likely have no effect on the recorded LFP, this says nothing about the effects of the mechanical disruption introduced by the electrode. Such effects would likely be dependent on electrode parameters such as size and taper angle, though an electrode's impedance or the size of its uninsulated region should not directly influence this. Additional caveats to consider are the effects of increased thermal noise and loss of signal due to shunt capacitance, both of which affect recorded voltages more as electrode impedance increases²². However, we believe that again the evidence suggests these will not have large enough effects on LFP recordings to be of notable concern for recordings made within typical ranges of parameters. With regards to thermal noise: its magnitude is dependent on signal bandwidth as well as electrode impedance, and LFP recordings typically take place over a limited bandwidth. Using electrode impedance spectra data from our previous work¹⁵ and the well-established formula for thermal noise (Johnson, 1928; Nyquist, 1928) we can derive estimates of the amount of thermal noise theoretically expected for different microelectrodes in the

frequency band from 0 to 150 Hz given their average impedance in this frequency band, which is a generous bandwidth for LFPs. The expected RMS value of this thermal noise was 7.7 μV for an electrode with a 3.3 M Ω impedance at 1 kHz and 4.2 μV for an electrode with a 500 k Ω impedance at 1 kHz. The different amount of noise between these electrodes, which approximately span the range of electrode impedances in use today, is all but negligible in comparison to the size of most LFP results of interest. With regards to signal loss through shunt pathways: the impact of shunt capacitance in recordings serves to effectively compromise the input impedance of the head stage at high frequencies (Cogan, 2008; Nelson et al., 2008; Robinson, 1968), which results in electrode impedance-dependent signal loss and distortions at those frequencies. However, this impact declines as frequency decreases. Indeed during test recordings with metallic resistors and electrodes suspended in saline, we found that as frequency decreased, shunt capacitance ceased to impact recordings starting in the 300 to 400 Hz range (Nelson et al., 2008), well above the LFP frequency ranges of interest. We should be clear however that shunt capacitance does depend on how the recording equipment is arranged and the impacts could be different in some recording configurations. However this has yet to be tested in the literature, and the available evidence we mentioned suggests this will not be a problem for LFP frequencies.

There is still a great deal of interesting future research that is needed to better understand the details of what can be inferred about neural activity from a given LFP trace. Indeed there are many curiosities and unknowns related to this. But we hope that neuroscientists interpreting LFP data can more freely compare results and continue the important work of using field potentials to understand the brain without worrying about the possible effect of electrode impedance and recording site geometry as one more unknown for concern.

REFERENCES

- Andersen, R.A., Hwang, E.J., and Mulliken, G.H. (2010). Cognitive neural prosthetics. *Annu. Rev. Psychol.* 61, 169–190.
- Buschman, T.J., and Miller, E.K. (2007). Top-down versus bottom-up control of attention in the prefrontal and posterior parietal cortices. *Science* 315, 1860–1862.
- Canolty, R.T., Edwards, E., Dalal, S.S., Soltani, M., Nagarajan, S.S., Kirsch, H.E., Berger, M.S., Barbaro, N.M., and Knight, R.T. (2006). High gamma power is phase-locked to theta oscillations in human neocortex. *Science* 313, 1626–1628.
- Cogan, S.F. (2008). Neural stimulation and recording electrodes. *Annu. Rev. Biomed. Eng.* 10, 275–309.
- Gregoriou, G.G., Gotts, S.J., Zhou, H.H., and Desimone, R. (2009). High-frequency, long-range coupling between prefrontal and visual cortex during attention. *Science* 324, 1207–1210.
- Johnson, J. (1928). Thermal agitation of electricity in conductors. *Phys. Rev.* 32, 97–109.
- Katzner S., Nauhaus I., Benucci A., Bonin V., Ringach D.L., and Carandini M. (2009). Local origin of field potentials in visual cortex. *Neuron* 61, 35–41.
- Lemon, R. (1984). *Methods for neuronal recording in conscious animals.* (Chichester, NY: Wiley-Interscience), pp. 74–75.

Liu, J., and Newsome, W.T. (2006). Local field potential in cortical area MT: stimulus tuning and behavioral correlations. *J. Neurosci.* *26*, 7779–7790.

Lubenov, E.V., and Siapas, A.G. (2009). Hippocampal theta oscillations are travelling waves. *Nature* *459*, 534–539.

Moxon, K.A. (1999). Multichannel electrode Design: Considerations for different applications. In *Methods for neural ensemble recordings*, M.A. Nicolelis, ed. (Boca Raton, FL: CRC Press), pp. 375–405.

Nelson, M.J., Pouget, P., Nilsen, E.A., Patten, C.D., and Schall, J.D. (2008). Review of signal distortion through metal microelectrode recording circuits and filters. *J. Neurosci. Methods* *169*, 141–157.

Nunez, P.L., and Srinivasan, R. (2006). *Electric fields of the brain: The neurophysics of EEG*, 2nd ed. (New York, NY: Oxford University Press), pp. 298–305.

Nyquist, (1928). Thermal agitation of electric charge in conductors. *Phys. Rev.* *32*, 110–113.

Paik, S.J., Park, Y., and Cho, D. (2003). Roughened polysilicon for low impedance microelectrodes in neural probes. *J. Micromech. Microeng.* *13*, 373–379.

Pesaran, B. (2009). Uncovering the mysterious origins of local field potentials. *Neuron* *61*, 1–2.

- Pesaran, B., Nelson, M.J., and Andersen, R. A. (2008). Free choice activates a decision circuit between frontal and parietal cortex. *Nature* 453, 406–409.
- Robinson, D.A. (1968). The electrical properties of metal microelectrodes. *Proc. IEEE*. 56, 1065–1071.
- Siegel, M., Warden, M.R., and Miller, E.K. (2009). Phase-dependent neuronal coding of objects in short-term memory. *Proc. Natl. Acad. Sci. U. S. A.* 106, 21341–21346.
- Suner, S., Fellows, M.R., Vargas-Irwin, C., Nakata, G.K., and Donoghue, J.P. (2005). Reliability of signals from a chronically implanted, silicon-based electrode array in non-human primate primary motor cortex. *IEEE. Trans. Neural Syst. Rehabil. Eng.* 13, 525–541.
- Tielen, A.M., Giesen, C., and Mollevanger, W. (1971) Some mechanical and electrical characteristics of metal microelectrodes. *Inst. of Med. Phys. TNO. Rep.* 2.3.65/1 MEI.
- Ward, M.P., Rajdev, P., Ellison, C., and Irazoqui, P.P. (2009). Toward a comparison of microelectrodes for acute and chronic recordings. *Brain Res.* 1282, 183–200.
- Womelsdorf, T., Fries, P., Mitra, P.P., and Desimone, R. (2006). Gamma-band synchronization in visual cortex predicts speed of change detection. *Nature* 439, 733–736.

Yaeli, S. Binyamin, E., and Shoham, S. (2009). Form-function relations in cone-tipped stimulating microelectrodes. *Front. Neuroeng.* 2:13, 1–8.

FIGURE LEGENDS

Figure 1. Electrode recording site sizes relative to the spread of LFPs. Even for a low impedance (300 k Ω) electrode with an extremely fine taper angle (10 degrees), the uninsulated recording site length is smaller than current estimates of the standard deviation of the spread of LFP signals. Larger taper angles or higher impedances correspond to even smaller recording site lengths. The average potential across the electrode's tip should thus not be appreciably affected by variations of recording site size within the range of electrodes used for extracellular recordings. Data for the spread of LFPs comes from Katzner et al. (2009), while data for electrode recording site sizes can be found in Lemon (1984), Tielen et al., (1971) and Yaeli et al. (2009).

Chapter 8

Physical model of coherent potentials measured with
different electrode recording site sizes

BACKGROUND

For many years, local field potentials (LFPs) have proven to be an important data source for improving our understanding of the brain. Despite this, questions surrounding their interpretation still remain unanswered, but have been a recent topic of renewed interest in the literature (Bedard, et al. 2010; Katzner et al. 2009; Logothetis et al. 2007; Xing, et al. 2009).

One such question that often arises is: what effect do properties like electrode impedance and shape have on recorded LFPs? We argued previously (Nelson and Pouget 2010) that when interpreting LFP recordings from microelectrodes, neurophysiologists can ignore for all practical purposes the particular size and shape of recording sites provided that they are within the ranges normally used for extracellular recordings. The basis for this argument originates from a physical model of microelectrode recording circuits (Robinson 1968) that we confirmed experimentally in our previous work (Nelson et al. 2008). There we explicitly showed that when using an amplifier of appropriately high input impedance, which is available in some but not all commercially available recording equipment, the impact on recorded signals of the electrical impedance of the microelectrode/tissue interface is negligible. The voltage recorded by a microelectrode in this case will equal the average voltage present across its uninsulated tip. Yet recording site size could still potentially influence recordings on a physical basis by affecting what that average voltage at the electrode's tip is. This could occur if the underlying voltage being measured varies spatially on a scale finer than an electrode's recording site size. However, current estimates of the spatial extent of the LFP suggest that 95% of the signals recorded at a given point in space originate from within a 250 micron radius (Katzner et al. 2009), which well exceeds the size of microelectrode recording sites for the ranges of microelectrodes typically used by neurophysiologists (Yaeli et al. 2009; Lemon 1984; Tielen et al. 1971). Thus, the particular size of these recording sites should not affect the LFP signals they record.

Claims that electrode size and shape should affect recorded LFPs have been made in the literature (e.g., Berens et al. 2008; Pesaran 2009, Kay and Lazzara 2010) without mention or apparent consideration of this generally accepted theoretical basis of the nature of microelectrode recordings (Robinson, 1968). Many neurophysiologists do have some familiarity with a notion that larger electrodes record signals from more distant sources, and that this results in differences between the signals recorded by electrodes of different sizes. But the separation of the discussion in the literature from the basic physical nature of the recordings may obscure to many in the field the fact that electrodes average only the signals that exist over the spatial extent of their recording site surface areas. Surprisingly, though electrode size has been modeled in different aspects before (e.g., Ollikainen et al. 2000, Moffitt & McIntyre 2005, Lempka et al 2011), models of how this simple spatial averaging directly affects recorded signals have not appeared in the literature to our knowledge. This is the case despite the existence of strong claims that, for example, this spatial averaging property should cause different microelectrode sizes within the brain to reveal fundamentally different voltage signals (Nunez and Srinivasan, 2006).

There have been some empirical investigations of the effect of electrode size on the coherence of recorded LFPs with unclear results. Bullock and McClune (1989) reported finding no difference in coherence when comparing electrode recording sites with 1 micron diameters to those with 50 micron diameters, nor when comparing those with 25 micron diameters to those with to 250 micron diameters. Kay and Lazzara (2010) later compared coherence between electrodes of very different sizes (200 μm vs. 2–3 μm diameters). They found that the much larger electrodes reported slightly more coherence, although the spectral power was the same between the different electrode sizes. Despite the very large difference in the size of the electrodes they compared, the effects that they report were very small, thus their results are not per se incompatible with our earlier claim. But if these effects do hold true for large electrode differences, it raises a question as to whether this should be considered when comparing LFPs to electroencephalogram (EEG) data

recorded from the scalp or electrocorticogram (ECoG) data recorded from the cortical surface, both of which are typically done with much larger electrodes.

In addition to the empirical ambiguity surrounding the question, the theoretical prediction of how averaging signals across larger regions of space should be expected to affect the coherence of recorded signals is unclear *a priori*. Competing effects are present as some effects would cause larger electrodes to tend to report more coherence, while some effects would cause smaller electrodes to tend to report more coherence. Thus, we sought to test what the expected overall effect is through quantitative simulations based on the theoretical basis of microelectrode recordings.

Here we explicitly describe a simple physical model to clearly illustrate the theoretical basis through which claims about the effect of electrode size and shape on recorded potentials should be considered. Importantly, this model highlights that for any differences between recording sites to occur, the underlying voltage profile must vary appreciably over the extent of the larger recording site's surface. We then use quantitative simulations of the model using simulated and real LFP traces to test the non-obvious result of whether larger electrodes should report higher levels of coherence. We find that the modeled low impedance electrodes do indeed report larger coherences between areas than the modeled high impedance electrodes. We show that this effect continuously increases as the voltage profile is increasingly nonuniform over the extent of the larger electrode's recording site, and that it is robust with respect to the strength of the coherence gradient along the voltage profile. We then quantitatively compare coherence reported in LFP, ECoG and EEG data across several studies and lab groups, and find evidence for a possible modest effect of electrode size in ECoG data only. We extend our simulations to quantify the effect on recorded coherence of any given ratio of electrode size to the spatial frequency of the underlying neural activity. Combining this with published estimates of the spatial frequencies present in each neurophysiological data type confirms the trends we observed in the literature.

MATERIALS AND METHODS

The model. It is trivial to conclude but bears mentioning *a priori* that the LFP signal must vary appreciably over the size of the lower impedance electrode tip for the electrode impedance to have the possibility to make any difference at all in the resulting recorded value (Nelson and Pouget, 2010). This point should be further obvious if one considers the extreme opposite case in which the LFP signal is spatially uniform. It is clear that in this case, the particular locations over which the voltage is averaged by electrodes of different sizes would not matter.

Figure 8.1A shows the most basic version of a physical model of how differences in coherence could be observed between electrodes of different sizes. In this model, some subregions are highly coherent between two distant locations while some are not. Potentials recorded in the subregions with high distant coherence are highly coherent with each other, while potentials in the subregions with low distant coherence are not coherent with either subregion. Very low impedance electrodes that are large relative to the size of the subregions would extend across the subregions (Figure 8.1B, left) and would thus always report the average activity between the subregions. In contrast, microelectrodes that are small relative to the size of the subregions would tend to fall into a single subregion and would thus reflect the activity of one or the other subregion by chance depending on the random precise placement of the electrode (Figure 8.1B, right). In this situation, the low impedance electrodes would reliably have moderate coherence as the voltage they record would always include that of the high distant coherence subregion, but this activity would also always be averaged with that of the less coherent low distant coherence subregion. In contrast, the microelectrodes would occasionally record very low coherence on some recordings when they happen to be in low distant coherence subregions, but they would also occasionally record very high coherences when both electrodes happened to be in high coherence subregions. Competing effects would thus be present in determining which electrode type would be expected to have the

higher coherence on average, with the result depending on the properties of signal averaging before calculating coherence.

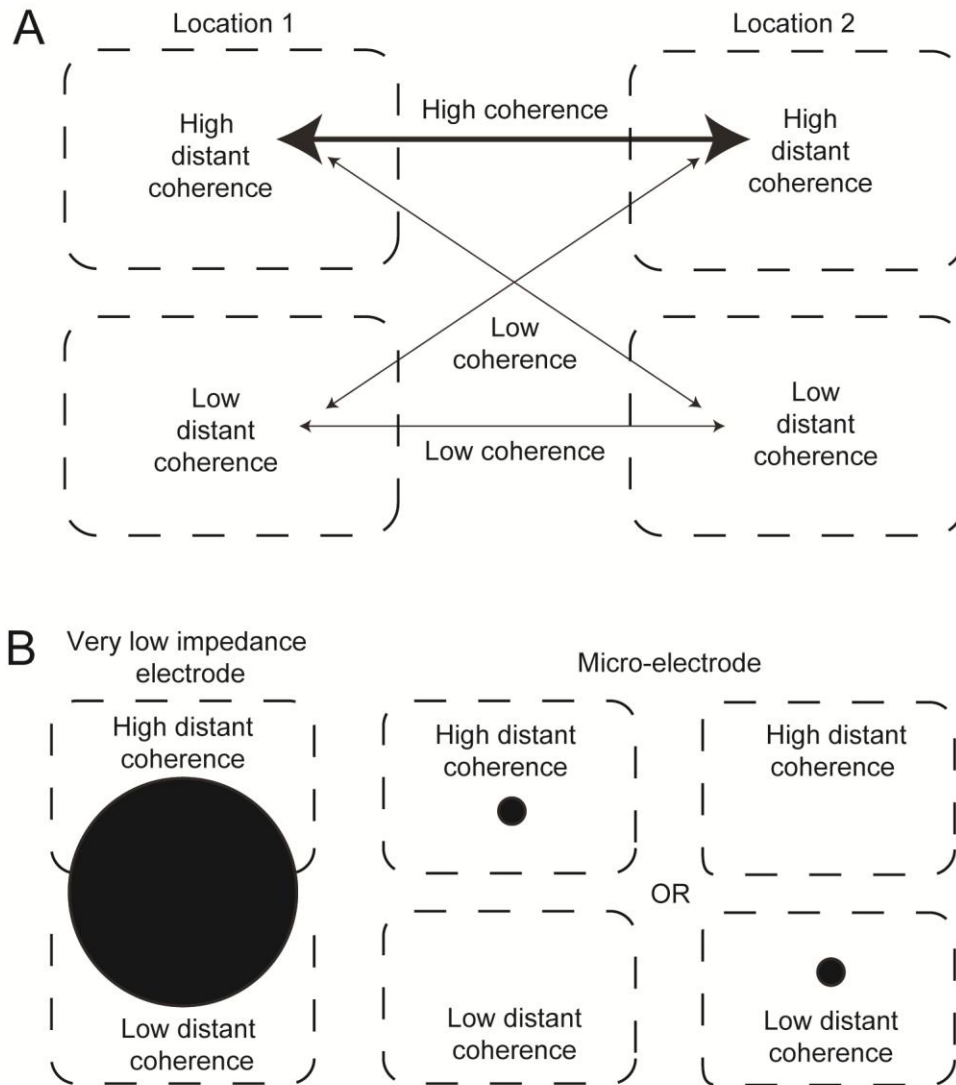


Figure 8.1

The basic model described above can be extended to make quantitative predictions for the expected effects of electrodes of particular sizes relative to the spatial variation of underlying neural activity. This can be done in the most general sense by modeling the underlying voltage profile as a spatial sine wave (Figure 8.6A), since any spatial variation of voltage can be described by the contributions of sine wave components at different spatial frequencies. In this version of the model, the voltage varies continuously by oscillating sinusoidally between high-and low-distant

coherence activity instead of having each type of activity separately confined to distinct subregions as in the basic model. Electrode recording sites are modeled to be of precise sizes in relation to the spatial wavelength of the sinusoidal voltage profile and placed at random phases of the voltage profile, averaging the activity present along their lengths. Using these results, the effects for any particular voltage profile and electrode size could then be predicted.

Simulating high-and low-distant coherent activity. To produce testable data that captures the key points of the above models, we created 4 LFP traces. Each of the two simulated electrode locations in the basic model was comprised of two traces: one corresponding to a high-distant coherence subregion and one corresponding to a low-distant coherence subregion. We did this both with purely simulated data and real LFP traces, following procedures described below. The goal in creating and selecting these traces for the primary simulations was to obtain two LFP traces that were highly coherent with each other, which represent the high-distant coherence subregions in each location, and two LFP traces that were neither coherent with each other nor the previous traces, which represent the low-distant coherence subregions in each location (see Figure 8.1A).

Using simulated data. We generated simulated LFP signals in Matlab (Natick, MA) by adding white noise to sinusoids with a simulated sampling rate of 1 kHz. The period of the sinusoid was set to 50.234 samples per cycle in order to avoid the unrealistic situation where this was exactly a multiple of the sampling period. This resulted in a signal frequency of just under 20 Hz. 200 trials of 4 seconds each were simulated for each session. The amplitudes and phases of the four signals across trials were determined by sampling from a multivariate normal distribution using the `mvnrnd` function in matlab. For the primary simulations, we set the correlation coefficient for both amplitudes and phases to 0.8 between the pair of high-distant coherence signals and 0.2 between all other signal pairs. For all signals, the mean amplitude was set to 10

arbitrary units with a variance of 2 and the arbitrary mean phase was set to 180 degrees with a standard deviation of 60 degrees. The standard deviation of the independent white noise added to the sinusoids was set to 1 for the two high-distant coherence traces, and 3 for the low-distant coherence traces.

We performed two additional sets of simulations in order to investigate the effects when the coherence differences between the individual traces are smaller. To generate traces with a moderate coherence difference, we set the amplitude and phase correlation coefficients to 0.65 between the high-coherence traces and 0.35 between all other traces. To generate traces with no coherence differences between them, we set the amplitude and phase correlation coefficients to 0.5 between all traces and we set the standard deviation of the independent white noise added to all traces to 1. All other parameters were identical parameters to those described above for the primary simulations.

For the primary simulations, the left panel of Figure 8.2A shows the 4 traces used from one sample trial using simulated data. The low-coherence pair shows more white noise and uncorrelated deviation in their phases and amplitudes than the high-coherence pair. The left panel of Figure 8.2B shows for one sample session the coherence of the 4 possible trace pairings between locations. This shows that the desired coherence pattern of a high-coherence between the two high-distant coherence traces, but a low coherence between all other pairings of traces was indeed achieved. For one of the additional simulations to generate traces with no coherence differences between pairings, the left panel of Figure 8.4A shows for one sample session the coherence of the 4 possible trace pairings between locations. This shows that the desired coherence pattern for this simulation of an equally moderate coherence between all pairings of traces across locations was again achieved, with some small random differences occurring each session by chance.

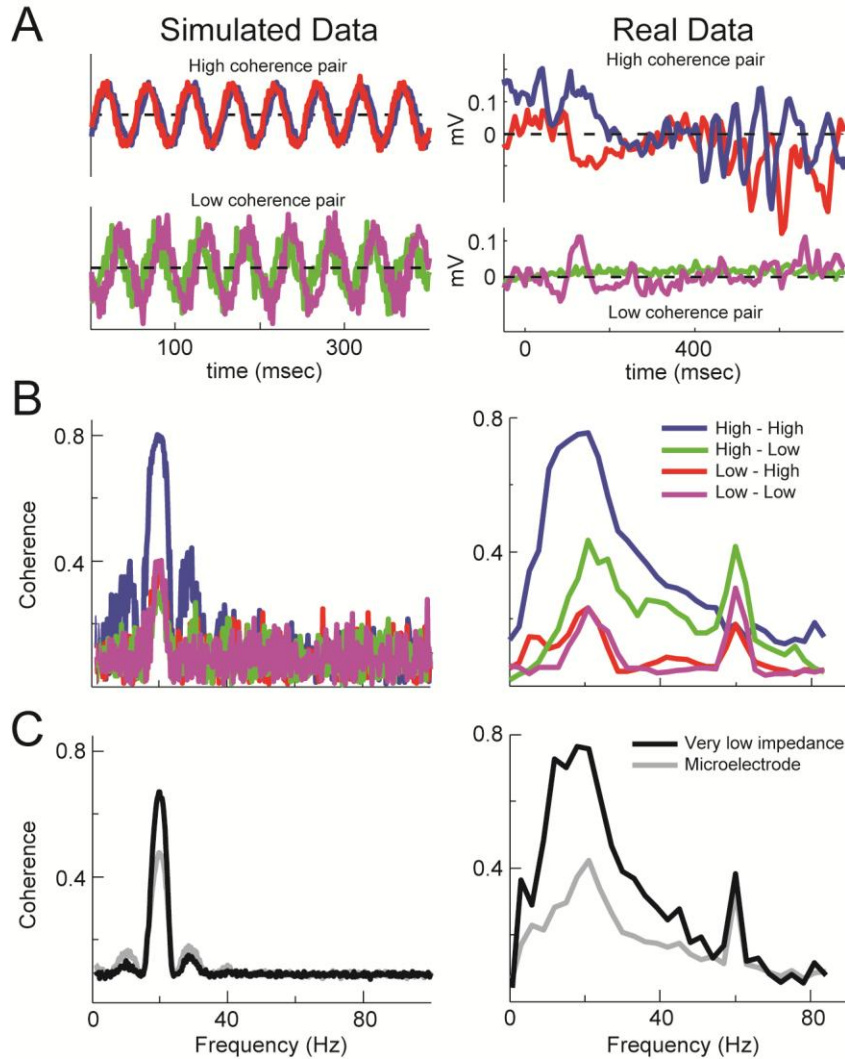


Figure 8.2

We also tested two other methods of simulating LFP traces with the desired coherence patterns. For one method the signal amplitudes were determined as described previously, but the relative phases of trace pairs rather than the absolute phases of each trace were determined according to independent normal distributions. In this method the relative phase between the traces of the higher coherence pair was selected to have a lower standard deviation than the relative phase between the traces of the lower coherence pair. In another method, both pairs were generated with the same phase distribution, but much more white noise was added to the lower coherence pair (100 arbitrary units), which served to sufficiently reduce the coherence involving

those signals. Both of these alternative simulation methods yielded identical conclusions to the data we present here, so we thus decided to omit the results using these methods for presentation clarity and simplicity.

Using real data. Data were collected from one adult monkey (*Macaca mulatta*).

The animal was cared for in compliance with the Guide for the Care and Use of Laboratory Animals and the guidelines of the Vanderbilt Animal Care and Use Committee. Two recording chambers (RC-1, Gray Matter Research; Bozeman, MT) were surgically implanted into the animal's skull, targeting the frontal eye fields in each area. An 8-Channel acute microdrive system (AC8-1, Gray Matter Research) was placed in each chamber. Recordings were subsequently made with glass-insulated tungsten microelectrodes (1–2 M Ω , Alpha Omega Engineering, Nazareth, Israel) from 1 to 2 millimeters below the depth at which spiking activity was first observed on each electrode. LFPs were measured relative to an externally grounded reference which was connected to the chamber and the microdrive casing. Voltage signals were amplified (x 1) by a high impedance HST/8050-G1 head stage (Plexon Inc., Dallas TX), filtered from 0.2 to 300 Hz using a custom built analog filter (Plexon Inc.), further amplified (x 1000), then digitally sampled at 1 kHz using a Plexon MAP system (Plexon, Inc.). The transfer function of the entire recording system was estimated and adjusted for using procedures described previously (Nelson et al., 2008). We performed a deconvolution using an inverse filter restricted to the bandwidth spanning from 0.5 Hz to 450 Hz. Data from frequencies outside this range were attenuated too strongly to recover a stable estimate.

Neural data was recorded while the monkey performed a search-step task, similar to that reported in Murthy et al. (2001). Analyses were performed on data within a time window spanning from 50 to 650 ms following the target presentation, during which the recorded LFPs exhibited 20 Hz activity. 342 correct trials across all target locations were used. 4 out of 15 simultaneously

recorded LFP traces were selected from a single recording session. The traces were selected manually upon inspection of coherence between the channels. For the primary simulations, the traces were selected such that the coherence was high between one pair (designated to be the high-distant coherence traces) and moderate to low between all other pairs. For an additional simulation performed in order to investigate the effects when coherence differences between the individual traces were smaller, a separate group of 4 traces was selected such that the coherence between all trace pairings was approximately equally moderate.

For the primary simulations, the right panel of Figure 8.2A shows the 4 traces used from one sample trial using real LFP data. The right panel of Figure 8.2B shows for one sample session the coherence of the 4 possible trace pairings between locations after assigning each trace to a location. Again, the desired coherence pattern was achieved in which the coherence was high between the two high-distant coherence traces but low between all other pairings of traces. For the additional simulation using traces with approximately equally moderate coherence between all trace pairings, the right panel of Figure 8.4A shows for one sample simulated session the coherence of the 4 possible trace pairings between locations. Again, the desired coherence pattern for this simulation of an approximately equally moderate coherence between all pairings of traces across locations was achieved.

Simulating electrode recordings-basic model. Using the 4 LFP traces generated from simulated or real data, for 500 simulated sessions we calculated the coherence between the locations for two simulated very low impedance electrodes and two simulated microelectrodes. To simulate the very low impedance electrodes, we calculated a weighted average of the activity of the high- and low-distant coherence traces for each location for each session (Figure 8.1B, left). To simulate the microelectrodes, the voltage for each electrode was independently randomly selected to be either the high- or low-distant coherence trace for each session (Figure 8.1B, right). To

simulate different proportions of subregion space having high- or low- distant coherence, we adjusted what we refer to as the high-distant coherent fraction. For the very low impedance electrodes, this fraction determined the relative weights of the high- and low-distant coherence traces when calculating the average between them. For microelectrodes, this fraction determined the probability that a high- or low-distant coherence trace would be selected each session. Simulations were run with this parameter set to 0.1, 0.25, 0.50, 0.75 and 0.9. Note that when using real data, the individual traces themselves were the same between each session. Thus the same precise values were used for the simulated very low impedance electrodes for every session, although the simulated microelectrode coherence values using the real data changed randomly between sessions.

Simulating electrode recordings-spatial sine-wave model. Using 4 simulated LFP traces, for 500 simulated sessions we calculated the coherence between locations for electrodes with different recording site lengths while the underlying voltage profile varied continuously between the high- and low-distant coherence traces for each location along a spatial sine wave. At the peak of the sine wave the voltage was set to the high-distant coherence activity for that location, at the trough of the sine wave the voltage was set to the low-distant coherence activity for that location, and in between the voltage was set to a continuously varying weighted average of the two. For example at the midway point of the sine wave, the voltage was the exact average of the two traces. Thus this weighted average precisely corresponds to the high-distant coherence fraction of the basic model described above. The individual traces were generated using the same parameters as the primary simulations of the basic model, which were the parameters used to generate the results shown in Figures 8.2 and 8.3. Electrode recording sites of different sizes were then modeled by averaging across different lengths of the sinusoid while randomly determining the phase each session according to a uniform distribution spanning from 0 to 360 degrees. Recording site lengths

were specified in units of the number of wavelengths of the underlying spatial sinusoid to allow for the generalization of the results to any voltage profile spatial frequency. The average activity along the recording site length was determined analytically through integration of the sinusoid.

Measuring coherence. We calculated the coherence across locations for each simulated session and electrode type, and report for all simulations the average coherence across sessions. We calculated the coherence using techniques described in Jarvis and Mitra (2001). For the simulated data, we used one large window with a length equal to that of the entire 4 seconds of the simulated trial. For the real data, we used a 200 ms window sliding in time across a trial with a 10 ms step size. We then report the average coherence across time windows for the period of the trial used for the analysis, with the center of the window spanning from 150 to 550 ms after the initial appearance of the target. In both cases, the first in the series of discrete prolate spheroidal sequences were used to window the data, which provided optimal frequency localization for each finite temporal window (Slepian, 1983). This provided a frequency bandwidth of ± 0.25 Hz and ± 5 Hz for the simulated and real data, respectively. We also investigated the results using the Fisher transformed and bias corrected z-scores of coherence as described in Bokil et al. (2007) and found no differences in the pattern of results.

RESULTS

Basic model

Figure 8.2C shows the resulting coherence between simulated very low impedance electrodes and microelectrodes based on the basic model (Figure 8.1A and B). The simulated very low impedance electrodes had higher coherence than the simulated microelectrodes using both simulated (left column) and real (right column) LFP traces.

The basic result of Figure 8.2C assumes a balance of subregion space corresponding to high and low distant coherence activity. If on the other hand a location is completely comprised of a single subregion, a trivial consequence of the model is that the high- and low-impedance electrodes will record the same values. To further elucidate the entire relationship of these results to the spatial inhomogeneity of the underlying voltage coherence profile, we manipulated the high-distant coherence fraction of the basic model (see Materials and Methods) across a range of values (Figure 8.3). As expected, when this fraction is near the limits of 0 and 1, smaller differences between the electrode types are observed. But at even modest departures from uniformity, considerable differences between the electrodes appear. These differences peak when the voltage coherence profile is farthest from uniform.

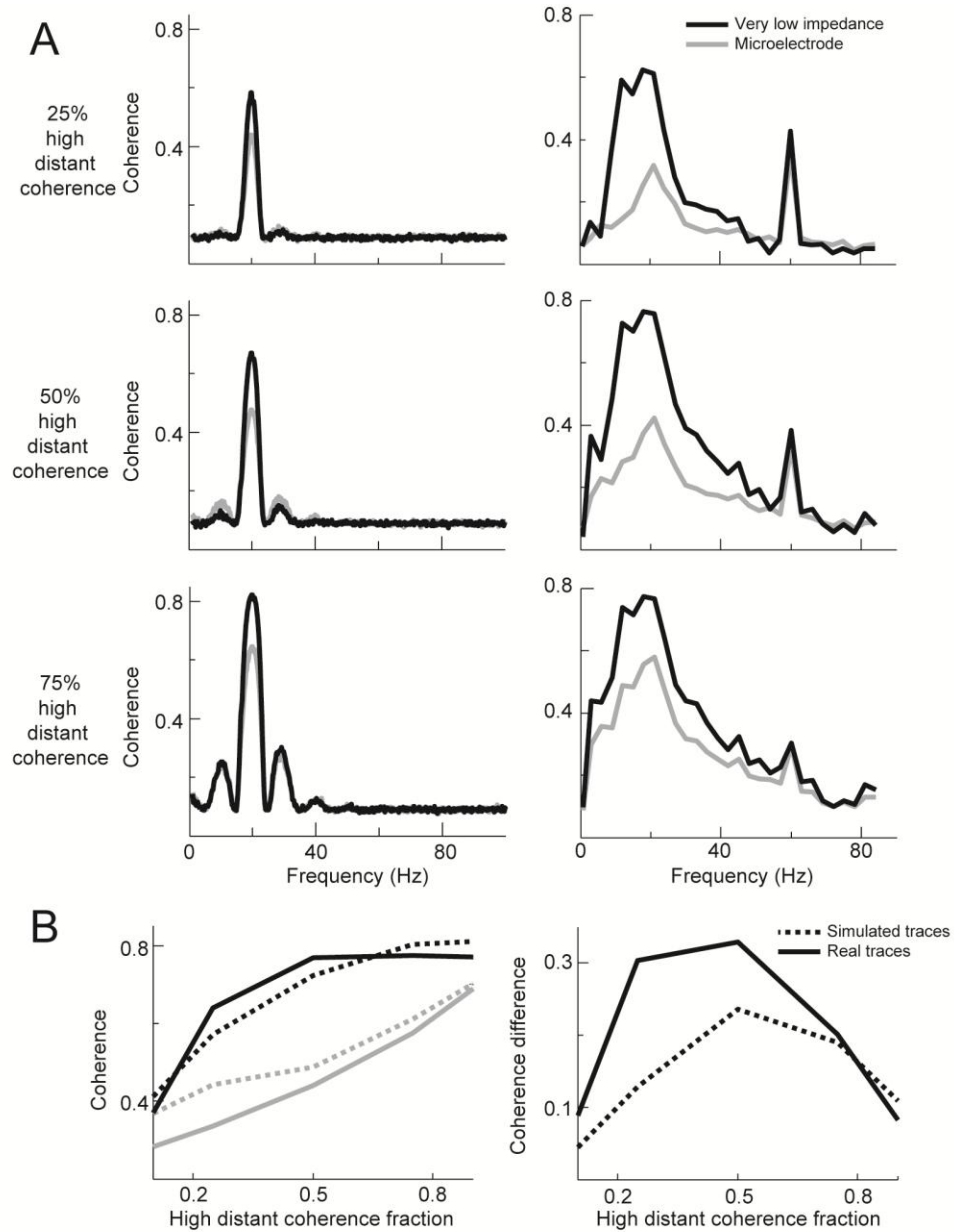


Figure 8.3

The results of Figure 8.3 show that when there is a relatively large difference in distant coherence between two subregions, averaging across them serves to increase the distant coherence reported. To what extent does this still occur when the voltages in the subregions are distinct, but with smaller or no differences in distant coherence between them? To investigate this, we simulated additional sessions using both simulated and real LFP traces with smaller or no coherence differences between the pairs of traces (see Materials and Methods). Figure 8.4 shows

that the increase in coherence for low impedance electrodes remained relatively strong for these simulations. Moreover, the increase continues to peak at a high-distant coherence fraction of 0.5. Thus, the inhomogeneity of an underlying voltage profile regardless of its overall distant coherence gradient appears to be the key factor driving this effect. These results were also consistent across further simulations we performed at different overall levels of coherence while varying the coherence differences between the trace pairs (results not shown). This further indicates the generality and robustness of this effect.

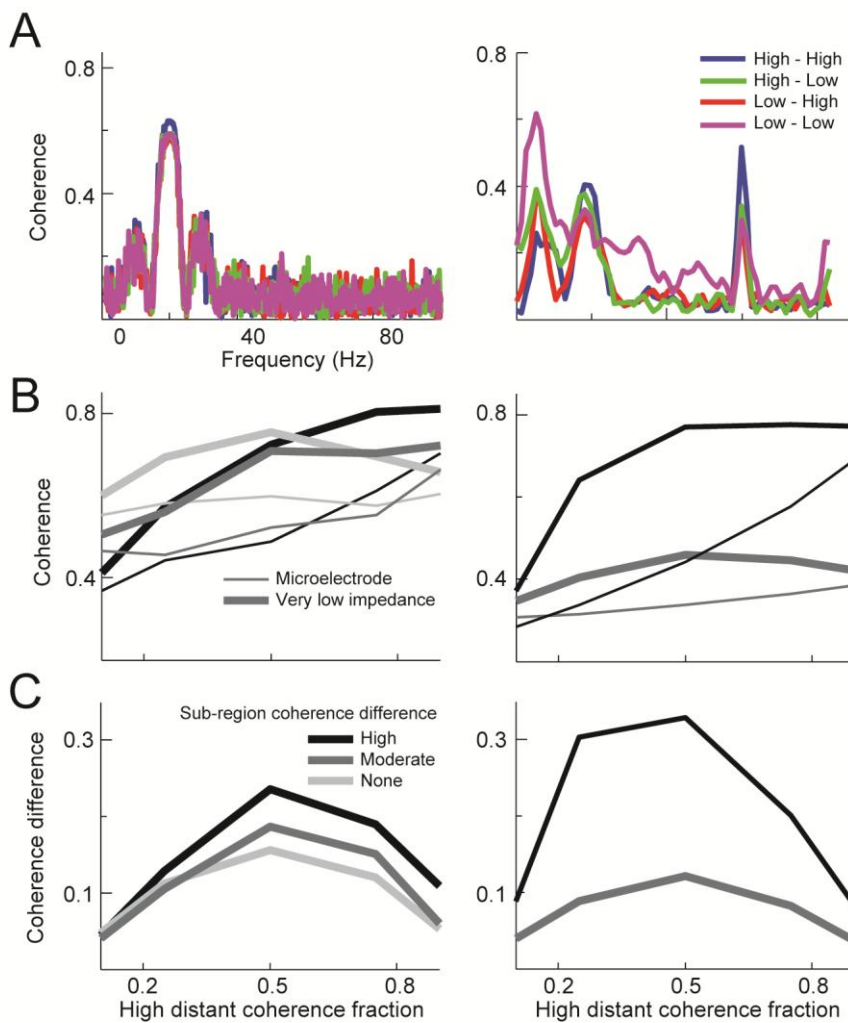


Figure 8.4

LFP, ECoG and EEG comparisons

Given the effect shown by the basic model, one might expect electrode size differences to play a role when comparing coherences between EEG, ECoG and LFP data which are typically recorded with electrodes of very different sizes. EEG electrodes are typically 5 to 10 mm in diameter (Nunez and Srinivasan, 2006), ECoG electrodes tend to be about 2 to 5 mm in diameter for human studies (e.g. Canolty et al. 2006) or smaller for animal studies (e.g., Sharott et al, 2006; Taylor et al. 2005), whereas the recording sites for LFP electrodes can have lengths on the order of tens of microns or even smaller (Yaeli et al. 2009).

However, it is important to first note that the very nature of the underlying voltages themselves differs between these different sources of data. Cortical surface voltages underlying ECoG data are thought to be more spatially spread than intracranial voltages underlying LFP data (Nunez and Srinivasan, 2006, 2010). Scalp voltages underlying EEG data are in turn thought to be more spatially spread than cortical surface voltages underlying ECoG data (Nunez and Srinivasan, 2006, 2010). Thus, electrode sizes cannot be directly compared between the data types as the important factor described in the theoretical model that can lead to an effect of electrode size on recordings is the size of the electrode in relation to the spatial variation of the underlying voltage being measured. For example, the electrode size-related coherence effect that might result from one particular size of electrode when recording potentials at the cortical surface would be different than what would occur for the same electrode recording potentials either within the brain or on the scalp. However, within each data type one can directly compare more moderate electrode size differences.

To demonstrate these differences between the data types and investigate if any effects of electrode size on coherence within any of the data types might be subtly visible across published studies, we performed a quantitative literature search of published coherence values. Coherence will depend on a number of factors, including frequency and behavioral state among others, though the effects of such factors can be difficult to predict (Bullock et al, 1995). However,

coherence shows a direct and consistent dependence on electrode separation for all three data types, resulting largely from the volume conduction of electrical signals. Thus it is important to consider the inter-electrode distance when comparing coherence across studies, and in particular across data types. In Figure 8.5 we plot available data in the literature for the coherence of different data types as a function of inter-electrode distance, documenting the electrode size and signal types for each data series. When possible, we selected the highest frequency data available in each study. We note the behavioral state of the subjects in each study in the figure caption.

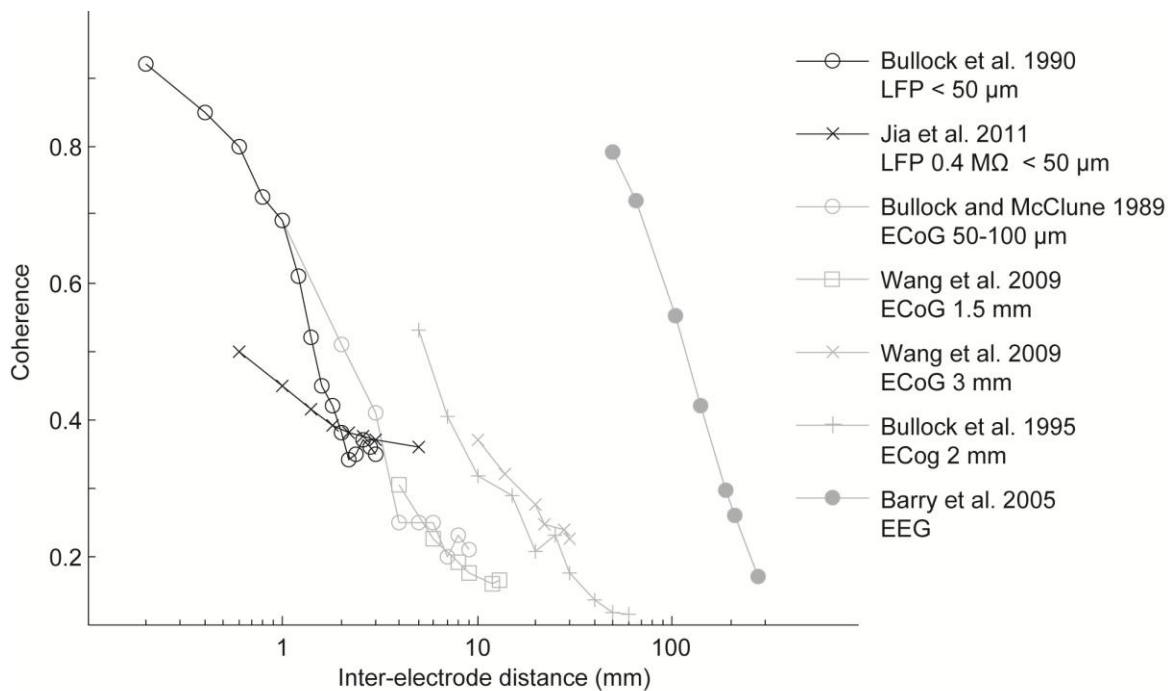


Figure 8.5

The differing spatial spread of the voltages underlying each data type is immediately apparent in Figure 8.5. Similar coherences tend to be found at increased inter-electrode distances for ECoG data relative to LFP data, and for EEG data relative to both ECoG and LFP data. For EEG data, scalp voltages are spatially spread out enough that recordings have been previously shown to be independent of electrode size for all practical purposes (Nunez and Srinivasan, 2006). For ECoG data however, further inspection of Figure 8.5 reveals that a modest trend may exist for larger electrodes to report higher coherence. Notably, this was investigated directly in one study

(Wang et al., 2009) that found that 3-mm-diameter electrodes showed higher coherence at the same inter-electrode distances than 1.5-mm-diameter electrodes recorded from simultaneously in the same patient. This agrees with the qualitative prediction of the basic model described above. For LFP data, there is insufficient published coherence results at multiple electrode distances to allow us to come to an empirically based conclusion of the presence or absence of a noticeable effect of electrode size on typical recordings of that data type.

Spatial sine-wave model

We used the spatial sine wave version of our model (Figure 8.6A) to quantify when and to what extent the effect of electrode size found in the basic model is expected to occur, and further to test if this agrees with the trends in the literature data shown in Figure 8.5. Figure 8.6B shows the resulting coherence for any ratio of an electrode's recording site length to the wavelength of the underlying spatial sine wave of activity in the model. This ratio captures the amount that the voltage profile changes over the extent of a recording site, which is the key factor described by the physical model as leading to possible effects of electrode size on recorded voltages. Moreover this ratio provides a "common currency" to compare expected electrode-size-related effects between data types, even as the nature of the underlying neural signals indeed varies between them. As anticipated given the results from the basic model, coherence generally increases as this ratio increases. However at both very low and very high values of this ratio, the coherence asymptotes and is generally insensitive to the precise electrode size. The results quantify a range between values of about 0.8 to about 8 where the ratio is more sensitive to the particular electrode size.

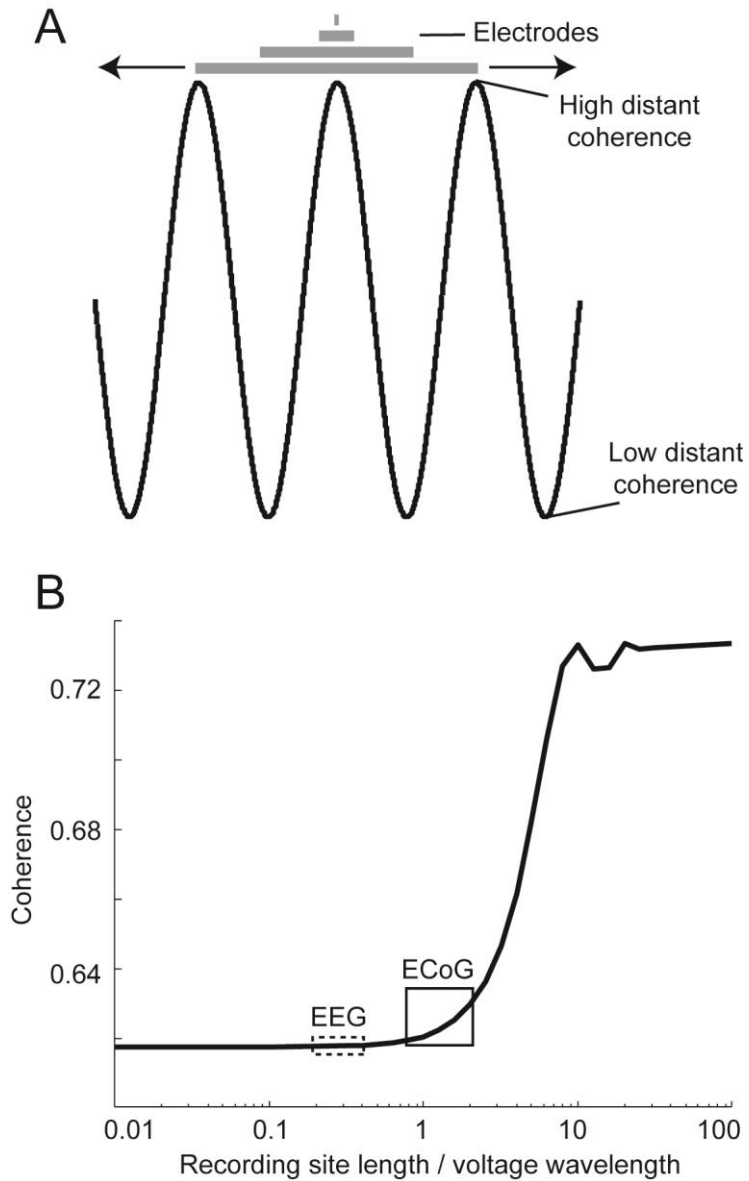


Figure 8.6

Quantitative predictions can be made from the information in Figure 8.6B by specifying one of the two variables in the ratio. For example, the corresponding wavelength of the highest spatial frequency present above noise levels in the human cortical surface potential has been estimated to be 2.5 mm per cycle (Freeman et al., 2000). For this spatial frequency, this ratio for typical ECoG electrodes would range between 0.8 and 2.0, as indicated on the figure. Modest effects of electrode size on coherence are indeed expected within this range, which is consistent with Wang et al. (2009) and the other ECoG studies shown in Figure 8.5. In contrast, the

corresponding wavelength of the highest spatial frequency present above noise levels in the human scalp potential has been estimated to be 2.5 cm per cycle (Freeman et al., 2003). For this spatial frequency, this ratio for typical EEG electrodes would range between 0.2 and 0.4, as indicated on the figure. No appreciable effects of electrode size are expected within this range, which confirms previous evidence that EEG data is independent of electrode size for the electrodes typically used to record it. For LFP data, the highest spatial frequency present above noise level within the brain has not yet directly been shown. However, while it is not a simple step to convert the estimates of the point spread function from Katzner et al. (2009) and Xing et al. (2009) into a maximum spatial frequency, a wavelength on the order of 250 microns per cycle might provide a reasonable educated guess. At this voltage profile wavelength, it seems reasonable that a 200-micron-diameter electrode (with a corresponding ratio of 0.8) might show subtle increases in coherence in some studies (Kay and Lazarra, 2010) but not others (Bullock et al., 1989). This would also suggest, however, that differences among the smaller sizes of microelectrodes typically used during depth recordings would not occur. More evidence of this spatial frequency limit in intracranial voltage is needed however to draw firmer conclusions about the model's prediction.

DISCUSSION

We developed and tested a simple physical model for LFP recordings of electrodes with large differences in recording site sizes. The model predicts that low impedance electrodes tend to report higher coherence than higher impedance microelectrodes. However, intrinsic to the model is that voltages must vary on a spatial scale smaller than the size of the larger electrode recording site for the electrode size to make a difference. Moreover, this difference between electrode sizes continuously increases as the voltage profile over the length of the electrode's recording site is increasingly inhomogenous. This effect is robust with respect to the strength of the coherence gradient along the spatial voltage profile. We compared previously published reports in the

literature for the coherence of LFP, ECoG and EEG data and found evidence for a modest effect of electrode size in ECoG data, but not in EEG or LFP data. We further developed the model to quantify at what electrode sizes relative to a given voltage profile spatial frequency the electrode size is expected to impact recorded coherence. Combining this with estimates in the literature for the spatial frequencies present in all these data types confirms the suggestions of the literature data.

As the model points out, the suggestion that a pair of lower impedance electrodes favors distantly coherent activity relies upon the spatial voltage profiles at the two recording locations. For the extreme example of spatially uniform voltages, the model trivially shows that there would be no expected effect of recording site size. But as the voltage profiles increasingly depart from uniform, both the basic model and the spatial sine wave model confirm that the electrode size effect continuously increases. In the basic model this can be observed as the high-distant coherence fraction changes (Figure 8.3 and 8.4). In the spatial sine wave model this can be observed as the coherence increases continuously as the number of voltage profile cycles along a recording site's length increases (Figure 8.6), excluding the plateaus observed for relatively very small or very large electrodes. The additional simulations varying the coherence gradient (Figure 8.4) further show that this effect is general to any voltage gradient, regardless of the amount that the distant coherence changes along it. It should be emphasized that though there were little to no coherence differences between the combinations of trace pairs used for these additional simulations, the individual traces were still distinct and sufficiently independent of each other, which is required for the effect to occur.

As we mentioned, the results of the spatial sine wave version of the model shown in Figure 8.6 can be used to estimate effects for LFP, ECoG or EEG data. The precision of any practical implication of the model however is limited by the accuracy of the knowledge of the spatial frequencies present in the underlying voltages. For LFPs, the scale of this spatial variation

has yet to be sufficiently quantified. Still, the estimates of Katzner et al. (2009) and Xing et al. (2009) do clearly suggest that LFP voltages will not appreciably vary on a scale of tens of microns, which is the lengths of electrode recording sites in typical use by neurophysiologists (Yaeli et al., 2009). Thus the effects of microelectrode sizes for recording LFPs should be negligible, as we have argued (Nelson and Pouget, 2010).

For ECoG data, further empirical evidence may be needed to corroborate the putative effect that we have shown in literature data and our simulations. This evidence would be useful either in the form of further direct tests similar to the study of Wang et al. (2009), or corroboration of the estimates of Freeman et al. (2000) of the spatial frequencies present in cortical surface potentials. If it holds true, the effect for ECoG data would not suggest per se that data from larger electrodes is faulty. Rather it would just be an effect that must be kept in mind when interpreting that data, particularly when considering coherence.

The model we present implies that once the electrode size is small enough relative to the spatial variation of the underlying voltages being measured, recorded data should be independent of electrode size. This together with well understood sampling theory dictates that using such sufficiently small electrodes with inter-electrode spacing that is small enough to avoid spatial aliasing of the signal guarantees the ability to recover all of the information present in the underlying voltages. Thus, it may be advisable to attempt to accomplish this during EEG, ECoG or LFP electrode array design, though it is conceivable that some tradeoffs and limitations surrounding this may exist for some applications. Still, knowledge of the physical model of electrode recordings and the nature of the underlying signals one is trying to record should prove helpful for the choice and design of arrays for any application.

It should also be noted that multiple spatial frequencies are present in LFP, ECoG and EEG data. Our results show that the effect of electrode size, to the extent that it exists at all for a given data type, should be increasingly larger for the higher spatial frequency signals present. The

ranges shown in Figure 8.6 for EEG and ECoG data correspond to the most affected spatial frequencies for these data types. Each data type also includes contributions from lower spatial frequency signals as well, which would correspond to regions to the left of these indicated ranges on the plot.

The model we present also suggests that the variance of coherence across sessions for different electrode sizes would be an interesting quantity to investigate empirically, with the prediction that this should be higher for smaller electrodes whenever the coherence is dependent on electrode size.

The model that we present is an intentionally simple model targeted at the electrodes themselves and exploring the theoretical physical nature of how and under what circumstances the sizes of their recording sites might affect their performance. Biological sources of signals could certainly be modeled, but the implications resulting from this would be tangential to our focus on electrodes and would come at a cost of undesirable added complexity. The basic model we tested applies the most extreme version of a spatial voltage gradient, essentially a step function, to demonstrate whether or not the effect could be a possibility for less extreme, more realistic profiles. This does not reflect a presumption that voltages in the brain would actually change as a step function between boundaries. Beyond this, the spatial sine wave model allows us to generalize to the expected effect for any spatial frequency present in the voltage profile. More complicated profiles could of course be modeled, but as Fourier analysis dictates, these would be identical to a summation of spatial sinusoids of different frequencies.

Existing studies have modeled electrode size under different contexts than what we have done here. Ollikainen et al. (2000) considers the electrical shunting effect of covering the scalp with conductive EEG electrodes. A notable pair of studies (Moffitt and McIntyre 2005, Lempka et al 2011) modeled the effect of electrode recording site size on recording spiking activity within the brain using a more complex finite element model with realistic biological sources of both the

signals being measured and the noise occluding it. Recording site sizes affect their model by changing the conductivity on the particular locations of an electrode between the much lower value for that of recording sites and the much higher value for that of the insulated shank. Thus the model they present did not directly look at the effects of simple spatial averaging of potentials as the model we present does. A further inspection of their model might reveal a near equivalence to that of the simple model we present here. However, it is not immediately clear that this is the case. Notably, in their description of their model or their results, the authors never explicitly mention this property of spatial averaging, which is inherent to the physical model of electrode recordings espoused by Robinson (1968). Further inspection of this in the model they present could be of theoretical interest. Interestingly, the model they present produces results for spiking activity amplitude that are similar to what we show here for LFP, ECoG and EEG coherence. Specifically, they suggest that spike recording is fairly independent of recording site size over the range of contact sizes typically employed by neurophysiologists (177 to 1250 μm^2 , the tungsten microelectrode equivalent of about 2.4 to 0.5 Mohm impedances (Yaeli et al., 2009)), but they did find decreased amplitudes for a very large electrode that they simulated (10,000 μm^2 , the tungsten microelectrode equivalent of at least < 0.1 Mohm impedance (Yaeli et al., 2009)).

In contrast, the model we present is macroscopic and considerably simple. We believe this is the appropriate level of complication for the aim of this study, which is to provide a simple intuitive model for members of the field to understand and apply. This is in contrast to more complicated models which may be treated too often as a “black box” by many readers rather than engendering an intuitive understanding of their underlying function.

We believe more adherence to and understanding of the physical nature of electrode recordings in the field and in the literature will aid the discussion of the putative effects of recording site shape and size on recorded potentials. Too many previous claims in the literature that these properties are important to account for while interpreting LFP data (Berens et al. 2008;

Pesaran 2009; Kay and Lazarra 2010) do not appear to adhere to any theoretical basis or provide any explanations as to precisely how or why effects of these properties would come about. The simple model we explore in our simulations provides a more solid theoretical basis on which to judge these claims. The results for LFP data indicate to the contrary, that these properties likely do not have a substantial effect for the electrodes typically employed by neurophysiologists. Data comparing microelectrodes of different impedances within this range of typical use will clearly be important to draw firmer conclusions.

ACKNOWLEDGEMENTS

We thank Jeff Schall for graciously sharing data collected in his laboratory. Matthew Nelson was supported by the Programme de bourses d'excellence Eiffel.

REFERENCES

- Barry RJ, Clarke AR, McCarthy R, Selikowitz M.** Adjusting EEG coherence for inter-electrode distance effects: an exploration in normal children. *International Journal of Psychophysiology* 55: 313–321, 2005.
- Bedard C, Rodrigues S, Roy N, Contreras D, Destexhe A.** Evidence for frequency-dependent extracellular impedance from the transfer function between extracellular and intracellular potentials. *J Comput Neurosci* 29: 405–421, 2010.
- Berens P, Keliris, GA, Ecker AS, Logothetis NK, Tolias AS.** Feature selectivity of the gamma-band of the local field potential in primate primary visual cortex. *Front Neurosci* 2: 199–207, 2008.

Bokil H, Purpura, K Schoffelen JM, Thomson D, Mitra P. Comparing spectra and coherences for groups of unequal size. *J Neurosci Meth* 159: 337–345, 2007.

Bullock TH, Buzsaki G, McClune MC. Coherence of compound field potentials reveals discontinuities in the CA1-subiculum of the hippocampus in freely-moving rats. *Neuroscience* 38: 609–619, 1990.

Bullock TH, McClune MC. Lateral coherence of the electrocorticogram: a new measure of brain synchrony. *Electroencephalography and clinical Neurophysiology* 73: 479–498, 1989.

Bullock TH, McClune MC, Achimowicz JZ, Iragui-Madoz VJ, Duckrow RB, Spencer SS. EEG coherence has structure in eth millimeter domain: subdural and hippocampal recordings from epileptic patients. *Electroencephalography and clinical Neurophysiology* 96: 161–177, 1995.

Canolty RT, Edwards E, Dalal SS, Soltani M, Nagrajan SS, Kirsch HE, Berger MS, Barbaro NM, Knight RT. High gamma power is phase-locked to theta oscillations in human neocortex. *Science* 313: 1626–1628, 2006.

Freeman WJ, Holmes MD, Burke BC, Vanhatalo S. Spatial spectra of scalp EEG and EMG from awake humans. *Clin Neurophysiol* 114: 1053–1068, 2003.

Freeman WJ, Rogers LJ, Holmes MD, Silbergeld DL. Spatial spectral analysis of human electrocorticograms including the alpha and gamma bands. *J Neurosci Meth* 95: 111–121, 2000.

Jarvis MR, Mitra PP. Sampling properties of the spectrum and coherency of sequences of action potentials. *Neural Comput* 13:717–749, 2001.

Jia X, Smith MA, Kohn A. Stimulus selectivity and spatial coherence of gamma components of the local field potential. *J Neurosci* 31: 9390–9403, 2011.

Katzner S, Nauhaus I, Benucci A, Bonin V, Ringach DL, Carandini M. Local origin of field potentials in visual cortex. *Neuron* 61, 35–41, 2009.

Kay LM, Lazzara P. How global are olfactory bulb oscillations? *J Neurophysiol* 104: 1768–1773, 2010.

Lemon R. *Methods for neuronal recording in conscious animals.* Chichester, NY: Wiley-Interscience, 1995, pp. 74–75.

Lempka SF, Johnson MD, Moffitt MA, Otto KJ, Kipke DR, McIntyre CC. Theoretical analysis of intracortical microelectrode recordings. *J Neural Eng* 8: 045006, 2011.

Logothetis NK, Kayser C, Oeltermann A. In vivo measurement of cortical impedance spectrum in monkeys: Implications for signal propagation. *Neuron* 55: 809–823, 2007.

Moffitt MA, McIntyre CC. Model-based analysis of cortical recording with silicon microelectrodes. *Clin Neurophysiol* 116: 2240–2250, 2005.

Murthy A, Thompson KG, Schall, JD. Dynamic dissociation of visual selection from saccade programming in frontal eye field. *J Neurophysiol* 86: 2634–2637, 2001.

Nelson MJ, Pouget P, Nilsen EA, Patten CD, Schall JD. Review of signal distortion through metal microelectrode recording circuits and filters. *J Neurosci Meth* 169: 141–157, 2008.

Nelson MJ, Pouget P. Do electrode properties create a problem in interpreting local field potential recordings? *J Neurophysiol* 103: 2315–2317, 2010.

Nunez PL, Srinivasan R. *Electric fields of the brain: The neurophysics of EEG 2nd edition*. New York, NY: Oxford University Press, 2006.

Nunez PL, Srinivasan R. Scale and frequency chauvinism in brain dynamics: too much emphasis on gamma band oscillations. *Brain Struct Funct* 215:67–71, 2010.

Ollikainen JO, Vauhkonen M, Karjalainen PA, Kaipio JP. Effects of electrode properties on EEG measurements and a related inverse problem. *Med Eng Phys* 22: 535–545, 2000.

Pesaran B. Uncovering the mysterious origins of local field potentials. *Neuron* 61: 1–2, 2009.

Robinson DA. The electrical properties of metal microelectrodes. *Proc IEEE* 56: 1065–1071, 1968.

Sharott A, Magill PJ, Bolam JP, Brown P. Directional analysis of coherent oscillatory field potentials in the cerebral cortex and basal ganglia of the rat. *J Physiol-London* 562: 951–963, 2005.

Slepian D. Some comments on Fourier analysis, uncertainty and modeling. *SIAM Review* 25:379–393, 1983.

Taylor K, Mandon S, Freiwald WA, Kreiter AK Coherent oscillatory activity in monkey area V4 predicts successful allocation of attention. *Cereb Cortex* 15: 1424–1437, 2005.

Tielen AM, Giesen C, Mollevanger W. (1971) Some mechanical and electrical characteristics of metal microelectrodes. *Inst. of Med. Phys. TNO. Rep. 2.3.65/1 MEI*, 1971.

Wang W, Degenhart AD, Collinger JL, Vinjamuri R, Sudre GP, Adelson PD, Holder DL, Leuthardt EC, Moran DW, Boninger ML, Schwartz AB, Crammond DJ, Tyler-Kabara EC, Weber DJ. Human motor cortical activity recorded with Micro-ECOG electrodes during individual finger movements. *Conf Proc IEEE Eng Med Biol Soc* 586–589, 2009.

Xing D, Yeh C-I, Shapley, RM. Spatial spread of the local field potential and its laminar variation in visual cortex. *J Neurosci* 29: 11540–11549, 2009.

Yaeli S, Binyamin E, Shoham S. Form-function relations in cone-tipped stimulating microelectrodes. *Front Neuroeng* 2:13, 1-8, 2009.

Figure legends

Figure 8.1. Simple model of an LFP activity profile to produce a difference in recorded coherence between electrode types. A: Diagram of discrete subregions in two distant locations with different patterns of coherent activity. The subregions between the locations with high-distant coherence are highly coherent with each other, while those subregions with low-distant coherence are neither coherent with each other, nor with the high-distant coherence subregions. B: Basic model of different electrode types within the two locations. Very low impedance electrodes span both subregion types and are modeled to average the activity between them for each session. Microelectrodes are located in only one subregion at a time and are modeled to report the activity of a single randomly selected subregion for each session.

Figure 8.2. Simulated coherence patterns using simulated and real LFP traces. The left column corresponds to results using simulated LFP traces and the right column corresponds to results using real LFP traces. A: Sample individual signals for the signals with high-distant coherence (red and blue) and the signals with low-distant coherence (green and magenta). B: Direct inter-subregion coherence across two locations as labeled on the figure for the four subregion combinations. The high-high (blue) trace shows the direct coherence between the high-distant coherence subregions in each location (see Figure 1A); the high-low (green) trace shows the direct coherence between the high-distant coherence subregion in location 1 and the low-distant coherence subregion in location 2; the low-high (red) trace shows the direct coherence between the low distant coherence subregion in location 1 and the high-distant coherence subregion in location 2; and the low-low (magenta) trace shows the direct coherence between the low-distant coherence subregions in each location. C: Average coherence across 500 sessions for simulated very low impedance electrodes (black lines) and simulated microelectrodes (gray lines). The high-distant coherence fraction was set to the default value of 0.5.

Figure 8.3. Simulated coherence patterns of the basic model while varying the high-distant coherence fraction. A: Average coherence across 500 sessions for simulated very low impedance electrodes and simulated microelectrodes while setting the high-distant coherence fraction to 0.25 (top row), 0.5 (middle row), and 0.75 (bottom row). The left column corresponds to results using simulated LFP traces and the right column corresponds to results using real LFP traces. B: Average 20 Hz coherence while varying the high-distant coherence fraction. The left panel shows the very low impedance electrode (black) and microelectrode (grey) average 20 Hz coherence across 500 simulated sessions using simulated (dashed) and real (solid) LFP traces at different values of the high-distant coherence fraction. The right panel shows for the same data the difference between the simulated very low impedance electrodes and microelectrodes.

Figure 8.4. Simulated coherence patterns of the basic model while varying the amount of coherence difference between subregions. The left column corresponds to results using simulated LFP traces and the right column corresponds to results using real LFP traces. A: Direct inter-sub-region coherence across two locations as labeled on the figure for the four sub-region combinations. The left panel reflects an example session of the simulations with no coherence difference between the individual traces (corresponding results shown in light grey in panels B and C). The right panel reflects an example session of real LFP traces selected to have approximately equally moderate coherence. Conventions are the same as in Figure 8.2B. B: Average 20 Hz coherence while varying the sub-region coherence difference and the high-distant coherence fraction. Both panels show the very low impedance electrode (thick) and microelectrode (thin) average 20 Hz coherence across 500 simulated sessions. Results where the underlying traces had high, moderate or no coherence differences are shown in black, dark grey and light grey, respectively. The high coherence difference results are duplicated from Figure 8.3B, and shown here for comparison. C: Difference in coherence between simulated very low impedance

electrodes and microelectrodes for the data in panel B. Plotting conventions are the same as in panel B.

Figure 5. Coherence against inter-electrode distance data in the literature for LFP, ECoG and EEG data. The referring article as well as the data type and the approximate electrode diameter for each data series is shown in the legend. Bullock et al. (1990) data are from their Figure 8.2B, 20–40 Hz, collected during slow-wave sleep and paradoxical sleep. We report the average across these two. This study lists the electrode shank diameter to be 50 μm , suggesting the diameter across the uninsulated tip is at least less than this. Jia et al. (2011) data are from their Figure 8D, 30–50 Hz, showing spontaneous activity with the subject under anesthesia. This study indicates the electrodes used had impedances of 0.4 M Ω . Given the geometrical constraints and the relation between impedance and surface area described in Yaeli et al. (2009), this likely suggests a tip size less than 50 μm . Bullock and McClune (1989) data are from their Figure 4 lower panel, 35–40 Hz, collected with the subject under light anesthesia. Wang et al. (2009) data are from their Figure 2B, 60–120 Hz, collected with the subject awake and relaxed with their eyes open. Bullock et al. (1995) data reflect averages of data shown in their Figures 3, 4 and 5, corresponding to frequency ranges spanning from 20 to 80 Hz, collected during slow wave sleep, alert or sedated behavioral states. Barry et al. (2005) data are from the regression line in their Figure 1 top panel, 1.5–25 Hz, collected with the subject in an awake resting state with their eyes closed.

Figure 8.6. Spatial sine-wave model and results A: Model illustration. In this version of the model, the amount of distant coherence at each point in space is varied continuously following a sine wave. Different sizes of electrode recording sites are modeled to average the underlying activity along their lengths with a randomly selected initial phase for each simulated session. B: Simulated coherence against the ratio of electrode recording site length to the wavelength of the

sinusoidal voltage profile. The average 20 Hz coherence across sessions using simulated data is shown. The putative ranges corresponding to typical EEG and ECoG electrodes at the corresponding highest spatial frequency of the voltage underlying each data type are indicated. For LFP recordings this spatial frequency is presently not clearly known.

Chapter 9

Electrical signal distortion in neural tissue on a
microscale

BACKGROUND

The extracellular environment in the brain is typically considered to be and modeled as a homogenous conductive milieu (e.g., Gold et al., 2006; Nunez and Srinivasan, 2006; Linden et al., 2011). However, on a microscale, extracellular space is unequivocally not homogenous (Bedard et al., 2006); a point which quickly becomes apparent upon viewing brain tissue in a slice preparation under a microscope. Very little of the extracellular space is actual “space”; rather it is mostly comprised of neural structures such as glial cells, neuronal cell bodies, axonal fibers, dendritic structures, blood vessels, and other inhomogeneities. Indeed extracellular fluid is thought to comprise only 12–25% of the brain’s volume (Peters et al., 1991; Braitenberg and Schuez, 1998).

This homogeneity assumption shapes the interpretation of extracellularly recorded data, particularly local field potentials (LFPs). Under this assumption, electrical current and potentials are viewed as propagating freely in all directions from all neural sources, as would happen if the neural sources were suspended in saline at the same positions. The LFP at a given point in space then would be considered to represent a ‘democratic’ summation of the electrical potential contributions resulting geometrically from sources and sinks everywhere in the brain. However, if the microscale inhomogeneities inherent to neural tissue had an appreciable effect on the propagation of electrical signals, this would not be the case. If, for example, the presence or absence of a nearby bundle of axonal fibers were shown to affect the contribution of a given source or sink to the potential at other locations in the extracellular space, it would reject this assumption and change this view of the nature of LFPs.

Recently in the field there has been a marked interest in understanding the origin and the underlying nature of the LFP (Logothetis et al., 2007; Katzner et al., 2009; Xing et al., 2009; Kajikawa and Schroeder, 2011; Linden et al., 2011), as well as in knowing the reverse effect that LFPs can have on the membrane voltages of individual cells (Frohlich and McCormick, 2010; Anastassiou et al., 2011;). All of these authors, however, do not consider or address the potential

impact of microscale tissue inhomogeneities. In an older work, David A. Robinson (1968) described how such inhomogeneities, specifically the ubiquitous presence of glial cells in brain tissue, would be expected to considerably impact the extracellular recording of spiking activity. Robinson, however, provides only anecdotal evidence to support his claim, and the effect of microscale inhomogeneities has until now never been directly tested experimentally.

It bears mentioning that it is already known in certain regards that LFPs are not a ‘democratic’ representation of the average activity of all cells in region (Linden et al., 2011). For example, it has been known that a cell type’s morphology determines the geometric distribution of sources and sinks that exist when the cell receives synaptic input, which affects how that cell will contribute to the extracellular potential at more distant locations (Leung, 1990; Nunez and Srinivasan, 2006). A cortical basket cell, for example, has a roughly spherical dendritic structure and comprises what has been called a closed field when the cell receives synaptic input (Leung, 1990; Nunez and Srinivasan, 2006). This is a field in which an equal amount of current sources, in this case the cell’s dendritic structure, surrounds the same amount of current sinks, in this case the central cell body, in a structure roughly mimicking concentric spheres (Lorente de Nó, 1947; Nicholson, 1979; Nunez and Srinivasan, 2006). Because of the geometric cancelation of current sources and sinks, such fields do not appreciably contribute to the extracellular potential beyond the extent of the dendritic structure of the cell itself (Lorente de Nó, 1947; Nicholson, 1979; Nunez and Srinivasan, 2006). The present work seeks to address whether the variations in the microscale inhomogeneities of neural tissue surrounding cells presents another ‘undemocratic’ factor that should be considered when contemplating the nature of LFP activity and interpreting LFP data. We also extend these implications to the ranges of frequencies comprising spiking activity as well.

RESULTS

We characterized the effect of microscale inhomogeneities on the transmission of electrical signals in the brain using a novel application of existing extracellular and intracellular recording techniques in rat brain slice preparations. Using 3 glass pipette electrodes in corticostriatal slices, we manipulated the intracellular voltage of an individual cell using the patch clamp technique while simultaneously recording extracellularly from two different locations- one with an obstructed path from the cell being patched and one with an unobstructed path. Sufficient recordings to warrant further analysis were performed for two different primary obstruction types- cell bodies, including glial cells and other neurons (n=33), and bundles of axonal fibers (n=18). These obstructions were readily visible during the experiment via a microscope, which was used to guide the placement of the extracellular pipettes, with the intent of maximizing the difference in the severity of obstructions between the obstructed and unobstructed pipettes. The patched cell's membrane voltage was manipulated using sine wave currents with frequencies spanning from the slow range of LFPs (< 10 Hz) to frequencies comprising action potential waveforms (~ 1 kHz) and higher. Images of example recordings for cell and fiber obstructions, and a diagram of the experiment performed are shown in Figure 9.1. The basic results here have been presented previously in abstract form (Nelson, Bosch, Venance and Pouget, 2010 *Soc Neurosci Abstr*).

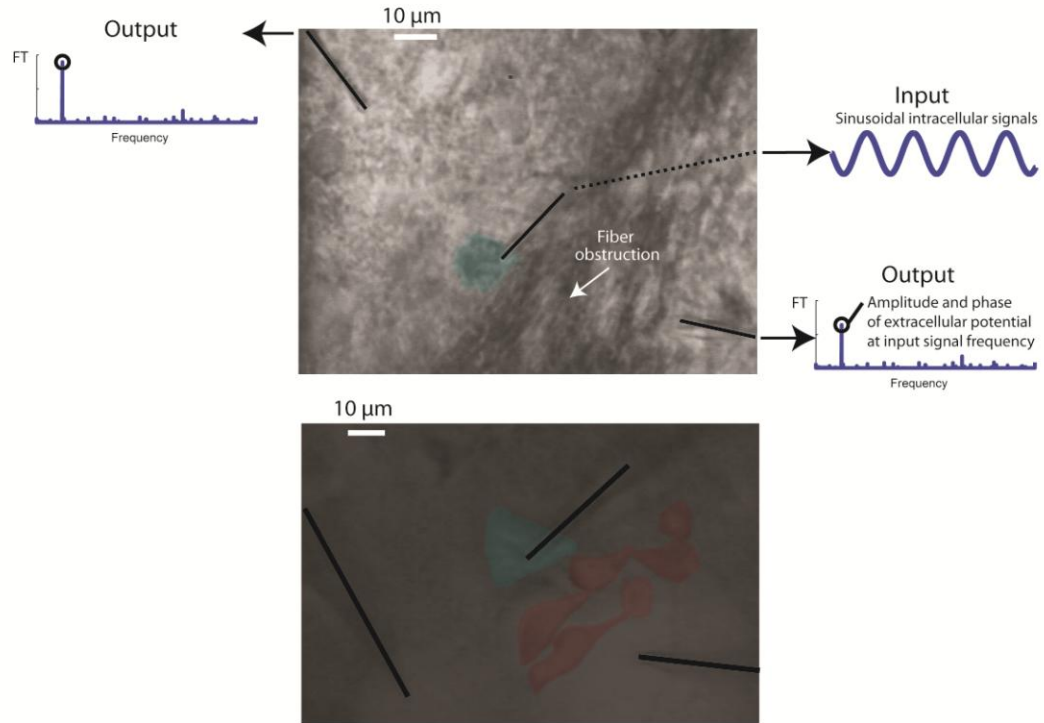
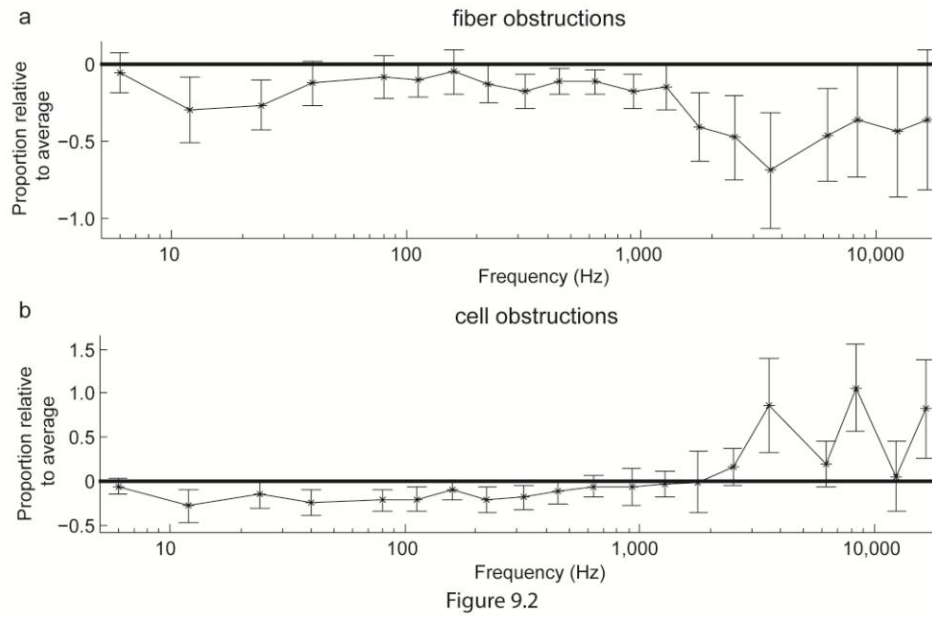


Figure 9.1

Figure 9.2 plots the average across experiments of the obstructed extracellular pipette amplitude minus the unobstructed pipette amplitude within each experiment, normalized so that

the resulting values are in units of the fraction of the average recording's amplitude (see Experimental Procedures). The resulting values thus reflect the fraction of the recorded signal that is changed based on the obstruction status of an extracellular measurement. Negative (positive) values on the plots reflect a relative decrease (increase) in amplitude for obstructed channels. Figure 9.2A shows that along an extracellular path, the presence of axonal fibers that could be seen online under the microscope led to *deleterious* amplitude effects over both low frequencies (defined as 6 to 926 Hz; n=181 across experiments and frequencies; mean: -0.140 (p<0.001); median: -0.109 (p<0.001)) and high frequencies (defined as 1282 Hz to 16.7 kHz; n=124 across experiments and frequencies; mean: -0.417 (p<0.001); median: -0.527 (p <0.01)). Figure 9.2B shows that the presence of cell bodies led to *deleterious* amplitude effects over low frequencies (n=262; mean: -0.156 (p<0.001); median: -0.054 (p<0.01) but *facilitative* effects at high frequencies (n=148; mean: 0.328 (p<0.05); median: 0.271 (p<0.05)).



If these obstructions truly impose a deleterious or facilitative effect on the propagation of signals as suggested in Figure 9.2, the magnitude of the amplitude effects imposed by a given

obstruction should correlate with the severity of the obstruction. For example, when an electrical signal traverses a very large and dense bundle of axonal fibers, a larger-amplitude drop should be observed than when the same signal traverses a smaller, sparser bundle. Across experiments and frequencies, we correlated the differences between the obstructed and unobstructed pipette's amplitudes with our estimation of the degree of the difference in severity of obstructions between the two pipettes for each experiment. The later was determined offline from inspection of microscope images taken at a series of depths during the experiment. A separate estimate for each experiment was used for cell and fiber obstructions individually. Axonal fiber obstruction severity correlated with deleterious amplitude effects for both low frequencies (Figure 9.3A upper panel, Spearman's rho: -0.097, $p < 0.05$, $n = 419$) and high frequencies (Figure 9.3A lower panel, Spearman's rho: -0.331, $p < 0.001$, $n = 260$). Cell body obstruction severity was not correlated with any amplitude effects for low frequencies (Figure 9.3B upper panel, Spearman's rho: 0.081, $p = 0.096$, $n = 419$), and was correlated with facilitative amplitude effects at high frequencies (Figure 9.3B lower panel, Spearman's rho: 0.134, $p < 0.05$, $n = 260$). Taken altogether, the correlations of amplitude effects with obstruction severity across experiments are consistent with and primarily supportive of the obstructions observed in Figure 9.2.

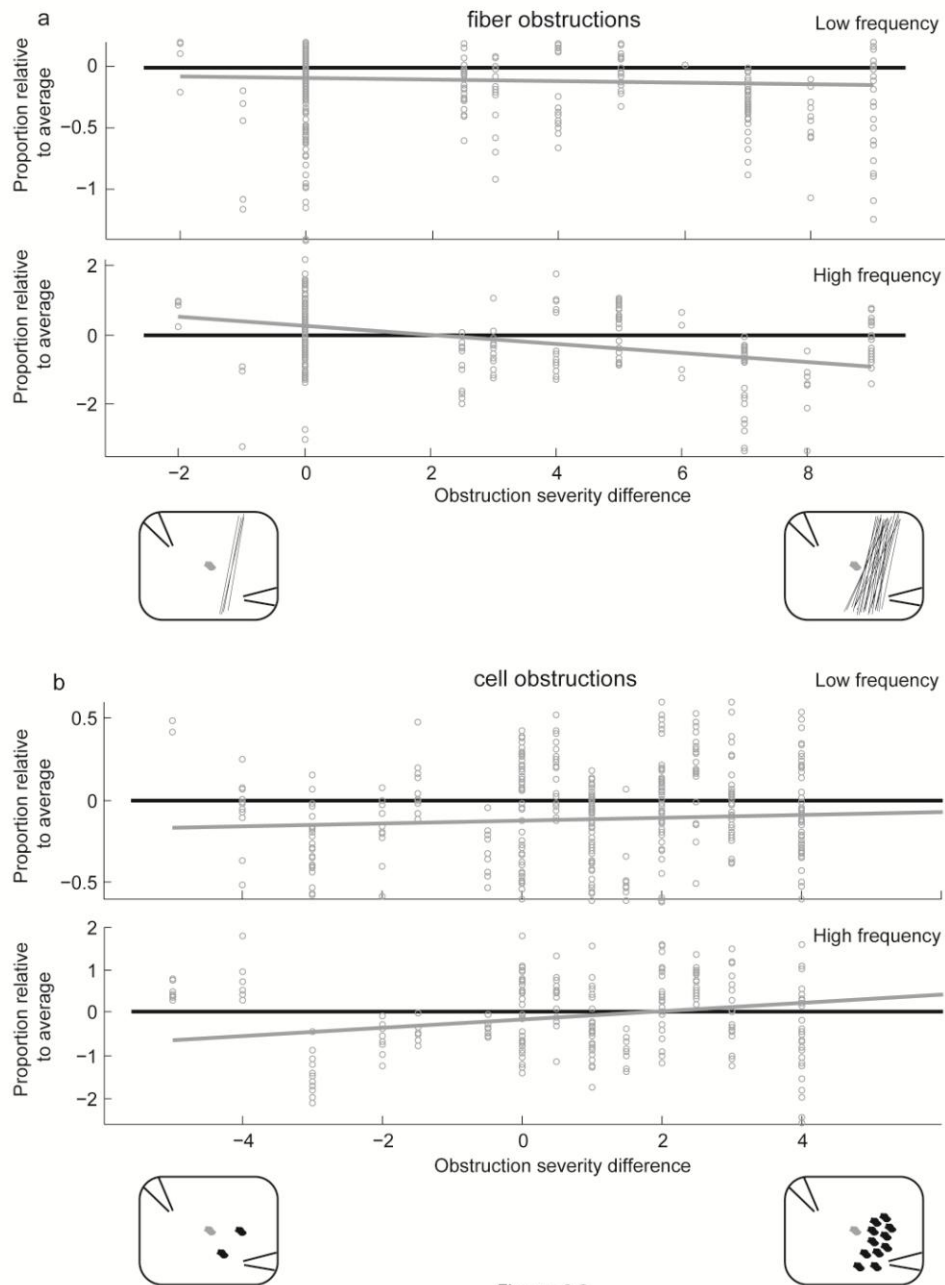
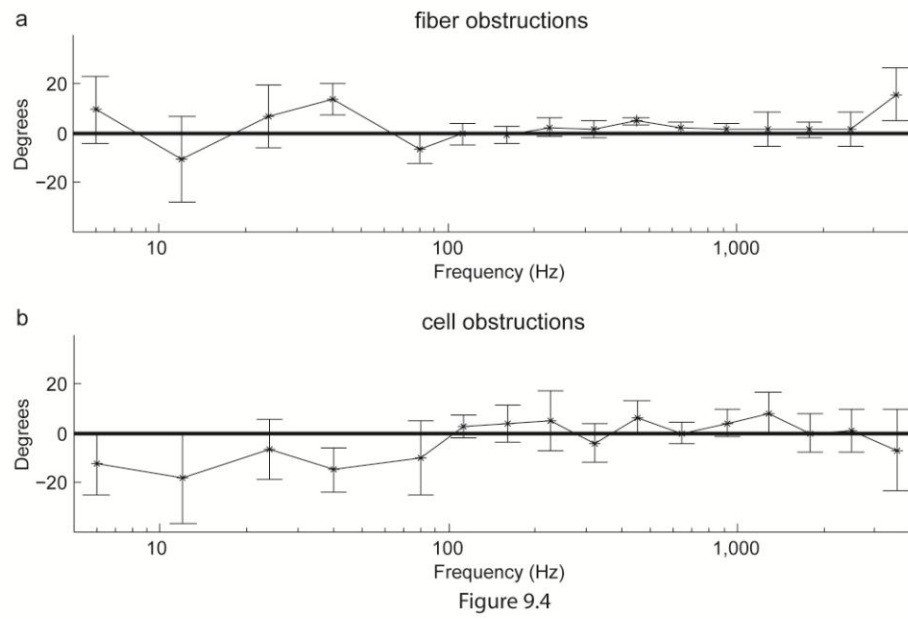


Figure 9.3

Amplitude changes imposed by the obstructions might be accompanied by concomitant phase shifts if the phase angle of the impedance across the obstruction differs from the phase angle

of the impedance of the extracellular space (for further explanation, see the Supplementary Note). Figure 9.4 plots the average across experiments of the obstructed extracellular pipette phase minus the unobstructed extracellular pipette phase within each experiment, normalized so that the resulting values reflect the change in phase of the extracellularly recorded voltage based on the obstruction status of an extracellular measurement (see Experimental Procedures). Positive (negative) values on the plots reflect the obstruction having a more capacitive (resistive) nature than the rest of the extracellular space. A phase near zero corresponds to no difference in the recorded phase between the obstructed and unobstructed channels. For both obstruction types and frequency ranges, we did not observe any phase effects in either direction (for fibers (Figure 9.4A): Low frequencies: $n=181$; mean: 2.17 degrees ($p=0.181$); median: 1.421 degrees ($p=0.747$); High frequencies: $n=124$; mean: -2.10 degrees ($p=0.053$); median: -1.68 degrees ($p=0.530$); for cells (Figure 9.4B): Low frequencies: $n=262$; mean: -3.39 degrees ($p=0.070$); median: 0.442 degrees ($p=0.951$). High frequencies: $n=148$; mean: 4.34 degrees ($p=0.275$); median: 2.67 degrees ($p=0.217$)). The phases also did not correlate with the differences in obstruction severity (for fibers: Low frequencies: Circular-linear correlation coefficient: 0.053, $p=0.154$, $n=419$; High Frequencies: Circular-linear correlation coefficient: 0.057, $p=0.240$, $n=260$; for cells: Low frequencies: Circular-linear correlation coefficient: -0.015, $p=0.697$, $n=419$; High frequencies: Circular-linear correlation coefficient: 0.020, $p=0.685$, $n=260$). This null result suggests that the impedance across the obstructions was on average the same phase as the impedance across an unobstructed extracellular path, though the amplitude results show that the impedance magnitudes are indeed affected by the presence of the obstructions.



DISCUSSION

We used simultaneous extracellular measurements of sinusoidal stimuli that we introduced intracellularly to determine if the presence of microscale inhomogeneities that are inherent to neural tissue affects the propagation of electrical signals originating from a single cell. Axonal fibers imposed deleterious amplitude effects at both high and low frequencies, both of which correlated with the severity of the axonal fiber obstruction. Cell bodies imposed deleterious amplitude effects at low frequencies and facilitative effects at high frequencies that correlated with the severity of the obstruction. However, no significant phase shifts were imposed by either obstruction, suggesting that the impedance across the obstructions had a similar phase angle, though a different magnitude, to that of the rest of the extracellular space.

The most important implications of our data are for the interpretation of measurements of extracellular potentials, specifically for LFPs. LFPs have had a wide impact on neuroscience (O'Keefe and Reece, 1993; Schroeder et al., 1998; Fries et al., 2001; Buzsaki et al., 2002; Peseran et al., 2002; Krieman et al., 2006; Womelsdorf et al., 2006; Peseran et al., 2008; Gregoriou et al., 2009), and there has been recent interest with recent strides made in improving our interpretation of them (Logothetis et al., 2007; Katzner et al., 2009; Xing et al., 2009; Kajikawa and Schroeder, 2011; Linden et al., 2011). This work provides an important piece of that puzzle. These results show that for the range of frequencies corresponding to LFP activity, microscale obstructions impose deleterious amplitude effects to signals propagating across them. Such effects provide a novel sense in which LFPs are not a 'democratic' representation of the average activity of all the cells in a region, in addition to others that have already been shown, though non-experimentally (Lorente de Nó, 1947; Nicholson, 1979; Nunez and Srinivasan, 2006; Linden et al., 2011). Instead, because of the cellular organization of the brain, certain neurons or neuron types would thus likely contribute more to the recorded LFPs than others based on differential presence of obstructions that tend to surround them. For similar reasons, these same effects may contribute to causing the

spiking activity of certain neuron types to be recorded less often than others, as we also observed obstruction effects over the range of spiking frequencies.

Our result suggesting that no considerable phase shifts are imposed across both cell body and fiber obstructions likewise has important consequences, which in this case does simplify the consideration of these effects for the interpretation of LFP data. It is worth clarifying that this result however does not imply that there are no phase shifts at all observed in the extracellular space, just that the phase of the signal does not depend on the presence or absence of these obstructions.

Additionally, this work will also be important to biophysicists and computational neuroscientists who model electrical signal propagation in the brain. Typically this has been modeled as being electrically homogenous (Gold et al., 2006; Nunez and Srinivasan, 2006; Linden et al., 2011), although the effect of the inhomogeneity of the extracellular space has been considered by some (Bedard et al., 2004, 2006). This work provides the first experimental proof of effects specifically related to these inhomogeneities. We show that electrically as well as physically, extracellular space in the brain indeed is not homogenous.

It should be noted that here we investigate the effect of obstructions on a microscale, specifically on the scale of tens of microns and the width of individual cells. The effects of such obstructions are simply untestable with larger electrode surface areas or large inter-electrode separations, for example with the 3 mm interelectrode separation of Logothetis et al. (2007). With such large separation, microscale inhomogeneities of the kind we investigate here would average out across measurements and in all directions tested. This would give the appearance of homogeneity and isotropy, which when considered on the scale of millimeters may indeed be reasonably accurate. It is important to note however that all neural electrical sinks and sources result from the activity of individual cells, on the scale that we investigate here. Thus, even if their effect cannot be studied with larger electrodes and electrode separations, microscale obstructions

should affect how each individual source and sink throughout the brain contributes to the LFP at other locations.

Our results suggest that cell bodies are more obstructive to electrical signals at low frequencies than at high frequencies, which is consistent with existing expectations for the flow of current through biological tissue, including neural tissue (Grimnes and Martinsen, 2000). It should be kept in mind though when comparing between low and very high frequencies in our data that lower stimulus amplitudes were applied at higher frequencies as a result of high-cut filters in the equipment (see Experimental Procedures).

The types of cells comprising the cell body obstructions in our experiments generally could not be distinguished, and likely include all neuronal and glial cell types. Earlier claims by David Robinson (1968) were that microscale inhomogeneities, and specifically the ubiquitous presence of glial cells, were responsible for obstructing the spatial propagation of extracellular action potential waveforms in the brain, and thereby affecting the ability of extracellular electrodes to record spiking activity. Our data is supportive of Robinson's overall claim, showing that axonal fibers are obstructive at the frequencies corresponding to action potential waveforms, and extends his claim further to demonstrate the obstruction of the propagation of LFP activity. However his specific claim that glial cells were the primary culprit hindering the extracellular propagation of action potentials appears not to be the case based on our data with cell body obstructions at high frequencies. Regardless of the specific source of the obstructions, our own anecdotal experience from performing awake behaving monkey extracellular recordings, and perhaps that of other neurophysiologists, agrees with the picture Robinson describes. Notably, this disagrees with the picture of an electrically homogenous space, which is explicitly portrayed best by Gold et al. (2006). If extracellular space were effectively homogenous, then as a recording electrode changes position, every neurons' action potential waveform would vary continuously in size and shape as the neuron moves closer to or further away from the electrode tip (Gold, et. al, 2006). In our

experience this does occur at times, but instead a majority of action potential waveforms often suddenly appear with a small advance of an electrode of a few microns.

The effects of axonal fiber obstructions were stronger, more straightforward and consistent across frequencies as compared to the effect of cell body obstructions. It seems likely that this effect may result from the myelination itself around the axonal fibers given the electrical properties of myelin (Weiss, 1997), which are known to be present in the striatum at the age of the rats we used. We did not attempt to specifically adjust the level of myelination of axonal fibers, either by large differences in the age of the rats or through the use of demyelination agents, though this could be an interesting manipulation to perform in future studies. A positive result might suggest that the use of electrical impedance measurements could perhaps be assistive for the diagnosis and assessment of clinical treatments for multiple sclerosis, for example.

Caveats and limitations

In our experiment, there are a number of variables across sessions that we could not control for with this methodology that could conceivably influence the results of any given recording session in any given direction. Importantly though, such effects would cancel out over the balance of our experiments. For example, other obstructions to current flow that are not visible with this methodology are certainly also present in the slice during these experiments, and these could bias the propagation of signals in any particular direction over another. Another example of such an effect is the morphology of the patched cells and their dendritic structures, which may favorably transfer current in particular directions. But such effects would be expected to occur equally as often in favor of a particular result as they occur against it. The net effect should be that these are just sources of random inter-experiment noise that effectively cancel out over the course of enough experiments. Our ability to effectively manage these sources of inter-experiment

variability is aided by the within experiment comparisons of our experimental design, and the balancing of any conditions that we could control.

The data we present here was recorded from the striatum, but there is no particular reason to think that the nature of these effects should differ from one brain area to another. Even if the packing densities of cells and the density and types of membrane channels differs between locations in the brain, the basic nature of cell bodies and axonal fibers as extracellular obstructions to electrical signal transmission in relation to brain extracellular fluid should be similar throughout the brain. At the very least, our demonstration of the effects of these obstructions in the striatum should call into doubt any claims of the effect not existing in other areas. Thus we feel our results apply to extracellularly record potentials everywhere in the brain.

We were limited to performing these experiments in brain slices in order to easily image the extracellular environment for placement of the extracellular pipettes into obstructed and unobstructed locations. However we believe our demonstration of these effects in an *ex-vivo* brain slice strongly indicates that the same basic effects would be present in the intact brain, even if there may be some quantitative differences in the magnitude of the effects. In fact it is possible that the effects would be even larger in an in-tact brain, given that in our slice preparation, current can easily travel out of the slice and through the bath and avoid obstructions and the tissue altogether, while in an intact brain, obstructions have the possibility to encapsulate electrical sources and sinks in all 3 dimensions. Further experiments in an intact brain however would of course be necessary to know the extent of these effects in that domain.

EXPERIMENTAL PROCEDURES

Recording procedures

All experiments were performed in accordance with local animal welfare committee (Center for Interdisciplinary Research in Biology) and EU guidelines (directive 86/609/EEC). Every precaution was taken to minimize stress and the number of animals used in each series of experiments.

Patch-clamp recordings of striatal neurons were performed in horizontal brain slices (330 μ m) from Oncins France Strain A (OFA) rats (Charles River, L'Arbresle, France) (postnatal days P₁₇₋₂₅), using procedures described previously (Fino et al., 2005). We chose to perform these recordings in the striatum because it is generally a silent structure in a slice preparation. This aided the signal-to-noise ratio of the detection of the small extracellular sinusoidal signals necessary for the experiment. Additionally, the less structured organization of the extracellular space within the striatum provided an opportunity to find a variety of obstruction types and environments for testing. Using a temperature control system (Bathcontroller V, Luigs & Neumann, Ratingen, Germany) most recordings were performed at 34°C, with several recordings performed at 26°C to ease the patching of target cells. Slices were bathed in and continuously superfused at 2–3 ml/min with an extracellular solution similar to artificial cerebro-spinal fluid (mM): 125 NaCl, 2.5 KCl, 25 glucose, 25 NaHCO₃, 1.25 NaH₂PO₄, 2 CaCl₂, 1 MgCl₂. Three borosilicate glass pipettes of 9–15 M Ω impedance were used during the experiment, one to patch an individual cell and two to perform simultaneous extracellular voltage recordings at nearby locations in the slice. The intracellular pipette was filled with (mM): 105 K-gluconate, 30 KCl, 10 HEPES, 10 phosphocreatine, 4 ATP-Mg, 0.3 GTP-Na, 0.3 EGTA (adjusted to pH 7.35 with KOH). The extracellular pipettes were filled with the same solution used to bathe the slice. Recordings were made with EPC 10-3 amplifiers (HEKA Elektronik; Lambrecht, Germany) with a very high input impedance (~ 1 T Ω). The series resistance for all pipettes were compensated at 75–80%. For all experiments, a circular reference electrode surrounding the slice was used to avoid biasing current travel in any direction.

During the experiment, individual neurons and the microscale local composition of the extracellular space were identified using infrared-differential interference contrast microscopy with a CCD camera (Optronis VX45; Kehl, Germany). A target cell was first chosen based on apparent cell health and the availability of two adequate extracellular recording locations relative to the cell. The extracellular locations were chosen to provide, at approximately the same absolute distances from the patched cell, a sufficiently large contrast between the two locations in the severity of obstructions that were visible in the microscope images along their extracellular paths from the target cell. The two extracellular pipettes were positioned in these locations, and the target cell was then patched with the intracellular pipette. Sinusoidal stimuli were then introduced intracellularly to the patched cell while simultaneously recording the voltages extracellularly in the two locations. The median distance between the patched cell and the extracellular pipettes was 65 microns, and the median absolute difference of this distance to the patched cell between the two extracellular pipettes within each recording was 10 microns.

Immediately following the experiment, microscope images were digitally recorded every 5–10 microns above and below the patched cell to verify offline the visible obstructions along the extracellular path between the patched cell and each extracellular pipette. Visible obstructions typically included cell bodies and clusters of cell bodies, axonal fibers and blood vessels. We focused on axonal fiber and cell body obstructions, performing 18 recordings with axonal fibers as the most prominent obstruction, and 33 recordings with cell bodies as the most prominent obstruction. For the image correlation analyses (see below) we included data from one recording with a blood vessel as the primary obstruction. The same hardware channel was always used to perform the intracellular patch. The obstructed and unobstructed status of the two extracellular hardware channels were balanced across experiments individually within both the group of axonal fiber obstruction recordings and the group of cell body obstruction recordings.

Stimuli

Recordings were performed while introducing electrical sinusoidal waveforms intracellularly. 20 different frequencies were tested, varying approximately evenly on a logarithmic scale ranging from 6 Hz to 16.7 kHz. The specific frequencies tested were: 6, 12, 24, 40, 80, 113, 160, 225, 321, 450, 641, 926, 1282, 1786, 2500, 3571, 6250, 8333, 12500, and 16667 Hz. Stimuli from 6 Hz to 1282 Hz were sampled at 16.7 kHz; stimuli above 1282 Hz were sampled at 50 kHz. Due to the occasional loss of the patch during the course of the experiment, not all frequencies were collected for every recording. Extracellularly recorded traces were weak and were typically not visibly apparent in single traces, but they could be detected after averaging multiple traces. 100 to 300 traces of 100 to 1500 ms in length were averaged before recording the data to disk for offline analyses. Longer stimulus lengths and more traces were necessary for the low frequency stimuli. For some recordings, the stimuli were presented in order of increasing frequency, but for the majority of the recordings the order of the presentation of the frequencies was randomized. Results were similar for each order of frequency presentation.

Stimuli were introduced with the intracellular electrode in current clamp mode for most experiments, and in voltage clamp mode for several recordings. Results between the two methods were similar and the data are thus pooled together. The injected current amplitudes ranged from 200 to 300 pA. At stimulus frequencies of 2.5 kHz and above, current amplitudes were progressively lower as a result of high-cut filters with a cutoff frequency of 10 kHz applied to the stimulus. Importantly, the extracellularly recorded voltages were unfiltered before their recording. Before conducting experiments, we verified that any amplitude changes or phase shifts in the recordings across frequencies were negligible, via control recordings with an external signal generator in the bath without a slice (Nelson et al., 2008).

Analyses

Offline analyses were conducted in Matlab (Natick, MA). We determined the amplitude and phase of each recorded digitized signal by first averaging the waveform across all the cycle lengths of the known input frequency corresponding to that recording. The amplitude was then taken as $\sqrt{2}$ times the root mean square of the resulting waveform. The phase was determined by taking the four quadrant inverse tangent of a 2 dimensional projection of the resulting waveform. The x coordinate of the projection was the correlation (in the signal processing sense) of the resulting waveform with a cosine waveform, and the y coordinate was the correlation with a cosine waveform shifted forward by 90 degrees. As indicated by the Fourier transform of a sample recording in Figure 9.1, the amplitude of the recorded extracellular signals at the frequency corresponding to the input stimulus was typically well-separated from the noise. We tested several other methods to measure the amplitude and phase of the digitized signals, including a normalized Fourier transform, all of which yielded near-identical results.

To view the effect of the obstructions, we normalized each recording as follows. Extracellular values were first normalized by the recorded estimates of the intracellular current in each experiment. We then computed the average normalized voltages recorded for each extracellular hardware channel across all the experiments in each analysis, which included an equal number of recordings when the hardware channel was obstructed or unobstructed. Each individual extracellular recording was then normalized relative to this mean for its channel, and within experiment comparisons were then performed across the extracellular channels using these normalized values. Normalization refers to dividing the original amplitude by the normalizing amplitude, and subtracting the normalizing phase from the original phase. For the within experiment comparison for the amplitude results, the unobstructed channel's amplitude was subtracted from the obstructed channel's amplitude. Thus the amplitude results can be interpreted as the fraction of the average recording amplitude represented by each signal that was changed

with the addition of the corresponding obstruction to the extracellular path. Negative (positive) values indicate that the amplitude was lower (higher) because of the presence of the obstruction. For the within experiment comparison for the phase results, the unobstructed channel's phase was subtracted from the obstructed channel's phase. Thus the phase can be interpreted as the voltage phase shifts imposed by the obstruction. Positive (negative) values indicate that the extracellular current paths to the obstructed pipette locations was more capacitive (resistive) than the unobstructed paths through the extracellular space itself. Note that a phase value of 0 would reflect that no additional phase shifts were imposed by the obstructions, and does not reflect that the intracellular current and the extracellular voltage were in phase with each other overall.

We also investigated using a separate normalization procedure in which we compared the values from each channel to the corresponding values from a nonpatch control recording in which the two extracellular pipettes were placed in a slice within a few microns of the normal intracellular pipette without a cell being patched. The results using this normalization were similar to the results we present here.

Statistics— mean and median effects

To test the mean and median differences, we pooled the data across low (6 to 926 Hz) and high (1282 Hz to 16.7 kHz) frequencies and tested each group separately. Note that none of the results are critically dependent on the specific divisions between high and low frequencies. For amplitudes, we tested the significance of the mean differences with paired t-tests between obstructed and unobstructed channels across frequencies and experiments, and we tested the significance of the median differences with signed rank tests. For phases, we tested the significance of mean differences following procedures described in Fisher (1993), and we tested the significance of median differences using code taken from the circular statistics toolbox in Matlab (Berens, 2009).

Image analysis

The microscope images recorded during each session were analyzed offline to verify that the effects of the obstructions on the recorded signals correlated with the severity of the obstructions. The offline image scoring was done blindly, with the same experimenter scoring all of the sessions. Each extracellular pipette from each session received two scores from 0 to 9 reflecting the severity of the corresponding obstruction type along the extracellular path from the cell to the pipette. One score was given for the severity cell body obstructions present, and one score was given for the severity of axonal fiber obstructions present.

The within experiment differences between the extracellular pipettes for the given obstruction type score was then correlated across sessions with the within experiment normalized amplitude and phase differences between the channels (see above). For the amplitudes, a nonparametric spearman correlation was used. A negative correlation corresponds to more deleterious amplitude effects as the difference in the severity of the obstructions between the two pipettes becomes larger. For the phases, a circular-linear correlation was performed, following procedures described in Fisher (1993, p. 161). A negative correlation corresponds to an increasingly more capacitive phase shift imposed by the obstruction as the difference in the severity of the obstructions between the two pipettes becomes larger. Values were pooled across frequencies into the same low and high frequency groups used to test the mean and median differences. There were 3 sessions for which the images could not be scored, and these were excluded from the analysis.

We also investigated other methods to score the images offline, including using a simple overall impression of the obstruction differences between the channels for each session, or by

focusing on just the obstructions near the patched cell or near each extracellular pipette. All of these methods yielded similar results.

ACKNOWLEDGEMENTS

Matthew Nelson was supported by the Programme de bourses d'excellence Eiffel.

REFERENCES

Anastassiou, A.C., Perin, R., Markram, H., and Koch, C. (2011). Ephaptic coupling of cortical neurons. *Nat. Neurosci.* *14*, 217–223.

Bedard, C., Kroger, H., and Destexhe, A. (2004). Modeling extracellular field potentials and the frequency-filtering properties of extracellular space. *Biophys. J.* *86*, 1829–1843.

Bedard, C., Kroger, H., and Destexhe, A. (2006). Modeling of low-pass filtering of local field potentials in brain tissue. *Phys. Rev. E* *73*, 051911.

Berens, P. (2009). CircStat: A Matlab Toolbox for Circular Statistics. *J Stat. Softw.* *31*, 1–21.

Buzsaki, G. (2002). Theta oscillations in the hippocampus. *Neuron* *33*, 325–340.

Braitenberg, V., and Schuez, A. (1998). *Cortex: Statistics and geometry of neuronal connectivity*, 2nd ed. (Berlin, Germany: Springer-Verlag).

Fino, E., Glowinski, J., and Venance, L. (2005). Bidirectional activity-dependent plasticity at corticostriatal synapses. *J. Neurosci.* 25, 11279–11287.

Fisher, N.I. (1993). *Statistical analysis of circular data.* (Cambridge, UK: Cambridge University Press).

Fries, P., Reynolds, J.H., Rorie, A.E., Desimone, R. (2001). Modulation of oscillatory neuronal synchronization by selective visual attention. *Science* 291, 1560–1563.

Frohlich, F., and McCormick, D.A. (2010). Endogenous electric fields may guide neocortical network activity. *Neuron* 67, 129–143.

Gold, C., Henze, D.A., Koch, C., and Buzsaki, G. (2006). On the origin of the extracellular action potential waveform: A modeling study. *J. Neurophys.* 95, 3113–3128.

Gregoriou, G.G., Gotts, S.J., Zhou, H., and Desimone, R. (2009). High-frequency, long-range coupling between prefrontal and visual cortex during attention. *Science* 324, 1207–1210.

Grimnes S., and Martinsen, O.G. (2000). *Bioimpedance & bioelectricity basics.* (London, UK: Academic Press: London), pp. 99–101.

Kajikawa, Y., and Schroeder, C.E. (2011). How local is the local field potential? *Neuron* 72, 847–858.

Katzner S., Nauhaus I., Benucci A., Bonin V., Ringach D.L., and Carandini M. (2009). Local origin of field potentials in visual cortex. *Neuron* 61, 35–41.

Krieman, G., Hung, C.P., Kraskov, A., Quiroga, R.Q., Poggio, T., and DiCarlo, J.J. (2006). Object selectivity of local field potentials and spikes in the macaque inferior temporal cortex. *Neuron* 49, 35–41.

Leung L.S. (1990). Field Potentials in the central nervous system: Recording, analysis, and modeling. In *Neuromethods, Vol. 15: Neurophysiological techniques: application to neural Systems*. (Clifton, NJ: The Humana Press Inc.), pp 277–312.

Linden, H., Tetzlaff, T., Potjans, T.C., Pettersen, K.H., Grün, S., Diesmann, M., and Einevoll, G.T. (2011) Modeling the Spatial Reach of the LFP. *Neuron* 72, 859–872.

Logothetis, N.K., Kayser, C., and Oeltermann, A. (2007). In vivo measurement of cortical impedance spectrum in monkeys: implications for signal propagation. *Neuron* 55, 809–823.

Lorente de Nó, R. (1947) Action potential of the motoneurons of the hypoglossus nucleus. *J. cell comp. Physiol.* 29, 207–288.

Nelson, M.J., Pouget, P., Nilsen, E.A., Patten, C.D., and Schall, J.D. (2008). Review of signal distortion through metal microelectrode recording circuits and filters. *J. Neurosci. Meth.* 169, 141–157.

Nicholson, C. (1979) Generation and analysis of extracellular field potentials. In *Electrophysiological techniques: Society for Neuroscience short course*. (Bethesda, MD: Society for Neuroscience), pp 93–148.

Nunez P.L., and Srinivasan, R. (2006) *Electric fields of the brain: The neurophysics of EEG 2nd edition* (New York, NY: Oxford University Press).

O'Keefe, J., and Recce, M.L. (1993). Phase-relationship between hippocampal place units and the EEG theta rhythm. *Hippocampus* 3, 317–330.

Pesaran, B., Pezaris, J.S., Sahani, M., Mitra, P.P., and Andersen, R.A. (2002). Temporal structure in neuronal activity during working memory in macaque parietal cortex. *Nat. Neurosci.* 5, 805–811.

Pesaran, B., Nelson, M.J., and Andersen, R.A. (2008). Free choice activates a decision circuit between frontal and parietal cortex. *Nature* 453, 406–409.

Peters, A., Palay, S.L., and Webster, H.F. (1991). *The Fine structure of the nervous system*. (Oxford, UK: Oxford University Press).

Robinson, D.A. (1968). The electrical properties of metal microelectrodes. *P. IEEE* 56, 1065–1071.

Schroeder, C.E., Mehta, A.D., and Givre, S.J. (1998). A spatiotemporal profile of visual system activation revealed by current source density analysis in the awake macaque. *Cereb. Cortex* 8, 575–592.

Siapas, A.G., Lubenov, E., and Wilson, M.A. (2005). [Prefrontal phase-locking to hippocampal theta oscillations](#). *Neuron* 46, 141–51.

Weiss T.F. (1997). *Cellular biophysics*. (Cambridge, MA: The MIT Press), pp. 293–350.

Womelsdorf, T., Fries, P., Mitra, P.P., and Desimone, R. (2006). Gamma-band synchronization in visual cortex predicts speed of change detection. *Nature* 439,733–736.

Xing, D., Yeh, C.I., and Shapley, R.M. (2009). Spatial spread of the local field potential and its laminar variation in visual cortex. *J Neurosci* 29, 11540–11549.

FIGURE LEGENDS

Figure 9.1. Diagram of Experiment. Microscope image taken during a sample experiment. The top panel shows an experiment with a fiber obstruction, and the bottom panel shows an experiment with a group of cell bodies obstruction. Black bars indicate the location of the pipettes. The patched cell in each panel has been shaded green. In the upper panel the fiber obstruction traversing the entire image has been indicated with a white arrow. In the lower panel, the extracellular obstruction cell bodies have been shaded red. Sine wave stimuli were introduced intracellularly, then simultaneously measured extracellularly at the two locations in the slice. As

indicated in the example, the amplitude of the extracellular voltage signal at the frequency of the input signal was well separated from the surrounding noise.

Figure 9.2. Amplitude effects. The mean change in the extracellular signal amplitude imposed by the presence of the corresponding obstruction type, taken as the mean across experiments of the obstructed channel's amplitude minus the unobstructed channel's amplitude. Errorbars show the standard error of the mean. Data is normalized to be in units of the proportion relative to the overall average signal amplitude. A. Axonal fiber obstructions. B. Cell body obstructions

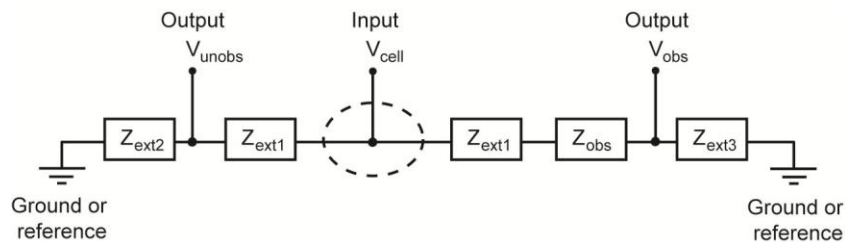
Figure 9.3. Correlations with obstruction severity. For each experiment and frequency, the normalized difference between the obstructed and unobstructed channel amplitudes is plotted against the difference between the two channels in the severity of the corresponding obstruction type, as assessed offline from inspection of the microscope images of each experiment. A. Axonal fiber obstructions. B. Cell body obstructions. The upper panels of A and B correspond to low frequency data, while the lower panels correspond to high frequency data. Linear regression lines are included. Some data exist outside the y-axis limits shown here.

Figure 9.4. Phase effects. The mean change in the extracellular signal phase imposed by the presence of the corresponding obstruction type, taken as the circular mean across experiments of the obstructed channel's phase minus the unobstructed channel's phase. Errorbars show the circular standard error of the mean. Phases above 6 kHz were more variable and are not shown. A. Axonal fiber obstructions. B. Cell body obstructions.

Supplementary Note for: Electrical signal distortion in neural tissue on a microscale

Matthew J. Nelson, Clémentine Bosch, Laurent Venance, Pierre Pouget

A simplified model of the electrical circuit for this experiment is shown below.



V_{unobs} corresponds to the voltage on the outer surface of the patched cell, which we indirectly manipulate with input intracellular sinusoidal stimuli. For simplification, this basic model assumes that that voltage is the same everywhere on the outer surface of the cell. The implications of the model that we discuss here hold whether considering voltage source or current source stimuli.

V_{obs} and V_{cell} correspond to the voltages measured at the unobstructed and obstructed pipette locations, respectively. Z_{ext1} and Z_{ext2} correspond to the impedance of over different portions of the ‘typical’ extracellular space. Z_{ext1} corresponds to the length from the cell to the pipettes, and Z_{ext2} corresponds to the length following the pipettes before reaching the ground or the reference electrode. On average, each Z_{ext} term on one side of the model circuit is expected to be equal to the same term on the other side of the circuit. Z_{obs} is the impedance of a given obstacle. Note that all of these values may be frequency dependent.

Modeling the experiment in this way, the only difference between what determines V_{obs} and

V_{unobs} is the added effect of Z_{obs} in determining V_{obs} . Recognizing that this circuit amounts

to a voltage divider on either side of Z_{in} , the outputs V_{out} and $V_{\text{out,ext}}$ are expressed by this model as:

$$V_{\text{out,ext}} = V_{\text{in}} \frac{Z_{\text{out,ext}}}{Z_{\text{in}} + Z_{\text{out,ext}}}; \quad V_{\text{out}} = V_{\text{in}} \frac{Z_{\text{out}}}{Z_{\text{in}} + Z_{\text{out,ext}} + Z_{\text{out}}} \quad (1)$$

All voltage (V) and impedance (Z) variables are complex values that have magnitudes and phases. For the voltages, the magnitude and phase determine the amplitude and phase, respectively, of the resulting sinusoidal waveform. The differences between V_{out} and $V_{\text{out,ext}}$ and the input V_{in} will be determined by the resulting phase and magnitude of the right-hand term involving all of the impedance components.

If the magnitude of Z_{out} is appreciable relative to $Z_{\text{in}} + Z_{\text{out,ext}}$ i.e. the entire impedance through the typical extracellular path, then the amplitude of V_{out} will be lower than the amplitude of $V_{\text{out,ext}}$.

The phase effect of Z_{out} is determined by both its magnitude and phase relative to Z_{in} and $Z_{\text{out,ext}}$. When multiplying and dividing complex numbers, phases are, respectively, added and subtracted independently of the numbers' magnitudes. When adding and subtracting complex numbers, the resulting phase is the phase of the separately summed real and imaginary fractions, which means that larger numbers contribute more to the phase of the resulting sum. This results in:

$$\angle(V_{\text{out,ext}}) - \angle(V_{\text{in}}) = \angle(Z_{\text{out,ext}}) - \angle(Z_{\text{in}} + Z_{\text{out,ext}}) \quad (2)$$

$$\angle(V_{\text{out}}) - \angle(V_{\text{in}}) = \angle(Z_{\text{out,ext}}) - \angle(Z_{\text{in}} + Z_{\text{out,ext}} + Z_{\text{out}}) \quad (3)$$

where $\angle (X)$ refers to the phase of X .

A purely resistive impedance has a phase of 0, while a purely capacitive impedance has a phase of -90. The phases of Z_{11} and Z_{22} are equal as they both result from the same typical extracellular path. Thus, $\angle(Z_{11} + Z_{22})$ would be the same as $\angle(Z_{22})$, and the phase of $Z_{11}Z_{22}$ would be the same as Z_{22} in this model.

If the magnitude of Z_{11} approaches zero, then its phase is irrelevant in determining $\angle(Z_{11} + Z_{22})$. However, if the magnitude of Z_{11} is appreciable relative to the magnitude of $Z_{11} + Z_{22}$, and the amplitude results of Figures 9.2 and 9.3 show that this is indeed the case for some obstructions, then the phase of Z_{11} will affect the phase of $Z_{11}Z_{22}$. This phase shift of the voltage will occur to the extent that the phase of Z_{11} is different than the phase of Z_{11} and Z_{22} . However if the phase of Z_{11} is the same as Z_{11} and Z_{22} , then regardless of its magnitude, the phase of $\angle(Z_{11} + Z_{22})$ would be the weighted average phase of three terms that all have the same phase. The resulting phase would thus be the same as $\angle(Z_{22})$, and as suggested by equation 3, there would be no resulting phase shift in $Z_{11}Z_{22}$. The pattern of results in the data we present where there are considerable amplitude attenuations but no significant phase shifts is suggestive that this is the case with the obstructions that we have tested.

More generally, any phase shift in the extracellular space would have to be brought about by changes in the phase of the individual components impeding current flow.

Chapter contributions and status of publications

Chapter 1: Contributions from Bijan Pesaran, Matthew J. Nelson and Richard A. Andersen

Division of Biology, Mail Code 216-76, California Institute of Technology,

Pasadena, CA 91125

Published in *Neuron*, 2006

Chapter 2: Contributions from Bijan Pesaran¹, Matthew J. Nelson² and Richard A. Andersen^{2,3}

¹*Center for Neural Science, New York University, New York, NY 10003*

²*Computation and Neural Systems Program, Mail Code 216-76, California Institute of Technology, Pasadena, CA 91125*

³*Division of Biology, Mail Code 216-76, California Institute of Technology, Pasadena, CA 91125*

Published in *Journal of Neuroscience*, 2010

Chapter 3: Contributions from Bijan Pesaran^{1,3}, Matthew J. Nelson² and Richard A. Andersen^{2,3}

¹*Center for Neural Science, New York University, New York, NY 10003, USA*

²*Computation and Neural Systems Program, California Institute of Technology, Pasadena, CA 91125, USA*

³*Division of Biology, California Institute of Technology, Pasadena, CA 91125, USA*

Published in *Nature*, 2008

Chapter 4: Contributions from Matthew J. Nelson^{1,2}, Ayan Ghoshal³, Ford F. Ebner³, Pierre Pouget¹

¹*CR-ICM, INSERM UMRS 975, CNRS 7225, Université Pierre et Marie Curie, Paris, France.*

²*Computation & Neural Systems, California Institute of Technology, Pasadena, CA, USA*

³*Department of Psychology, Vanderbilt University, Nashville, TN, USA*

Accepted to special issue of *Frontiers in Perception Science*, 2011

Chapter 5: Contributions from Matthew J. Nelson^{1,2}, Leanne Boucher¹, Gordon D. Logan¹, Thomas J. Palmeri¹, Jeffrey D. Schall¹

¹ *Center for Integrative & Cognitive Neuroscience, Vanderbilt Vision Research Center, Department of Psychology, Vanderbilt University, Nashville, TN, USA.*

² *California Institute of Technology, Pasadena CA, USA.*

Published in *Attention, Perception & Psychophysics*, 2011

Chapter 6: Contributions from Matthew J. Nelson^{1,2}, Pierre Pouget¹, Erik A. Nilsen³, Craig D. Patten³, Jeffrey D. Schall¹

¹ *Center for Integrative & Cognitive Neuroscience, Vanderbilt Vision Research Center, Department of Psychology, Vanderbilt University, Nashville, TN, USA.*

² *California Institute of Technology, Pasadena CA, USA.*

³ *Plexon Inc. Dallas TX, USA.*

Published in *Journal of Neuroscience Methods*, 2008

Chapter 7: Contributions from Mathew J. Nelson^{1,2}, Pierre Pouget¹

¹ *CRICM,, Inserm UMRS 975, CNRS 7225, Université Pierre et Marie Curie, Hôpital de la Salpêtrière, Paris, France 75651.*

² *California Institute of Technology, Pasadena CA, USA 91125*

Published commentary in *Journal of Neurophysiology*, 2010

Chapter 8: Contributions from Matthew J. Nelson^{1,2}, Pierre Pouget¹

¹ *CRICM, Inserm UMRS 975, CNRS 7225, Université Pierre et Marie Curie, Hôpital de la Salpêtrière, Paris, France 75651.*

² *California Institute of Technology, Pasadena CA, USA 91125*

Published in *Journal of Neurophysiology*, 2012

Chapter 9: Contributions from Matthew J. Nelson^{1,2}, Clémentine Bosch^{3,4}, Laurent Venance^{3,4}, Pierre Pouget¹

¹ *CRICM, Inserm UMRS 975, CNRS 7225, Université Pierre et Marie Curie, Hôpital de la Salpêtrière, Paris, France 75651.*

² *California Institute of Technology, Pasadena CA, USA 91125*

³ *Team Dynamic and Pathophysiology of Neuronal Networks, Center for Interdisciplinary Research in Biology (CIRB), CNRS UMR 7241/Inserm U1050, Collège de France, Paris, France 75005*

⁴ *University Pierre et Marie Curie, ED 158, 75005 Paris, France*

Preparing to submit

Minor publications

Pouget P., Stepniewska I., Crowder E. A., Leslie M. W., Emeric E. E., **Nelson M. J.**, and Schall J. D. (2009) Visual and motor connectivity and the distribution of calcium-binding proteins in macaque frontal eye field: implications for saccade target selection. *Frontiers in Neuroanatomy*. 3:2.

Pouget, P., **Nelson, M. J.**, Cohen, J. Y., and Heitz, R. P. (2007) Pulse-pattern sensitivity in the frontal eye field of the macaque monkey. *Journal of Neuroscience* 27: 11780-11781. (Commentary)

